Additively manufactured biodegradable porous metals

Li, Yageng

Important note
To cite this publication, please use the final published version (if applicable).
Please check the document version above.

Additively manufactured biodegradable porous metals

Yageng LI

Additively manufactured biodegradable porous metals

Dissertation

for the purpose of obtaining the degree of doctor
at Delft University of Technology
by the authority of the Rector Magnificus prof. dr. ir. T.H.J.J. van der Hagen
chair of the Board for Doctorates
to be defended publicly on
Wednesday 18 March 2020 at 12:30 o' clock

by

Yageng Li

Master of Engineering, University of Science and Technology Beijing, Beijing, China
born in Shanxi, China

This dissertation has been approved by the

promotors: Prof. dr. A. A. Zadpoor and Dr. ir. J. Zhou

An electronic version of this dissertation is available at

https://repository.tudelft.nl/.

Summary

For the treatment of large bony defects, no perfect solution has been yet found, partially due to the unavailability of ideal bone implants. Additively manufactured (AM) biodegradable porous metals provide unprecedented opportunities to fulfil the requirements for ideal bone implants to be used in such treatments. Firstly, the multi-scale geometry of these implants can be customized to mimic the human bone in terms of both micro-architecture and mechanical properties. Secondly, a porous structure with interconnected pores possesses a larger surface area and is favorable for the adhesion and proliferation of bone cells. Finally, the biodegradation property could be exploited to maintain the structural integrity of the implant during the healing process while ensuring that the biomaterial disappears afterwards, paving the way for full bone regeneration.

In Chapter 2-4, we used selective laser melting (SLM) to fabricate topologically ordered porous magnesium (WE43), iron, and zinc scaffolds based on the diamond unit cell. We conducted comprehensive studies on the microstructure, *in vitro* biodegradation behavior (up to 4 weeks), electrochemical performance, time-dependent mechanical properties, and cytocompatibility of the developed scaffolds. For AM WE43 scaffolds, a unique mechanism of biodegradation was observed that started with uniform corrosion, followed by localized corrosion, particularly in the center of the scaffolds. For AM iron scaffolds, electrochemical tests showed up to ≈ 12 times higher rates of biodegradation as compared to the degradation rate of cold-rolled (CR) iron, while 3.1% of weight loss was measured after 4 weeks of immersion tests. The biodegradation mechanisms were found to be topology-dependent and different between the periphery and central parts of the scaffolds. AM zinc scaffolds lost 7.8% of their weight after 4 weeks of dynamic biodegradation. The biodegradation mechanisms were found to be location-dependent as well and differed from the top of the specimens to the bottom. The mechanical properties of the AM WE43 (E = 700-800 MPa) scaffolds, iron scaffolds (E = 1600-1800 MPa), and zinc scaffolds (E = 700-1000 MPa) fell within the range of the values reported for the trabecular bone even after 4 weeks of biodegradation. AM magnesium scaffolds showed level 0 cytotoxicity up to 72 h (according to ISO 10993-5 and -12), except for one time point (*i.e.*, 24 h). Intimate contact between cells (MG-63) and the magnesium scaffolds was observed in SEM images. While direct contact between MG-63 cells and AM iron scaffolds revealed substantial and almost instant cytotoxicity in static cell culture, as compared to Ti-6Al-4V, the cytocompatibility was reasonable in *in vitro* indirect assays for up to 72 h. For AM zinc scaffolds, indirect cytotoxicity revealed excellent cellular activity up to 72 h.

Live-dead staining confirmed the good viability of the MG-63 cells cultured on the surface of AM porous zinc. Intimate contact between MG-63 cells and the zinc scaffolds was observed.

In Chapter 5-7, we evaluated and compared the fatigue behaviors of AM magnesium, iron, and zinc scaffolds in air and the in revised simulated body fluid (r-SBF). Biodegradation decreased the fatigue strength of the AM magnesium from 30% to 20% of its yield strength. In contrast, AM porous iron exhibited extraordinarily high fatigue resistance with fatigue strengths amounting to 70% and 65% of their yield strength in air and r-SBF, respectively. Surprisingly, AM porous zinc showed even higher fatigue resistance in r-SBF than in air. Moreover, functionally graded design was found to improve the fatigue strength of AM biodegradable porous zinc. Fracture planes were observed for the magnesium scaffolds but not for the iron and zinc specimens tested either in air or in r-SBF. The moderate effects of biodegradation on the fatigue strength of AM iron scaffolds could be attributed to the low biodegradation rate and excellent ductility of pure iron, while the biodegradation products formed on AM zinc scaffold struts contributed to the improvement of the fatigue resistance during the *in vitro* biodegradation experiments. The mechanistic aspects of how biodegradation and cyclic loading interacted with each other on different scales were revealed as well. On the micro-scale, cracks initiated at the biodegradation pits and propagated transgranularly. Cyclic loading caused microscale internal stresses that tend to favor pit formation. On the macro-scale, cracks preferred initiating at the strut junctions where tensile stresses were concentrated, as revealed by a finite element analysis of the porous material under compressive loading.

In Chapter 8-9, we designed functionally graded porous structures based on diamond unit cells and compared their performance with uniform designs. Iron and zinc specimens were fabricated by SLM, followed by experimental and computational analyses of their permeability, dynamic biodegradation behavior, cytocompatibility, and mechanical properties. We found that the topological design realized through functional gradients strongly affected the fluid flow, mass transport properties, and biodegradation behavior of the AM porous specimens. Up to four-fold variations in the permeability and up to three-fold variations in the biodegradation rate were observed for the different experimental groups of AM iron specimens, which is similar to the values we measured for the AM zinc specimens. After 4 weeks of *in vitro* biodegradation, the AM iron scaffolds lost 5-16% of their weight, while the AM zinc scaffolds lost 7.1-11.9% of their weight dependent on designs. Design-dependent cell viability did not differ from the gold standard controls for up to 48 h for AM iron scaffolds. AM porous zinc showed excellent biocompatibility and did not differ from the gold standard controls for up to 72 h independent of designs.

In Chapter 10, the overall conclusions are drawn and recommendations are made for further studies. AM biodegradable porous metal, particularly a metallic material based on zinc, with sufficient mechanical properties, precisely controlled interconnected porous structure, tunable biodegradation rate, and good biocompatibility, holds great potential to fulfil the requirements of an ideal bone substituting material that could be used to treat large bony defects. Material type, processing, and topological design all affect the properties of AM biodegradable porous metal, which can be further optimized by proper alloying, process optimization, and structural optimization.

iv

CONTENTS

1

Introduction

1

1.1. Background

Our societies are currently experiencing an increasing demand for bone implants. It is estimated that more than two million bone-grafting operations are performed annually in the world [1]. Although bone is known to have self-healing abilities, large bony defects cannot heal, when left untreated. Interventions such as bone-grafting are, therefore, necessary to restore the bone tissue [2]. The clinically available bone grafts normally include autografts (bone taken from the same person's body), allografts (bone tissue from a deceased donor), and xenografts (bone tissue from an animal), among which autografts are superior to the other two that have notable limitations including immune response complications, the risk of disease transmission, and the lack of osteogenesis [3]. However, even autografts suffer from major limitations of which limited supply, a need for multiple (lengthy) operations, and donor-site morbidity are the most important. To address the above-mentioned challenges, the concept of synthetic bone substitutes has emerged. Apart from being biocompatible, an ideal bone substitute should have mechanical properties close to those of the native bone to provide enough mechanical support and avoid stress shielding [4], present a fully-interconnected porous structure to allow for bone ingrowth [5, 6], and degrade in the human body as the bone regenerates [7]. However, it has so far been challenging to find such a porous biomaterial that can fulfill all the requirements mentioned above. The quest for an ideal bone substituting material is, therefore, still at its full swing [8].

1.2. Choice of materials

A variety of bone-substituting porous biomaterials based on polymers, ceramics, and metals have been developed in recent years [9]. Among the three types of biomaterials, polymer-based biomaterials have great design flexibility for tailored biodegradation behavior and offer a multitude of routes to biofunctionalization [10]. Ceramic-based biomaterials are well known for their favorable biodegradability and superior osteoconductivity [11]. Nevertheless, the main drawback of polymer-based biomaterials is their low mechanical properties, while ceramic-based biomaterials are normally brittle [1]. On the contrary, metallic porous biomaterials, because of their remarkable strength and significant energy absorption capacity, are considered to be the most suitable candidates for load-bearing bone implants [12]. Traditional metallic biomaterials are made from metals with high corrosion resistance. Such metals, however, do not biodegrade over time, meaning that bone regeneration cannot be completed, while the surface of the implant may be colonized by bacteria that cause implant-associated infections [13]. Bio-inert implants may also cause long-term endothelial dysfunction, permanent physical irritation, and chronic inflammatory local reactions [14]. Metallic biomaterials with proper biodegradability are, therefore, of great

potential utility for orthopedic and trauma surgeries. It is, of course, important for such biodegradable metallic biomaterials to only release biodegradation products that are biocompatible and are metabolized by the human body. The major elements constituting a biodegradable metal are, therefore, often the essential trace elements that naturally occur in the body. To date, magnesium, iron, and zinc as well as their alloys have been considered to be the most appropriate candidates [15].

1.3. Design

It is well known that the human bone has a highly hierarchical structure at different length scales including macroscale, microscale, sub-microscale, nanoscale, and sub-nanoscale (Figure 1) [16]. At the macroscale level, the bone can be classified as being either cortical or trabecular with varied porosities and mechanical properties. To better mimic the mechanical properties and functionalities of the bone, ideal bone substitutes need to possess bone-mimicking geometries. Moreover, an appropriate design of a porous metallic biomaterial requires a careful selection of the pore shape, pore size, and porosity. These characteristics can not only affect the mechanical properties [17] but also significantly influence the biological performance of porous metallic biomaterials, such as cell adhesion and proliferation, nutrient transportation, and bone ingrowth [6].
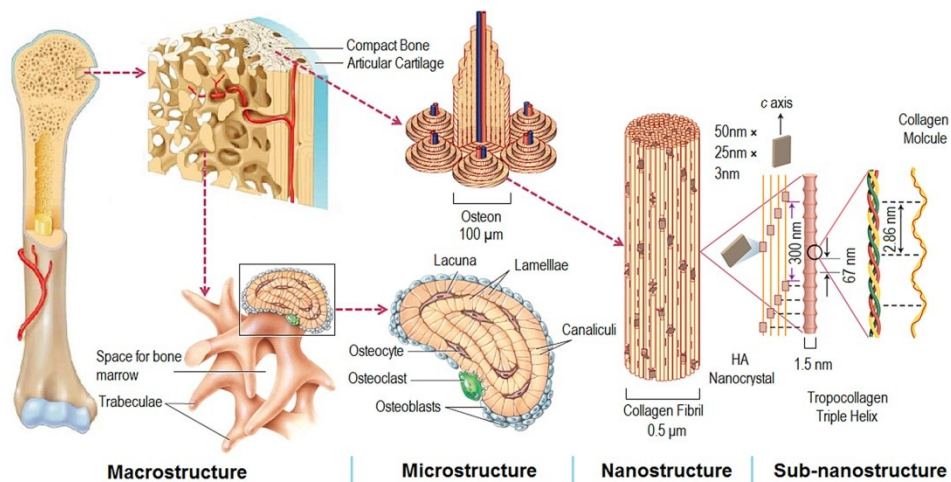
Figure 1. The hierarchical structure of the bone [16].

1.4. Fabrication

As previously mentioned, exquisite design is necessary for an ideal porous metallic biomaterial. To realize such designs in practice, much effort have been spent on

developing porous biodegradable metals through casting, sintering, foaming, and chemical vapor deposition [18-24]. However, these methods can neither precisely control the geometry nor achieve an appropriate level of mechanical properties [25]. The advent and recent progress in additive manufacturing (AM) has provided an unprecedented opportunity to tackle the dilemma of free-form design and manufacturing feasibility. Up until now, three main types of metal AM techniques including directed energy deposition (DED), powder bed fusion (PBF), and binder jetting have been applied for the fabrication of AM porous implants (Figure 2) [26]. DED and PBF are considered as direct AM metal printing, while binder jetting needs post treatment, typically debinding and sintering. According to the heat source, like laser (L) or electron beam (EB), DED and PBF can be further categorized as DED-L (Figure 2a), DED-EB (Figure 2b), selective laser melting (SLM) (Figure 2c), and electron beam melting (EBM) (Figure 2c). While DED is normally used for large rough parts, PBF is considered as the most appropriate method for building complex porous structures [26].
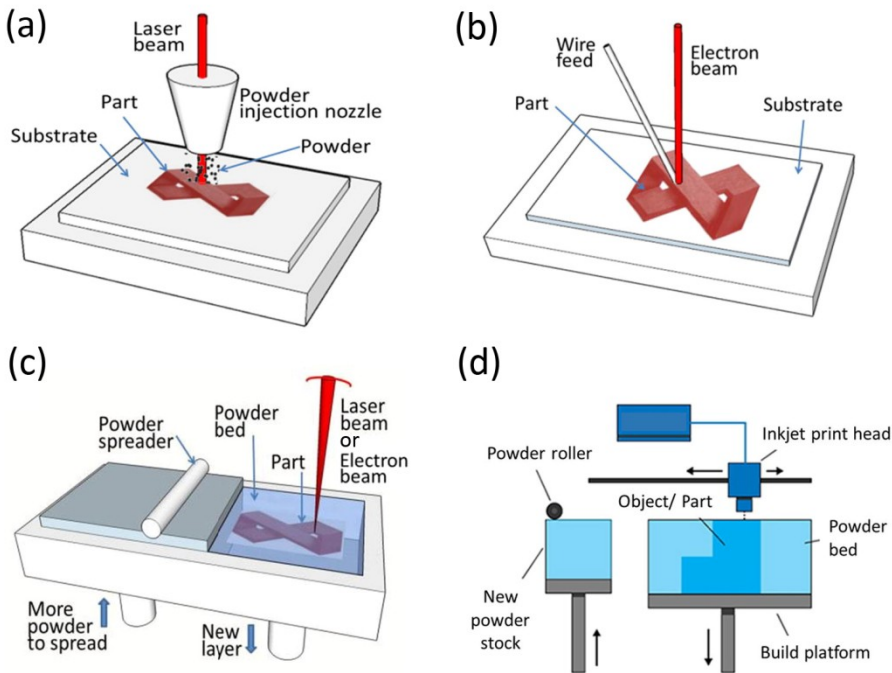
Figure 2. Schematic diagrams of (a) DED-L, (b)DED-EB, (c) PBF (SLM or EBM), and (d) binder jetting processes [26].

A large number of AM bio-inert metallic materials have been investigated, such as titanium alloys [27-29], stainless steel [30], tantalum [31], and cobalt-chromium [32]

which combine a high level of interconnected porosity with bone-mimicking mechanical properties. However, as mentioned in subsection 1.2, they do not biodegrade over time, meaning that bone regeneration cannot be completed. AM biodegradable porous metals have the great potential to meet the requirements for ideal bone implants. However, unlike AM bio-inert titanium or cobalt-chromium, AM biodegradable metals pose many processing challenges, such as severe evaporation and high chemical activity, especially for Mg and Zn [25]. Under any inappropriate processing conditions, defects including voids, lack of fusion, rough surface, severe residual stresses, and distortions may appear. Even for Fe, evaporation was found to play an important role in densification during laser melting [33]. Precise process planning and control are, therefore, required for successful application of AM technologies to fabricate topologically ordered porous implants from biodegradable metals.

1.5. Thesis Aim and Outline

Due to the abovementioned challenges and the limited time since introduction of AM technologies, there have been no prior reports of successful fabrication and thorough characterization of AM topologically ordered porous biodegradable metals. The work presented in this dissertation, therefore, marks the birth of a new category of porous metallic biomaterials where biodegradation and complex topological designs are both present and significantly contribute towards the observed behavior of the biomaterial. More specifically, the principal aim of this dissertation was to answer the following research questions:

"*Can we use SLM to additively manufacture biodegradable porous metals? What are the different types of the properties of the obtained specimens?*"

Chapter 2-4 show that biodegradable porous Mg, Fe, and Zn can be additively manufactured by SLM with precisely controlled geometries. Moreover, we answer the second question by conducting comprehensive studies on the microstructures, mechanical properties, biodegradation behavior, and biocompatibility of the manufactured specimens.

Moreover, any such biomaterial should be capable of serving under high levels of repetitive mechanical loading, leading us to ask the question

"*How can biodegradation and cyclic loading affect each other for AM porous biodegradable metals?*"

1

In Chapter 5-7, we investigated the biodegradation-affected fatigue behaviors of AM porous Mg, Fe, and Zn through a self-designed *in-situ* fatigue set-up. With this question answered, we were ready to further exploit the full advantages of AM and to improve the performance of porous biodegradable metals:

"*Can we use topological design to adjust the biodegradation behavior and mechanical properties of AM biodegradable porous metal?*"

To explore this idea, in Chapter 8-9, we designed uniform porous structures with different porosities as well as functionally graded porous structures and showed that topological design could be an important tool to adjust the biodegradation behavior and mechanical properties of AM porous biodegradable metal.

The structure of the thesis work is visualized below (Figure 3):
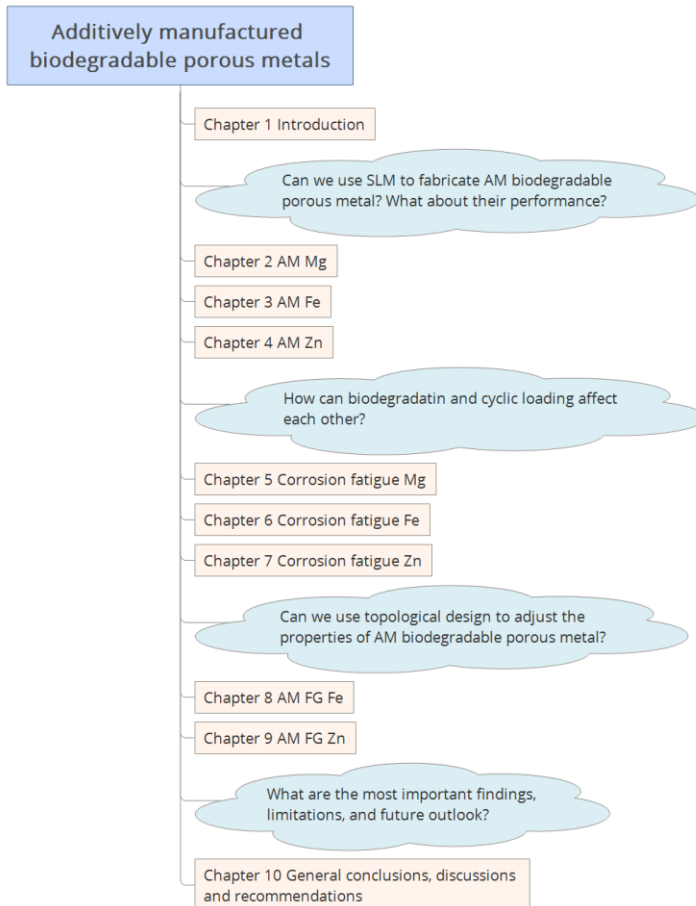
Figure 3. The structure of the dissertation.

References

[1] L. Zhang, G. Yang, B. N. Johnson, X. Jia. Three-dimensional (3D) printed scaffold and material selection for bone repair. Acta Biomater. 2019;84:16-33.

[2] S. Wu, X. Liu, K. W. K. Yeung, C. Liu, X. Yang. Biomimetic porous scaffolds for bone tissue engineering. Mater Sci Eng R Rep. 2014;80:1-36.

[3] R. Dimitriou, E. Jones, D. McGonagle, P. V. Giannoudis. Bone regeneration: current concepts and future directions. BMC Med. 2011;9:66.

[4] I.-H. Oh, N. Nomura, N. Masahashi, S. Hanada. Mechanical properties of porous titanium compacts prepared by powder sintering. Scripta Mater. 2003;49:1197-1202.

[5] C. E. Wen, M. Mabuchi, Y. Yamada, K. Shimojima, Y. Chino, T. Asahina. Processing of biocompatible porous Ti and Mg. Scripta Mater. 2001;45:1147-1153.

[6] A. A. Zadpoor. Bone tissue regeneration: the role of scaffold geometry. Biomater Sci. 2015;3:231-245.

[7] Y. Chen, Z. Xu, C. Smith, J. Sankar. Recent advances on the development of magnesium alloys for biodegradable implants. Acta Biomater. 2014;10:4561-4573.

[8] A. Oryan, S. Alidadi, A. Moshiri, N. Maffulli. Bone regenerative medicine: classic options, novel strategies, and future directions. J Orthop Surg Res. 2014;9:18.

[9] A.-V. Do, B. Khorsand, S. M. Geary, A. K. Salem. 3D Printing of Scaffolds for Tissue Regeneration Applications. Advanced Healthcare Materials. 2015;4:1742-1762.

[10] X. Liu, P. X. Ma. Polymeric Scaffolds for Bone Tissue Engineering. Ann Biomed Eng. 2004;32:477-486.

[11] H. Seitz, W. Rieder, S. Irsen, B. Leukers, C. Tille. Three-dimensional printing of porous ceramic scaffolds for bone tissue engineering. J Biomed Mater Res B Appl Biomater. 2005;74B:782-788.

[12] Q. Chen, G. A. Thouas. Metallic implant biomaterials. Mater Sci Eng R Rep. 2015;87:1-57.

[13] I. A. van Hengel, M. Riool, L. E. Fratila-Apachitei, J. Witte-Bouma, E. Farrell, A. A. Zadpoor, S. A. Zaat, I. Apachitei. Selective laser melting porous metallic implants with immobilized silver nanoparticles kill and prevent biofilm formation by methicillin-resistant Staphylococcus aureus. Biomaterials. 2017.

[14] M. Moravej, D. Mantovani. Biodegradable metals for cardiovascular stent application: interests and new opportunities. Int J Mol Sci. 2011;12:4250.

[15] H. Hermawan. Updates on the research and development of absorbable metals for biomedical applications. Prog Biomater. 2018;7:93-110.

[16] X. Wang, S. Xu, S. Zhou, W. Xu, M. Leary, P. Choong, M. Qian, M. Brandt, Y. M. Xie. Topological design and additive manufacturing of porous metals for bone scaffolds and orthopaedic implants: A review. Biomaterials. 2016;83:127-141.

[17] A. A. Zadpoor. Mechanical performance of additively manufactured meta-biomaterials. Acta Biomater. 2019;85:41-59.

[18] Y. Xie, L. Zhao, Z. Zhang, X. Wang, R. Wang, C. Cui. Fabrication and properties of porous Zn-Ag alloy scaffolds as biodegradable materials. Mater Chem Phys. 2018;219:433-443.

[19] L. Zhao, Z. Zhang, Y. Song, S. Liu, Y. Qi, X. Wang, Q. Wang, C. Cui. Mechanical properties and in vitro biodegradation of newly developed porous Zn scaffolds for biomedical applications. Mater Des. 2016;108:136-144.

[20] R. Alavi, A. Trenggono, S. Champagne, H. Hermawan. Investigation on mechanical behavior of biodegradable iron foams under different compression test conditions. Metals. 2017;7:202.

[21] M. Heiden, E. Nauman, L. Stanciu. Bioresorbable Fe-Mn and Fe-Mn-HA Materials for Orthopedic Implantation: Enhancing Degradation through Porosity Control. Adv Healthc Mater. 2017;6.

[22] K. Bobe, E. Willbold, I. Morgenthal, O. Andersen, T. Studnitzky, J. Nellesen, W. Tillmann, C. Vogt, K. Vano, F. Witte. In vitro and in vivo evaluation of biodegradable, open-porous scaffolds made of sintered magnesium W4 short fibres. Acta Biomater. 2013;9:8611-8623.

[23] M.-q. Cheng, T. Wahafu, G.-f. Jiang, W. Liu, Y.-q. Qiao, X.-c. Peng, T. Cheng, X.-l. Zhang, G. He, X.-y. Liu. A novel open-porous magnesium scaffold with controllable microstructures and properties for bone regeneration. Sci Rep. 2016;6:24134.

[24] G. Jiang, G. He. A new approach to the fabrication of porous magnesium with well-controlled 3D pore structure for orthopedic applications. Mater Sci Eng, C. 2014;43:317-320.

[25] Y. Qin, P. Wen, H. Guo, D. Xia, Y. Zheng, L. Jauer, R. Poprawe, M. Voshage, J. H. Schleifenbaum. Additive manufacturing of biodegradable metals: current research status and future perspectives. Acta Biomater. 2019.

[26] T. DebRoy, H. L. Wei, J. S. Zuback, T. Mukherjee, J. W. Elmer, J. O. Milewski, A. M. Beese, A. Wilson-Heid, A. De, W. Zhang. Additive manufacturing of metallic components – Process, structure and properties. Prog Mater Sci. 2018;92:112-224.

[27] F. S. L. Bobbert, K. Lietaert, A. A. Eftekhari, B. Pouran, S. M. Ahmadi, H. Weinans, A. A. Zadpoor. Additively manufactured metallic porous biomaterials based on minimal surfaces: A unique combination of topological, mechanical, and mass transport properties. Acta Biomater. 2017;53:572-584.

[28] J. Van der Stok, O. P. Van der Jagt, S. Amin Yavari, M. F. P. De Haas, J. H. Waarsing, H. Jahr, E. M. M. Van Lieshout, P. Patka, J. A. N. Verhaar, A. A. Zadpoor, H. Weinans. Selective laser melting-produced porous titanium scaffolds regenerate bone in critical size cortical bone defects. J Orthop Res. 2013;31:792-799.

[29] S. Ahmadi, S. Yavari, R. Wauthle, B. Pouran, J. Schrooten, H. Weinans, A. Zadpoor. Additively manufactured open-cell porous biomaterials made from six different space-filling unit cells: the mechanical and morphological properties. Materials. 2015;8:1871.

[30] C. Yan, L. Hao, A. Hussein, P. Young, D. Raymont. Advanced lightweight 316L stainless steel cellular lattice structures fabricated via selective laser melting. Mater Des. 2014;55:533-541.

[31] R. Wauthle, J. van der Stok, S. Amin Yavari, J. Van Humbeeck, J.-P. Kruth, A. A. Zadpoor, H. Weinans, M. Mulier, J. Schrooten. Additively manufactured porous tantalum implants. Acta Biomater. 2015;14:217-225.

[32] S. Limmahakhun, A. Oloyede, K. Sitthiseripratip, Y. Xiao, C. Yan. Stiffness and strength tailoring of cobalt chromium graded cellular structures for stress-shielding reduction. Mater Des. 2017;114:633-641.

[33] J. P. Kruth, L. Froyen, J. Van Vaerenbergh, P. Mercelis, M. Rombouts, B. Lauwers. Selective laser melting of iron-based powder. J Mater Process Technol. 2004;149:616-622.

1

1

2

Additively manufactured biodegradable porous magnesium

Here we present topologically ordered porous magnesium (WE43) scaffolds based on the diamond unit cell that were fabricated by selective laser melting (SLM) and satisfy all the requirements. We studied the in vitro biodegradation behavior (up to 4 weeks), mechanical properties and biocompatibility of the developed scaffolds. The mechanical properties of the AM porous WE43 (E = 700-800 MPa) scaffolds were found to fall into the range of the values reported for trabecular bone even after 4 weeks of biodegradation. Scanning electron microscopy (SEM), Fourier transform infrared spectroscopy (FTIR), electrochemical tests and μCT revealed a unique biodegradation mechanism that started with uniform corrosion, followed by localized corrosion, particularly in the center of the scaffolds. Biocompatibility tests performed up to 72 h showed level 0 cytotoxicity (according to ISO 10993-5 and -12), except for one time point (i.e., 24 h). Intimate contact between cells (MG-63) and the scaffolds was also observed in SEM images. The study shows for the first time that AM of porous Mg may provide distinct possibilities to adjust biodegradation profile through topological design and open up unprecedented opportunities to develop multifunctional bone substituting materials that mimic bone properties and enable full regeneration of critical-size load-bearing bony defects. [1]

2

2.1. Introduction

Magnesium and its alloys, as promising biodegradable metallic biomaterials, have been extensively investigated for potential orthopedic applications [1]. First, magnesium is an essential mineral for human nutrition and crucial to bone health [2]. Moreover, the mechanical properties of Mg alloys are close to those of bone [3]. Furthermore, Mg implants have been reported to stimulate new bone formation [3]. Therefore, Mg lends itself to the development of orthopedic implants [4]. However, as hydrogen released from the corrosion of Mg is problematic in many medical applications, the corrosion rate of Mg and its alloys should be carefully controlled [5]. One of the approaches to control the corrosion rate is adding alloying elements to Mg [6]. The addition of rare earth (RE) elements could improve both the mechanical strength and corrosion resistance [7-9]. Among Mg-RE alloys, WE43 has been considered suitable for orthopedic implant applications, based on pre-clinical and human trials in recent decades [10-12]. Up to now, several techniques to prepare magnesium scaffolds have been developed, including powder metallurgy with space holder, directional solidification, vacuum foaming, laser perforation, fiber deposition hot pressing and melt-extracted short fibers sintering [13-24]. It is, however, difficult (if not impossible) to use any of these methods to create fully interconnected porous structures, particularly when complex external shapes and intricate internal architectures in combination with adequate stiffness and strength are all required.

While AM techniques generally allow for the fabrication of complex and fully interconnected porous structures [25], their application to biodegradable metals in general and magnesium in particular has been very limited so far [26-28]. That is partially due to the fact that laser or electron beam processing of magnesium is technically extremely challenging. Magnesium is flammable even in its bulk form, let alone in the powder form that greatly increases the surface area and could cause dust explosion. Most laboratories therefore avoid AM of Mg out of safety concerns. Indeed, other than two abstracts [29, 30], we are not aware of any previous reports on AM of porous Mg. Moreover, the biodegradation behavior of such scaffolds and the change in their mechanical properties along with biodegradation are not yet understood.

In this study, we applied SLM to build topographically ordered biodegradable WE43 scaffolds that have the potential to satisfy all the three above-mentioned requirements and conducted a full-scale study on their biodegradation behavior, biocompatibility, the electrochemical aspects of their corrosion behavior, and the evolution of their mechanical properties during the degradation process.

2.2. Material and methods

2.2.1. Scaffold manufacturing and post processing

Diamond lattice (Fig. 1a) was adopted to design cylindrical porous specimens (Fig. 1b) with a diameter of 10 mm and a height of 11.2 mm. A strut size of 400 μm and a pore size of 600 μm were used, resulting in a relative density of 67% (design values). The specimens were then additively manufactured using a laboratory-scale SLM machine [30], in which argon was fed to maintain an inert atmosphere with oxygen content below 10 ppm. The optical system of the SLM machine consisted of a single-mode ytterbium fiber laser (IPG YLR-200) with a maximum output power of 230 W, a galvanometric scanner (SCANLAB hurrySCAN 20), and an f-theta focusing lens (SILL S4LFT 3254/126). The WE43 powder (4wt% yttrium and 3wt% rare earth elements) with a nearly spherical particle shape (Magnesium Elektron UK, Manchester, M27 8BF, UK) was gas atomized and sieved to a particle size range of 25 to 60 μm. After SLM, all samples were chemically polished for 2 min in a solution composed of 5% (in volume) HCl, 5% HNO_3, and 90% C_2H_5OH.
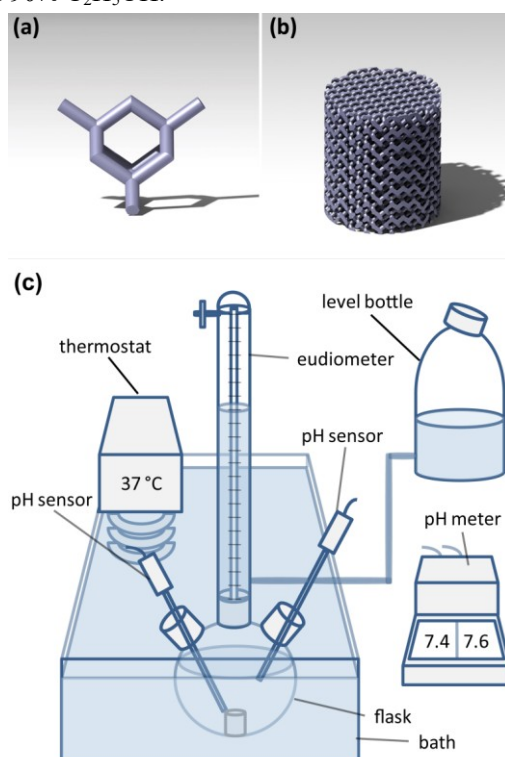
Figure 1. Design of WE43 scaffolds and degradation study set-up: (a) diamond unit cell, (b) CAD model of the scaffold and (c) *in vitro* degradation eudiometer system.

2.2.2. Microstructural characterization

Microstructures and compositions of WE43 specimens were examined using a scanning electron microscope (SEM, JSM-IT100, JEOL) equipped with an energy-disperse spectrometer (EDS). Phase identification was performed on the cross section using an X-ray diffractometer (XRD, Bruker D8 Advance diffractometer Bragg-Brentano geometry and Lynxeye position sensitive detector), operating at 40 kV and 40 mA with a step size of 0.034° and a dwell time of 2 s per step using Cu Ka radiation.

2.2.3. Immersion test

The rate of hydrogen gas evolution was determined eudiometrically in a custom-built set-up (Fig. 1c) placed in a thermal bath at 37 °C throughout the whole testing period of 28 days. Each sample was immersed inside a suspended 4-neck glass flask in the thermal bath with two micro pH meter electrodes (tip diameter: 3 mm, resolution: 45 µL, inLab NMR, METTLER TOLEDO) measuring pH values at the scaffold surface (i.e., local) and pH values further away (7 cm) from the sample (i.e., distant). The eudiometer connected to the flask had a volume of 400 ml with water as the confining liquid and was connected to a levelling bottle. The hydrogen produced in the flask supplanted the confining water in the eudiometer into the leveling bottle of 1000 ml. The gas volume was read when the leveling bottle was placed at the same level as the confining water in the eudiometer tube. For each reading, the temperature and air pressure were recorded in order to convert the measured gas volume to the gas volume in the standard state in accordance with DIN 38414-8. The following equation was used to calculate the standard gas volume values at different time points:

$$V_0 = V \cdot \frac{(P_l - P_w) \cdot T_0}{P_0 \cdot T}$$

V_0 - standard gas volume, ml
P_l - air pressure at the time of reading, mbar
P_w - vapor pressure of the water at the surrounding temperature, mbar
T_0 - standard temperature, K
P_0 - standard pressure, mbar

In total, 600 ml of revised simulated body fluid [31] (r-SBF) with 5% fetal bovine serum (FBS) was used for the tests, which were performed in triplicates. The medium was sampled after 1, 2, 7, 14, and 28 days of degradation and analyzed using an inductively coupled plasma optical emission spectroscope (ICP-OES, iCAP duo 6500 Thermo Fisher). Mg, Ca, and P ion concentrations in the solution were determined at different time points.

2.2.4. Characterization of degradation products

The morphology and composition at the surface of the specimens retrieved after the degradation tests were analyzed at selected time points by using the same SEM. In

addition, Fourier-transform infrared spectroscopy (FTIR) spectra were obtained from a Thermo-Nicolet Nexus FTIR apparatus, equipped with a liquid-nitrogen cooled MCT-A (mercury-cadmium-telluride) detector and a SAGA grazing angle accessory at an incident angle of 80°. To collect absorption spectra, an infrared background was collected on a freshly polished sample prior to the analysis of the degraded samples, and the final spectra were compared against this background. For each spectrum, 128 scans at a resolution of 2 cm^{-1} were co-added.

2.2.5. Electrochemical tests

For electrochemical tests, specimens with an exposed surface area of 0.28 cm^2 to electrolyte were mounted in an epoxy resin and ground with 800 grit SiC sandpaper. Copper screws were placed inside the resin to make these specimens conductive and electrochemical tests were performed in a 1250/1255 Solartron potentiostat in r-SBF with 5% FBS at 37 °C. A conventional three-electrode electrochemical cell was set up with platinum mesh as the counter electrode, Ag/AgCl as the reference electrode, and WE43 specimen as the working electrode. Open circuit potential (OCP) of the samples after immersion for different immersion periods up to 14 days was measured for 1 h. Potentiodynamic polarization (PDP) tests were then started at an initial potential of -0.3 V below OCP and was increased to +0.5 V above OCP at a scan rate of 0.5 mV/s.

2.2.6. Topological characterization

WE43 porous structures before and after immersion were imaged by µCT (Quantum FX, Perkin Elmer, USA) with a tube current of 180 µA and a tube voltage of 90 kV, a scan time of 3 min, and a resolution of 30 µm. µCT images were automatically reconstructed and converted into a series of 2D images using Analyze 11.0 (Perkin Elmer, USA). Then the images were exported to Fiji (NIH, Bethesda, MD, USA) and regions of interest (ROIs) were defined. Two different thresholds (80 and 119) were applied to segment samples with the lower value incorporating most of the degradation products and the higher value segmenting the degradation products apart from the Mg alloy. After segmentation in Fiji, the ratio of the void volume to the 3D ROI volume, strut size, and pore size were calculated by the prebuilt plugin of BoneJ (available in ImageJ). In addition to µCT, SEM and back-scattered electron imaging (BSE) were applied to observe the cross section of the degraded scaffolds at low magnifications.

2.2.7. Mechanical characterization

Compression tests were carried out using an Instron machine (10 kN load cell) at a crosshead speed of 2 mm/min. The mechanical properties of the porous structures were determined according to ISO 13314:2011. For the as-built, as-polished, and as-degraded specimens, the quasi-elastic gradient (hereafter referred to as Young's modulus) and yield strength were obtained. The slope of the initial linear part of the stress-strain curve was measured to determine the Young's modulus of the porous structures. The initial

2

linear part of the stress-strain curve was offset by 0.2% and its intersection with the stress-strain curve was taken to calculate the yield strength. The stress-strain curves were measured at different immersion time points (i.e., 1, 2, 7, 14 and 28 days). The tests were performed in triplicates per time point and the average values of Young's modulus and yield strength were calculated.

2.2.8. Cell culture assays

Human osteoblast-like cell line MG-63 (ATCC, CRL-1427) was cultured in Dulbecco's modified eagle medium (DMEM, Sigma-Aldrich) with 10% FBS (PAN-Biotech GmbH, Aidenbach, Germany) at 37 °C, 5% CO_2 and 95% humidity. After immersion in 2-propanol (Merck, Darmstadt, Germany) for 30 min, specimens were weighed and incubated in DMEM (Sigma-Aldrich) with 10% FBS (PAN-Biotech GmbH, Aidenbach, Germany) under physiological conditions (5% CO_2, 95% humidity and 37 °C) according to the recommendation of Wang et al. [32]. Extracts were prepared according to EN ISO standards 10993-12 using a mass-to-volume ratio for irregularly shaped devices as the ratio of sample mass to extractant volume. For WE43, we used the ISO 10993 standard of 0.2 g/mL of medium with the recently recommended modification of ISO10993-12 for biodegradable magnesium-based materials by Wang et al. [32]: 10-times diluted extracts of five randomly chosen WE43 scaffolds from the same production batch were used for assessing *in vitro* cytotoxicity. As per ISO 10993-12, specifically acceptable extraction condition, we used 37 °C for 72 h under static condition. Our earlier reported biocompatible SLM-built titanium (Ti-6Al-4V) specimens of similar design [33] served as reference material (positive control) (extraction ratio 0.2 g/ml) and sulforaphane (10 µM), for which cytotoxic effects were reported for MG-63 cells [34], was used as negative control.

In a 96 well plate, 2,500 MG-63 cells were seeded per well and pre-cultivated for 12 h as described above, prior to exchanging the culture medium with WE43 extracts. Cells were then incubated for 0, 24, 48 and 72 h under the same cell culture conditions. The cytotoxicity of WE43 extracts was evaluated using the MTS assay (Promega, CellTiter 96® AQueous One Solution Cell Proliferation Assay G3580) according to the supplier's instructions. Briefly, prior to adding MTS tetrazolium compound, control media and WE43 extracts were replaced with fresh cell culture medium in order to prevent any interference of the magnesium extract with the tetrazolium salt [35]. At the indicated time points, 20 µl of CellTiter 96® AQueous One Solution Reagent was added per well, containing MG-63 indicator cells in 100 µl of culture medium, prior to incubation at 37 °C for 2 h. Absorbance was recorded at 490 nm using a 96-well plate reader.

For the live-dead assay, WE43 and Ti-6Al-4V specimens were incubated for 48 h with DMEM + 10% FBS, as described above. After incubation, the specimens were carefully, dropwise seeded with 75,000 MG-63 cells per mm height in fresh cell culture

medium and incubated for 1 h under cell culture conditions, prior to adding 2 mL of fresh medium. After 24 h of incubation, live and dead dye (Live and Dead Cell Assay kit, Abcam, ab115347) was applied to the specimens according to the supplier's instructions and incubated for 10 min at room temperature. Cell seeded scaffolds were analyzed using fluorescent microscopy (LIVE: Emission (max): 495 nm, Excitation (max): 515 nm and DEAD: Emission (max): 528 nm).

SEM analysis of the cell-seeded specimens was performed as previously described [36]. Briefly, cell-seeded scaffolds were carefully rinsed in phosphate buffered saline and fixed for 1 h in 3% glutaraldehyde (Agar scientific, Wetzlar, Germany) in 0.1 M Soerensen's phosphate buffer (Merck, Darmstadt, Germany) at room temperature followed by 10min dehydratation steps in 30, 50, 70, 90 and 100% ethanol (last step twice). The samples were then air-dried at room temperature prior to sputter-coating (Sputter Coater EM SCD500, Leica, Wetzlar, Germany) with 12.5 nm of gold-palladium and imaged at 10 kV in SEM (ESEM XL 30 FEG, FEI, Eindhoven, Netherlands).

2.2.9. Statistical analysis

Optical density data (MTS) were normalized to the lysis buffer and unconditioned culture medium controls. Cytotoxicity was then analyzed by two-way ANOVA and post-hoc Tukey's multiple comparisons test ($\alpha = 0.05$) with $p<0.0001$, ****; $p<0.001$, ***; $p<0.01$, **; $p<0.05$, *; $n.s.$ = not significant.

2.3. Results

2.3.1. Surface morphology and microstructure of the scaffolds

Unmelted powder particles were present on the surface of the as-built specimens (Fig. 2a). After chemical polishing, the surface of the specimens on the periphery became relatively smooth (Fig. 2a), while the roughness of struts in the center was still high. Flake-shaped, homogeneously distributed white second-phase particles were found on the surface of the as-polished specimens (Fig. 2a). The stacking of the melt pools in the build direction could be observed in all struts (Fig. 2b). Two different microstructural features were observed in the as-built specimens. At the bottom of the struts, the microstructure was dominated by rose-like fine grains with grain sizes around 5 μm (Fig. 2c). At the top of the struts, however, the microstructure was featured by cellular morphology with a width of <1 μm (Fig. 2d). White flake-shaped second-phase particles were present throughout the magnesium matrix. EDS analysis showed that these white particles (Fig. 2e, spot 002) contained a higher concentration of yttrium than the magnesium matrix (Fig. 2e, spot 001). XRD revealed the presence of Y_2O_3 and Mg_3Nd
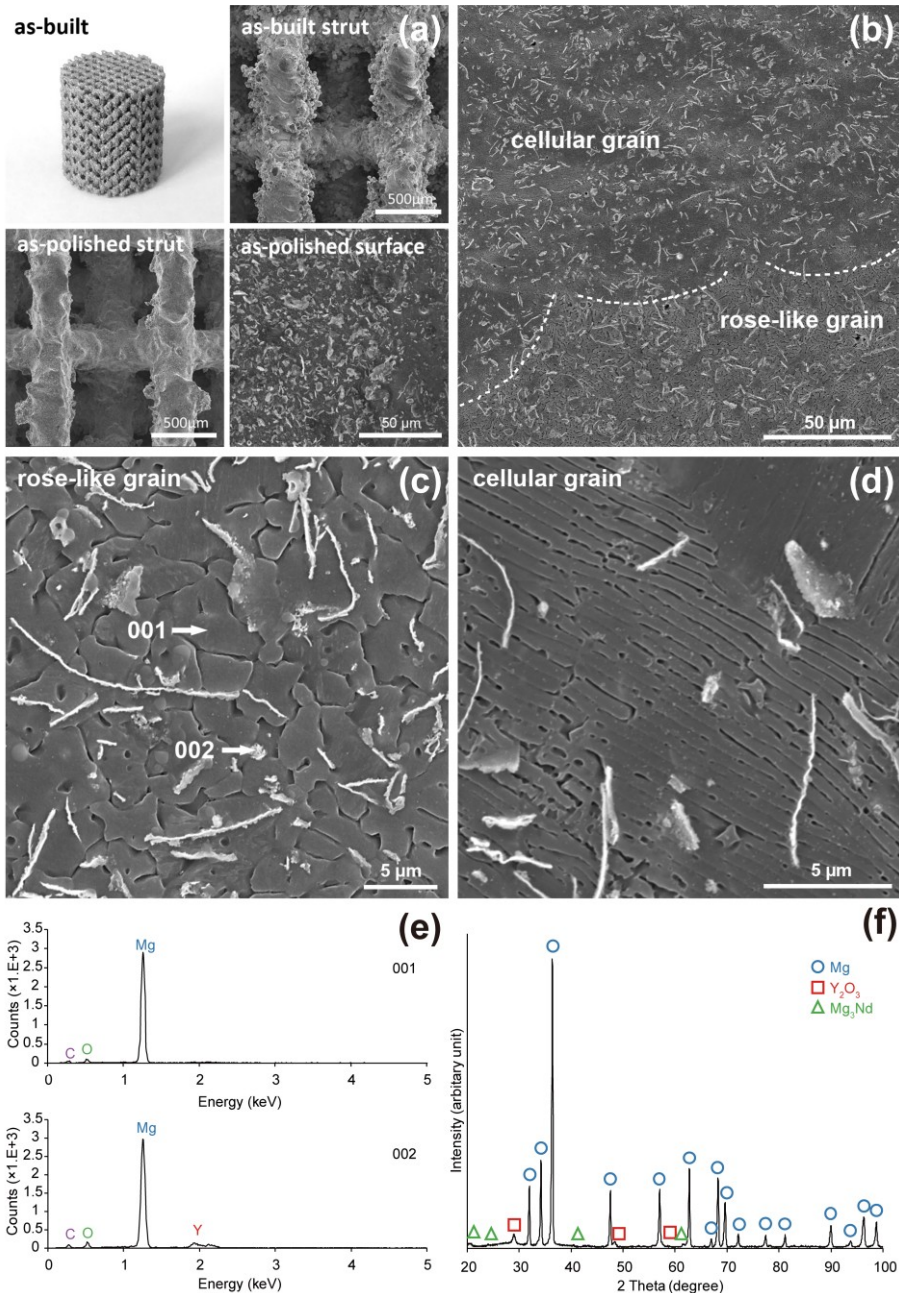
2

Figure 2. Surface morphology, microstructure and composition analyses: (a) surface morphology on the periphery of scaffolds, (b) SEM image of melt pool, (c)(d) SEM imagesof rose-like grains and cellular morphology at higher magnification, (e) EDS analysis and (f) XRD analysis.

in the as-built material (Fig. 2f), suggesting that the white particles could be yttrium oxide.

The stacking of the melt pools in the build direction could be observed in all struts (Fig. 2b). Two different microstructural features were observed in the as-built specimens. At the bottom of the struts, the microstructure was dominated by rose-like fine grains with grain sizes around 5 μm (Fig. 2c). At the top of the struts, however, the microstructure was featured by cellular morphology with a width of <1 μm (Fig. 2d). White flake-shaped second-phase particles were present throughout the magnesium matrix. EDS analysis showed that these white particles (Fig. 2e, spot 002) contained a higher concentration of yttrium than the magnesium matrix (Fig. 2e, spot 001). XRD revealed the presence of Y_2O_3 and Mg_3Nd in the as-built material (Fig. 2f), suggesting that the white particles could be yttrium oxide.

2.3.2. *In vitro* degradation behavior of the scaffolds

White degradation products gradually formed on the surface of the struts along with increasing immersion time (Fig. 3a). At day 28, the scaffolds still maintained their structural integrity without obvious detachment of degraded particles.

Hydrogen gas evolution increased rapidly at the early time points, but slowed down gradually after day 1 (Fig. 3b). However, at some time intervals (e.g., 4-6 days), the slope of the hydrogen release curve increased again. Until day 28, Mg ion concentration increased from 37.5 to 145.7 mg/L (Fig. 3c) with a substantial increase between days 2 and 7. Over this period, Ca and P ion concentrations decreased. The pH changes were very different in the proximity of the scaffold and further away (Fig. 3d, e). During the first 3 h, the local pH increased from 7.4 to 8.1 and decreased gradually thereafter, while the distant pH was still within the biological (neutral) range of pH 7.4 to 7.5 (Fig. 3d). For longer immersion times, the local pH values were always slightly higher than the distant pH values (Fig. 3e).

2.3.3. Characterization of degradation products on the scaffolds

The surfaces of the degraded specimens contained cracks and were covered by a deposition layer (Fig. 4a). After 1 day, small white degradation products formed on the surface close to the flake-shaped particles (Fig. 4a, spot 001). The degradation products contained Mg, C, O, and Y (Fig. 4b, spot 001) and were most likely hydroxides and carbonates. At day 2, the white degradation products became larger, but with the elemental composition similar to day 1 (Fig. 4b, spot 002). At day 7, some needle-shaped crystals formed on the surface of the former layer and P was detected for the first time (Fig. 4b, spot 003). After 14 days, apart from carbonates, rod-like products appeared on the surface, which contained Ca and P (Fig. 4b, spot 004). After 28 days, a compact layer formed with a Ca/P ratio around 1.5 (Fig. 4b, spot 005). FTIR spectra

2

further revealed the presence of phosphates and carbonates in the corrosion layer (Fig. 4c) with characteristic phosphate-specific absorption bands at about 1200 and 940 cm^{-1}, respectively, corresponding to the v3 and v1 vibrational modes [37], while the peaks at 1740 cm^{-1}likely resulted from CO_3^{2-} [38]. Carbonate absorption peaks emerged during the first day of the immersion tests (Fig. 4c) and increased onwards, which was accompanied by the appearance of the peaks of phosphates from day 2 (Fig. 4c), suggesting the formation of an apatite-like corrosion layer.
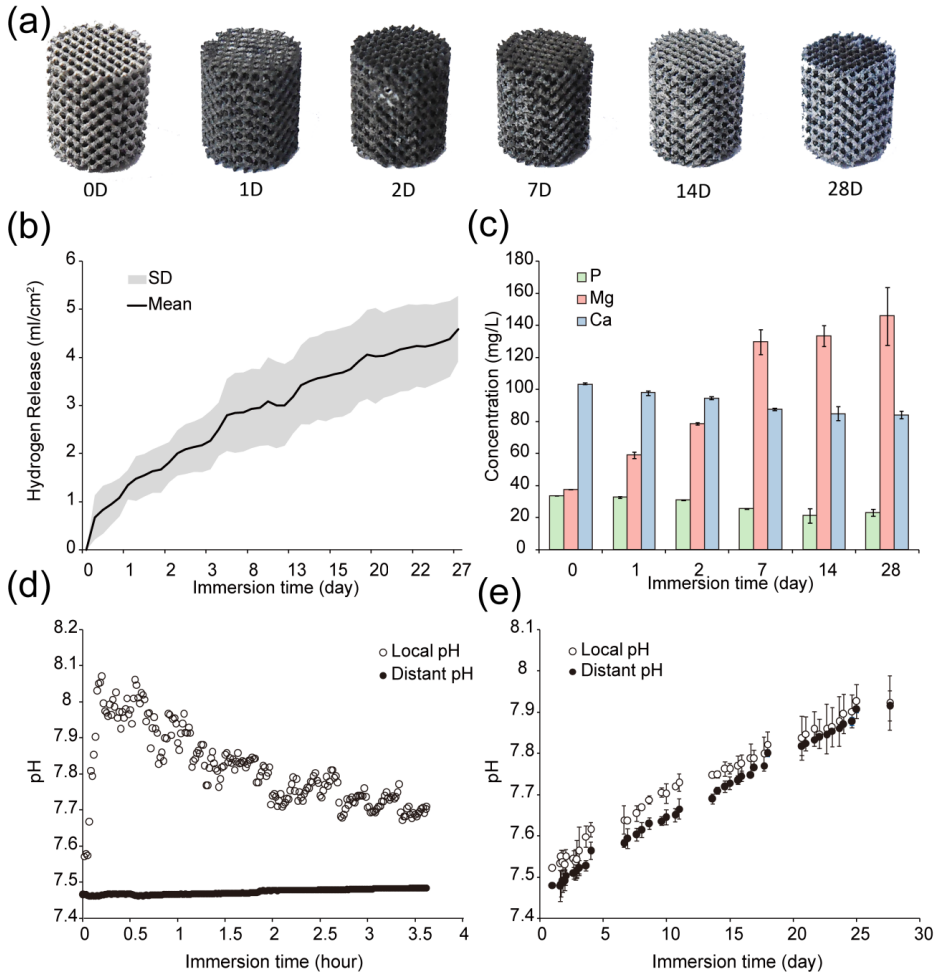
Figure 3. *In vitro* degradation tests: (a) visual evaluation of as-degraded samples, (b) hydrogen release, (c) ion release, (d) short term pH variation and (e) long term pH variation.
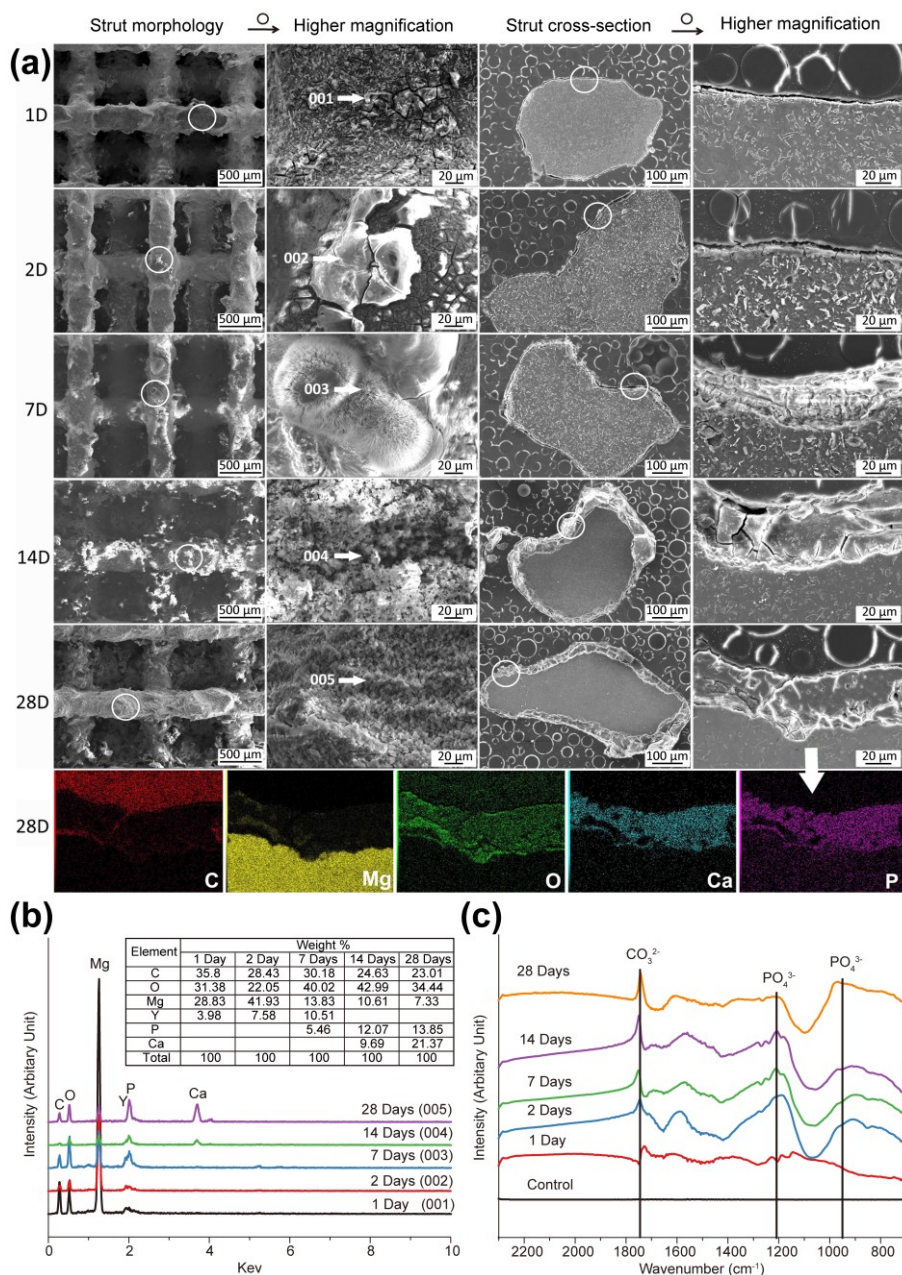
Figure 4. Characterization of degradation products on the periphery of scaffolds: (a) SEM images and EDS mapping, (b) EDS analysis and (c) FTIR analysis.

2.3.4. Electrochemical behaviors

Polarization curves of specimens at different immersion time points (Fig. 5a) showed a passivation stage in the anodic polarization branch for all the samples. Noble shift of OCP was observed from 1 h to 5 h, while the potential began to decrease from day 1 to day 2 and increased again after day 7 (Fig. 5b). Corrosion current density i_{corr} values were calculated by using the cathodic Tafel extrapolation considering the non-symmetrical polarization curves between the anodic and cathodic branches. The current density increased from $3.1 \cdot 10^{-5}$ to $6.1 \cdot 10^{-5}$ A·cm^{-2} during 24 h and began to fall after 24 h, decreasing to $2.1 \cdot 10^{-5}$ A·cm^{-2} by day 14 (Fig. 5b).
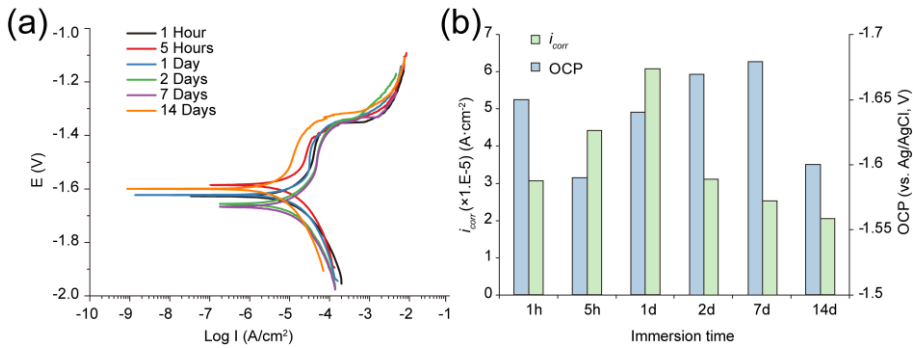
Figure 5. Electrochemical tests: (a) PDP curves, (b) OCP and corrosion current density change with immersion time.

2.3.5. Topological characterization

The as-built scaffolds were measured (threshold 2) to have an average strut size of 420 ± 4 µm (design value = 400 µm) and porosity of 64% ± 0.2% (design value = 67%) (Fig. 6a, c).

When both WE43 and degradation products were segmented with the lower threshold of 80, the strut size slightly increased after 1 day and 2 days, reaching the maximum value at day 7 followed by continuous decrease till day 28 (Fig. 6a). Similarly, the pore size decreased continuously until day 14 and then increased at day 28 (Fig. 6b).

Segmenting the scaffold material at the higher threshold of 119 (thus removing the corroded material), however, showed that the strut size decreased with increasing immersion time, and subsequently a slight increase at day 28 (Fig. 6a).The pore size showed only slight changes till day 2, while increasing from day 7 to day 28 (Fig. 6b). During 28 days, scaffolds lost 20.7% of their volume (Fig. 6c), which was comparable with amass reduction of 19.2% calculated from hydrogen release. The changes in

porosity were similar to those of pore size regardless of the segmentation threshold (Fig. 6d).
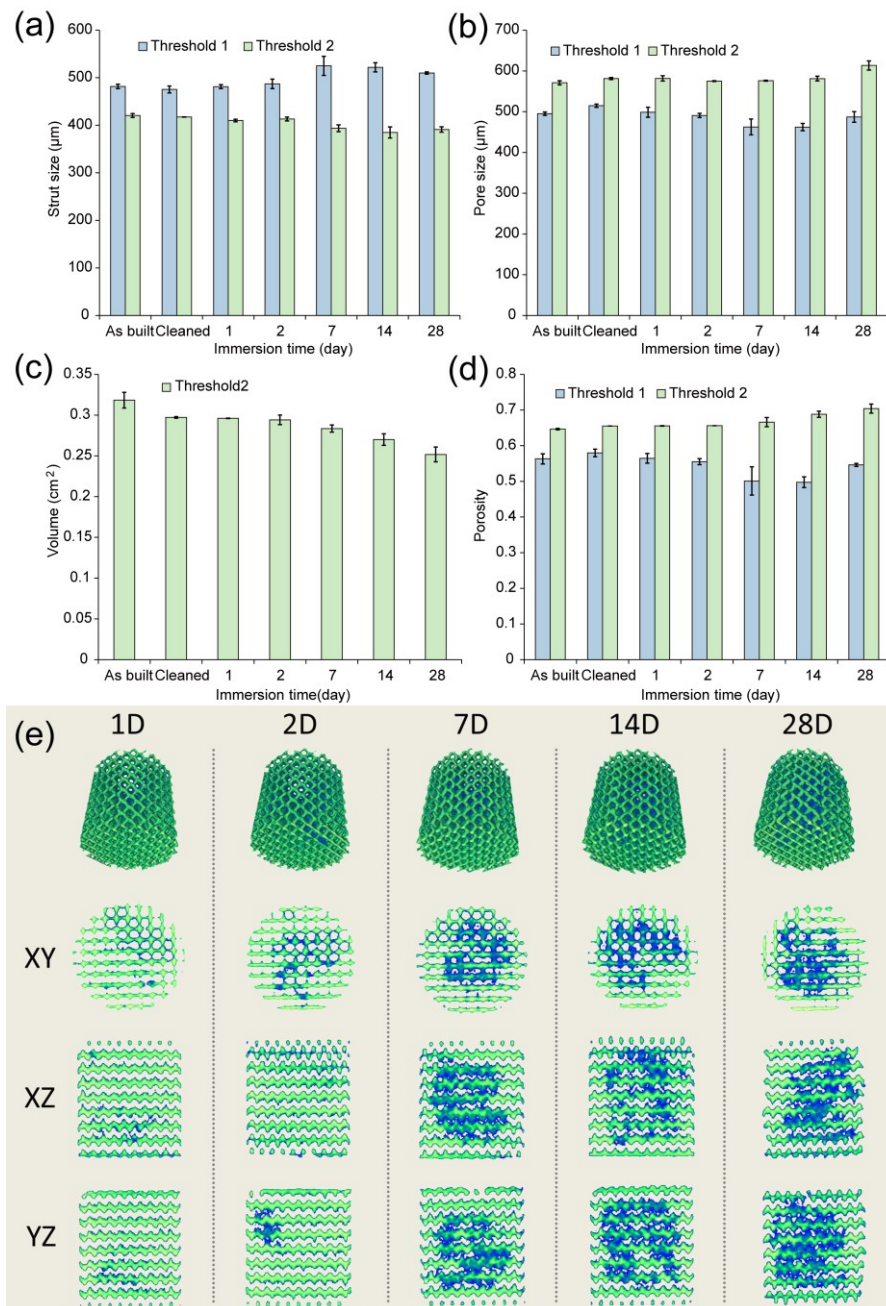
Figure 6. Micro-CT analysis: (a) strut size, (b) pore size, (c) volume, (d) porosity and (e) 3D reconstruction.

2
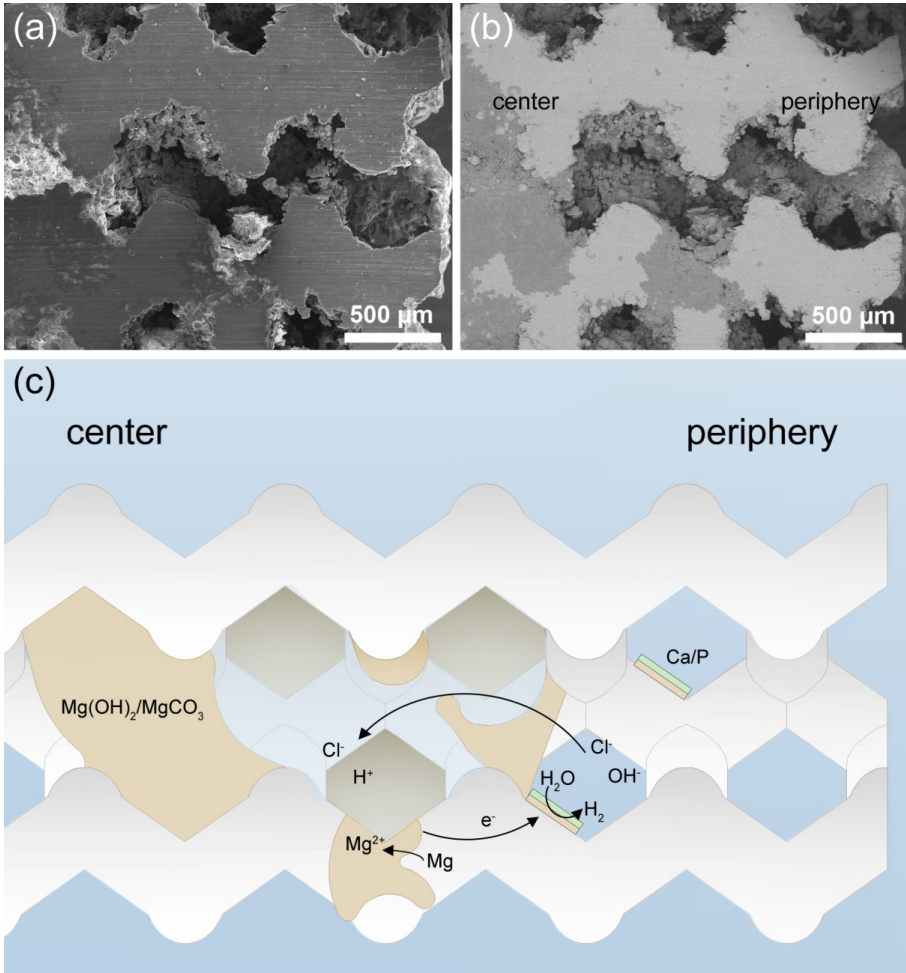
Figure 7. Macroscopic degradation behavior of scaffolds on the cross-section after 7-day immersion: (a) SEM image, (b) BSE image and (c) schematic illustration of degradation at the center of the WE43 scaffolds.

There were differences between threshold 1 and threshold 2 segmentations even for the as-built specimens, meaning that these two thresholds could not perfectly separate the scaffold material from degradation products, as there was some overlap between the attenuation coefficients of both materials. Nevertheless, the general (qualitative) trends reported here remain valid.

Reconstructed μCT images (green = WE43, blue = degradation products) showed significant formation of degradation products at the center of the scaffolds, while only limited quantities of degradation products were formed at the outer layers of the specimens (Fig. 6e). SEM images particularly in the BSE mode confirmed the μCT

results, showing that WE43 (white) was replaced by more degradation products (gray) at the center of the scaffolds than that at the periphery (Fig. 7 a, b).

2.3.6. Mechanical properties

Under compression, the as-built and as-polished scaffolds exhibited the typical stress-strain behavior of porous structures (Fig. 8a). The curve started with a linear elastic region, after which its slope rapidly decreased, followed by a plateau stage with fluctuations (Fig. 8a). The final increase in stress corresponded to the densification of the porous structure (Fig. 8a). The differences in Young's modulus and yield strength between the as-built and as-polished samples were insignificant (Fig. 8a). After 1 day and 2 days, the yield strength decreased and less stress fluctuations were observed after the peak stress as compared to the as-built and as-polished specimens (Fig. 8a). After 7 days, specimens showed almost no plateau stage or densification stage and still less stress fluctuations after the peak stress (Fig. 8a). The Young's modulus increased substantially after 1 day but decreased sharply from day 2 to day 7 (Fig. 8b). The Young's modulus then remained almost unchanged until day 28, while the yield strength showed a moderate decrease from 22 to 20 MPa during the first 14 days (i.e. 9% reduction) and then decreased significantly between day 14 and day 28 from 20 to 13 MPa (i.e. 35% reduction) (Fig. 8c).

2.3.7. Biocompatibility in vitro

Standardized cell seeding resulted in more (semi-quantitatively) effective cell adherence on Ti-6Al-4V as compared to WE43 (Fig. 9a, d). Live-dead staining with subsequent dual channel fluorescent optical imaging (FOI) showed hardly any cell death on Ti-6Al-4V shortly (i.e., 4 h) after seeding (Fig. 9a), while a significant percentage of MG-63 cells in direct contactwithWE43 appeared to be dying 4 h after immediate seeding (Fig. 9d). The pre-incubation of both scaffolds for 48 h in physiological serum-containing culture medium resulted in a substantial number of cells being viable even after 24 h of direct contact (Fig. 9c, f). Cells in intimate contact with strut surface were detectable by SEM on both materials (Fig. 9c, f). MG-63 cells seemed to adopt different phenotypes on both metal surfaces: on the relatively rough surface of Ti-6Al-4Vspecimens, cells developed a lot of far-stretching filopodia-like protrusions (Fig. 9c, upper arrows). On the eroded WE43 surface (Fig. 9f), cell morphology appeared more condensed, while adherent cells on Ti-6Al-4V appeared larger. After 24 h, few viable (green) cells were detectable on WE43 (Fig. 9f, FOI inlay), while the majority of the cells revealed compromised membrane integrity, being evident from their red fluorescence. The dead-live cell ratio was the opposite on the Ti-6Al-4V scaffolds (Fig. 9c, FOI inlay), showing at least 80% viable cells by semi-quantitative counting (data not shown).

2
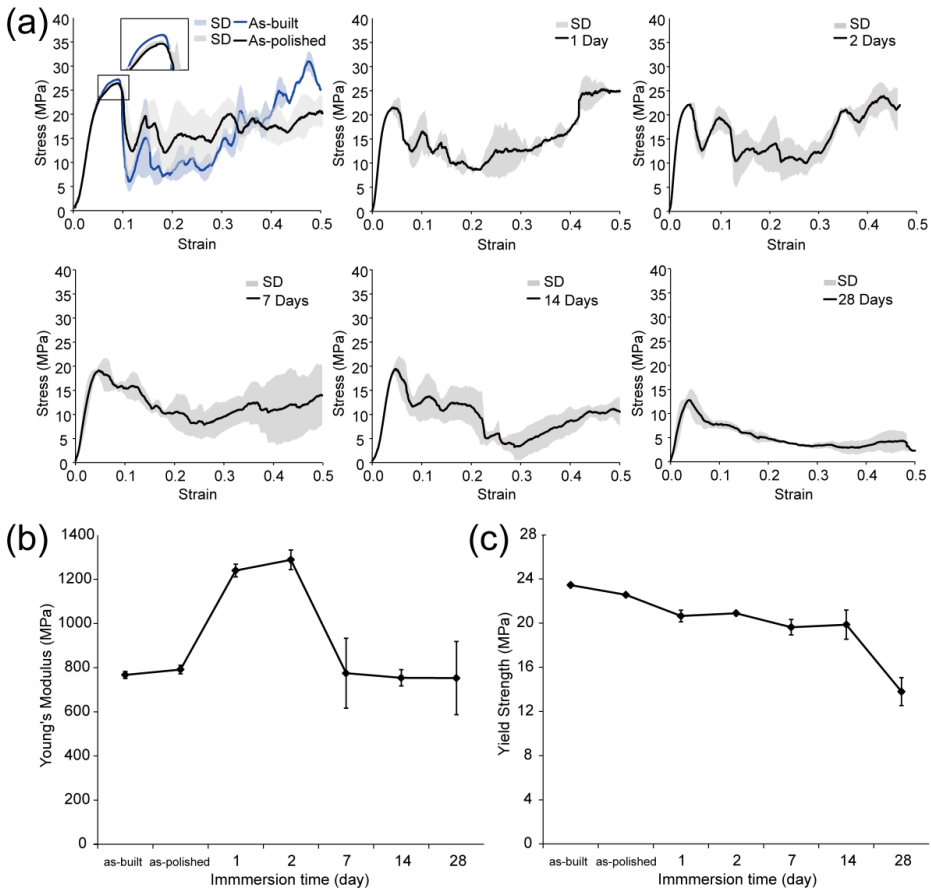
Figure 8. Mechanical behavior: (a) compressive stress-strain curves, (b) stiffness change with immersion time and (c) yield strength change with immersion time.

2.3.8. In vitro cytotoxicity

At the beginning, all treatments revealed close to 100% cellular activity. As expected, for the Sulforaphane group, the cellular activity quickly dropped to about 50% within 24 h and to about 25% after 72 h (Fig. 9g). In contrast, Ti-6Al-4V extracts revealed close to 100% cellular activity at all tested time points, confirming level 0 cytotoxicity (i.e. <25% cytotoxicity, according to ISO) of this material. WE43 extracts revealed similar cytotoxicity, with level 0 cytotoxicity at 75% of the investigated time points (Fig. 9g) with only the 24 h extracts just reaching level I cytotoxicity (i.e., breaching the >75% viability threshold). At 48 h, however, the cytotoxicity of WE43 extracts was again indistinguishable from that of Ti-6Al-4V extracts (Fig. 9g).
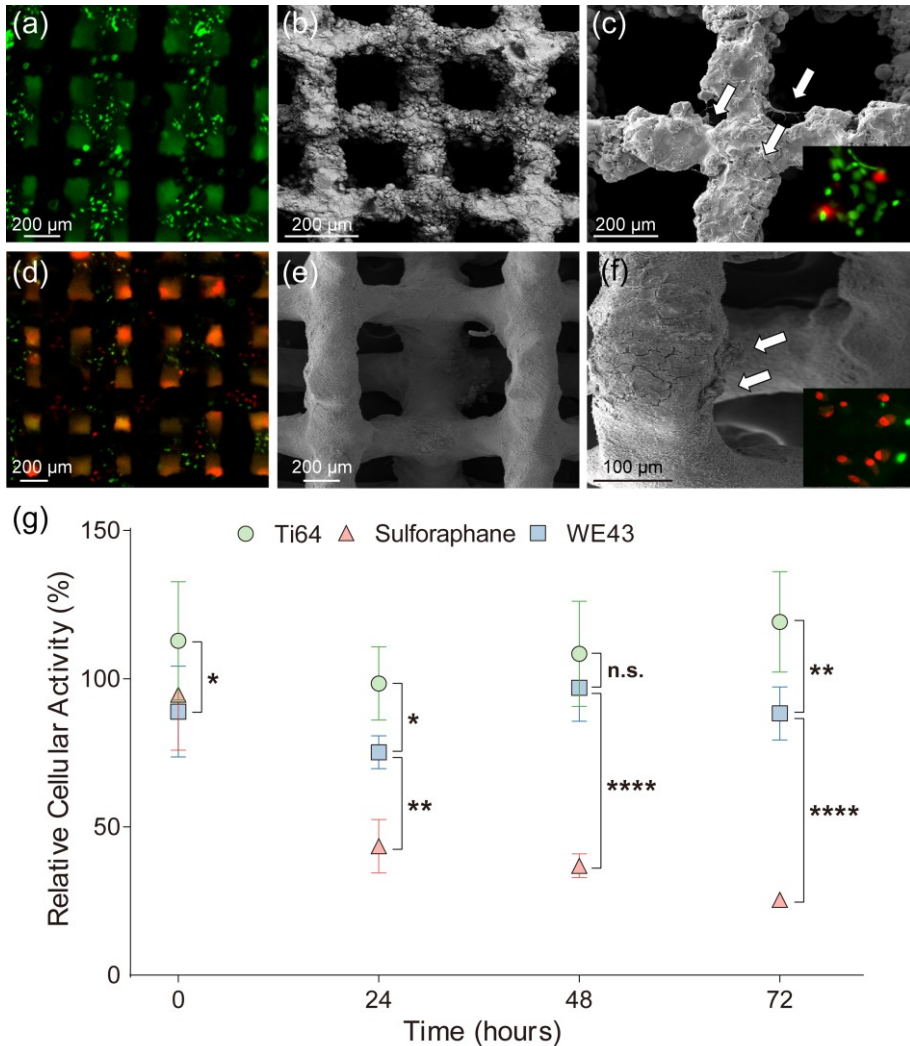
Figure 9. Biocompatibility and cytotoxicity of AM scaffolds *in vitro*: (a)(d) low magnification fluorescent optical images (FOI) of MG-63cells on Ti-6Al-4V (a) and WE43 (d) scaffolds 4 h after seeding, (b)(e) higher magnification SEM of Ti-6Al-4V (b) and WE43 (e) scaffolds before seeding, (c)(f) SEM and FOI of Ti-6Al-4V (c) and WE43 (f) scaffolds 24 h after seeding (arrows indicate individual cells: live cells, green; dead cells, red),(g) cytotoxicity screening of scaffolds *in vitro*, experiments were performed with extracts of randomly chosen replicate scaffolds (*n=5*) and analyzed in at least technical triplicates (WE43, *n=5*; Ti-6Al-4V, *n=3*).

2.4. Discussion

The AM porous Mg developed in this work satisfied all the three requirements mentioned in the introduction. First, the mechanical properties of these scaffolds particularly the Young's modulus were high enough to provide mechanical support in a bony environment (E= 700-800MPa) and were within the range of those reported for trabecular bone (*E*= 500-20000 MPa [39]) even after 28 days of biodegradation. Secondly, the actual topology of the porous structures closely matched the designed topology including a fully interconnected porous structure, high porosity, and precisely controlled geometry of the unit cells. Thirdly, AM porous Mg specimens showed a satisfactory biodegradation behavior with ≈20% volume loss after 4 weeks. From a biological viewpoint, they showed only limited cytotoxicity.

2.4.1. Microstructure

High cooling rates involved in SLM resulted in much smaller grains than those achievable with conventional methods [40]. At the bottom of the struts, the material experienced more cycles of re-melting than that at the top, as a result of the overlapping of the horizontal and vertical scan lines, thereby producing a relatively moderate temperature gradient. The moderate temperature gradient is likely the reason for the development of the rose-like grains, whereas towards the top of struts, rose-like grains became cellular due to a higher temperature gradient [41]. The yttrium-containing second phase particles were uniformly distributed in the microstructure of the α-Mg matrix, probably because laser melting caused temperature gradients in the melt pool that contributed to the formation of strong Marangoni convection and resulted in homogenous dispersion of alloying elements within the melt pool.

2.4.2. Biodegradation behavior

There are still no standards available concerning the evaluation of the degradation rate of magnesium *in vitro*. Researchers have developed several methods, such as weight loss measurement, hydrogen evolution measurement, electrochemical methods and μCT. Feyerabend et al. [42] compared these commonly applied methods with their respective advantages and disadvantages. Weight loss measurement is the most widely applied method. For accurate measurement, the corrosion layers on the magnesium substrate must be carefully and thoroughly removed, usually by using chromic acid, without attacking the magnesium substrate. Our previous controlled experiments to see how much of coatings and surface layers could be removed from AM porous biomaterials have, however, shown that this method is less reliable for volume-porous materials with huge surface areas and relatively small pore sizes. Therefore, in this study, we turned to the other three methods.

In comparison to *in vitro* degradation of conventionally-fabricated counterparts, AM WE43 scaffolds had overall slower hydrogen evolution although temporary

increases in corrosion rate occurred a few times over the whole immersion period, which could be attributed to the refined microstructure and complex corrosion mechanisms operating in the scaffolds, in addition to environmental factors. It is therefore clear that the topological design is important when one wishes to adjust the degradation behavior of AM porous Mg.

The biodegradation rate of 0.17 ml/cm^2·day over 4 weeks is lower than the values reported for most cast or extruded WE43 magnesium alloy (i.e., 0.3-2 ml/cm^2·day [9, 43-47]). For the interpretation of our *in vitro* degradation results, the immersion test solution matters: r-SBF with 5% FBS. While most researchers used SBF [48] with a high concentration of Cl$^-$ and a low concentration of CO$_3^{2-}$ as compared to r-SBF, the latter has ion concentrations more similar to those in human plasma. Although an addition of 5% FBS to it may have contributed to a decreased corrosion rate *in vitro*, as protein adsorption to the Mg surface may shield it from corrosion [49], this protein concentration is quite sub-physiological and supposed to better mimic a vascularized *in vivo* environment. To this end, protein adsorption to implants may be a contributing factor, explaining the overall relatively lower *in vivo* degradation rates of magnesium implants as compared to most *in vitro* results. Furthermore, it is well known that the CO$_2$ content of the immersion medium can influence the outcome of degradation tests [50]. We acknowledge that our experimental set-up is still far away from representing *in vivo* conditions, as we used static conditions in a closed container without CO$_2$ control. Cell metabolism and fluid flow may further influence Mg degradation. These are the limitations of the present study and should be addressed in future projects. Ideally, Mg scaffold degradation should be evaluated in complex *in vitro* environments employing, for example, bioreactors.

In addition to the environmental effects, the fine microstructure of the WE43 alloy resulting from SLM might be a contributor as well. Although finer grains correspond to a large area of grain boundaries that cause galvanic corrosion, large grain boundaries could act as a more effective physical barrier to corrosion, as compared to coarse grains [51]. In addition, a high fraction of grain boundaries is likely to accelerate passivation kinetics and reduce the intensity of micro galvanic coupling between grains and grain boundaries [52, 53]. Furthermore, the homogeneously distributed second phase in the grain interior also favors the uniform corrosion of grains [54, 55] and the galvanic corrosion triggered by these second phase particles may be compromised by later-on formed corrosion layers.

To reveal the corrosion mechanisms of the WE43 scaffolds, we further investigated the corrosion behavior from micro to macro scales. At the micro level, the presented results (SEM, FTIR, OCP and PDP) suggested the gradual formation of corrosion layer with time. At the beginning of *in vitro* immersion, the magnesium matrix dissolved as the anode, making the flake-shaped second phase embossed, because the second phase is nobler and less reactive than the magnesium matrix. Simultaneously, hydrogen was

2

produced through a cathodic reaction, which resulted in a local alkaline environment. The formation of a magnesium hydroxide $Mg(OH)_2$ layer on the magnesium surface acted as a protective barrier to further corrosion. This corresponds to the OCP value shifting to more positive potential after 5-h immersion. However, $Mg(OH)_2$ is not stable and could be transformed into soluble $MgCl_2$ in the solution containing chloride ions [56]. That is why the OCP value of the 1-day immersion specimen was even more negative than the 5-h immersion. After 1 day, the rupture and formation of this layer competed with each other. At the same time, carbonates and phosphates started to form on the surface around the second-phase particles. Thereafter, an apatite-like material formed because the previously formed passive layer provided favorable sites for apatite nucleation and its continuous growth was maintained by consuming Ca and P species in the surrounding solution [57]. The formation of less soluble precipitates explains the potential increase and i_{corr} values decrease from day 2 onwards. After a longer immersion time, an equilibrium between the formation and dissolution of degradation products was established.

At the macro level, μCT and BSE analyses suggest that the scaffolds experienced uniform corrosion at the periphery and a localized corrosion in the center. Hydrogen released very fast at the beginning and then slowed down due to the formation of a passive corrosion layer. As corrosion proceeded, localized corrosion contributed more than uniform corrosion to overall corrosion and hydrogen release rate increased several times after day 3. Besides, hydrogen bubbles entrapped inside the scaffolds might have influenced the measurable hydrogen release rate. Logically, the pH value of the solution increased more in the center of the scaffolds as compared to the periphery, which made the degradation layer more stable in the center. The accumulation of degradation products between the struts created relatively narrow spaces that could lead to limited diffusion of Mg ions in the center where crevice-like corrosion might occur (Fig. 7c), which resulted in the build-up of Mg ions with a concentration gradient set up between the entrance and the end of the space. Then, the negatively charged Cl ions migrated into the narrow space under the attraction of the positively charge Mg ions. Hydrolysis of chloride lowered pH and breached the passive layer locally inside the narrow space. At the same time, the periphery of the specimens with a passive layer might act as a cathode, building a corrosion cell with the magnesium alloy inside the scaffolds, which further accelerated the corrosion in the center (Fig. 7c). In addition to the crevice-like corrosion mechanism, the difference in surface roughness of struts between the periphery and center of the scaffolds could lead to different corrosion behaviors, although the exact effect is still debatable, as opposite results have been obtained [58].The differentiated corrosion rates and corrosion mechanisms between the scaffold center and periphery indicate that in addition to the choice of material, the design of open porous structures is of great importance and an optimum scaffold design should take these factors into account.

2.4.3. Mechanical behavior

During degradation, the specimens may be considered as a composite material composed of metal (magnesium) and ceramics (degradation products). The corrosion appeared to influence the stiffness differently from the yield strength. That is perhaps related to the different influence of interfacial bonding, which is between the degradation products and magnesium alloy in our case, on the Young's modulus and yield strength of a composite material [59]. Since the Young's modulus was measured at relatively low deformation, there was insufficient dilation to cause interface separation and the load could still be carried by these two phases. As a result, the Young's modulus of the WE43 scaffolds increased with increasing amount of degradation products. After localized corrosion occurred around day 7, the Young's modulus of the scaffolds was not only affected by the amount of degradation products but also by the structural changes within the scaffolds. The Young's modulus of 7-day specimen decreased to a value similar to that measured before immersion, because localized corrosion could lead to stress concentrations in some severely degraded struts. For the yield strength of a composite structure, interfacial bonding is of particular importance, especially at strains close to the yield point. For poorly bonded degradation products, stress transfer at the degradation product/magnesium interface may be inefficient, the degradation products cannot carry much of the load and thus the yield strength is primarily dependent on the strength of the remaining magnesium. As a result, the strength of the degraded scaffolds decreased with increasing amounts of degradation products and the decreasing amount of magnesium alloy along with biodegradation.

2.4.4. Biological evaluation

Only 24 h WE43 extracts revealed cytotoxicity level I by MTS analysis, while all other extracts fulfilled cytotoxicity level 0 requirements. The longest recommended 72 h extraction period [60] showed less than 25% cytotoxicity, similar to our positive control, i.e., Ti-6Al-4V extracts. To avoid any interference of corroded magnesium with tetrazolium salt by converting it into formazan [60, 61],we followed established procedures and replaced culture media [60] prior to adding the MTS reagent. We further used Sulforaphane (10 µM) as an established cytotoxic (i.e., negative) control in the MTS assay, confirming earlier data [34].

We noticed morphological changes in MG-63 cells after 24 h of contact to both WE43 and Ti-6Al-4V. Similar observations have been reported by Li et al. [62] who compared the biocompatibility of titanium rods with that of pure and oxidized magnesium rods (solid). The authors did hardly find live MG-63 cells on pure Mg after 24 h of incubation, while micro-arc oxidized Mg had a much weaker cytotoxic effect, but slightly stronger than that of titanium. This is in good agreement with our data as the 48 h *in vitro* pre-incubation of our WE43 scaffolds prior to cell seeding may have resulted in a protective surface coating of immature 'hydroxyapatite' and serum proteins.

2

Many systematic corrosion studies on magnesium alloys with different corrosion media are reported, with the composition of the corrosion media always influencing the Mg corrosion behavior. Proteins such as albumin, are known to form a corrosion-blocking layer on Mg alloys *in vitro* [63, 64], which usually is enriched in calcium and phosphates from the culture medium [63, 64]. While real hydroxyapatite would unlikely form under these conditions, even immature apatite-like layers concomitantly would participate in corrosion protection [65], which was also evident from our own corrosion data in the present study.

Direct contact evaluation *in vitro* suggests that WE43 may not *per se* be an ideal substrate to grow MG-63 cells on. However, cytotoxicity testing based on ISO 10993-5 and -12 standards was initially intended for non-degradable metals and (degradable) polymers [66]. An increasing body of evidence now suggests that these standards may be inappropriate for evaluating biodegradable Mg-based implants as usually less than 75% cell viability *in vitro* is reported [66]. Importantly, this is in sharp contrast to very promising *in vivo* findings [67, 68]. It is important to realize that, in contrast to the *in vitro* environment, the released magnesium and hydroxyl ions are promptly diluted *in vivo* by the surrounding body fluid and diffuse into circulation to be rapidly excreted from the body. To better mimic the *in vivo* situation, the latest recommendation is to use a 10-times higher extraction ratio [32, 35] as the 0.2 g/mL specimen-to-weight extraction ratio suggested by EN ISO 10993-5 and 10993-12. The latter extracts appeared reasonably safe based on our cell activity data (Fig. 9g) and are in good agreement with our pH measurements, revealing sharp differences between the pH values at the scaffold surface as compared to those in the bulk medium. Undiluted extracts from WE43also have high osmolality, while 400 mOsm/kgor less is well tolerated by primary osteoblasts and MG-63 cells alike [35]. Of note, our highly porous WE43 scaffolds further have a very large surface area (25.4 cm^2) as compared to earlier tested solid materials, but still never revealed more than 25% of viability loss. *In vivo*, the human body actively regulates local changes in the pH, osmolality, and hydrogen levels by interstitial transport. Comprehensive *in vitro* and *in vivo* studies are therefore needed to better understand the biological performance of AM WE43. In addition, according to data given by Zheng et al. [4], the daily allowance of Mg in the human body is 700 mg while the highest daily Mg ion release in our immersion tests was only 13 mg at day 1, which means, theoretically, 50 times larger scaffolds (in volume) than the current one (10*11.2 mm) could still be safely implanted.

2.5. Conclusions

We used AM to fabricate biodegradable porous Mg that has the potential to satisfy all the functional requirements regarding an ideal bone substituting material. First, its mechanical properties are high enough for proper mechanical support and within those reported for trabecular bone even after 4 weeks of biodegradation. Secondly, they

present a fully interconnected porous structure with precise control over topology. Thirdly, the biodegradation rate of the biomaterials is satisfactory with ≈20% volume loss after 4 weeks. Moreover, WE43 scaffolds revealed less than 25% cytotoxicity *in vitro*. Although pure WE43 itself may not be an ideal surface for cell adhesion, with the right design and coating, Mg-based biomaterials could be part of a new generation of functional degradable biomaterials, particularly in orthopedic applications.

References

[1] F. Witte. The history of biodegradable magnesium implants: A review. Acta Biomater. 2010;6:1680-1692.

[2] C. Palacios. The role of nutrients in bone health, from A to Z. Crit Rev Food Sci Nutr. 2006;46:621-628.

[3] M. P. Staiger, A. M. Pietak, J. Huadmai, G. Dias. Magnesium and its alloys as orthopedic biomaterials: A review. Biomaterials. 2006;27:1728-1734.

[4] Y. F. Zheng, X. N. Gu, F. Witte. Biodegradable metals. Mater Sci Eng R Rep. 2014;77:1-34.

[5] B. Zberg, P. J. Uggowitzer, J. F. Loffler. MgZnCa glasses without clinically observable hydrogen evolution for biodegradable implants. Nat Mater. 2009;8:887-891.

[6] Q. Peng, Y. Huang, L. Zhou, N. Hort, K. U. Kainer. Preparation and properties of high purity Mg–Y biomaterials. Biomaterials. 2010;31:398-403.

[7] N. Hort, Y. Huang, D. Fechner, M. Störmer, C. Blawert, F. Witte, C. Vogt, H. Drücker, R. Willumeit, K. U. Kainer, F. Feyerabend. Magnesium alloys as implant materials – Principles of property design for Mg–RE alloys. Acta Biomaterialia. 2010;6:1714-1725.

[8] D.-T. Chou, D. Hong, P. Saha, J. Ferrero, B. Lee, Z. Tan, Z. Dong, P. N. Kumta. In vitro and in vivo corrosion, cytocompatibility and mechanical properties of biodegradable Mg–Y–Ca–Zr alloys as implant materials. Acta Biomater. 2013;9:8518-8533.

[9] A. C. Hänzi, P. Gunde, M. Schinhammer, P. J. Uggowitzer. On the biodegradation performance of an Mg–Y–RE alloy with various surface conditions in simulated body fluid. Acta Biomater. 2009;5:162-171.

[10] C. Di Mario, H. U. W. Griffiths, O. Goktekin, N. Peeters, J. A. N. Verbist, M. Bosiers, K. Deloose, B. Heublein, R. Rohde, V. Kasese, C. Ilsley, R. Erbel. Drug-Eluting Bioabsorbable Magnesium Stent. J Interv Cardiol. 2004;17:391-395.

[11] R. Erbel, C. Di Mario, J. Bartunek, J. Bonnier, B. de Bruyne, F. R. Eberli, P. Erne, M. Haude, B. Heublein, M. Horrigan, C. Ilsley, D. Böse, J. Koolen, T. F. Lüscher, N. Weissman, R. Waksman. Temporary scaffolding of coronary arteries with bioabsorbable magnesium stents: a prospective, non-randomised multicentre trial. The Lancet. 2007;369:1869-1875.

2

[12] M. Haude, R. Erbel, P. Erne, S. Verheye, H. Degen, D. Böse, P. Vermeersch, I. Wijnbergen, N. Weissman, F. Prati, R. Waksman, J. Koolen. Safety and performance of the drug-eluting absorbable metal scaffold (DREAMS) in patients with de-novo coronary lesions: 12 month results of the prospective, multicentre, first-in-man BIOSOLVE-I trial. The Lancet. 2013;381:836-844.

[13] K. Bobe, E. Willbold, I. Morgenthal, O. Andersen, T. Studnitzky, J. Nellesen, W. Tillmann, C. Vogt, K. Vano, F. Witte. In vitro and in vivo evaluation of biodegradable, open-porous scaffolds made of sintered magnesium W4 short fibres. Acta Biomater. 2013;9:8611-8623.

[14] Z. Chen, X. Mao, L. Tan, T. Friis, C. Wu, R. Crawford, Y. Xiao. Osteoimmunomodulatory properties of magnesium scaffolds coated with β-tricalcium phosphate. Biomaterials. 2014;35:8553-8565.

[15] M.-q. Cheng, T. Wahafu, G.-f. Jiang, W. Liu, Y.-q. Qiao, X.-c. Peng, T. Cheng, X.-l. Zhang, G. He, X.-y. Liu. A novel open-porous magnesium scaffold with controllable microstructures and properties for bone regeneration. Sci Rep. 2016;6:24134.

[16] G. Jiang, G. He. A new approach to the fabrication of porous magnesium with well-controlled 3D pore structure for orthopedic applications. Materials Science and Engineering: C. 2014;43:317-320.

[17] A. P. Md Saad, R. A. Abdul Rahim, M. N. Harun, H. Basri, J. Abdullah, M. R. Abdul Kadir, A. Syahrom. The influence of flow rates on the dynamic degradation behaviour of porous magnesium under a simulated environment of human cancellous bone. Materials & Design. 2017;122:268-279.

[18] A. P. Md. Saad, N. Jasmawati, M. N. Harun, M. R. Abdul Kadir, H. Nur, H. Hermawan, A. Syahrom. Dynamic degradation of porous magnesium under a simulated environment of human cancellous bone. Corros Sci. 2016;112:495-506.

[19] I. Morgenthal, O. Andersen, C. Kostmann, G. Stephani, T. Studnitzky, F. Witte, B. Kieback. Highly Porous Magnesium Alloy Structures and Their Properties Regarding Degradable Implant Application. Adv Eng Mater. 2014;16:309-318.

[20] F. Witte, H. Ulrich, C. Palm, E. Willbold. Biodegradable magnesium scaffolds: Part II: peri-implant bone remodeling. Journal of Biomedical Materials Research Part A. 2007;81:757-765.

[21] F. Witte, H. Ulrich, M. Rudert, E. Willbold. Biodegradable magnesium scaffolds: Part 1: appropriate inflammatory response. Journal of Biomedical Materials Research Part A. 2007;81:748-756.

[22] X. Zhang, X.-W. Li, J.-G. Li, X.-D. Sun. Preparation and mechanical property of a novel 3D porous magnesium scaffold for bone tissue engineering. Materials Science and Engineering: C. 2014;42:362-367.

[23] H. Zhuang, Y. Han, A. Feng. Preparation, mechanical properties and in vitro biodegradation of porous magnesium scaffolds. Materials Science and Engineering: C. 2008;28:1462-1466.

[24] T. L. Nguyen, M. P. Staiger, G. J. Dias, T. B. F. Woodfield. A Novel Manufacturing Route for Fabrication of Topologically-Ordered Porous Magnesium Scaffolds. Adv Eng Mater. 2011;13:872-881.

[25] A. A. Zadpoor, J. Malda. Additive manufacturing of biomaterials, tissues, and organs. Springer; 2017.

[26] D. Hu, Y. Wang, D. Zhang, L. Hao, J. Jiang, Z. Li, Y. Chen. Experimental Investigation on Selective Laser Melting of Bulk Net-Shape Pure Magnesium. Mater Manuf Processes. 2015;30:1298-1304.

[27] C. C. Ng, M. Savalani, H. C. Man. Fabrication of magnesium using selective laser melting technique. Rapid Prototyping Journal. 2011;17:479-490.

[28] Y. Yang, P. Wu, X. Lin, Y. Liu, H. Bian, Y. Zhou, C. Gao, C. Shuai. System development, formability quality and microstructure evolution of selective laser-melted magnesium. Virtual and Physical Prototyping. 2016;11:173-181.

[29] L. Jauer, B. Jülich, M. Voshage, W. Meiners. Selective Laser Melting of magnesium alloys. European Cells and Materials. 2015;30.

[30] W. Frank, J. Lucas, M. Wolfgang, K. Zienab, S. Kristin, S. Tanja. Open-porous biodegradable magnesium scaffolds produced by selective laser melting for individualized bone replacement. Frontiers in Bioengineering and Biotechnology. 2016;4.

[31] A. Oyane, H.-M. Kim, T. Furuya, T. Kokubo, T. Miyazaki, T. Nakamura. Preparation and assessment of revised simulated body fluids. J Biomed Mater Res A. 2003;65A:188-195.

[32] J. Wang, F. Witte, T. Xi, Y. Zheng, K. Yang, Y. Yang, D. Zhao, J. Meng, Y. Li, W. Li, K. Chan, L. Qin. Recommendation for modifying current cytotoxicity testing standards for biodegradable magnesium-based materials. Acta Biomater. 2015;21:237-249.

[33] J. van der Stok, M. Koolen, M. de Maat, S. A. Yavari, J. Alblas, P. Patka, J. Verhaar, E. van Lieshout, A. A. Zadpoor, H. Weinans. Full regeneration of segmental bone defects using porous titanium implants loaded with BMP-2 containing fibrin gels. Eur Cell Mater. 2015;2015:141-154.

[34] J. M. P. Ferreira de Oliveira, C. Remédios, H. Oliveira, P. Pinto, F. Pinho, S. Pinho, M. Costa, C. Santos. Sulforaphane induces DNA damage and mitotic abnormalities in human osteosarcoma MG-63 cells: correlation with cell cycle arrest and apoptosis. Nutr Cancer. 2014;66:325-334.

[35] J. Fischer, D. Pröfrock, N. Hort, R. Willumeit, F. Feyerabend. Reprint of: Improved cytotoxicity testing of magnesium materials. Materials Science and Engineering: B. 2011;176:1773-1777.

[36] R. Beckmann, A. Houben, M. Tohidnezhad, N. Kweider, A. Fragoulis, C. Wruck, L. Brandenburg, B. Hermanns-Sachweh, M. Goldring, T. Pufe, H. Jahr. Mechanical

forces induce changes in VEGF and VEGFR-1/sFlt-1 expression in human chondrocytes. Int J Mol Sci. 2014;15:15456.

[37] I. REHMAN, W. BONFIELD. Characterization of hydroxyapatite and carbonated apatite by photo acoustic FTIR spectroscopy. J Mater Sci Mater Med. 1997;8:1-4.

[38] A. C. Taş, P. J. Majewski, F. Aldinger. Chemical Preparation of Pure and Strontium-and/or Magnesium-Doped Lanthanum Gallate Powders. J Am Ceram Soc. 2000;83:2954-2960.

[39] J. Parthasarathy, B. Starly, S. Raman, A. Christensen. Mechanical evaluation of porous titanium (Ti6Al4V) structures with electron beam melting (EBM). J Mech Behav Biomed Mater. 2010;3:249-259.

[40] C. C. Ng, M. M. Savalani, M. L. Lau, H. C. Man. Microstructure and mechanical properties of selective laser melted magnesium. Appl Surf Sci. 2011;257:7447-7454.

[41] V. Manakari, G. Parande, M. Gupta. Selective Laser Melting of Magnesium and Magnesium Alloy Powders: A Review. Metals. 2016;7:2.

[42] F. Feyerabend. In vitro analysis of magnesium corrosion in orthopaedic biomaterials. in: P Dubruel, S van Vlierberghe (Eds) Biomaterials for bone regeneration Cambridge, UK: Woodhead Publishing. 2014:225-269.

[43] F. Witte, J. Fischer, J. Nellesen, H.-A. Crostack, V. Kaese, A. Pisch, F. Beckmann, H. Windhagen. In vitro and in vivo corrosion measurements of magnesium alloys. Biomaterials. 2006;27:1013-1018.

[44] X. N. Gu, W. R. Zhou, Y. F. Zheng, Y. Cheng, S. C. Wei, S. P. Zhong, T. F. Xi, L. J. Chen. Corrosion fatigue behaviors of two biomedical Mg alloys – AZ91D and WE43 – In simulated body fluid. Acta Biomater. 2010;6:4605-4613.

[45] A. C. Hänzi, I. Gerber, M. Schinhammer, J. F. Löffler, P. J. Uggowitzer. On the in vitro and in vivo degradation performance and biological response of new biodegradable Mg–Y–Zn alloys. Acta Biomater. 2010;6:1824-1833.

[46] W. Jin, G. Wu, H. Feng, W. Wang, X. Zhang, P. K. Chu. Improvement of corrosion resistance and biocompatibility of rare-earth WE43 magnesium alloy by neodymium self-ion implantation. Corros Sci. 2015;94:142-155.

[47] M. A. Leeflang, J. S. Dzwonczyk, J. Zhou, J. Duszczyk. Long-term biodegradation and associated hydrogen evolution of duplex-structured Mg–Li–Al–(RE) alloys and their mechanical properties. Materials Science and Engineering: B. 2011;176:1741-1745.

[48] T. Kokubo, H. Takadama. How useful is SBF in predicting in vivo bone bioactivity? Biomaterials. 2006;27:2907-2915.

[49] C. Liu, Y. Xin, X. Tian, P. K. Chu. Degradation susceptibility of surgical magnesium alloy in artificial biological fluid containing albumin. J Mater Res. 2011;22:1806-1814.

[50] R. Willumeit, J. Fischer, F. Feyerabend, N. Hort, U. Bismayer, S. Heidrich, B. Mihailova. Chemical surface alteration of biodegradable magnesium exposed to corrosion media. Acta Biomater. 2011;7:2704-2715.

[51] N. N. Aung, W. Zhou. Effect of grain size and twins on corrosion behaviour of AZ31B magnesium alloy. Corros Sci. 2010;52:589-594.

[52] G. R. Argade, S. K. Panigrahi, R. S. Mishra. Effects of grain size on the corrosion resistance of wrought magnesium alloys containing neodymium. Corros Sci. 2012;58:145-151.

[53] M. Alvarez-Lopez, M. D. Pereda, J. A. del Valle, M. Fernandez-Lorenzo, M. C. Garcia-Alonso, O. A. Ruano, M. L. Escudero. Corrosion behaviour of AZ31 magnesium alloy with different grain sizes in simulated biological fluids. Acta Biomater. 2010;6:1763-1771.

[54] A. Atrens, G.-L. Song, M. Liu, Z. Shi, F. Cao, M. S. Dargusch. Review of recent developments in the field of magnesium corrosion. Adv Eng Mater. 2015;17:400-453.

[55] G. v. Baril, C. Blanc, N. Pébère. AC impedance spectroscopy in characterizing time-dependent corrosion of AZ91 and AM50 magnesium alloys characterization with respect to their microstructures. J Electrochem Soc. 2001;148:B489.

[56] M. Esmaily, J. E. Svensson, S. Fajardo, N. Birbilis, G. S. Frankel, S. Virtanen, R. Arrabal, S. Thomas, L. G. Johansson. Fundamentals and advances in magnesium alloy corrosion. Prog Mater Sci. 2017;89:92-193.

[57] Y. Xin, T. Hu, P. K. Chu. Degradation behaviour of pure magnesium in simulated body fluids with different concentrations of HCO3. Corros Sci. 2011;53:1522-1528.

[58] X. Li, X. Liu, S. Wu, K. W. K. Yeung, Y. Zheng, P. K. Chu. Design of magnesium alloys with controllable degradation for biomedical implants: From bulk to surface. Acta Biomater. 2016;45:2-30.

[59] S.-Y. Fu, X.-Q. Feng, B. Lauke, Y.-W. Mai. Effects of particle size, particle/matrix interface adhesion and particle loading on mechanical properties of particulate–polymer composites. Composites Part B: Engineering. 2008;39:933-961.

[60] J. Fischer, M. H. Prosenc, M. Wolff, N. Hort, R. Willumeit, F. Feyerabend. Interference of magnesium corrosion with tetrazolium-based cytotoxicity assays. Acta Biomater. 2010;6:1813-1823.

[61] M. Yazdimamaghani, M. Razavi, D. Vashaee, K. Moharamzadeh, A. R. Boccaccini, L. Tayebi. Porous magnesium-based scaffolds for tissue engineering. Materials Science and Engineering: C. 2017;71:1253-1266.

[62] M. Li, L. Ren, L. Li, P. He, G. Lan, Y. Zhang, K. Yang. Cytotoxic effect on osteosarcoma MG-63 cells by degradation of magnesium. Journal of Materials Science & Technology. 2014;30:888-893.

[63] R. Rettig, S. Virtanen. Time-dependent electrochemical characterization of the corrosion of a magnesium rare-earth alloy in simulated body fluids. Journal of Biomedical Materials Research Part A. 2008;85A:167-175.

[64] C. Liu, Y. Xin, X. Tian, P. K. Chu. Degradation susceptibility of surgical magnesium alloy in artificial biological fluid containing albumin. J Mater Res. 2007;22:1806-1814.

2

[65] F. Witte, N. Hort, C. Vogt, S. Cohen, K. U. Kainer, R. Willumeit, F. Feyerabend. Degradable biomaterials based on magnesium corrosion. Curr Opin Solid State Mater Sci. 2008;12:63-72.

[66] D. Zhao, F. Witte, F. Lu, J. Wang, J. Li, L. Qin. Current status on clinical applications of magnesium-based orthopaedic implants: A review from clinical translational perspective. Biomaterials. 2017;112:287-302.

[67] D. Dziuba, A. Meyer-Lindenberg, J. M. Seitz, H. Waizy, N. Angrisani, J. Reifenrath. Long-term in vivo degradation behaviour and biocompatibility of the magnesium alloy ZEK100 for use as a biodegradable bone implant. Acta Biomater. 2013;9:8548-8560.

[68] C. Rössig, N. Angrisani, P. Helmecke, S. Besdo, J.-M. Seitz, B. Welke, N. Fedchenko, H. Kock, J. Reifenrath. In vivo evaluation of a magnesium-based degradable intramedullary nailing system in a sheep model. Acta Biomater. 2015;25:369-383.

3

Additively manufactured biodegradable porous iron

Here, we present the first report on topologically ordered porous iron based on a repetitive diamond unit cell made by Direct Metal Printing (DMP). We conducted a comprehensive study on the in vitro biodegradation behavior (up to 28 days), electrochemical performance, time-dependent mechanical properties, and biocompatibility of the scaffolds. The mechanical properties of AM porous iron (E = 1600-1800 MPa) were still within the range of the values reported for trabecular bone after 28 days of biodegradation. Electrochemical tests showed up to ≈12 times higher rates of biodegradation for AM porous iron as compared to that of cold-rolled (CR) iron, while only 3.1% of weight loss was measured after 4 weeks of immersion tests. The biodegradation mechanisms were found to be topology-dependent and different between the periphery and central parts of the scaffolds. While direct contact between MG-63 cells and scaffolds revealed substantial and almost instant cytotoxicity in static cell culture, as compared to Ti-6Al-4V, the cytocompatibility according to ISO 10993 was reasonable in in vitro assays for up to 72 h. This study shows how DMP could be used to increase the surface area and decrease the grain sizes of topologically ordered porous metallic biomaterials made from metals that are usually considered to degrade too slowly (e.g., iron)，opening up many new opportunities for the development of biodegradable metallic biomaterials.[1]

3.1. Introduction

Among biodegradable metals, those based on magnesium and iron have been studied the most [1-10]. The important challenge when dealing with magnesium-based biomaterials is that their degradation rates are relatively high [11, 12]. On the contrary, the major disadvantage for iron-based materials is their slow degradation rates [13]. AM porous metallic biomaterials generally have much larger surface area as compared to their solid counterparts [14]. This may be not an advantage for magnesium-based materials, because larger surface area normally results in an even higher biodegradation rate. Increased surface area could, however, be an important advantage for materials that degrade too slowly such as iron and its alloys. Besides, iron-based alloys possess better mechanical properties than Mg-based alloys [15], making them more interesting as porous biomaterials.

In addition, iron is inexpensive [10] and does not release hydrogen gas during biodegradation. Moreover, a number of animal studies have reported that iron-based biomaterials exhibit good biocompatibility [13, 16-18]. So far, only a few studies on the development of iron scaffolds for orthopedic applications have appeared in the literature and powder metallurgy techniques [19-21], electrodeposition [22], ink/binder-jetting [1, 15], or space holder [23-26] have been used.

Here, we demonstrate for the first time how direct metal printing (DMP) could be used to fabricate topologically ordered porous iron. We also present a comprehensive study on the biodegradation behavior, electrochemical performance, biocompatibility, and the evolution of the mechanical properties of the scaffolds over time.

3.2. Material and methods

3.2.1. Scaffold manufacturing and post processing

Design files were prepared with Magics (Materialise, Belgium) and DMP Control software (3D Systems, Belgium). The samples were designed to have a height of 10.5 mm, a diameter of 10 mm, a relative density of 20%, and a diamond unit cell with a strut thickness 200 µm and a cell size of 1 mm (Fig. 1a, b). A ProX DMP 320 machine (3D Systems, Belgium) was used for sample preparation. We used a nitrogen gas atomized Fe powder (Material Technology Innovations Co., Ltd., China) (Fig. 1c) with the following characteristics: purity: 99.88%; particle sizes: D_{10}=32 µm, D_{50}=48 µm and D_{90}=71 µm; morphology: spherical; apparent density: 4.09 g/cm^3; tap density: 4.88 g/cm^3; angle of repose: 157 °; carbon content: 0.0044%. The microstructure (Fig. S1) of the iron powder was also analyzed. The powder was deposited in layers of 30 µm during DMP. Given the low relative density of the samples, only contour but no hatch

vectors were used (Fig. 1d, 0.33 W/mm energy density). The samples were built on a steel base plate and were later on removed from this base plate with electrical discharge machining (EDM). Powder particles entrapped in pores were removed by means of ultrasonic cleaning in 96 % ethanol for 20 min. Then, the samples were chemically cleaned in 50% HCL for 1 min to remove residuals from EDM and loose powder particles, followed by 5 min ultrasonic cleaning in 96 % ethanol again to wash out HCl.
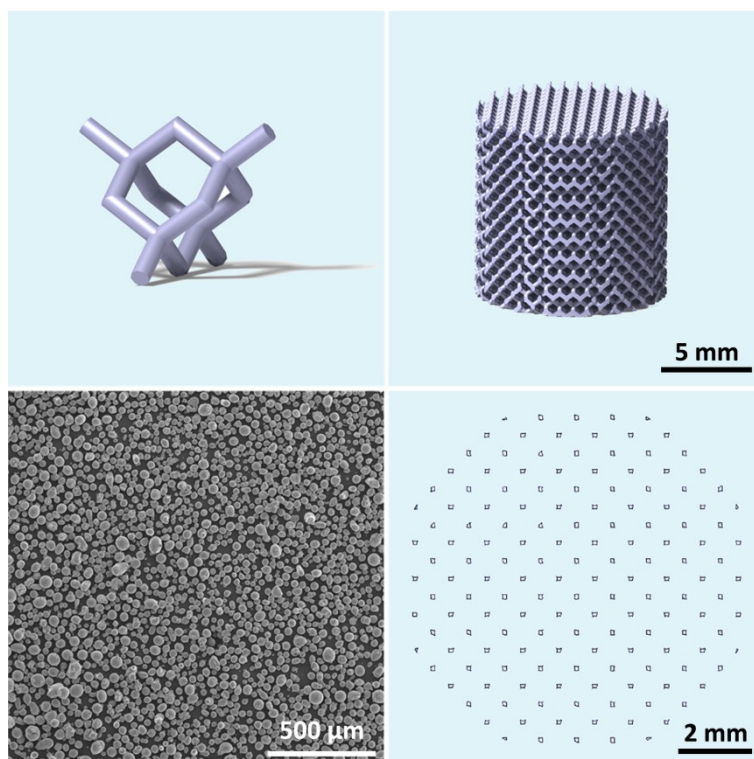
Figure 1. Scaffold design and manufacturing: (a) diamond unit cell, (b) scaffold design, (c) Fe powder particle morphology, (d) an example of one layer scanned in the AM process (DMP Control software).

3.2.2. Topological characterization

The iron scaffolds were imaged using micro-computed tomography (μCT) (Quantum FX, Perkin Elmer, USA) at a tube current of 180 μA , a tube voltage of 90 kV, a scan time of 3 min, and a resolution of $(30 \ \mu m)^3$ with a total 3600 projections. μCT images were automatically reconstructed and converted into a series of 2D images using Analyze 11.0 (Perkin Elmer, USA). Then, the images were exported to FIJI (NIH,

Bethesda, MD, USA) and locally thresholded using Bernsen algorithm (radius = 15). This allowed accurate segmentation of the scaffolds and capturing of their morphological features. Afterwards, circular regions of interest (ROIs) with a diameter of 10 mm were created on the cross section of the scaffolds. After thresholding and using the cylindrical ROIs which overlay the total volume of the scaffolds, porosity (defined as the ratio of the void volume to the scaffold volume), averaged strut thickness (Tb.Th) and averaged strut spacing (Tb.Sp), i.e., pore size, were calculated using BoneJ (a plugin of FIJI).

3.2.3. Microstructural characterization

The microstructures of the as-built iron samples were examined using an optical microscope (OM, model BX60M, Olympus) after etching by a 5% Nital reagent (5 ml HNO_3 per 100 ml C_2H_5OH). The microstructure of the as-received cold rolled (CR) Armco iron samples (AK Steel, the Netherlands) with high purity (> 99.85%) was examined as a reference material. The average grain size was measured using the line intercept method.

3.2.4. Immersion tests

In vitro degradation tests were conducted in revised simulated body fluid [27] (r-SBF) in open beakers and the beakers were kept in a stirred thermostatic bath at 37 °C for up to 28 days. To determine weight changes, samples were taken out of the r-SBF solution, ultrasonically cleaned with 99% acetone and 96% ethanol for 30 min each, dried at room temperature, and finally weighed using a balance with an accuracy of 0.1 mg. pH values (accuracy: ± 0.002, InLab Expert Pro-ISM, METTLER TOLEDO) of the medium were registered after 1, 2, 7, 14, and 28 days of *in vitro* degradation. Fe, Ca, and P ion concentrations in the solution were analyzed at different time points using an inductively coupled plasma optical emission spectroscope (ICP-OES, iCAP 6500 Duo, Thermo Scientific).

3.2.5. Characterization of degradation products

The morphology and composition of the degradation products on the surface of the samples after the biodegradation tests were analyzed at selected time points with a scanning electron microscope equipped with energy-dispersive X-ray spectroscopy (EDS) (SEM, JSM-IT100, JEOL). In addition to observing the periphery of the samples, we cut the samples and observed the degradation products in the center. Phase identification of the degradation products was performed using an X-ray diffractometer (XRD, Bruker D8 Advance diffractometer in Bragg-Brentano geometry). The diffractometer was equipped with a graphite monochromator and Vantec position

sensitive detector and operated at 45 kV and 35 mA with a step size of 0.034° and a dwell time of 30 s per step using Co Ka radiation. In addition, Fourier-transform infrared spectroscopy (FTIR) spectra were obtained from a Thermo-Nicolet Nexus FTIR apparatus equipped with a liquid-nitrogen cooled MCT-A (mercury-cadmium-telluride) detector and a SAGA grazing angle accessory at an incident angle of 80°. An infrared background spectrum was collected on a freshly polished sample prior to the analysis of the degraded samples. The final spectra were compared against this background. For each spectrum, 128 scans at a resolution of 4 cm^{-1} were co-added.

3.2.6. Electrochemical tests

For electrochemical tests, AM iron samples were mounted in an epoxy resin and ground with 800 grit SiC sandpaper. The picture of the sample's cross section was imported into ImageJ and the surface area of 0.24 cm^2 exposed to electrolyte of was measured through the Analyze Particles option in ImageJ. Copper screws were placed inside the resin to make the samples conductive. Electrochemical tests were performed in a 1250/1255 Solartron potentiostat in r-SBF at 37 °C. A three-electrode electrochemical cell was set up with a platinum mesh as the counter electrode, Ag/AgCl as the reference electrode, and Fe specimen as the working electrode. Potentiodynamic polarization (PDP) was applied to test the sample after 1-day and 28-day immersion. The set-up was first stabilized for 1 h to reach the open circuit potential (OCP). Then, the polarization started at an initial potential of -0.3 V below OCP and was increased to +0.5 V above OCP at a scan rate of 0.5 mV/s. Electrochemical impedance spectroscopy (EIS) was conducted at different immersion time points (1, 2, 3, 7, 14, 21, and 28 days). The amplitude of the signal was 10 mV versus OCP over a frequency range between 100 kHz and 10 mHz for impedance data acquisition. The CR iron samples with surface area of 0.5 cm^2 (> 99.85% purity, ARMCO Iron) were also analyzed as a reference material.

3.2.7. Mechanical characterization

Compression tests were carried out using an Instron machine with 10 kN load cell at a crosshead speed of 2 mm/min. No lubrication was applied on the compression plates. The mechanical properties of the as-built, as-polished, and as-degraded AM porous iron were determined according to ISO 13314:2011 and the quasi-elastic gradient (hereafter referred to as the elastic modulus) and yield strength were obtained. Elastic modulus of the porous material was determined as the slope of the initial linear part of the stress-strain curve using linear fitting in Origin software. The initial linear part of the stress-strain curve was offset by 0.2 % and its intersection with the stress-strain curve was taken to calculate the yield strength. Stress-strain curves were obtained at different immersion time points (i.e., 1, 2, 7, 14 and 28 days). The tests were performed in

triplicate per time point and the average values of the elastic modulus and yield strength were calculated.

3.2.8. Biocompatibility assessment

3.2.8.1. Extract preparation

Biocompatibility evaluation was essentially performed as described before [28]. Briefly, AM iron scaffolds were stored dry and at ambient temperature to prevent corrosion. Prior to assessing cytotoxicity, scaffolds (Ø 10 mm x 10 mm, $n = 5$) were weighed, immersed for 30 min in 100 % isopropanol (Merck, Darmstadt, Germany) at room temperature, air-dried and subsequently incubated in Dulbecco's modified eagle medium (DMEM) with low glucose (Sigma) supplemented with 10% fetal calf serum (PAN Biotech) for 72 h under physiological conditions (5% CO_2, 20% O_2, 95% humidity, 37 °C). Extracts were then prepared according to EN ISO standards 10993:5 and 10993:12, respectively, with a specimen weight to extraction medium ratio of 0.2 g/mL being 1X. Less concentrated extracts (e.g., 10X) were likewise prepared using more extraction medium. In parallel, Ti-6Al-4V (ASTM Grade 5) extracts (1X) were prepared as negative controls [28]. Dimethyl sulfoxide (DMSO) (20%) was used as positive controls [29]. Prior to cytotoxicity testing, extracts were sterile filtered using a 0.2 µm syringe filter.

3.2.8.2. Cytotoxicity assays

For indirect cytotoxicity tests, 2,500 MG-63 cells were seeded, in technical triplicates, per well of a 96-well plate and pre-cultured for 12 h prior to exchanging DMEM for Fe-extracts. Cell viability was then tested using MTS assay (CellTiter 96® AQueous One Solution Cell Proliferation Assay, Promega, G3580) at 0, 24, 48 and 72 h, with unconditioned DMEM as negative control. Prior to the addition of MTS tetrazolium compound, all media and extracts were replaced with fresh cell culture medium in order to prevent any interference of metal extract with the tetrazolium salt. MTS test was further performed according to manufacturer's instructions. Briefly, at respective time points, 20 µl of CellTiter 96® AQueous One Solution Reagent was pipetted into each well of the 96-well plate containing indicator cells in 100 µl of culture medium. Plates were incubated at 37 °C for 2 h and the absorbance was subsequently recorded at 490 nm. Relative cellular activity (X) was calculated using the following formula:

$$X = \frac{OD\ (test)}{OD\ (negative\ control)} \times 100\%$$

Independently, lactate dehydrogenase (LDH) release into the medium was quantified as another biomarker for cytotoxicity. Briefly, MG-63 cells were seeded as

described above (see MTS assay) prior to assessing cytotoxicity using Pierce™ LDH Cytotoxicity Assay Kit (Thermo Scientific, 88954) according to the manufacturer's instructions with spontaneous LDH Activity Controls (water) and Maximum LDH Activity Controls (10X Lysis Buffer added 45 min before measurement). At respective time points, 50 µL of each sample was pipetted in replicates with 50 µL of Reaction Mixture into clean 96-well wells prior to incubation at room temperature for 30 min protected from light. Stop Solution (50 µL) was then added and absorbance was measured at 490 and 680 nm. Relative percentage of LDH activity was calculated according to the manufacturer's description.

3.2.8.3. Direct cytotoxicity assay

Cytotoxicity was further evaluated using live/dead staining (Live and Dead Cell Assay kit; Abcam, ab115347), as we described before [28]. Cells were analyzed using fluorescent microscopy (KEYENCE; live Emission$_{max}$ 495 nm, Excitation$_{max}$ 515 nm and dead Em$_{max}$ 528 nm, Ext$_{max}$ 617 nm. Per iron (Ø 10 mm x 1 mm) and titanium (Ø 15 mm x 1 mm) scaffold, 50,000 and 75,000 MG-63 cells were seeded and incubated for 1 h. Thereafter, 2 ml of fresh medium was added prior to 24 h incubation in replicates, after which live/dead staining was performed, as described above.

SEM analyses were performed, as previously described [28]. Briefly, cell-seeded scaffolds were carefully rinsed in phosphate buffered saline (1X PBS) and fixed for 1 h in 3% glutaraldehyde (Agar Scientific, Wetzlar, Germany) in 0.1 M Sorensen's phosphate buffer (Merck, Darmstadt, Germany) at room temperature, followed by 10 min dehydration steps in 30, 50, 70, 90 and 100 % ethanol (last step twice). Samples were then air-dried at room temperature prior to sputter-coating (Sputter Coater EM SCD500, Leica, Wetzlar, Germany) with 12.5 nm of gold-palladium and imaged at 10 kV in SEM (ESEM XL 30 FEG, FEI, Eindhoven, The Netherlands).

3.2.9. Statistical analysis

Optical density data (MTS, LDH) were normalized to respective controls and relative cytotoxicity was analyzed by two-way ANOVA ($\alpha = 0.05$) and post-hoc Tukey's multiple comparisons test ($\alpha = 0.05$) with $p<0.0001$, ****; $p<0.001$, ***; $p<0.01$, **; $p<0.05$, *; *n.s.* = not significant.

3.3. Results

3.3.1. Topological and surface characteristics of the scaffolds

The as-built scaffolds had an average strut size of 249 ± 6 µm (design value = 200 µm) and a pore size of 749 ± 22 µm (design value = 800 µm) (Table 1). The porosity of the scaffolds was 77.7 ± 1% or 73.2 ± 0.1% respectively, calculated from µCT or weighing, (Table 1). The reconstructed 3D model from µCT is shown in Fig. S2. The weighing method was based on the formula: Porosity =1- (W_{iron}/V_{bulk})/ρ_{iron}, where W_{iron} is the weight of the sample, V_{bulk} the bulk volume of the scaffold and ρ_{iron} the density of pure iron. The surface of the as-built sample was relatively smooth both on the periphery (supplementary document, Fig. S3a) and in the center (supplementary document, Fig. S3c) of the scaffolds. After chemical polishing, a reduced number of unmelted powder particles were present on the external struts of the scaffolds (supplementary document, Fig. S3b), while the struts in the center were less affected by chemical polishing (supplementary document, Fig. S3d). The weight reduction after chemical polishing was 2.2% ± 0.1%.

Table 1- Topological characteristics of AM iron scaffolds.

AM iron scaffolds	Strut size(µm)	Pore size (µm)	Porosity
Design	200	800	80%
Micro CT	249±6	749±22	77.7±1%
Weight	-	-	73.2±0.1%

3.3.2. Microstructure of the scaffolds

AM iron had much finer grains with an average size of 12 ± 6 µm (Fig. 2a) than CR iron that had an average grain size around 65 ± 22 µm (Fig. 2b). However, the gains of CR Fe iron were more regularly shaped than those of AM iron (Fig. 2).
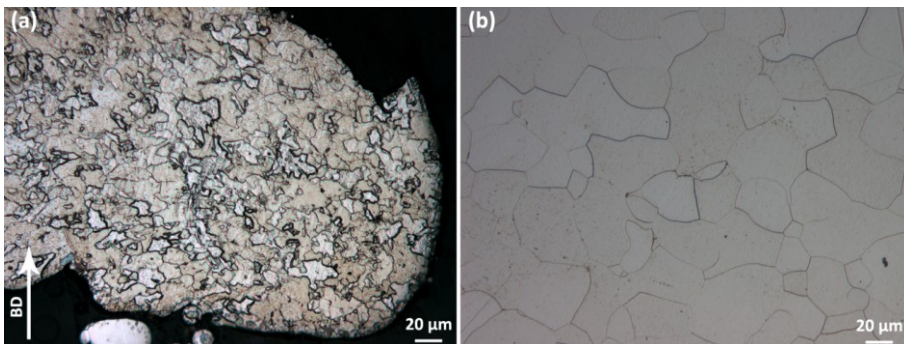

Figure 2. Microstructures of iron samples: (a) AM porous iron and (b) CR Fe.

3.3.3. In vitro degradation behavior of the scaffolds

Brownish degradation products appeared on the surface of the scaffolds on day 1 (Fig. 3a). From day 2 to day 28, the degradation product layer became thicker and the color became darker (Fig. 3a). After 28 days, the samples were completely covered by brownish degradation products (Fig. 3a). At day 28, the iron scaffolds showed a 3.1 % weight reduction (Fig. 3b) after sample cleaning. The pH values of the r-SBF solution increased from 7.4 to 7.8 after 28-day immersion (Fig. 3c). Fe ion concentration increased from 0.98 to 6.03 mg/L until day 7 (Fig. 3d) and then it started to decrease at day 14 (Fig. 3d). Ca and P ion concentrations kept decreasing during the whole immersion test period of 28 days (Fig. 3d).

3.3.4. Characterization of degradation products

The degradation products contained iron protoxide (FeO) and iron carbonate ($FeCO_3$) (Fig. 3e) according to XRD patterns. However, the intensity peaks of these degradation products in the XRD patterns were quite low (Fig. 3e). The FTIR spectra revealed that carbonates, hydroxides and phosphates were present in the corrosion layer (Fig. 3f) with characteristic hydroxide-specific absorption bands at about 3400 cm^{-1} [30], while the peaks at 1750 cm^{-1}and 1000 cm^{-1} likely resulted from CO_3^{2-} and PO_4^{3-} functional groups, respectively [31, 32].

SEM analysis of the external struts showed that, after 1 day immersion, a thin layer of white degradation products (white in SEM and brown from visual observation) already adhered to the surface (Fig. 4a, 1D). From day 7, groups of shiny white loose degradation products formed on the strut surface (Fig. 4a, 7D and 14D) while they covered almost the whole strut surface at day 28 (Fig. 4a, 28D). Different degradation behavior was observed from center to periphery of the scaffolds (Fig. 4b). The degradation products at day 7 were thinner and more condensed at the center of the samples (Fig. 4c) while loose and thicker degradation products (Fig. 4d) were formed on the periphery. The degradation products in the center (Fig. 4c, spot 1) and on the periphery (Fig. 4d, spot 1) all contained C, O, P, Ca, and Fe, with higher P and Ca concentrations on the periphery. After 28 days of immersion, the degradation products in the center had two types of ordered crystal-like structures, one being spherically shaped and containing C, O, Ca and Fe (Fig. 4e, spot 1) and the other being feather-shaped and containing C, O and Fe only (Fig. 4e, spot 2), all without P. The morphologies of the degradation products on the periphery exhibited features similar to those observed after 7 days (Fig. 4d). The compositions were also similar to those observed after 7 days with increased O and decreased Fe concentrations (Fig. 4f, spot 1).

3
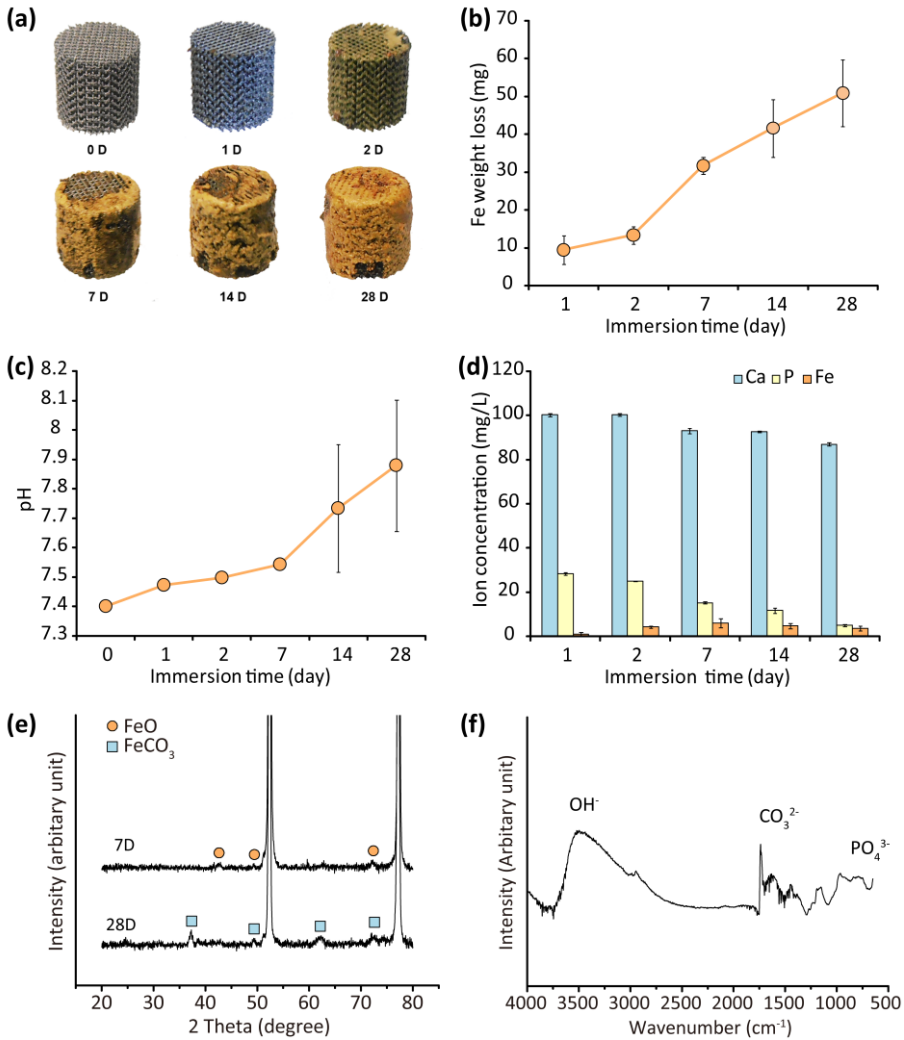
Figure 3. *In vitro* degradation behavior of iron scaffolds: (a) visual inspection of as-degraded scaffolds, (b) weight loss, (c) pH variation with immersion (error bar invisible before day 7 because of small deviation), (d) ion concentration variation with immersion time, (e) XRD analysis and (f) FTIR analysis of degradation products.
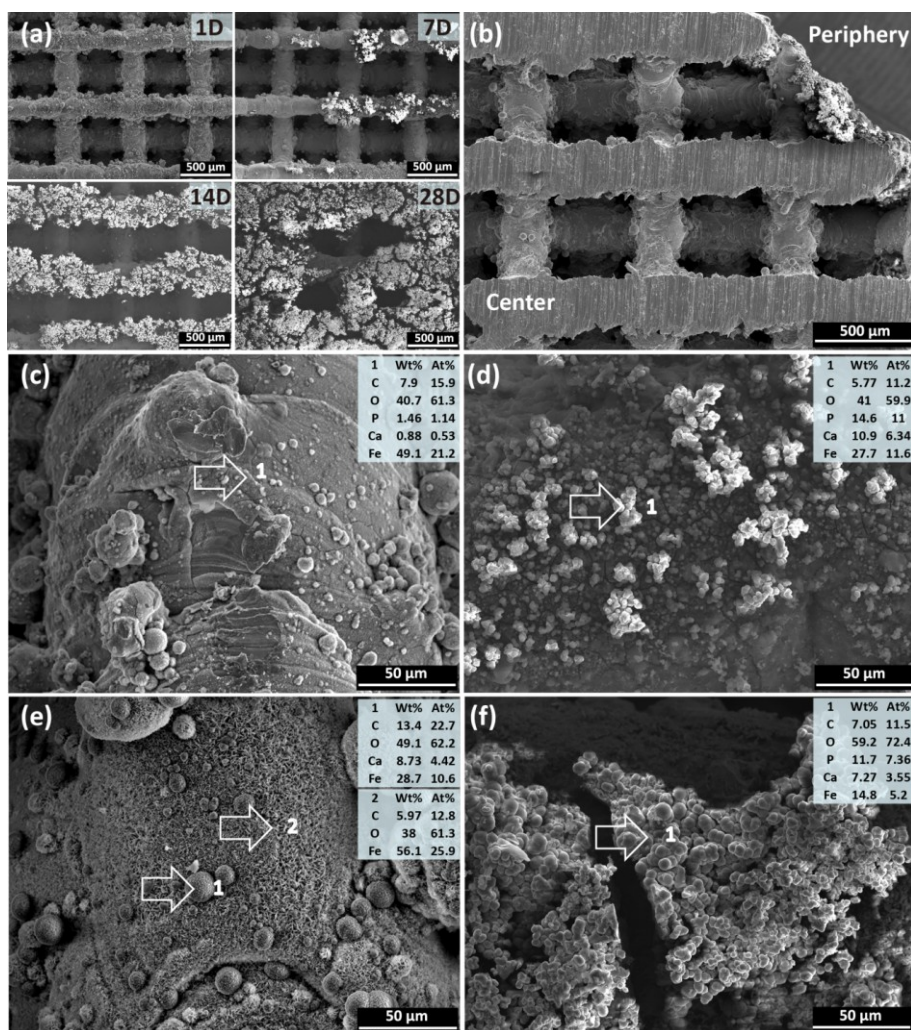
Figure 4. SEM and EDS analyses of degradation products from the scaffold periphery to the center: (a) degradation products on the periphery at different immersion time points, (b) cross section of the scaffolds after 7-day immersion, (c) degradation products in the center and (d) on the periphery after 7-day immersion, (e) degradation products in the center and (f) on the periphery after 28-day immersion. 1 and 2 indicates the spot where EDS analysis was performed.

3.3.5. Electrochemical behavior

According to the potentiodynamic polarization curves, AM iron exhibited higher corrosion current densities as compared to CR iron both at day 1 and at day 28 (Fig. 5a,

3

b), while the OCP values were similar. The corrosion current density at day 1 was 102.8 ± 19.2 μA/cm^2 and 8.6 ± 0.9 μA/cm^2 for AM iron and CR iron samples (Fig. 5a), respectively. The corrosion rates, assuming relatively uniform corrosion, calculated for AM iron and iron CR specimens according to ASTMG59 were 1.18 ± 0.22 and 0.10 ± 0.01 mm/year, respectively.

Both AM and CR samples exhibited increases in impedance modulus values at low and medium frequency from day 1 to 3, as observable in the Bode impedance modulus diagram (Fig. 5c, d). The impedance started decreasing from day 7 and remained decreasing up to day 28 (Fig. 5c, d). At the same immersion time points, AM iron samples always showed smaller impedance modulus values than CR iron samples at both low ($|Z|_{0.01Hz}$) and medium frequency ($|Z|_{10Hz}$) (Fig. 5e, f).

3.3.6. Mechanical properties

Under uniaxial compression, the as-built, as-polished, and degraded specimens without cleaning exhibited smooth stress-strain curves (Fig. 6a, b) without sudden drop. The curves all followed similar patterns with a linear elastic region at beginning and a rapidly decreased slope afterwards, followed by a plateau stage with almost no fluctuations (Fig. 6a, b). The differences in the elastic modulus and yield strength between the as-built and as-polished samples were negligible (Fig. 6a). The elastic modulus decreased after 1-day immersion, but it increased from day 2 and remained almost unchanged until day 14. Then, it decreased again at day 28 (Fig. 6c). From day 1 to day 28, the yield strength decreased gradually from 23.7 to 22.4 MPa (Fig. 6d).
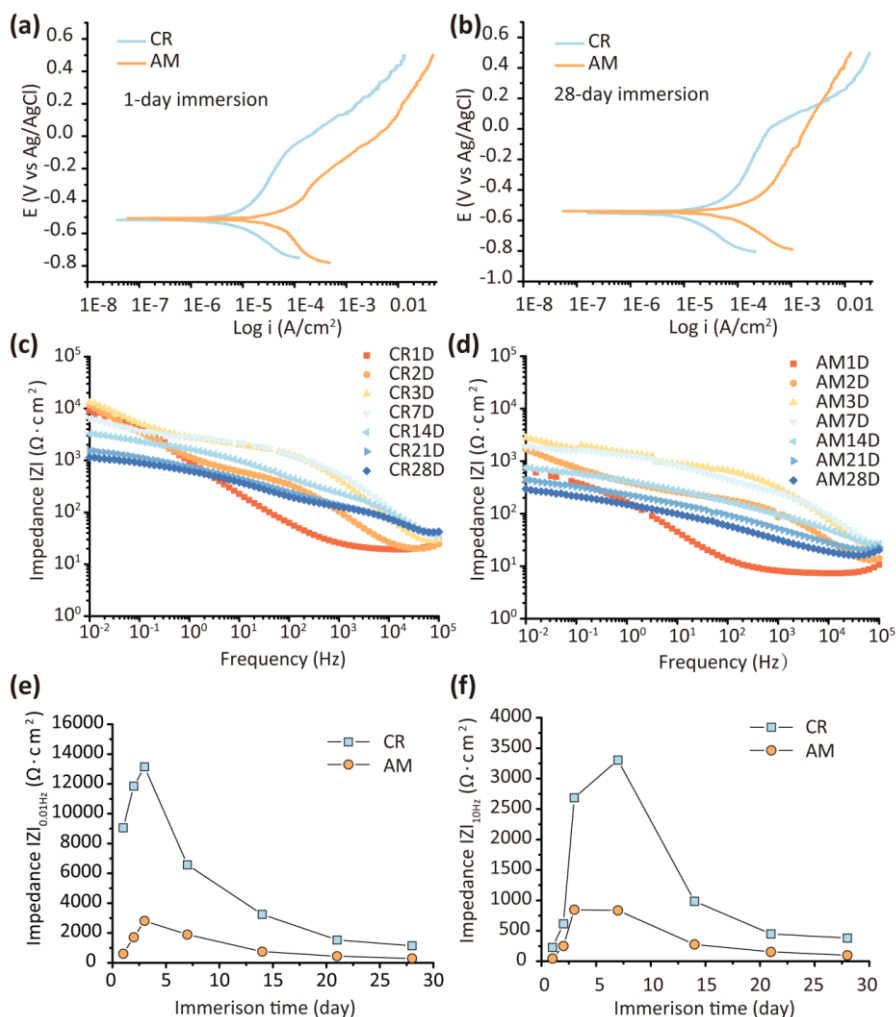
Figure 5. Electrochemical performance of AM porous iron in comparison with CR iron: (a) PDP curves after 1-day immersion and (b) after 28-day immersion, (c), (d) Bode impedance modulus of CR iron (d) and AM porous iron (d), (e),(f) impedance modulus value at (e) low (0.01 Hz) and (f) medium (10 Hz) frequency of samples as a function of immersion time.
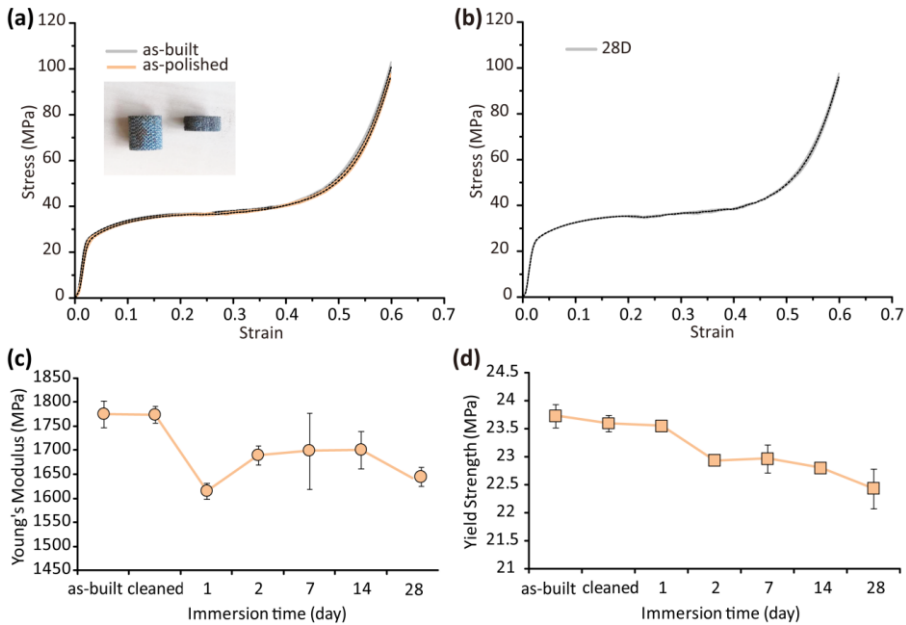
Figure 6. Mechanical behavior: (a) compressive stress-strain curves of as-built and as-polished scaffolds (inset showing the specimen at the start and at a strain of 60%), (b) compressive stress-strain curves of porous iron after 28 day immersion, (c) elastic modulus change with immersion time and (d) yield strength change with immersion time.

3.3.7. Biocompatibility in vitro

Direct cytocompatibility assays (Figs. 7 and 8), employing live-dead staining and SEM, were relatively hard to quantify, although clearly only limited numbers of MG-63 appeared to survive direct exposure to iron scaffolds (Fig. 7). Of note, micrographs (Fig. 8) revealed MG-63 cells in intimate contact to the iron scaffold. While cells developed filopodia-like protrusions on Ti-6Al-4V, a more condensed cell morphology appeared on eroded iron surface (Fig. 8d). After 24 h, viable cells (green) were hardly detectable on iron (Fig. 7), while red fluorescence from the majority of cells revealed compromised membrane integrity. Live-dead staining on Ti-6Al-4V scaffolds showed that the vast majority of cells were viable (green).
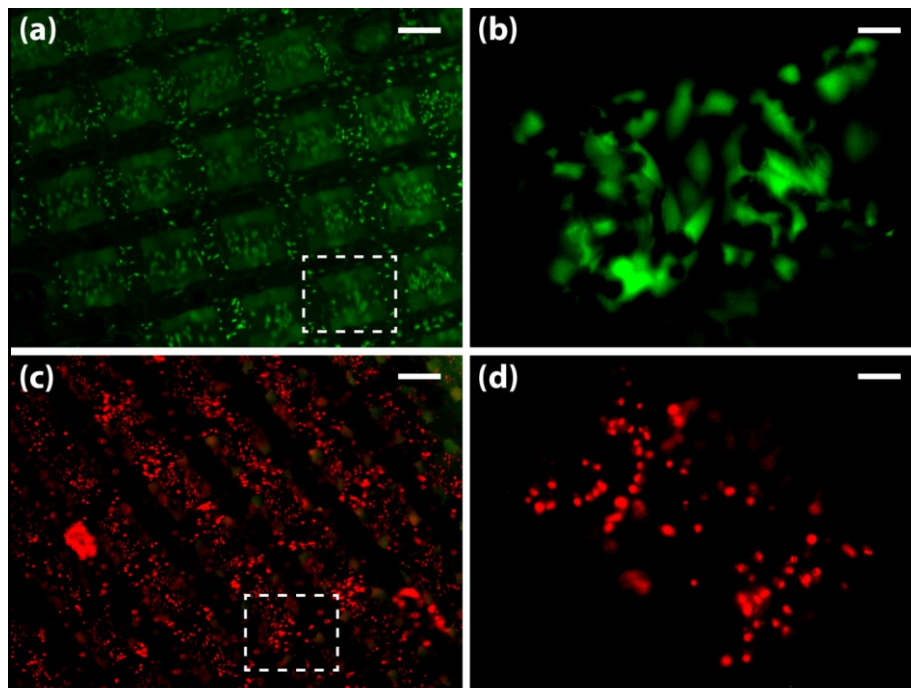
Figure 7. Biocompatibility of AM iron scaffolds *in vitro*. MG-63 cells on Ti-6Al-4V (a, b) and iron (c, d) scaffolds, respectively. Low magnification fluorescent optical images (FOI) of cells attached to struts (a, c). Higher magnification of the boxed area of the lattice structure (b, d). Live cells, green; dead cells, red. Scale bars indicate 300 μm (a, c) and 30 μm (b, d).

LDH assay (Fig. 9a) revealed level 0 cytotoxicity (i.e., ≤ 25% cell death) for Ti-6Al-4V at all time points, with the largest SD at 72 h. DMSO was 100% cytotoxic after 72-h incubation. Level 1 cytotoxicity was determined for Fe, with increasing levels of cytotoxicity with increasing extraction time, ranging from 25 % after 24 h to just below 40 % after 72 h. As an independent means to assess cytocompatibility, cell viability was determined using MTS assay (Fig. 9b): with Ti-6Al-4V extracts, MG-63 cells were about 100% viable independent of the extraction time, with slightly higher SD at longer time points. MG-63 cells on iron extracts revealed 75 % viability at 24 h, with a decreasing trend with longer incubations; reaching 40 % viability for the 72-h extraction.
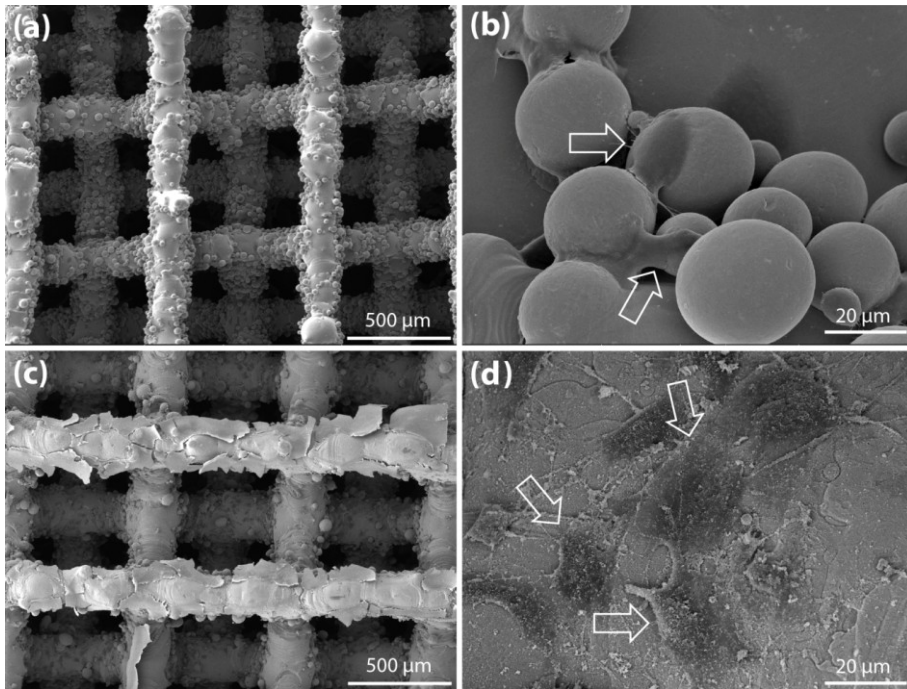
Figure 8. Ultrastructural analyses of cell attachment *in vitro*. MG-63 cells on Ti-6Al-4V (a, b) and iron (c, d), respectively. Lower magnification scanning electron micrographs (SEM) of scaffold lattice structures (a, c) and higher magnifications (b, d) after seeding. Arrows indicate individual cells. Magnification indicated by scale bar.
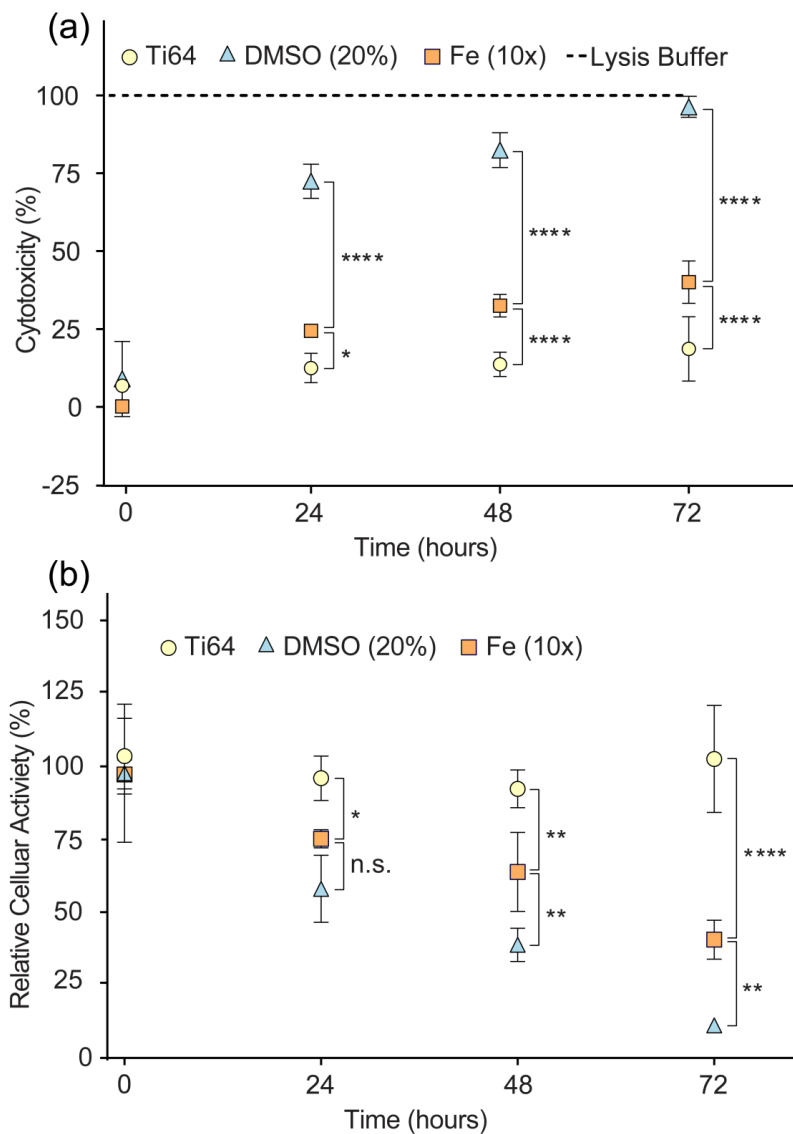
Figure 9. Cytotoxicity *in vitro*. Relative cytotoxicity (a) and remaining celluar activity (b) of MG-63 cells upon exposure to AM iron scaffolds, as measured by LDH and MTS assay, respectively. Experiments were performed with extracts of randomly chosen replicate Fe-scaffolds (squares, n=5) and compared to AM Ti-6Al-4V (balls, Ti64) scaffolds of the same design (n=3). Dimethylsulfoxide (DMSO, triangles) and cell Lysis Buffer (dotted line, set to 100% in (a)) were used as controls. *n.s.,* not significant; *, p<0.05; **, p<0.01; ***, p<0.001; ****, p<0.0001.

3.4. Discussion

3.4.1. Microstructure

Micro melt pools formed [33] during DMP leads to high cooling rates (10^3 to 10^8 K/s) [34], which results in a non-equilibrium solidification process and enhances grain refinement. The average grain size of AM porous iron was more than 5 times smaller than that of CR iron. Moreover, unlike previously reported AM solid iron [35, 36], the AM porous scaffolds had no elongated grains oriented in parallel with the building direction. This indicates that the effects of directional solidification were not as strong as in the case of solid counterparts, as the struts of the scaffolds were built in a tilted direction.

3.4.2. Biodegradation behavior

Based on the PDP results, AM porous iron showed higher values of corrosion current density as compared to CR iron (with similar OCP values). The corrosion rate of CR iron after 1 day (0.10 ± 0.01 mm/year) was comparable with the values found by others (0.17-0.24 mm/year) [37, 38]. The corrosion rate of AM porous iron after 1 day was 1.18 mm/year, which is ≈12 times higher than that of CR iron and also higher than the values found for the iron samples fabricated using other techniques [39-41] and most of the iron alloys that have been studied so far [11]. This clearly shows the advantages of the refined microstructure from AM in increasing the biodegradation rate of slowly degrading metals such as iron. It is well known that microstructural features such as texture and dislocation density may affect the corrosion rate [37]. Particularly relevant here is that the decrease in grain size may contribute to passive film destabilisation [42]. The specific solidification process experienced during AM creates smaller grain sizes that in turn increase the grain boundary area with defects in the crystal structure and high internal energy [43]. Grain boundaries of large area are expected to be more chemically active in a corrosive medium [38, 44].

The Bode impedance diagram showed that the changes of impedance had similar trends for AM and CR iron samples. The impedance modulus values at the low frequency range can provide information about the charge transfer resistance and separation processes at the metal surface of the corroding system and the impedance modulus value changes in the middle frequency range relate to resistive and capacitive evolutions of a layer on the surface of the substrate, e.g. by growth or (partial) dissolution of a corrosion product layer [45-47]. The increase of the impedance modulus at low frequency ($|Z|_{0.01Hz}$) from day 1 to day 3 relates to increasing corrosion resistance and could be attributed to the formation of a corrosion product layer at the beginning of the immersion test [32], also shown by the increasing impedance modulus values in the

mid-frequency range ($|Z|_{10Hz}$). Then, the impedance modulus values at both low and mid frequency ranges decreased at day 7, probably resulting from relatively limited integrity and protectiveness of the corrosion product layer and hence increasing corrosion susceptibility of the underlying substrate. At the same immersion time points, AM iron samples always had lower impedance modulus values (or corrosion resistance) as compared to CR iron samples, which is in agreement with the results obtained from the PDP tests and further confirms the increased biodegradation rate of AM iron as compared to that of CR iron.

The immersion tests of the whole scaffolds showed a 3.1% weight reduction only after 28 days of immersion. If we normalize this with respect to a total theoretical surface area of 28 cm^2, the corrosion rate of the scaffolds is only 0.03 mm/year, which is one order of magnitude lower than the values reported by other researchers [37-39]. Visual inspection and SEM analysis suggested that there were different corrosion mechanisms operating from the periphery to the center of the scaffolds. At the periphery, degradation took place quite fast, as evidenced by the formation of a brownish layer after day 1 (Fig. 3a). In the center of the scaffolds, however, there were no brownish corrosion products even after 28 days. SEM revealed thinner, more adherent crystal-like corrosion products formed at the center of the samples with a thickness that increased with the immersion time (Fig. 4c, e). The degradation products were, however, loose and irregularly shaped on the periphery of the samples. EDS showed that the corrosion layer of external struts contained Ca and P elements (Fig. 4d, f), while no P element was found in the center of the scaffolds even after 28 days of immersion (Fig. 4e). Combined with ICP results (Fig. 3d), it was concluded that the Ca and P elements found on the corrosion layer came from r-SBF. To understand the different degradation mechanisms better, we inspected the surface morphology of the degraded struts after ultrasonic cleaning (Fig. 10). It was observed that r-SBF attacked the struts on the periphery of the samples and exposed the grains on their surfaces (Fig. 10a, b). The struts in the center of the samples, however, stayed almost intact (Fig. 10d). This explains why the normalized degradation rate is much smaller than the results reported in the literature. The local pH value is therefore expected to be different from the center to the periphery of the samples. In static immersion tests, scaffolds may have stagnant flow in the center and the diffusion of ions may be hampered. Gradually formed corrosion products on the outer surface of the scaffolds may further restrict the diffusion process. In addition, accumulation of OH$^-$ ions in the center of the scaffolds may lead to the stabilization of the passive layer formed on the struts.

Another reason for the low weight loss measured here may be related to the limitations of the weight loss measurement and sample cleaning. For solid samples, weight loss measurement works quite well, because it is feasible to remove all the corrosion products with minimum attack to the sample itself. In the case of highly

3

porous scaffolds, however, it is difficult to remove all the corrosion products, especially those in the center of the scaffolds. After cleaning, there were still corrosion products remaining not only in the center (Fig. 10d) but also on the periphery (Fig. 10c) of the scaffolds. The retained corrosion products on the periphery contained C, O, P, Ca and Fe (Fig. 10c, spot 001). In the center, the sphere-shaped corrosion products remained, which contained C, O, Fe and Ca (Fig. 10d. spot 1). As compared to the corrosion products before cleaning (Fig. 4e), the feather-like corrosion products could be removed, but the sphere-like structures still remained. Other researchers used acids or alkalis to remove the corrosion products [17, 48-50], but this would cause extra deduction of the struts of the porous iron samples, especially on the periphery. ICP-OES analysis showed even less iron release to r-SBF as compared to the weight loss measurements, because iron ions participated in the formation of the corrosion products. That is why iron ion concentration even decreased after day 7.

Based on the reasoning above, it is clear that in addition to the microstructure and chemical composition, the topology of AM porous scaffolds greatly influences their degradation behavior. Optimizing the topological design of the porous structure could therefore be an effective measure for adjusting the degradation behavior of AM porous iron. For example, a larger pore size or a smaller diameter may further increase the degradation rate of iron scaffolds.

Moreover, the *in vitro* test environment affects the degradation rate as well. The inorganic ion concentrations in the immersion medium used here (r-SBF) are similar to the blood plasma. Hanks' solution [51] with higher Cl^- and lower HCO_3^- concentrations tends to increase the corrosion rate of iron. In addition, other researchers have reported higher degradation rates of iron in dynamic immersion tests [52]. Furthermore, without CO_2 control, the bulk pH of the medium keeps increasing, which could slow down the biodegradation. Follow-up studies in bioreactors and using other more complex biodegradation environments may alleviate some of these limitations. Finally, the degradation behavior of iron scaffolds needs to be evaluated *in vivo*. From the results obtained from earlier research [13], pure iron pin did not exhibit pronounced reduction in volume or mass in a rat model. Other researchers reported noticeable degradation of pure iron stents, while voluminous degradation products formed and remained even after longer implantation [18, 53]. Peuster et al. [16] found that macrophages carrying iron contributed to the clearance of corrosion products from the implantation site as the solubility of iron degradation products in body fluid was low. Since a layer of corrosion products was also observed from our *in vitro* immersion tests, it would be of great interest to perform an *in vivo* study to compare additively manufactured iron scaffolds and solid iron in *in vivo* degradation behavior.
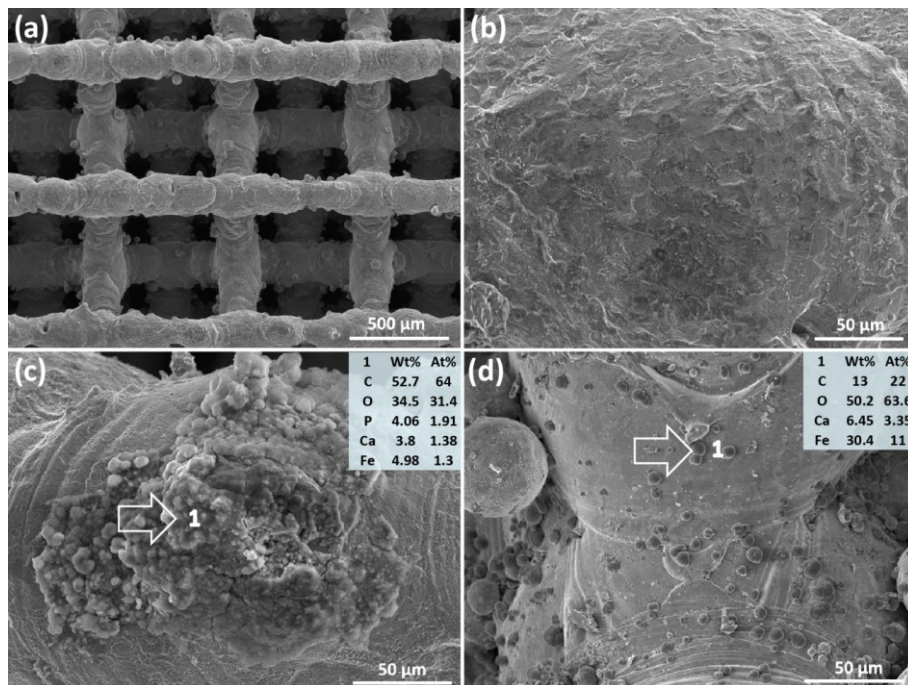
Figure 10. SEM and EDS analyses of retained degradation products (28-day immersion) after cleaning: (a) strut morphology at a low magnification, (b) at a high magnification, (c) retained degradation products on the periphery and (d) in the center of the scaffolds. 1 indicates the spot where EDS analysis was performed.

3.4.3. Mechanical behavior

The mechanical properties of the AM porous iron specimens remained within the ranges of the values of mechanical properties reported for trabecular bone (i.e., E= 500-20,000 MPa [54], σ_y= 0.2-80 MPa [55]) after 28 days of biodegradation. In the case of porous magnesium, which is reported to lose its structural integrity within a much shorter time, alloying or surface treatment is always needed [56-59]. In the case of porous iron, however, without any additional treatments or potentially toxic alloying elements, it has high mechanical properties, which is a distinct advantage.

Unlike other AM porous structures based on the diamond unit cell [60, 61], the iron scaffolds studied here showed smooth stress-strain curves during uniaxial compression without fluctuations after the maximum stress. In addition, no sudden failure occurred and specimens still had a cylindrical shape at a strain of 60% (Fig. 6a inset). These could be explained by the high ductility of pure iron. Similar behaviors have been observed for other highly ductile porous materials, such as AM porous structures made

from pure titanium and tantalum [62, 63]. After *in vitro* immersion at given time points, it appeared that biodegradation has different influences on the stiffness from the yield strength of porous iron. It could be related to the different effects of interfacial bonding [64] (between the degradation products and iron) on the elastic modulus and yield strength of AM porous iron. Since the elastic modulus was measured over a narrow range of small strains, lateral dilation was insufficient to cause the interfacial separation and the load could still be carried by iron and its degradation products. As a result, accumulation of degradation products increased the elastic modulus of AM porous iron from day 2. After more corrosion occurred on the struts, despite increased amounts of degradation products, the elastic modulus of the scaffolds was also affected by the strut thickness. After 28 days of immersion, the elastic modulus of the specimens decreased to a value similar to that measured at day 1. This could be attributed to the trade-off between the reduction in the strut thickness and accumulation of corrosion products. For the yield strength of porous iron, the interfacial bonding became important. Load transfer at the interface between the degradation products and iron might be inefficient for poorly bonded degradation products, especially at strains close to the yield point. Then much of the load could not be carried by the degradation products and yield strength relied on the strength of the remained iron primarily. As a result, the strength of the degraded porous structure decreased, although in a small range, as the biodegradation process progressed.

3.4.4. Biological evaluation

In order to evaluate the potential of AM porous iron scaffolds for biomedical applications, we characterized their biocompatibility by using three different techniques: (i) a direct contact live-dead staining assay, (ii) visual inspection of attached cells in direct contact with the iron struts using electron micrographs, and (iii) two independent quantitative indirect cytotoxicity assays.

While SEM analyses (Fig. 8) showed polygonal shaped MG-63 cells in close contact with the iron surface (Fig. 8d; arrows, black) 24 h after seeding, in the magnified fluorescent images of the live-dead staining (Fig. 7) cells appeared to be more spherically condensed (Fig. 7d) on the iron surface as compared to more polygonal/spindle-shaped cells on Ti-6Al-4V (Fig. 7b) controls. Moreover, most cells appeared to be alive on Ti-6Al-4V but only a few on the iron surface from the dual channel images. Although classification of cell death remains challenging [65], from a morphological point of view, the observed condensation of MG-63 cells may be indicative of apoptosis, which is characterized by e.g., rounding-up, retraction of pseudopods, and a pyknotic cell volume reduction. The red fluorescence, on the other hand, is indicative of a loss of plasma membrane integrity and altogether hints towards a certain iron-mediated toxicity.

Although pure iron showed good biocompatibility during long time implantation as a biodegradable stent or pin [13, 16, 66, 67], direct contact cytotoxicity was observed in several *in vitro* studies with different type of cells [68, 69]. In contrast to the *in vitro* situation, released ions can be diluted *in vivo* and excreted from the local site into the body so that local concentrations will be diminished [18]. While *in vitro* cell seeding was conducted in a culture dish where released Fe ions can accumulate in a high concentration. The local Fe ion concentration on the surface of iron sample can be even higher. Furthermore, in our case, according to the former electrochemical tests, AM iron sample with fine grain structures are prone to rapider degradation and release a larger quantity of Fe ions. The higher Fe ion concentration can promote the formation of highly reactive oxygen species such as hydroxyl and superoxide radicals, which were highly toxic due to their rapid reaction ability with most molecules found in living cell [48]. In future studies, to better mimic the *in vivo* condition, bioreactor with dynamic and perfused environment should be applied to assess cytotoxicity.

We further employed two indirect contact assays to appreciate the influences of scaffold degradation products on cell metabolism: LDH and MTS assays. Compared to direct contact between AM iron scaffolds to MG-63 cells, the cytocompatibility according to ISO 10993 was reasonable in *in vitro* assays for up to 72 h. To better mimic the *in vivo* situation *in vitro*, we applied the latest recommended modification of EN ISO 10993-5 and 10993-12 and used a 10-times higher extraction ratio [70, 71] for iron than the 0.2 g/mL that was used for Ti-6Al-4V. However, for our AM porous sample which has a larger surface area, 10-times dilution maybe still insufficient.

Besides Fe ion concentration, methodological differences or the used cell type may also play an important role for *in vitro* cytotoxicity study as shown by the contradictory results from literatures. Several other studies also used MG-63 to assess cytotoxicity of e.g., sandblasted 99.5% pure iron foils and observed that the "spreading behavior" of the cells was inhibited, showing a similar round-shape morphology [32]. While virtually all MG-63 cells on 'bare' iron revealed a green fluorescence even after 48 h, no live-dead ratio was calculated. A good *in vitro* cytocompatibility of 3D printed iron–manganese scaffolds, compared to tissue culture plastic, was earlier reported [15]. Interestingly, cell viability in MTT assays of undiluted short-term extracts was about 45% and surprisingly 80% in undiluted long-term extracts, using mouse calvaria-derived osteoblast-like MC3T3 cells, while live-dead staining in direct contact did not show any signs of physiological apoptosis even in supraconfluent 3-day cultures.

The typical iron concentration of mammalian cell culture media, like DMEM, is 0.25-3 μM [72] and thus substantially lower than the average 23 μM iron in plasma. Increasing iron content in culture media may also stimulate cell growth [72], as shown for mouse L-929 fibroblasts [73]. In contrast, toxic effects of iron are further abundantly reported: in a murine hepatocyte cell line just 25 μM $FeSO_4$ induced 50 % cell death within 3 h [72]. Interestingly, in neuroblastoma cells, 50 % apoptosis occurred at 15 mM

iron and none at 10 mM [74]. A diversity in the response to iron even between two different studies using the same cells reflects the idea that minor differences can lead to significant alterations in a cell's response to iron [72]. In addition, some contradictions in the literature may result from the differences in timing – although most studies used 24-48 h incubations [72]. Future studies should therefore apply ISO 10993 guidelines, providing sufficiently long time points (e.g., 24, 48, 72 h), disclose extraction ratios, and ideally use (more than one) relevant human indicator cells or cell lines. Finally, *in vivo* tests are required to investigate biodegradation and bone tissue response in terms of the iron-based orthopedic implant.

3.5. Conclusions

We demonstrated for the first time how DMP could be used to fabricate topologically ordered porous iron. The scaffolds presented a precisely controlled topology with fully interconnected pores. Over a period of 28 days of immersion tests, the elastic modulus and yield strength of the porous iron decreased insignificantly, i.e., 7% and 5%, respectively. The mechanical properties of porous iron remained within the values reported for trabecular bone even after 28 days of biodegradation. Electrochemical tests showed that the degradation rates of AM porous iron are up to ≈12 times higher than those of CR iron. During 28 days of immersion testing, the weight of the porous structures decreased by 3.1%. Different mechanisms were found to determine the biodegradation behavior on the periphery of the cylindrical scaffolds and in their center. This suggests that topological design plays an important role in adjusting the biodegradation behavior of AM porous iron. While direct contact between MG-63 cells and scaffolds revealed instant cytotoxicity in static cell culture, the cytocompatibility according to ISO 10993 was reasonable in *in vitro* assays for up to 72 h. Further systematic *in vitro* cytotoxicity study and *in vivo* implantation of the AM iron is necessary, a study that will be planned in the near future. Nevertheless, being the first reported study fabricating iron scaffolds through DMP, we believe that with appropriate design and bioactive coating [75], DMP porous Fe-based materials hold potential to become a new generation of functional and degradable biomaterials for orthopedic applications.

References

[1] D. Hong, D.-T. Chou, O. I. Velikokhatnyi, A. Roy, B. Lee, I. Swink, I. Issaev, H. A. Kuhn, P. N. Kumta. Binder-jetting 3D printing and alloy development of new biodegradable Fe-Mn-Ca/Mg alloys. Acta Biomater. 2016;45:375-386.

[2] N. Ikeo, R. Nakamura, K. Naka, T. Hashimoto, T. Yoshida, T. Urade, K. Fukushima, H. Yabuuchi, T. Fukumoto, Y. Ku, T. Mukai. Fabrication of a magnesium alloy with excellent ductility for biodegradable clips. Acta Biomater. 2016;29:468-476.

[3] X. Li, X. Liu, S. Wu, K. W. K. Yeung, Y. Zheng, P. K. Chu. Design of magnesium alloys with controllable degradation for biomedical implants: From bulk to surface. Acta Biomater. 2016;45:2-30.

[4] D. Zhao, S. Huang, F. Lu, B. Wang, L. Yang, L. Qin, K. Yang, Y. Li, W. Li, W. Wang, S. Tian, X. Zhang, W. Gao, Z. Wang, Y. Zhang, X. Xie, J. Wang, J. Li. Vascularized bone grafting fixed by biodegradable magnesium screw for treating osteonecrosis of the femoral head. Biomaterials. 2016;81:84-92.

[5] D. Bian, W. Zhou, J. Deng, Y. Liu, W. Li, X. Chu, P. Xiu, H. Cai, Y. Kou, B. Jiang, Y. Zheng. Development of magnesium-based biodegradable metals with dietary trace element germanium as orthopaedic implant applications. Acta Biomater. 2017;64:421-436.

[6] Y. Liu, Y. Wu, D. Bian, S. Gao, S. Leeflang, H. Guo, Y. Zheng, J. Zhou. Study on the Mg-Li-Zn ternary alloy system with improved mechanical properties, good degradation performance and different responses to cells. Acta Biomater. 2017;62:418-433.

[7] J. Wang, Y. Wu, H. Li, Y. Liu, X. Bai, W. Chau, Y. Zheng, L. Qin. Magnesium alloy based interference screw developed for ACL reconstruction attenuates peri-tunnel bone loss in rabbits. Biomaterials. 2018;157:86-97.

[8] H. Hermawan. Updates on the research and development of absorbable metals for biomedical applications. Prog Biomater. 2018.

[9] A. Francis, Y. Yang, S. Virtanen, A. R. Boccaccini. Iron and iron-based alloys for temporary cardiovascular applications. J Mater Sci Mater Med. 2015;26:1-16.

[10] J. He, F.-L. He, D.-W. Li, Y.-L. Liu, Y.-Y. Liu, Y.-J. Ye, D.-C. Yin. Advances in Fe-based biodegradable metallic materials. RSC Adv. 2016;6:112819-112838.

[11] Y. F. Zheng, X. N. Gu, F. Witte. Biodegradable metals. Mater Sci Eng R Rep. 2014;77:1-34.

[12] Q. Peng, Y. Huang, L. Zhou, N. Hort, K. U. Kainer. Preparation and properties of high purity Mg–Y biomaterials. Biomaterials. 2010;31:398-403.

[13] T. Kraus, F. Moszner, S. Fischerauer, M. Fiedler, E. Martinelli, J. Eichler, F. Witte, E. Willbold, M. Schinhammer, M. Meischel, P. J. Uggowitzer, J. F. Löffler, A. Weinberg. Biodegradable Fe-based alloys for use in osteosynthesis: Outcome of an in vivo study after 52weeks. Acta Biomater. 2014;10:3346-3353.

[14] I. A. J. van Hengel, M. Riool, L. E. Fratila-Apachitei, J. Witte-Bouma, E. Farrell, A. A. Zadpoor, S. A. J. Zaat, I. Apachitei. Selective laser melting porous metallic implants with immobilized silver nanoparticles kill and prevent biofilm formation by methicillin-resistant Staphylococcus aureus. Biomaterials. 2017;140:1-15.

[15] D.-T. Chou, D. Wells, D. Hong, B. Lee, H. Kuhn, P. N. Kumta. Novel processing of iron–manganese alloy-based biomaterials by inkjet 3-D printing. Acta Biomater. 2013;9:8593-8603.

3

[16] M. Peuster, C. Hesse, T. Schloo, C. Fink, P. Beerbaum, C. von Schnakenburg. Long-term biocompatibility of a corrodible peripheral iron stent in the porcine descending aorta. Biomaterials. 2006;27:4955-4962.

[17] W. Lin, L. Qin, H. Qi, D. Zhang, G. Zhang, R. Gao, H. Qiu, Y. Xia, P. Cao, X. Wang, W. Zheng. Long-term in vivo corrosion behavior, biocompatibility and bioresorption mechanism of a bioresorbable nitrided iron scaffold. Acta Biomater. 2017;54:454-468.

[18] D. Andreas, H. Thomas, B. F. Wilhelm, P. Matthias. In vitro and in vivo corrosion properties of new iron–manganese alloys designed for cardiovascular applications. J Biomed Mater Res B Appl Biomater. 2015;103:649-660.

[19] J. Čapek, D. Vojtěch, A. Oborná. Microstructural and mechanical properties of biodegradable iron foam prepared by powder metallurgy. Materials & Design. 2015;83:468-482.

[20] J. Farack, C. Wolf-Brandstetter, S. Glorius, B. Nies, G. Standke, P. Quadbeck, H. Worch, D. Scharnweber. The effect of perfusion culture on proliferation and differentiation of human mesenchymal stem cells on biocorrodible bone replacement material. Materials Science and Engineering: B. 2011;176:1767-1772.

[21] P. Quadbeck, R. Hauser, K. Kümmel, G. Standke, G. Stephani, B. Nies, S. Rößler, B. Wegener. Iron based cellular metals for degradable synthetic bone replacement. PM2010 World Congress. PM Biomaterials2010. p. 1-8.

[22] Z. Wen, L. Zhang, C. Chen, Y. Liu, C. Wu, C. Dai. A construction of novel iron-foam-based calcium phosphate/chitosan coating biodegradable scaffold material. Materials Science and Engineering: C. 2013;33:1022-1031.

[23] N. Mohd Daud, N. B. Sing, A. H. Yusop, F. A. Abdul Majid, H. Hermawan. Degradation and in vitro cell–material interaction studies on hydroxyapatite-coated biodegradable porous iron for hard tissue scaffolds. Journal of Orthopaedic Translation. 2014;2:177-184.

[24] M. Heiden, E. Nauman, L. Stanciu. Bioresorbable Fe-Mn and Fe-Mn-HA Materials for Orthopedic Implantation: Enhancing Degradation through Porosity Control. Adv Healthc Mater. 2017;6.

[25] R. Alavi, A. Trenggono, S. Champagne, H. Hermawan. Investigation on Mechanical Behavior of Biodegradable Iron Foams under Different Compression Test Conditions. Metals. 2017;7:202.

[26] Y. Su, S. Champagne, A. Trenggono, R. Tolouei, D. Mantovani, H. Hermawan. Development and characterization of silver containing calcium phosphate coatings on pure iron foam intended for bone scaffold applications. Materials & Design. 2018;148:124-134.

[27] A. Oyane, H.-M. Kim, T. Furuya, T. Kokubo, T. Miyazaki, T. Nakamura. Preparation and assessment of revised simulated body fluids. J Biomed Mater Res A. 2003;65A:188-195.

[28] Y. Li, J. Zhou, P. Pavanram, M. A. Leeflang, L. I. Fockaert, B. Pouran, N. Tümer, K. U. Schröder, J. M. C. Mol, H. Weinans, H. Jahr, A. A. Zadpoor. Additively manufactured biodegradable porous magnesium. Acta Biomater. 2018;67:378-392.

[29] T. Huang, J. Cheng, Y. F. Zheng. In vitro degradation and biocompatibility of Fe–Pd and Fe–Pt composites fabricated by spark plasma sintering. Mater Sci Eng, C. 2014;35:43-53.

[30] A. H. M. Yusop, N. M. Daud, H. Nur, M. R. A. Kadir, H. Hermawan. Controlling the degradation kinetics of porous iron by poly (lactic-co-glycolic acid) infiltration for use as temporary medical implants. Sci Rep. 2015;5.

[31] A. C. Taş, P. J. Majewski, F. Aldinger. Chemical Preparation of Pure and Strontium-and/or Magnesium-Doped Lanthanum Gallate Powders. J Am Ceram Soc. 2000;83:2954-2960.

[32] J. Zhou, Y. Yang, M. Alonso Frank, R. Detsch, A. R. Boccaccini, S. Virtanen. Accelerated Degradation Behavior and Cytocompatibility of Pure Iron Treated with Sandblasting. ACS Appl Mater Interfaces. 2016;8:26482-26492.

[33] B. Song, X. Zhao, S. Li, C. Han, Q. Wei, S. Wen, J. Liu, Y. Shi. Differences in microstructure and properties between selective laser melting and traditional manufacturing for fabrication of metal parts: A review. Front Mech Eng. 2015;10:111-125.

[34] L.-E. Loh, C.-K. Chua, W.-Y. Yeong, J. Song, M. Mapar, S.-L. Sing, Z.-H. Liu, D.-Q. Zhang. Numerical investigation and an effective modelling on the Selective Laser Melting (SLM) process with aluminium alloy 6061. Int J Heat Mass Transfer. 2015;80:288-300.

[35] A. Simchi, H. Pohl. Effects of laser sintering processing parameters on the microstructure and densification of iron powder. Mater Sci Eng, A. 2003;359:119-128.

[36] B. Song, S. Dong, Q. Liu, H. Liao, C. Coddet. Vacuum heat treatment of iron parts produced by selective laser melting: Microstructure, residual stress and tensile behavior. Mater Des. 2014;54:727-733.

[37] C. S. Obayi, R. Tolouei, C. Paternoster, S. Turgeon, B. A. Okorie, D. O. Obikwelu, G. Cassar, J. Buhagiar, D. Mantovani. Influence of cross-rolling on the micro-texture and biodegradation of pure iron as biodegradable material for medical implants. Acta Biomater. 2015;17:68-77.

[38] C. S. Obayi, R. Tolouei, A. Mostavan, C. Paternoster, S. Turgeon, B. A. Okorie, D. O. Obikwelu, D. Mantovani. Effect of grain sizes on mechanical properties and biodegradation behavior of pure iron for cardiovascular stent application. Biomatter. 2016;6:e959874.

[39] M. Moravej, A. Purnama, M. Fiset, J. Couet, D. Mantovani. Electroformed pure iron as a new biomaterial for degradable stents: In vitro degradation and preliminary cell viability studies. Acta Biomater. 2010;6:1843-1851.

3

[40] F. L. Nie, Y. F. Zheng. Surface chemistry of bulk nanocrystalline pure iron and electrochemistry study in gas-flow physiological saline. Journal of Biomedical Materials Research Part B: Applied Biomaterials. 2012;100B:1404-1410.

[41] T. Jurgeleit, E. Quandt, C. Zamponi. Magnetron sputtering a new fabrication method of iron based biodegradable implant materials. Advances in Materials Science and Engineering. 2015;2015.

[42] K. Ralston, N. Birbilis. Effect of grain size on corrosion: a review. Corrosion. 2010;66:075005-075005-075013.

[43] F. Witte, N. Hort, C. Vogt, S. Cohen, K. U. Kainer, R. Willumeit, F. Feyerabend. Degradable biomaterials based on magnesium corrosion. Curr Opin Solid State Mater Sci. 2008;12:63-72.

[44] M. Moravej, S. Amira, F. Prima, A. Rahem, M. Fiset, D. Mantovani. Effect of electrodeposition current density on the microstructure and the degradation of electroformed iron for degradable stents. Mater Sci Eng, B. 2011;176:1812-1822.

[45] C. V. Vidal, A. I. Muñoz. Electrochemical aspects in biomedical alloy characterization: electrochemical impedance spectrosopy. Biomedical Engineering, Trends in Materials Science: InTech; 2011.

[46] J. Tedim, M. L. Zheludkevich, A. C. Bastos, A. N. Salak, A. D. Lisenkov, M. G. S. Ferreira. Influence of preparation conditions of Layered Double Hydroxide conversion films on corrosion protection. Electrochimica Acta. 2014;117:164-171.

[47] B. Van der Linden, H. Terryn, J. Vereecken. Investigation of anodic aluminium oxide layers by electrochemical impedance spectroscopy. J Appl Electrochem. 1990;20:798-803.

[48] E. Zhang, H. Chen, F. Shen. Biocorrosion properties and blood and cell compatibility of pure iron as a biodegradable biomaterial. J Mater Sci Mater Med. 2010;21:2151-2163.

[49] J. Čapek, Š. Msallamová, E. Jablonská, J. Lipov, D. Vojtěch. A novel high-strength and highly corrosive biodegradable Fe-Pd alloy: Structural, mechanical and in vitro corrosion and cytotoxicity study. Mater Sci Eng, C. 2017;79:550-562.

[50] P. Mariot, M. A. Leeflang, L. Schaeffer, J. Zhou. An investigation on the properties of injection-molded pure iron potentially for biodegradable stent application. Powder Technol. 2016;294:226-235.

[51] H. Hermawan, D. Dubé, D. Mantovani. Degradable metallic biomaterials: Design and development of Fe–Mn alloys for stents. Journal of Biomedical Materials Research Part A. 2010;93A:1-11.

[52] B. Liu, Y. F. Zheng. Effects of alloying elements (Mn, Co, Al, W, Sn, B, C and S) on biodegradability and in vitro biocompatibility of pure iron. Acta Biomater. 2011;7:1407-1420.

[53] D. Pierson, J. Edick, A. Tauscher, E. Pokorney, P. Bowen, J. Gelbaugh, J. Stinson, H. Getty, C. H. Lee, J. Drelich, J. Goldman. A simplified in vivo approach for

evaluating the bioabsorbable behavior of candidate stent materials. J Biomed Mater Res B Appl Biomater. 2012;100B:58-67.

[54] J. Parthasarathy, B. Starly, S. Raman, A. Christensen. Mechanical evaluation of porous titanium (Ti6Al4V) structures with electron beam melting (EBM). J Mech Behav Biomed Mater. 2010;3:249-259.

[55] M. Yazdimamaghani, M. Razavi, D. Vashaee, K. Moharamzadeh, A. R. Boccaccini, L. Tayebi. Porous magnesium-based scaffolds for tissue engineering. Mater Sci Eng, C. 2017;71:1253-1266.

[56] M. E. Iskandar, A. Aslani, H. Liu. The effects of nanostructured hydroxyapatite coating on the biodegradation and cytocompatibility of magnesium implants. Journal of Biomedical Materials Research Part A. 2013;101A:2340-2354.

[57] M. Yazdimamaghani, M. Razavi, D. Vashaee, V. R. Pothineni, J. Rajadas, L. Tayebi. Significant degradability enhancement in multilayer coating of polycaprolactone-bioactive glass/gelatin-bioactive glass on magnesium scaffold for tissue engineering applications. Appl Surf Sci. 2015;338:137-145.

[58] M. Yazdimamaghani, M. Razavi, D. Vashaee, L. Tayebi. Surface modification of biodegradable porous Mg bone scaffold using polycaprolactone/bioactive glass composite. Materials Science and Engineering: C. 2015;49:436-444.

[59] M. Razavi, M. Fathi, O. Savabi, D. Vashaee, L. Tayebi. Improvement of Biodegradability, Bioactivity, Mechanical Integrity and Cytocompatibility Behavior of Biodegradable Mg Based Orthopedic Implants Using Nanostructured Bredigite (Ca7MgSi4O16) Bioceramic Coated via ASD/EPD Technique. Ann Biomed Eng. 2014;42:2537-2550.

[60] S. Ahmadi, S. Yavari, R. Wauthle, B. Pouran, J. Schrooten, H. Weinans, A. Zadpoor. Additively Manufactured Open-Cell Porous Biomaterials Made from Six Different Space-Filling Unit Cells: The Mechanical and Morphological Properties. Materials. 2015;8:1871.

[61] R. Hedayati, S. M. Ahmadi, K. Lietaert, B. Pouran, Y. Li, H. Weinans, C. D. Rans, A. A. Zadpoor. Isolated and modulated effects of topology and material type on the mechanical properties of additively manufactured porous biomaterials. J Mech Behav Biomed Mater. 2018;79:254-263.

[62] R. Wauthle, S. M. Ahmadi, S. Amin Yavari, M. Mulier, A. A. Zadpoor, H. Weinans, J. Van Humbeeck, J.-P. Kruth, J. Schrooten. Revival of pure titanium for dynamically loaded porous implants using additive manufacturing. Mater Sci Eng, C. 2015;54:94-100.

[63] R. Wauthle, J. van der Stok, S. Amin Yavari, J. Van Humbeeck, J.-P. Kruth, A. A. Zadpoor, H. Weinans, M. Mulier, J. Schrooten. Additively manufactured porous tantalum implants. Acta Biomater. 2015;14:217-225.

3

[64] S.-Y. Fu, X.-Q. Feng, B. Lauke, Y.-W. Mai. Effects of particle size, particle/matrix interface adhesion and particle loading on mechanical properties of particulate–polymer composites. Composites Part B: Engineering. 2008;39:933-961.

[65] G. Kroemer, W. S. El-Deiry, P. Golstein, M. E. Peter, D. Vaux, P. Vandenabeele, B. Zhivotovsky, M. V. Blagosklonny, W. Malorni, R. A. Knight, M. Piacentini, S. Nagata, G. Melino. Classification of cell death: recommendations of the Nomenclature Committee on Cell Death. Cell Death Differ. 2005;12:1463.

[66] A. Francis, Y. Yang, S. Virtanen, A. R. Boccaccini. Iron and iron-based alloys for temporary cardiovascular applications. J Mater Sci Mater Med. 2015;26:138.

[67] M. Peuster, P. Wohlsein, M. Brügmann, M. Ehlerding, K. Seidler, C. Fink, H. Brauer, A. Fischer, G. Hausdorf. A novel approach to temporary stenting: degradable cardiovascular stents produced from corrodible metal—results 6–18 months after implantation into New Zealand white rabbits. Heart. 2001;86:563-569.

[68] C. Yang, Z. Huan, X. Wang, C. Wu, J. Chang. 3D Printed Fe Scaffolds with HA Nanocoating for Bone Regeneration. ACS Biomater Sci Eng. 2018;4:608-616.

[69] R. Oriňáková, A. Oriňák, L. M. Bučková, M. Giretová, Ľ. Medvecký, E. Labbanczová, M. Kupková, M. Hrubovčáková, K. Kovaľ. Iron based degradable foam structures for potential orthopedic applications. Int J Electrochem Sci. 2013;8:12451-12465.

[70] J. Fischer, D. Pröfrock, N. Hort, R. Willumeit, F. Feyerabend. Reprint of: Improved cytotoxicity testing of magnesium materials. Mater Sci Eng, B. 2011;176:1773-1777.

[71] J. Wang, F. Witte, T. Xi, Y. Zheng, K. Yang, Y. Yang, D. Zhao, J. Meng, Y. Li, W. Li, K. Chan, L. Qin. Recommendation for modifying current cytotoxicity testing standards for biodegradable magnesium-based materials. Acta Biomater. 2015;21:237-249.

[72] R. Eid, N. T. T. Arab, M. T. Greenwood. Iron mediated toxicity and programmed cell death: A review and a re-examination of existing paradigms. Biochim Biophys Acta. 2017;1864:399-430.

[73] R. R. Zombola, R. C. Bearse, P. A. Kitos. Trace element uptake by L-cells as a function of trace elements in a synthetic growth medium. J Cell Physiol. 1979;101:57-65.

[74] K. C. Chew, E.-T. Ang, Y. K. Tai, F. Tsang, S. Q. Lo, E. Ong, W.-Y. Ong, H.-M. Shen, K.-L. Lim, V. L. Dawson. Enhanced autophagy from chronic toxicity of iron and mutant A53T α-synuclein implications for neuronal cell death in Parkinson disease. J Biol Chem. 2011;286:33380-33389.

[75] S. Ray, U. Thormann, M. Eichelroth, M. Budak, C. Biehl, M. Rupp, U. Sommer, T. El Khassawna, F. I. Alagboso, M. Kampschulte, M. Rohnke, A. Henß, K. Peppler, V. Linke, P. Quadbeck, A. Voigt, F. Stenger, D. Karl, R. Schnettler, C. Heiss, K. S. Lips,

V. Alt. Strontium and bisphosphonate coated iron foam scaffolds for osteoporotic fracture defect healing. Biomaterials. 2018;157:1-16.

3

Supplementary information
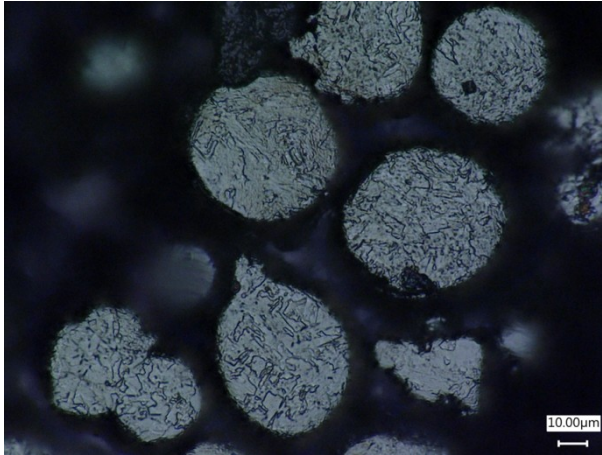
Figure S1. Microstructure of iron powder.
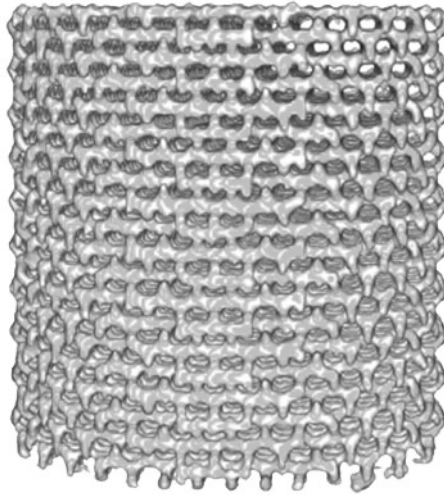
Figure S2. Reconstructed 3D model from µCT scanning.

3

3
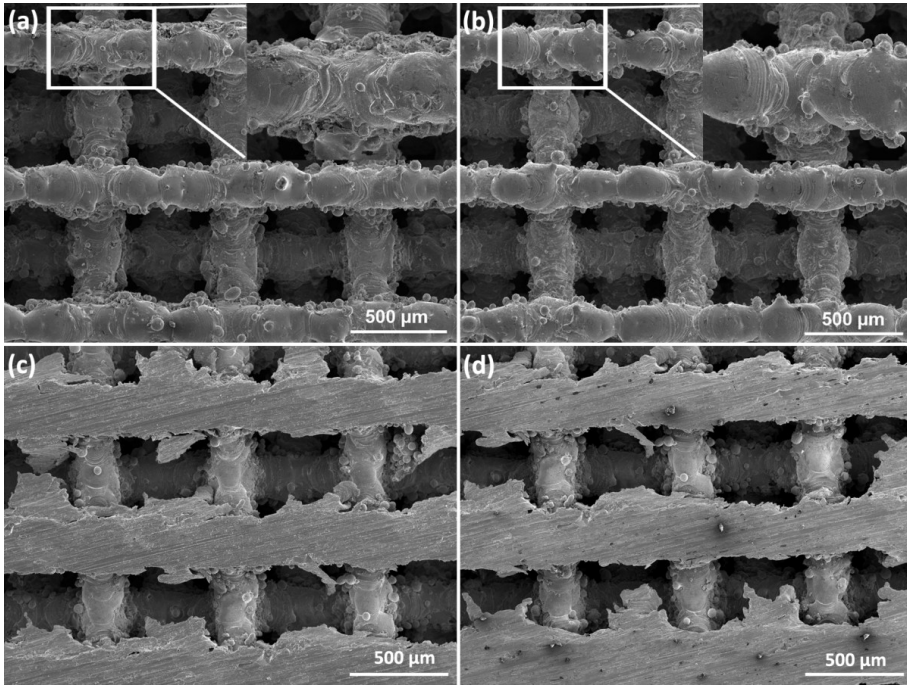
Figure S3. Strut surface morphology and microstructure of AM porous iron: (a) as-built and (b) as-polished strut surfaces on the sample periphery, (c) as-built and (d) as-polished strut surfaces at the sample center.

4

Additively manufactured biodegradable porous zinc

Here, we applied powder bed fusion to fabricate porous zinc with a topologically ordered diamond structure. An integrative study was conducted on the static and dynamic biodegradation behavior (in vitro, up to 4 weeks), evolution of mechanical properties with increasing immersion time, electrochemical performance, and biocompatibility of the AM porous zinc. The specimens lost 7.8% of their weight after 4 weeks of dynamic immersion in a revised simulated body fluid. The mechanisms of biodegradation were site-dependent and differed from the top of the specimens to the bottom. During the whole in vitro immersion time of 4 weeks, the elastic modulus values of the AM porous zinc (E = 700-1000 MPa) even increased and remained within the scope of those of cancellous bone. Indirect cytotoxicity revealed good cellular activity up to 72 h according to ISO 10993-5 and -12. Live-dead staining confirmed good viability of MG-63 cells cultured on the surface of the AM porous zinc. These important findings could open up unprecedented opportunities for the development of multifunctional bone substituting materials that will enable reconstruction and regeneration of critical-size load-bearing bone defects.[1]

4.1. Introduction

Among the known biodegradable metals, magnesium (Mg) and iron (Fe) have been studied the most [1, 2]. The well-known challenge in developing Mg-based biomaterials concerns their excessively high biodegradation rates [2, 3]. Hydrogen released during the biodegradation of Mg alloys is another concern [4]. Fe-based biomaterials, on the other hand, degrade too slowly [5], meaning that the implant stays in the human body longer than necessary and may hinder the process of full tissue regeneration. Moreover, according to the *in vivo* tests of pure Fe stents, voluminous biodegradation products are formed and remain in the human body for long periods after implantation [6, 7]. Although developing new alloys and functional coatings could improve the performance of biodegradable Mg and Fe [8, 9], an alternative and potentially more rewarding approach would be to develop biomaterials based on the other types of biodegradable metals. Zinc (Zn) and its alloys are considered highly promising candidates for this purpose, as they are capable of tackling some of the fundamental engineering challenges associated with the use of biodegradable Mg and Fe [10]. Zn offers multiple advantages as compared to Mg- and Fe-based biomaterials. First, Zn is one of the most abundant essential trace elements in the human body, confined primarily to skeletal muscles and bones (86%) [11]. Furthermore, over 600 enzymes rely on Zn for proper orientation and function [12]. Moreover, Zn plays catalytic, structural, and regulatory roles in the functions of human cells [13, 14]. From this perspective, Zn ions released from the implant could participate in the metabolic activity of the host cells instead of causing systemic toxic side effects [15]. Secondly, the biodegradation process of Zn does not generate hydrogen gas. Thirdly, being similar to Mg but opposed to Fe, the biodegradation products of Zn are biocompatible [16]. Finally, as the chemical potential of Zn falls between the chemical potential values of Mg and Fe, it should exhibit a more suitable biodegradation rate, as compared to fast degrading Mg or slowly degrading Fe [17, 18]. Ideally, the biodegradation rate of implants should match the bone regeneration rate, during which the implants provide enduring mechanical support for 3-6 months and fully degrade in 1-2 years [10]. Rapid degradation may compromise the mechanical integrity during the healing process [19], while slow degradation causes long-term implant retention and in turn metabolic complications [6].

However, unlike AM bio-inert titanium or cobalt-chromium, AM biodegradable metals pose many processing challenges, such as severe evaporation and high chemical activity, especially for Mg and Zn [20]. Under any inappropriate processing conditions, defects including voids, lack of fusion, rough surface, severe residual stresses and distortions have been observed. Even for Fe, evaporation was found to play an important role in densification during laser melting [21]. Precise process control is therefore needed in order to obtain eligible samples from AM for further investigation.

Up to date, only a few studies on powder bed fusion AM porous biodegradable Mg, Fe, and Zn have appeared in the literature [22-27]. AM porous Mg and Fe have both demonstrated unique biodegradation behaviors, as compared to their bulk counterparts [22, 23]. However, as AM porous Zn has just been realized [24, 28, 29], no information regarding its biodegradation, biocompatibility, and mechanical property changes along with its *in vitro* biodegradation is available in the literature. Here, for the first time, we present an integrative study on the static and dynamic biodegradation behavior in a revised simulated body fluid, evolution of mechanical properties with increasing immersion time, electrochemical performance, and biocompatibility of the AM porous Zn.

4.2. Material and methods

4.2.1. Scaffold manufacturing

Cylindrical scaffolds (with dimensions of 10 mm in height and 11.2 mm in diameter, Figure 1a) based on a diamond unit cell (unit cell size: 1.4 mm, strut thickness: 0.4 mm) were designed (Figure 1b). Specimens were produced by laser powder bed fusion AM (ProX DMP 320 machine, 3D Systems, Belgium). The machine had a maximum laser power of 500 W and could reach oxygen levels below 50 ppm in the build chamber. A nitrogen-atomized Zn powder was used in this study with the following properties: particle sizes: D_{10}: 26 µm, D_{50}: 39 µm, and D_{90}: 60 µm; O content: 2551±81 ppm, N content: 17±2 ppm, and H content: 7.6±0.8 ppm. The morphology of powder particles was analyzed before [30]. The powder layer thickness was 60 µm and the energy density 39.0 J/mm^3. The specimens were removed from the steel baseplate by wire electrical discharge machining (WEDM). 96% ethanol was used to ultrasonically remove powder particles entrapped in the pores of the specimens for 20 min. Subsequently, the specimens were cleaned by using a solution composed of 5% (by volume) hydrochloric acid, 5% nitric acid, and 90% ethanol for 2 min to further remove loose powder particles, after which 96% ethanol was used again to wash away residual hydrochloric acid.

4.2.2. Morphological characterization

Micro-computed tomography (μCT) was used to scan the Zn scaffolds (Phoenix Nanotom, GE Sensing Inspection Technologies GmbH, Germany) with the following parameters: 220 μA tube current, 130 kV tube voltage, 500 ms exposure time, 12 μm^3 resolution, and 1440 projections. Phoenix Datos|x 2.0 (GE Sensing & Inspection Technologies GmbH, Germany) was used to reconstruct and transform the acquired data into 2D images (i.e., DICOM image stacks). To extract quantifiable data from these images, the following steps were taken. First, the images were locally thresholded (FIJI,

NIH, Bethesda, MD, USA) over a range of 107 to 255 for the Zn material. Then, circular regions of interest (ROIs) (diameter: 10 mm) were outlined to include all the structures. BoneJ (a plugin of FIJI) was used to calculate the porosity, pore size, and average strut thickness of the AM porous Zn. Furthermore, the weighing method was applied to determine the porosity: *Porosity* $=1-(W_{Zn}/V_{bulk})/\rho_{Zn}$, where W_{Zn} and V_{bulk} are the weight and apparent volume of the specimen, respectively, and ρ_{Zn} is the theoretical density of pure Zn.

After the biodegradation tests, two different ranges, i.e., 45–107 and 107–255, were applied to segment the biodegradation products and porous Zn structure, respectively. After segmentation in FIJI, the volume of Zn and that of the biodegradation products were calculated with BoneJ (a plugin of FIJI). The images were then exported for 3D reconstruction (AVIZO Fire, VSG, France).
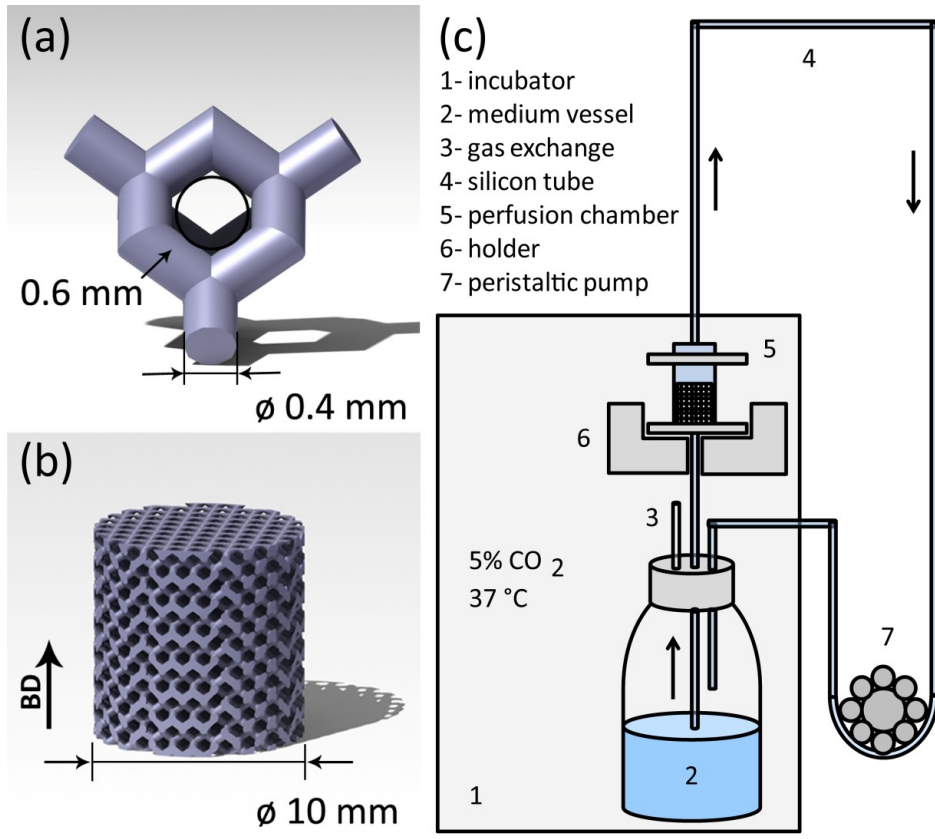

Figure 1. Topological design of AM porous zinc specimens: (a) diamond unit cell and (b) zinc scaffold, and (c) dynamic degradation setup. BD: building direction.

4.2.3. Microstructural characterization

Electron back-scattered diffraction (EBSD) was conducted with an HKL Nordlys II detector, attached to a field emission gun scanning electron microscope (FEGSEM) (JEOL JSM-6500 F, Japan), at 200 nm step size. TSL OIM® Analysis (EDAX Inc., USA) was used to reconstruct the inverse pole figure (IPF) maps and image quality (IQ). The average grain width was calculated by using the line intercept method, according to ASTM E112-12. Pole figures (PF) with (0001) and (1010) reflections were measured. EBSD specimens were ground, mechanically polished up to 1 μm with lubricant, followed by further mechanical polishing with 0.04 μm silica.

4.2.4. Static and dynamic biodegradation tests

Static *in vitro* immersion tests were performed inside an incubator (5% CO_2, 20% O_2, 37 °C) using 300 ml revised simulated body fluid [31] (r-SBF), i.e., a r-SBF volume to sample surface (25 cm^2) ratio of 12, for up to 28 days. In addition, dynamic *in vitro* immersion tests were performed in r-SBF up to 28 days using a self-designed bioreactor (5% CO_2, 20% O_2, 37 °C) (Figure 1c) at a unidirectional flow rate of 0.3 ml/min [32-34]. Medium pH values were registered (InLab Expert Pro-ISM, METTLER TOLEDO, Switzerland) at 1, 2, 7, 14, and 28 days of static and dynamic biodegradation. An inductively coupled plasma optical emission spectroscope (ICP-OES, iCAP 6500 Duo, Thermo Scientific, USA) was used to determine the concentrations of Zn, Ca, and P ions in the medium. All the tests were performed in triplicate.

4.2.5. Characterization of the biodegradation products

The morphologies and compositions of the biodegradation products were analyzed using a scanning electron microscope equipped with an energy-dispersive X-ray spectroscope (EDS) (SEM, JSM-IT100, JEOL, Japan). To observe the biodegradation layer of the specimens, a dual focused ion beam (FIB) available as part of a scanning electron microscope setup (FIB-SEM) (Helios G4 CX, FEI, The Netherlands) was used for cross-section milling and EDS mapping. The cross-section milling was performed at a tilting angle of 52° with a Ga ion beam operated at 30 kV over a current range of 0.5 to 20 nA.

For the analysis of the biodegraded specimens, Fourier-transform infrared spectroscopy (FTIR) spectra were collected at 4 cm^{-1} resolution over 128 scans for each spectrum, using a Thermo-Nicolet Nexus FTIR (USA) apparatus. Prior to the analysis of the biodegradation products, a background spectrum was collected from a sample

before biodegradation. The final spectra were subtracted from this background. Moreover, an X-ray diffractometer (XRD, Bruker D8 Advance diffractometer in Bragg-Brentano geometry, Germany) was used for the identification of the phases in the biodegradation products. The diffractometer was operated at 45 kV and 40 mA (power: 1.8 kW) using Cu Ka radiation with 0.035° step size and 10 s dwell time per step. In addition, X-ray photoelectron spectroscopy (XPS, Thermo Fisher Scientific, K Alpha model, USA) was used to characterize the surface chemical states of the specimens following the biodegradation tests. The XPS measurements were performed under normal emission at 250 μm spot size and at 10^{-8} mbar base pressure using a monochromated Al Kα X-ray source. Thermo Avantage v5.903 software (Thermo Fisher Scientific, USA) was used to process and analyze the spectra.

4.2.6. Electrochemical tests

AM porous Zn specimens were mounted in an epoxy resin and ground using 2000 grit SiC sandpapers for electrochemical tests. Surface area (*i.e.*, 0.28 cm^2) of the specimen exposed to the electrolyte was measured by using ImageJ (NIH, Bethesda, MD, USA). Specimens were made conductive by placing copper screws inside the resin. Electrochemical tests were performed in r-SBF at 37 °C with a Bio-Logic SP-200 potentiostat (Bio-Logic Science Instruments, Claix, France). A three-electrode electrochemical cell was set up with Zn specimen as the working electrode, graphite as the counter electrode, and a saturated calomel electrode as the reference electrode. Potentiodynamic polarization (PDP) measurement was performed after the open circuit potential (OCP) was reached and stabilized for 2 h. Afterwards, the specimen was polarized from -0.2 V to +0.5 V potential versus OCP at 0.5 mV/s scan rate. For electrochemical impedance spectroscopy (EIS), the tests were repeated at 1, 2, 7, 14, 21 and 28 days with 10 mV amplitude within a 100 kHz to 10 mHz frequency range. The impedance data were analyzed with the EC-Lab software (Bio-Logic Science Instruments, Claix, France) and fitted to the equivalent electrical circuits, where R_s represented the solution resistance; R_f and constant phase element CPE_f were applied to describe the resistance and non-ideal capacitance properties of the biodegradation film, respectively; the charge transfer resistance R_{ct} and the constant phase element representing the non-ideal double layer capacitance CPE_{dl} in parallel were used to describe the electrochemical interface of the electrolyte solution and the Zn substrate. The linear polarization resistance (LPR) of the samples was also measured consecutively at different immersion time points at ± 15 mV versus OCP at 0.167 mV s^{-1} potential sweep rate. The tests were performed in triplicate.

4.2.7. Mechanical characterization

Compression tests were carried out at 2 mm/min (10 kN, Instron, Germany). The specimens had a height of 10 mm and a diameter of 11.2 mm. The yield strengths and quasi-elastic gradients (elastic modulus) of the AM porous Zn specimens before and after the immersion tests were determined according to ISO 13314:2011 [23]. The tests were performed in triplicate.

Hardness was measured by using a microhardness tester (DuraScan, G5, Austria) at 1 N indentation load. Three tests were carried out on the cross section of the AM Zn substrate and another three indentations on the biodegradation products.

4.2.8. Cytocompatibility

Human osteoblast-like cells (MG-63, ATCC, CRL-1427) were cultured in 10% fetal calf serum (PAN Biotech) containing Dulbecco's modified eagle medium with low glucose 100 mg/L (DMEM LG) (Sigma) under physiological conditions (5% CO_2, 20% O_2, and 95% humidity) at 37 ˚C. The biocompatibility of AM porous Zn specimens were evaluated through direct cell seeding and indirect extract-based cytotoxicity tests. Cleaned specimens were sterilized in 100% isopropanol (Merck; Darmstadt, Germany) for 30 min.

Extracts were prepared at 0.2 g/ml concentration by incubating the specimens in the DMEM LG medium with serum for 72 h under physiological conditions, as recommended in EN ISO standards 10993:5 and 10993:12. Prepared 1x extract was diluted to 10x using the same medium. A 1x extract from AM Ti-6Al-4V porous scaffolds of the same dimensions served as control. All the extracts were sterile filtered (0.2 μm). 20% Dimethyl sulfoxide (DMSO) was used as the positive control. The methodology followed for the preparation of the extracts and MTS assay was the same as that previously reported by us [23]. After MG-63 cells reached optimal adherence, the serum-containing DMEM LG medium was replaced with 10x extracts and cells were further incubated for 0, 24, 48 and 72 h under physiological conditions. Relative cellular activity was tested using CellTiter 96® AQueous One Solution Cell Proliferation Assay (G3580, Promega, USA) [22].

Previously cleaned and sterilized specimens were seeded with 3×10^6 MG-63 cells and incubated for 24 h in the serum-containing DMEM LG medium under physiological conditions. Cell-seeded specimens were cut longitudinally (Figure S1a) and stained using Live and Dead Dye from Live and Dead Cell Assay kit (ab115347, Abcam, UK). A 5x concentration of the dye was added to the specimens with cells and then incubated at room temperature for 10 min. The cells were analyzed by fluorescent optical imaging

first and the same specimens after rinsing in 1X phosphate buffered saline were fixed and used for SEM analysis (ESEM XL 30 FEG, FEI, Eindhoven, The Netherlands) [22].

4.2.10. Statistical analysis

A two-way ANOVA test ($\alpha = 0.05$) and a post-hoc test (*i.e.*, Tukey's multiple comparison test, $\alpha = 0.05$) were run to analyze the relative cytotoxicity ($p < 0.0001$, ****; $p < 0.001$, ***; $p < 0.01$, **; $p < 0.05$, *; *n.s.* = not significant).

4.3. Results

4.3.1. Macrostructure and microstructure of the specimens

The average strut size and pore size of the as-built scaffolds were 441 ± 1 µm (design value = 400 µm) and 550 ± 38 µm (design value = 600 µm), respectively (Table 1). The porosity of the specimens was calculated to be $62 \pm 2\%$ (µCT) or $60 \pm 1\%$ (dry weighing) (Table 1). Columnar grains along the building direction were observable from the IPF mapping on the longitudinal section of the struts (Figure 2a, c). The average width of the elongated grain was about 16.0 ± 1.6 µm. On the horizontal section of the AM porous Zn specimens, the grains appeared to be well rounded (Figure 2d, f). There were several peaks in (0001) PF, in which some of them were in the building direction while others were perpendicular to the building direction (Figure 2b, e).

Table 1- Topological characteristics of AM Zn scaffolds.

AM Zn scaffold	Strut size (µm)	Pore size (µm)	Porosity
Design	400	600	67%
Micro CT	441±1	550±38	62±2%
Weighing method	-	-	60±1%
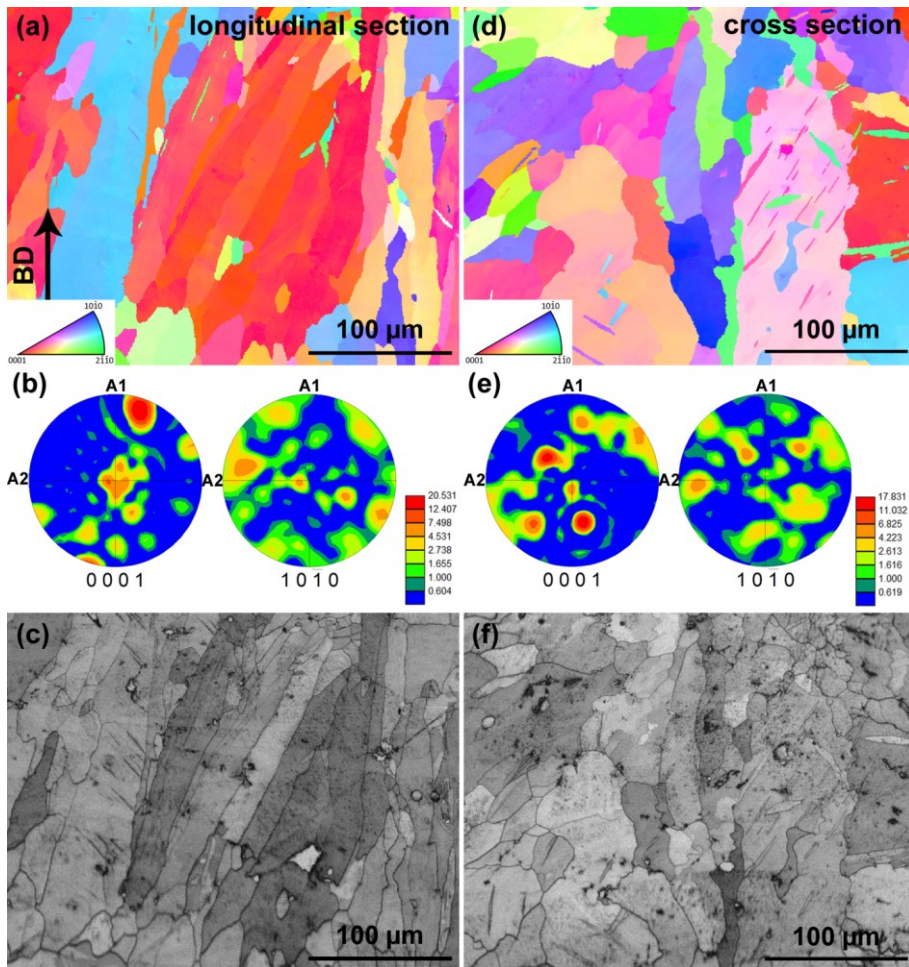
Figure 2. EBSD characterization of the struts of AM zinc specimens: (a) IPF map, (b) PF, and (c) IQ map on the longitudinal section, (d) IPF map, (e) PF, and (f) IQ map on the cross section. BD: building direction

4.3.2. In vitro biodegradation behavior of the specimens

During both dynamic and static immersion tests, white biodegradation products were gradually generated on the surface of the struts, as immersion time increased (Fig. 3a). However, the dynamic biodegradation tests appeared to produce more biodegradation products than the static ones. Interestingly, the biodegradation products mainly formed at the bottom of the specimens (attached to the beaker) under the static condition, but on

the top of the specimens (the outlet side of the medium flow) under the dynamic condition (Fig. 3a).
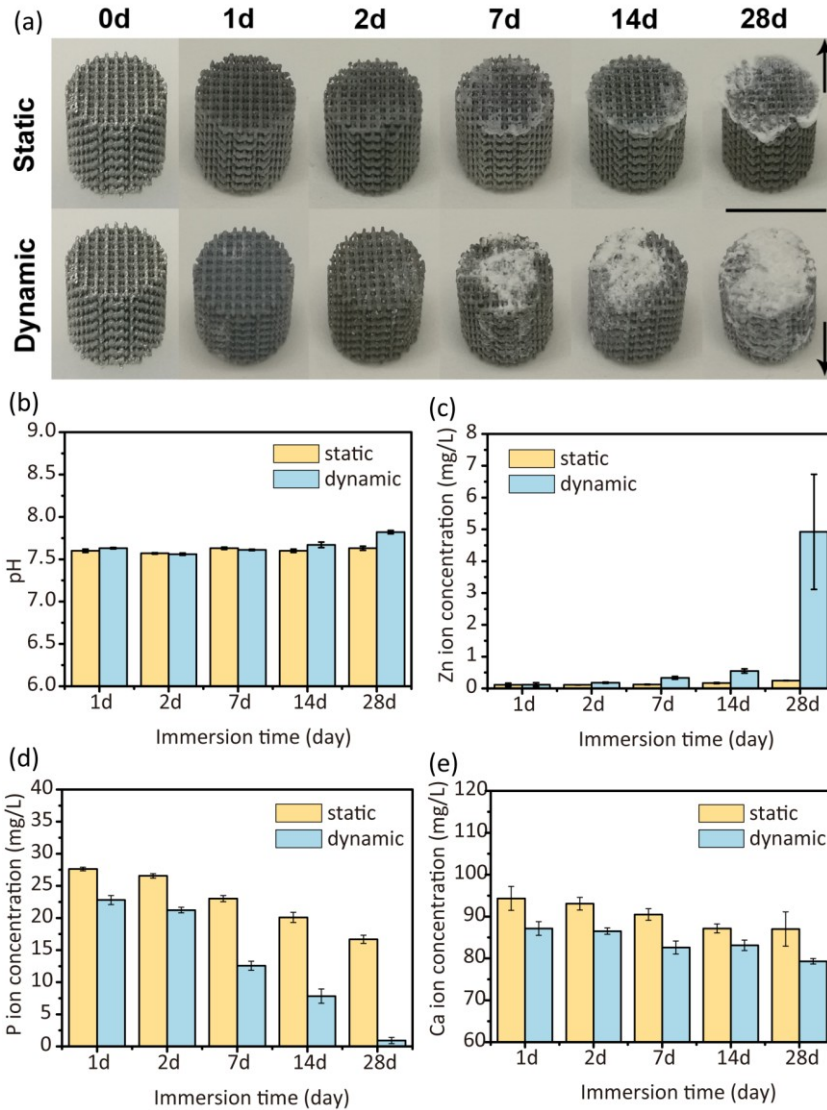
Figure 3. Biodegradation behavior of AM porous Zn: (a) visual inspection of the as-degraded scaffolds, (b) pH variation with immersion time, (c) Zn ion concentration variation with immersion time, (d) P ion concentration variation with immersion time, and (e) Ca ion concentration variation with immersion time. Arrow in (a) points to the bottom side of the scaffolds during degradation. Building direction is opposite to the arrow. Scale bar in (a): 1 cm.

The pH value remained stable around 7.5 and 7.6 during both static and dynamic biodegradation tests up to 14 days, and increased during the dynamic tests to 7.7 at day 28 (Fig. 3b). Under the static condition, the concentration of Zn ion slightly increased from 0.11 to 0.25 mg/L after 28 days. In contrast, the specimens tested under the dynamic condition exhibited higher Zn ion concentrations (as compared to those tested statically) at day 2, which further increased to 4.9 mg/L at day 28 (Fig. 3c). Over this period, the concentrations of P and Ca ions decreased under both conditions (Fig. 3d, e). The P and Ca ion concentrations were always lower under the dynamic test condition as compared to the static test condition (Fig. 3d, e).

4.3.3. Characteristics of the biodegradation products on the scaffolds

White particles gradually formed on the surfaces of the biodegraded specimens (Fig. 4a, b, c) along with increasing immersion time. After 1 day, small-size, white biodegradation products appeared on the surface of the specimens (Fig. 4d), which contained Zn, C, O, P, and Ca (Fig. 4d, inlay) according to EDS. At day 14, the white biodegradation products with a spherical morphology had grown in size, while the P and Ca contents in these products were increasing (Fig. 4e, inlay). At day 28, the biodegradation layer became increasingly compact, while the O, P, and Ca contents increased further (Fig. 4f, inlay). EDS mapping on the FIBed section allowed for the analysis of elemental distribution across the biodegradation layer (Fig. 4g), revealing that O had formed earlier (adjacent to the Zn substrate), followed by P and Ca. C was mainly present at the top of the biodegradation layer (Fig. 4g). XRD analysis showed the presence of ZnO, $Zn_5(CO_3)_2(OH)_6$, $Ca_3(PO_4)_2$, and $Zn_5(OH)_6Cl_6 \cdot H_2O$ at day 1, with increased intensities of these biodegradation products at day 28 (Fig. 4h). The FTIR spectrum with peaks at 1040 and 1650 cm^{-1} revealed the presence of PO_4^{3-} and HPO_4^{2-} (Fig. 4i), respectively [35], while the broad band from 1400 to 1550 cm^{-1} likely resulted from CO_3^{2-} [36]. HPO_4^{2-} absorption peaks emerged from day 7 and increased onwards, together with the increases of CO_3^{2-} and PO_4^{3-} peaks.

The total spectrum of XPS revealed that the biodegradation products were composed of Zn, O, C, P, Ca, Na, Mg, S, N, and Cl (Fig. 5a). Although there were no differences in the types of the elements between the different immersion time points, with increasing immersion time, the percentages of Ca, O, and P increased, while the percentage of Zn decreased. In addition, high-resolution XPS spectra of Zn2p3/2, C1s, and P2p were collected from the surfaces of the specimens and fitted. The peaks located at 1022 and 1024 eV might be attributed to ZnO and $Zn(OH)_2$, respectively (Fig. 5c,d) [37]. The atomic percentage of ZnO increased from 0.28 at day 1 (Fig. 5c) to 0.50 at day 28 (Fig. 5d). As for C1s, the peaks were well fitted with three signals at 284, 286,

and 288 eV (Fig. 5d, e). The 284 eV signal was assigned to C–C bonds, while the 286 and 288 eV signals were attributed to C–O and C=O, respectively [38, 39]. The atomic percentage of C=O also increased from 0.10 at day 1 to 0.14 at day 28. Finally, the P2p peaks observed at about 133 and 134 eV (Fig. 5f) could be characterized to be PO_4^{3-} and HPO_4^{2-} [40].
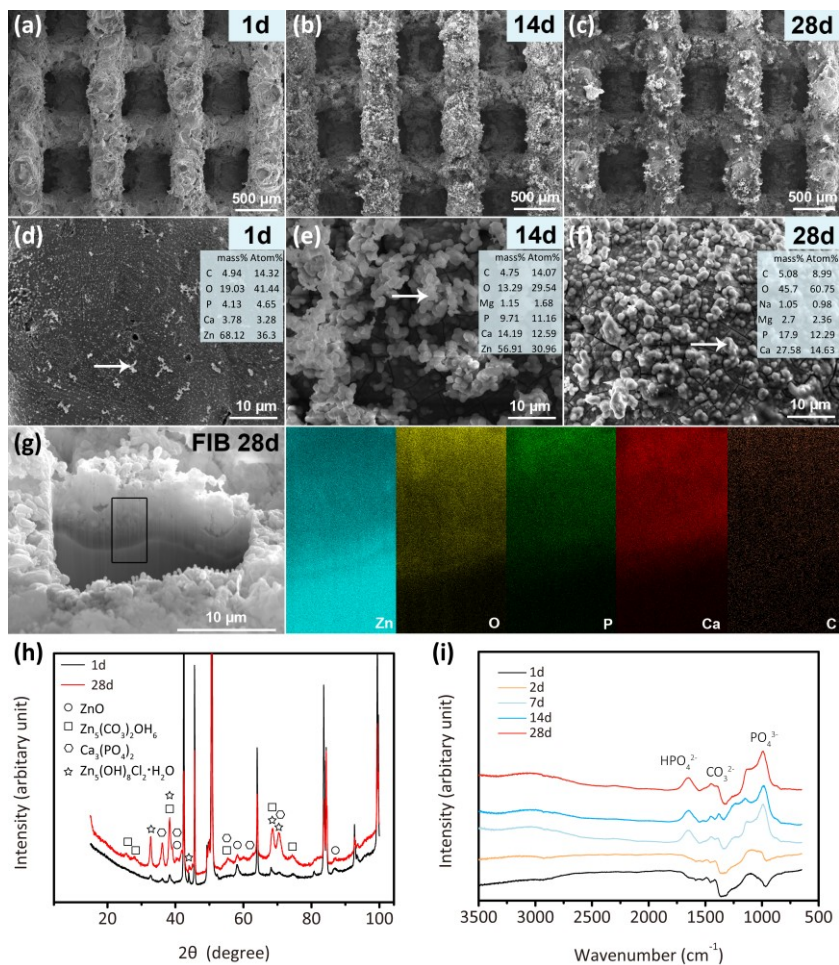
Figure 4. Biodegradation product analyses of AM porous zinc: (a) (b) (c) SEM images of degradation products at day 1 (a), day 14 (b), and day 28 (c), (d) (e) (f) higher magnification SEM images and EDS analyses at day 1 (d), day 14 (e), and day 28 (f), (g) FIB and EDS mapping of the degradation layer at day 28, (h) XRD analysis, and (i) FTIR analysis of degradation products. Arrow: EDS point analysis. Square: EDS mapping area.
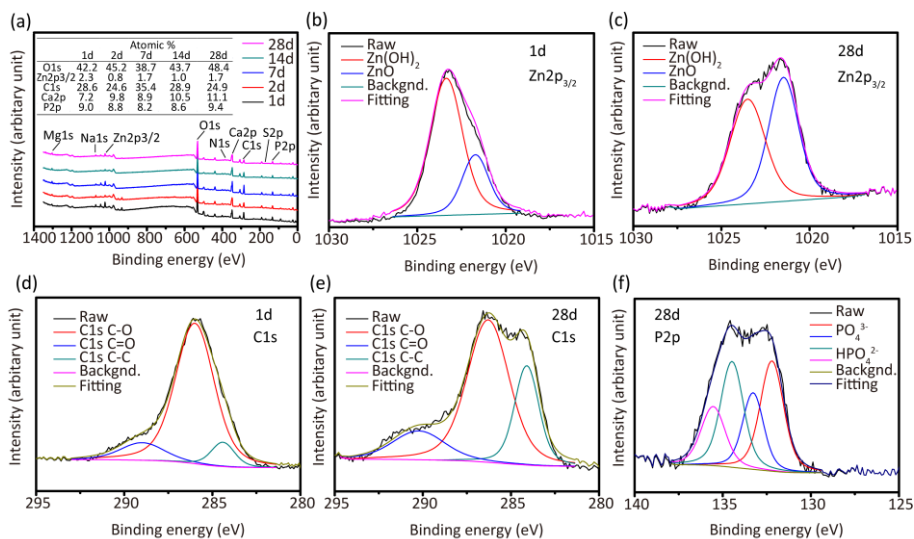
Figure 5. XPS spectra of AM porous zinc after degradation: (a) total spectrum, (b) (c) Zn2p$_{3/2}$ peaks at day 1 (b) and day 28 (c), (d) (e) C1s peaks at day 1 (d) and day 28 (e), (f) P2p peaks at day 28.

In addition to mostly homogeneous biodegradation profiles, we found several localized biodegradation spots within the AM porous Zn specimens (Fig. 6). A crystal-like morphology was observed at these spots and EDS analysis revealed a high percentage of Cl in these areas (Fig. 6a, b). EDS mapping (Fig. 6d) also showed the accumulation of Cl at the localized biodegradation sites on the cross-section of the biodegradation layers (Fig. 6c).
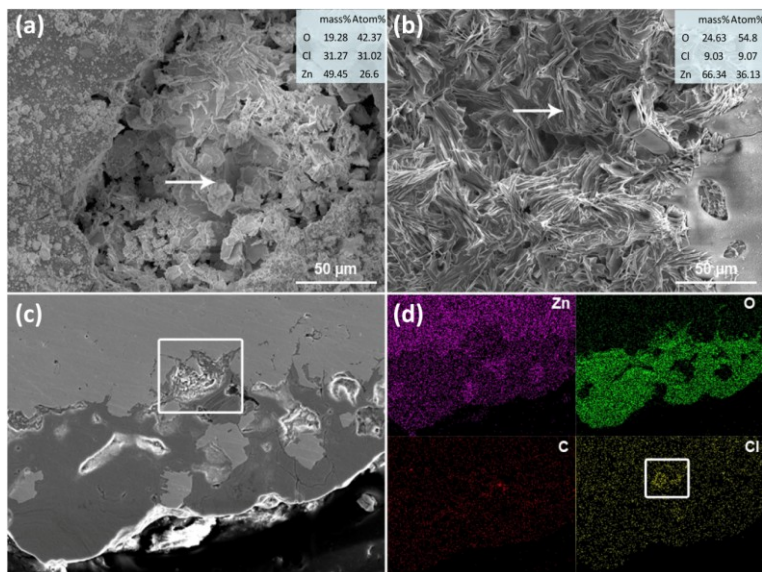
Figure 6. Localized degradation of AM porous zinc after degradation at day 28: (a) and (b) morphology of localized degradation and EDS point analysis, (c) cross section of localized degradation, and (d) EDS mapping. Arrow: EDS point analysis. Square: localized degradation.

4.3.4. Electrochemical responses

According to the PDP results (Figure S2), the corrosion current density of the AM porous Zn was 45 ± 2 µA/cm^2. The biodegradation rate was calculated to be 0.67 ± 0.04 mm/year based on ASTM G59. According to the Nyquist plots (Fig. 7a), the diameter of the capacitive loop increased after 7 days of immersion, and then decreased from day 14 to day 21, followed by further growth afterwards. The Bode plots (Fig. 7b, c) showed similar trends of impedance modulus at the 0.01 Hz (low) and 10 Hz (medium) frequencies. According to the data resulting from the fitted equivalent circuit for the AM porous Zn specimens (Fig. 7a, Table 2), R_f and R_{ct} gradually increased until day 14, decreased after day 14, and increased again after day 21. The LPR value showed a trend similar to the values of R_f and R_{ct} (Fig. 7d).
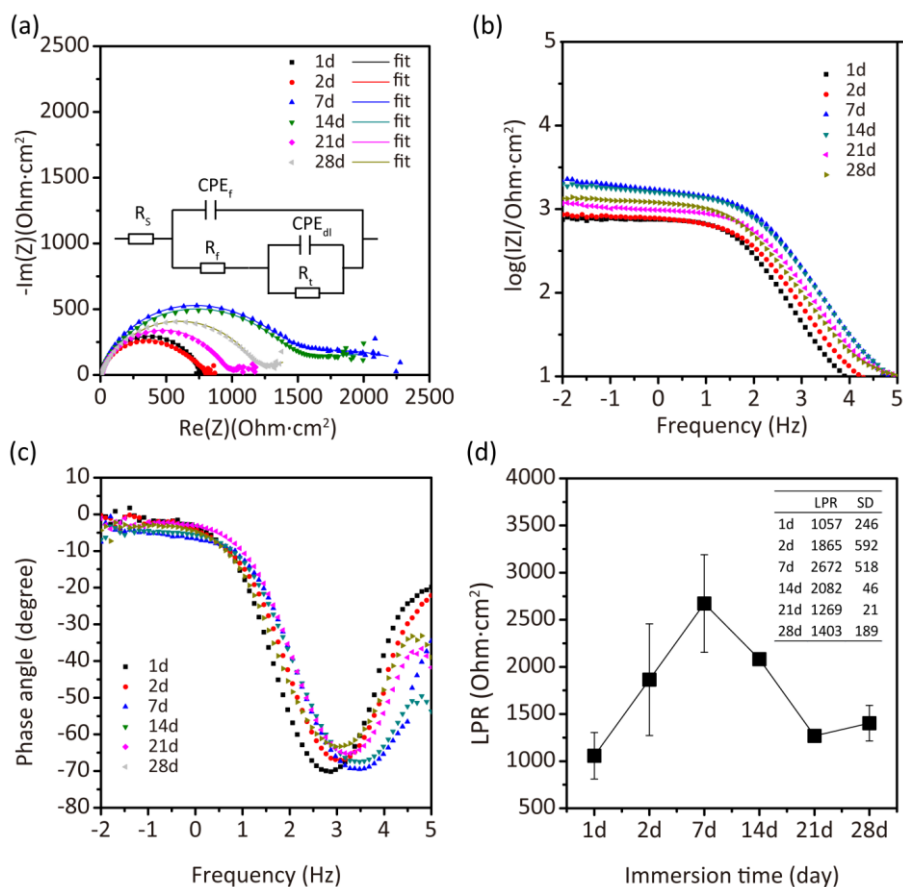
Figure 7. Electrochemical characterization of AM porous zinc after immersion tests at different time points: (a) Nyquist plots and equivalent circuits, (b) Bode plots of impedance modulus |Z| vs. frequency, (c) Bode plots of phase angle vs. frequency, and (d) LPR variation with immersion time.

4.3.5. Mechanical properties

Under compression, the AM porous Zn showed smooth stress-strain curves (Fig. 8a) with no abrupt drop even after biodegradation for 4 weeks. Following a similar trend, the curves all began with a steep slope in the elastic region. Afterwards, the stress decreased substantially and then a plateau stage appeared with almost no fluctuations (Fig. 8a). Interestingly, after 28 days of dynamic biodegradation, the yield strength of the AM porous Zn gradually increased from 11.8 to 13.9 MPa (Fig. 8b). While the yield strengths of the specimens undergoing static biodegradation were lower than those

exposed to dynamic biodegradation, they were higher than the yield strength of the as-built specimens (10.8 MPa), even after 28 days (12.0 MPa). The elastic modulus of the AM porous Zn increased at day 1, but decreased afterwards (Fig. 8c). Similarly, the elastic modulus of AM porous Zn after 28 days of dynamic biodegradation (879.3 MPa) was higher than that of the as-built specimens (785.7 MPa).

The average hardness value of the degradation products was 197 ± 4 HV, while the value of the AM Zn was 41 ± 3 HV.

Table 2- EIS fitting parameters of AM Zn after immersion tests at different time points.

Immersion time	R_s $\Omega\cdot cm^2$	CPE_f $10^{-6}\cdot \Omega^{-1}\cdot cm^{-2}\cdot s^{n1}$	n_1	R_f $\Omega\cdot cm^2$	CPE_{dl} $10^{-4}\cdot \Omega^{-1}\cdot cm^{-2}\cdot s^{n2}$	n_2	R_{ct} $\Omega\cdot cm^2$	Chi-square 10^{-3}
1d	6.0±0.1	10.1±0.2	0.88	669±17	8.2±3.6	0.60	99±16	1.1
2d	6.5±0.1	8.3±0.2	0.85	642±6	3.4±0.4	0.82	154±6	0.9
7d	4.9±0.2	3.4±0.1	0.83	1389±1	5.1±0.3	0.65	616±16	0.9
14d	5.3±0.2	4.2±0.1	0.81	1303±1	4.4±0.5	0.61	504±17	1.3
21d	7.9±0.1	5.6±0.1	0.83	902±5	9.0±0.1	0.85	110±6	1.0
28d	8.3±0.1	9.9±0.1	0.79	1137±6	13.0±0.2	0.90	129±8	0.7
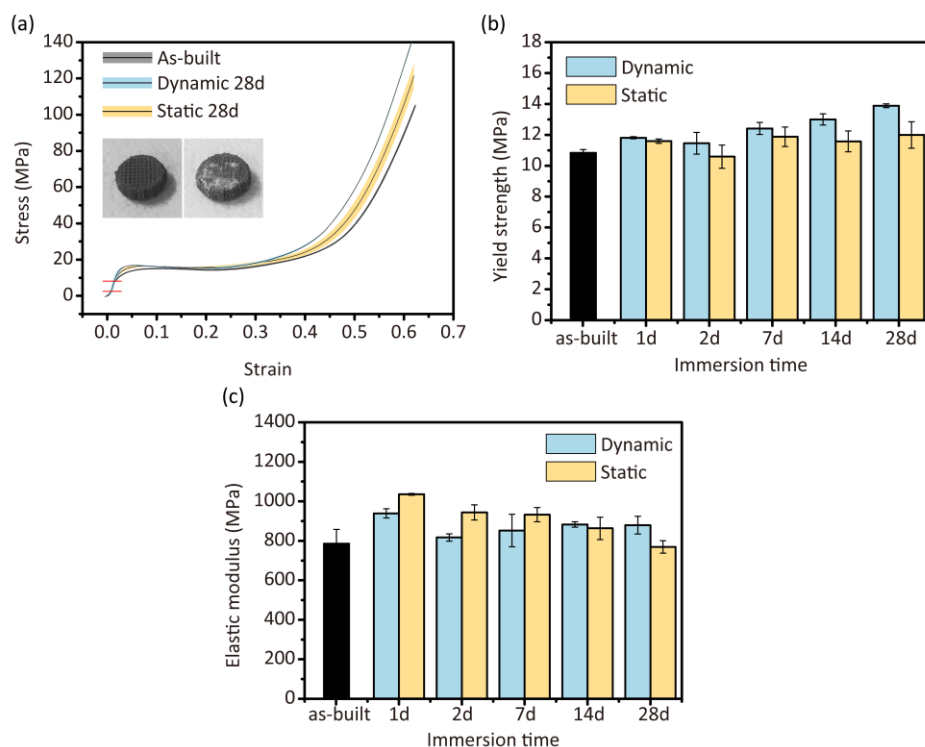
Figure 8. Mechanical behavior of AM porous Zn: (a) compressive stress-strain curves of Zn scaffolds before and after 28 days of degradation, (b) yield strength change with immersion time, and (c) elastic modulus change with immersion time. Red line in (a) indicated the elastic region.

4.3.6. Surface morphology of specimens after biodegradation

When the as-built specimens were segmented using a threshold range of 107 to 255, the total volume of the scaffolds was 345.2 ± 0.5 mm^3. After 28 days of biodegradation, this value decreased to, respectively, 332.1 ± 2.3 mm^3 and 319.0 ± 3.4 mm^3 (*i.e.*, 3.6% and 7.8% of weight reduction or 0.07 and 0.13 mm/year) under the static and dynamic conditions. The AM Zn scaffolds appeared to have experienced a higher degree of localized biodegradation under the static condition (Fig. 9, square), while the dynamic flow resulted in more homogeneous biodegradation. Quantification of the biodegradation products using a threshold range that separated Zn and the biodegradation products from each other showed that the dynamic condition resulted in a larger volume of biodegradation products (104 ± 9 mm^3), as compared to that for the static condition (59

± 8 mm³) (Fig. 9). Furthermore, the biodegradation products appeared to have mostly formed on a specific side of the specimens, which depended on the test condition, as well as in the center (Fig. 9). Under the static test condition, the biodegradation products mainly formed on the bottom side of the specimens, which was in contact with the beaker (Fig. 9, arrow). Under the dynamic test condition, however, the biodegradation products were found more on the top side of the specimens, which was the outlet side of the r-SBF flow (Fig. 9).

Figure 9. Micro-CT analysis of AM porous Zn after 28 days immersion. DP: degradation products. Square: localized degradation. Grey: Zn. Red: biodegradation products. Black arrow points to the bottom side of the scaffolds during degradation. Blue arrow indicates the flow direction for dynamic tests. Scale bar: 5 mm.

4.3.7. In vitro cytotoxicity
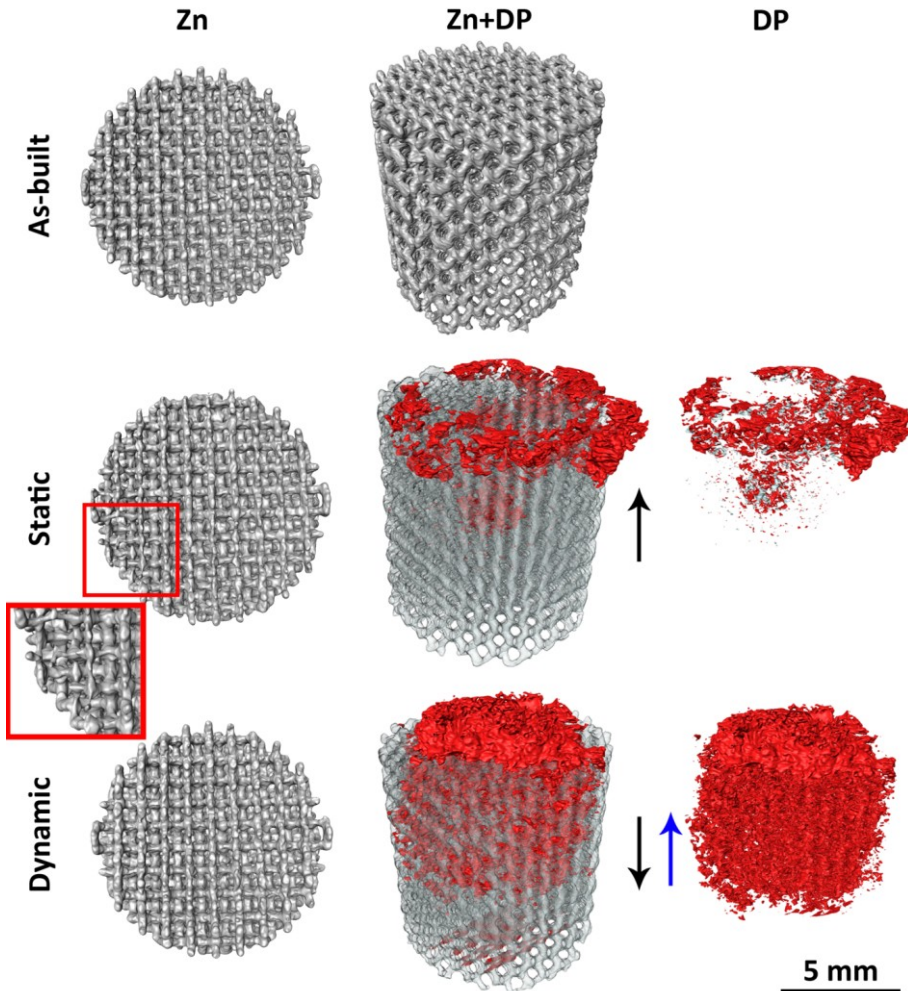
The metabolic activity of MG-63 cells cultured with the extracts from the AM porous Zn specimens was assayed and compared to that of the extracts from AM Ti-6Al-4V specimens (positive controls). Both extracts, from Zn and Ti-6Al-4V, resulted in around 95% cellular activity after 24 and 48 h, thus exhibiting level 0 cytotoxicity (*i.e.*, < 25%), according to ISO 10993. Even after 72 h of incubation, a large fraction of MG-63 cells cultured in the Zn extracts were viable (*i.e.*, 85%), conforming to a high level of cytocompatibility (*i.e.*, level 0 cytotoxicity). In contrast, cellular activity in the negative DMSO controls dropped quickly to ≈ 55% after 24 h and to ≈15% after 72 h (Fig. 10a).

4.3.8. Biocompatibility in vitro

Live-dead staining of MG63 cells showed that most of cells were viable (fluorescing green) even after 24 h of direct contact with the AM porous Zn specimens (Fig. 10b). The number of cells with compromised cell membrane integrity (yellow-red) was similar to the gold standard biomaterial (i.e., Ti-6Al-4V). MG-63 cells had intimate contact with the struts of the AM porous Zn with far-stretching filopodia-like protrusions (Fig. 10c), similar to their phenotype on Ti-6Al-4V. Cells not only were distributed around the periphery of the scaffolds but also colonized the inner core, as evident from the cross-sectional images (Fig. S1b).

4.4. Discussion

The AM porous Zn showed great potential to meet the three basic requirements of bone scaffolds: (i) the Zn scaffolds had sufficiently high mechanical properties, particularly elastic moduli during the 28-day biodegradation (E = 700-1000 MPa), to provide mechanical support, as these values are comparable with those reported for cancellous bone (E = 10-2000 MPa [41]). Surprisingly, the mechanical properties of the AM porous Zn even increased after four weeks of *in vitro* immersion; (ii) the Zn scaffolds had high porosity, totally interconnected pores and high-precision unit cell geometry; (iii) the AM porous Zn specimens showed a very promising biodegradation rate (≈7.8% volume loss after 4 weeks), which is an intermediate value between fast degrading Mg-based alloys and slowly degrading Fe-based alloys. This intermediate rate of biodegradation is deemed appropriate for most skeletal applications where wound healing is expected to complete within six months to one year. From a biological viewpoint, AM porous Zn showed good cytocompatibility, based on a high degree of cell viability and the intimate contact between MG-63 cells and the specimen surface.

4
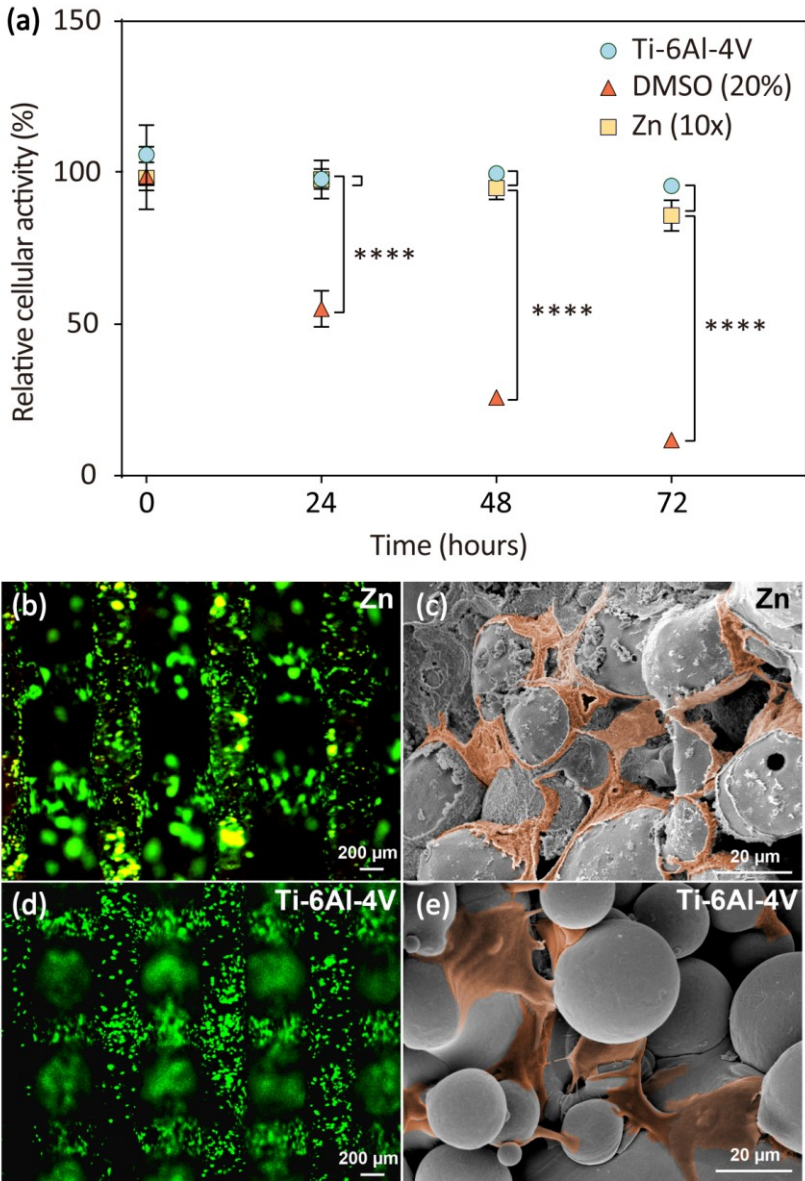
Figure 10. Biocompatibility and cytotoxicity of AM porous Zn *in vitro: R*emaining cellular activity of MG63 cells upon exposure to Zn scaffolds (a), as measured by MTS assay. Experiments were performed with extracts of randomly chosen replicate scaffolds (*n=5*) and analyzed in at least technical triplicates (Zn, *n=5*; Ti-6Al-4V, *n=3*). Fluorescent optical images (FOI) of cells attached to AM Zn scaffolds after 24 h (b) and AM Ti-6Al-4V scaffolds (d). SEM images of cells attached to AM Zn scaffolds after 24 h (c) and AM Ti-6Al-4V scaffolds (e). Brown masks indicate individual cells.

4.4.1. Microstructural features

Refined grains (Fig. 2) in the as-built Zn can be attributed to the high cooling rates (10^3-10^8 K/s) during laser powder bed fusion [42], which is similar to the observation of AM Zn reported by other researchers [24]. Fine grains can improve the mechanical performance of AM porous Zn. The elongation of the grains along the building direction was caused by the thermal gradients experienced during the process of layer-by-layer laser melting [43]. During the laser powder bed fusion process, the melting layer and the previous layer has the same chemical composition. New phase nucleation is not required for grains to grow epitaxially further from the substrate layer [44]. The direction of grain growth depends on the maximum heat transfer direction during solidification, which is perpendicular to the melt pool boundary. Thus, elongated grains along the building direction were observed in the AM porous Zn.

4.4.2. In vitro biodegradation characteristics

In order to better mimic the *in vivo* environment, we developed a dynamic biodegradation set-up (Fig. 1c) and compared the dynamic biodegradation behavior of AM porous Zn with its static degradation behavior. During 28 days of immersion, pH value stayed almost unchanged (around 7.6), meaning that AM Zn degraded slowly and 5% CO_2 worked effectively as a buffer. As the dynamic biodegradation process progressed, the accumulation of OH^- caused a slight increase of the pH value (*i.e.*, to 7.7 at 28 days) (Fig. 3b). According to the ICP results, the dynamic flow of r-SBF increased the biodegradation rate of the AM porous Zn (Fig. 3c). Under the dynamic condition, the surface of the AM porous Zn specimens was constantly washed by the medium. The circulation of the medium over the surface of the specimen inhibited local pH increase, thereby increasing the rate of biodegradation [45]. However, the concentration of Zn ions measured at day 28 (under the dynamic condition) was only 4.9 mg/L (Fig. 3c), which equaled to 1.47 mg of released Zn for 300 mL medium. This value was much lower than the volume reduction (*i.e.*, a volume loss of 7.8%) of 178 mg released Zn (equivalent to 0.13 mm/year) determined using the µCT analysis. The main reason for this difference could be the participation of Zn ions in the formation of the biodegradation products. The white biodegradation products (Fig. 3a) indeed contained Zn, according to the EDS analysis (Fig. 4d-g). XRD also confirmed the presence of Zn oxide on the surface of the AM porous Zn specimens after *in vitro* immersion (Fig. 4h). The biodegradation rate was the highest from the PDP tests, being 0.67 mm/year. Based on this rate, the weight reduction of the AM porous Zn would be 917 mg (36.7% reduction) after 28 days. As an accelerated test, PDP can only represent a snapshot of biodegradation at the time when it is performed [46, 47], *i.e.,* 2 h after immersion in the present case, which means that Zn still had a relatively fresh surface. Moreover, when

the PDP tests were performed, the surface of the specimens had experienced a strong polarization effect [48]. Nevertheless, as a straightforward and quantitative technique, PDP can be of help in designing or screening of Zn-based materials before time-consuming immersion tests and *in-vivo* tests [46].

Compared to the results obtained by other researchers using PDP, the AM porous Zn specimens studied here showed a higher rate of biodegradation (*i.e.*, 0.67 mm/year) than the conventionally manufactured ones (*i.e.*, 0.025-0.325 mm/year) [47, 49-55]. This might be attributed to the grain refinement and more grain boundaries caused by the laser processing, which could increase the biodegradation rate of pure Zn. However, the effect of grain size on the biodegradation rate of Zn has not yet been studied. It is therefore suggested that further studies are needed to establish a quantitative relationship, particularly given the fact that laser-based AM processes may then be used as a way to tune the biodegradation rate of AM porous Zn. According to the immersion tests, the rate of Zn biodegradation found in this research (0.07 and 0.13 mm/year under static and dynamic condition, respectively) is comparable with the values reported by other researchers in their *in vitro* static immersion tests (*i.e.*, 0.011-0.084 mm/year [47, 49, 52, 55-59]). The static biodegradation rate of the AM porous Zn falls between the values of the AM porous Mg (0.23 mm/year) and Fe scaffolds (0.03 mm/year) [22, 23], confirming its moderate degradation profile. Furthermore, it is interesting to note that, for pure Zn, the results of *in vitro* biodegradation tests are consistent with those of *in vivo* tests (0.010-0.065 mm/year) [16, 60-65]. It should, however, be noted that in most of the *in vivo* tests the pure Zn wires or stents used for those measurements were implanted in abdominal aorta. Obviously, it is important to find the *in vivo* biodegradation rate of AM porous Zn as a bone implant and its interactions with the surrounding tissues.

4.4.3. Static and dynamic in vitro biodegradation mechanisms

The reactions of Zn in the body fluid can be described as:

$$Zn \rightarrow Zn^{2+} + 2e^-$$

$$2H_2O + O_2 + 4e^- \rightarrow 4OH^-$$
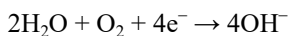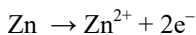
leading to the formation of corrosion products:

$$Zn^{2+} + 2OH^- \rightarrow Zn(OH)_2$$

$$Zn^{2+} + 2OH^- \rightarrow ZnO + H_2O$$
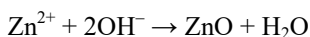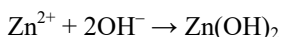
Due to the presence of chloride ions in the body fluid, the corrosion products react with chloride ions to form soluble chloride salts:

$$6Zn(OH)_2 + Zn^{2+} + 2Cl^- \rightarrow 6Zn(OH)_2 \cdot ZnCl_2$$

$$4ZnO + 4H_2O + Zn^{2+} + 2Cl^- \rightarrow 4Zn(OH)_2 \cdot ZnCl_2$$

To reveal the static and dynamic biodegradation mechanisms of the AM porous Zn specimens, we also studied their biodegradation behavior at micro- and macro-scales. At the micro-scale, SEM, FTIR, and XPS analyses revealed the gradual formation of the biodegradation products with immersion time. At the start of the *in vitro* biodegradation tests, Zn was dissolved and $Zn(OH)_2$ formed on the surface of the specimen. As ZnO 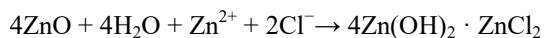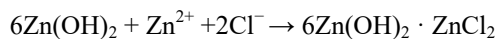is more stable than $Zn(OH)_2$, $Zn(OH)_2$ gradually transformed into ZnO, which was confirmed by the XPS analysis, showing the gradually increasing percentages of ZnO (Fig. 5b, c). At the same time, CO_3^{2-}, P, and Ca participated in the formation of the biodegradation products, as shown by both the ICP results and EDS analysis. The concentrations of P and Ca ions in the medium gradually decreased with time (Fig. 3d, e), while the atomic percentages of P and Ca in the biodegradation products increased, as indicated by the EDS analysis (Fig. 4d-f). Similar trends were observed in the FTIR results (Fig. 4i). At the more advanced stages of biodegradation, carbonates appeared to have formed on the top of the biodegradation layer (Fig. 4g), which can also be observed in the FTIR (Fig. 4i) and XPS graphs (Fig. 5d, e). The formed protective layer enhanced the biodegradation resistance of Zn, while it was simultaneously being attacked by Cl⁻. At the beginning, the buildup of the biodegradation layer was more dominant than the damage caused by Cl⁻. That is why R_f, R_t, and LPR increased up to 7 days. After day 7, the dissolution of the protective layer may have caused R_f, R_t, and LPR to decrease. After day 21, R_f, R_t, and LPR increased again, probably because of the further formation of the passive layer [38]. The Bode impedance graph exhibited a similar trend of impedance variation. At the low frequency range, the impedance modulus values indicated the resistance of charge transfer and separation processes of the degrading system at the Zn surface. In the middle frequency range, the impedance modulus changes related to capacitive and resistive evolutions by formation or (partial) dissolution of the biodegradation layer on the Zn surface.

At the macro level, μCT suggested that the specimens experienced more localized biodegradation under the static condition. Moreover, localized biodegradation mainly occurred at the bottom and at the core of the specimens (Fig. 9, red square). This phenomenon was likely caused by the stagnant flow of r-SBF entrapped in the narrow gap between the specimens and the beaker. Cl⁻ became accumulated at these locations and destroyed the passive layer locally. Pitting or crevice-like corrosion would then take place. On the contrary, the dynamic flow prevented the adsorption of Cl⁻ on the surface

of the corroded layer, thereby ensuring the homogeneity of the biodegradation process (Fig. 9) [45, 66]. In total, larger volume of biodegradation products was formed under the dynamic biodegradation condition than the static one, indicating a faster rate of biodegradation. The ICP results also showed that the concentrations of P and Ca ions were lower under the dynamic flow condition (Fig. 3d, e). The differences between the static condition and dynamic condition in biodegradation rate and biodegradation mechanism observed at different locations within the specimens underscore the fact that, besides the selection of the biomaterial, the topological design of the porous structure is equally important in controlling the biodegradation profile of the resulting implants.

4.4.4. Unique mechanical behavior

Similar to AM porous pure Fe [23], titanium, and tantalum [67, 68], the AM porous Zn specimens showed smooth stress-strain curves with no undulations at the plateau stage during the uniaxial compression tests. The curve started linearly, meaning that the porous structure was still in the elastic region. Then, the slope decreased rapidly when plastic deformation in the struts occurred, after which the plateau region appeared with almost no fluctuations. The specimens maintained their cylindrical shape at 60% strain (Fig. 8a inlay). This could be ascribed to the highly ductile behavior of pure Zn. Towards the end of the test, the slope increased significantly again, which could be attributed to the densification of the porous structure. The mechanical properties of the AM porous Zn ($E = 786$ MPa, $\sigma_y = 10.8$ MPa) stayed within the scope of the values of cancellous bone ($E = 10 – 2000$ MPa, $\sigma_y = 0.2$ - 80 MPa [41]). As the bulk pure Zn has a tensile strength of 28-120 MPa [10], AM Zn-based alloys with good biocompatibility [69], such as Zn-Mg, Zn-Ca et al., should be developed in the future in order to improve its mechanical properties to match those of cortical bone ($\sigma_y = 170$ - 193 MPa [70]). Surprisingly, after *in vitro* biodegradation tests, the mechanical properties of AM porous Zn improved as compared to those of the as-built specimens. Although similar results were found at the early stages of biodegradation of AM porous Mg and Fe [22, 23], the mechanical properties of biodegraded AM porous Zn were higher than those of its as-built counterpart, even after 4 weeks of *in vitro* immersion (Fig. 8b, c). Interestingly, the specimens subjected to the dynamic biodegradation condition had a higher yield strength and a higher elastic modulus, as compared to those biodegraded statically. Considering a 7.8% volume reduction of the Zn scaffold during the dynamic immersion tests for 28 days, the increases in the mechanical properties of the biodegradable metal over time could be attributed to the contributions of the biodegradation products. The hardness of the biodegradation products, which can be converted into strength, is almost 5 times as high as the hardness of the AM Zn [71]. The AM porous Zn during biodegradation may be hypothetically regarded as a composite material consisting of a metal (Zn) substrate and a ceramic surface layer (the biodegradation products). While

the progressing biodegradation deteriorated the mechanical properties of the Zn metal, the formation of the biodegradation products could help in retaining or even improving its mechanical properties. In the case of the statically tested specimens, however, smaller volume of biodegradation products was less effective in playing this role and more localized biodegradation led to decreases in yield strength. This may also explain the fluctuations of the yield strength of the statically tested specimens with time.

These observations, together with the absolute values of the bone-mimicking mechanical properties of AM porous Zn, suggest that AM porous Zn is a promising candidate for the design and fabrication of bone-substituting orthopedic implants. Furthermore, as the degradation products can indeed improve the mechanical properties of porous Zn, one can imagine that, with the regeneration of tissues over time, the mechanical properties can be further improved. It is then important to reconsider what should be the required mechanical properties of a biodegradable porous implant. The initial mechanical properties may not be necessarily as high as those of human bone. Of course, *in vivo* tests are still needed to further confirm the observed changes in mechanical property over time. Moreover, thorough mechanical tests, including fatigue and creep, in relation to natural aging and static recrystallization should be performed to address the mechanical compatibility issues of AM porous Zn fully [69].

4.4.5. In vitro cell responses

Using the latest modification of ISO 10993 for evaluating the biocompatibility of medical devices, we investigated the biological safety of the biodegradable AM porous Zn [72, 73]. To this end, we used direct and indirect (extraction-based) cytocompatibility testing and compared the AM Zn scaffolds with identically produced and likewise treated scaffolds of Ti-6Al-4V - a gold standard material for orthopedic implants. Of note, we used a harsh 72 h extraction regime with the serum-containing medium that allowed for the extraction of both polar and non-polar substances (ISO10993-5, 2009) [73, 74] in a physiological cell culture environment (*i.e.*, 37ºC, pH 7.2-7.4, 5% CO_2). *In vivo*, vascularization ensures, among others, waste product removal. In agreement with ISO 10993, modified for bioabsorbable biomaterials, we used diluted (*i.e.*, 10X) Zn extracts, which is further in line with previous reports recommending to use 9X to 14X diluted extracts from biodegradable metals, such as Mg alloys [73]. Using 10X diluted extracts was also reported earlier in the cases of AM porous Mg and Fe [22, 23]. We further used MTS assays as the most accepted *in vitro* evaluation for extract-based cytotoxicity screening [73]. Until 48 h, the cytotoxicity profiles of Zn extracts were not significantly different from those derived from identically designed Ti-6Al-4V specimens. Even in the extended incubations up to 72 h, which is the longest recommended period by ISO 10993 [75], the Zn extracts were well tolerated by osteoblast-like cells, showing compromised metabolic activity only in

about 15% of the cell population and demonstrating a concentration-dependent effect, which is consistent with the findings of other researchers [76]. The majority of the currently available studies report good cell viability of diluted Zn extracts [48, 77, 78]. However, a few studies have recently reported good cytocompatibility of even undiluted extracts [79, 80]. The desirable cytocompatibility of Zn may be attributed to its low biodegradation rate in plasma and less severe changes in the local pH [12, 50].

In addition to indirectly evaluating the cytocompatibility of the AM porous Zn specimens, we investigated the cell viability directly on the Zn scaffolds through fluorescent live/dead imaging. While this approach is semi-quantitative, it enabled us to study the cell morphology on the scaffolds, and cell distribution within the scaffolds. From peripheral scanning and cross-sectional imaging of the scaffolds, MG-63 cells appeared to be evenly distributed around and within the scaffolds. The majority of cells was further viable and appeared to be intimately attached to the Zn scaffold surface, already after 24 h of seeding. Cell morphologies on Zn were similar to those on Ti-6Al-4V: cells covered all surfaces of the specimens. This is in agreement with earlier studies showing that Zn-based biomaterials supported cell adhesion, viability, and proliferation [81]. Interestingly, several studies have recently reported that Zn ions can enhance gene expression, cell survival and growth, as well as the differentiation of progenitor cells [82-84]. At low concentrations, Zn^{2+} has been furthermore reported to have a positive effect on the cellular activity of human vascular cells [85, 86]. Although Zn is also reported to be involved in modulating pro-inflammatory responses, it is actually crucial for sustaining a proper immune function, too [87]. AM porous Zn implants, therefore, holds a lot of potential for orthopedic applications, as their biodegradation products may facilitate vascularization and, thus, bone regeneration.

4.5. Conclusions

AM topologically ordered biodegradable porous Zn showed potential to fulfill the multiple requirements for an ideal bone-substituting biomaterial. First, the mechanical properties of the as-built AM porous Zn (E = 786 MPa, σ_y = 10.8 MPa) are within the scope reported for cancellous bone and thus are high enough to provide adequate mechanical support. After 4 weeks of *in vitro* immersion, the mechanical properties of the AM porous Zn even increased (E = 879 MPa, σ_y = 12.0 MPa). Secondly, the fabricated scaffolds presented a precise topology and completely interconnected pores, as designed. Thirdly, the biodegradation rate of the AM porous Zn was moderate with ≈7.8% and ≈3.6% volume losses after 4 weeks of dynamic and static *in vitro* immersion, respectively. Moreover, the AM porous Zn exhibited good biocompatibility *in vitro*. Therefore, with the proper scaffold design and alloying, Zn-based biomaterials will hold great potential to become one group of the next-generation functional biodegradable

biomaterials for orthopedic applications and to provide long-awaited solutions to the treatment of large bony defects.

References

[1] H. Hermawan. Updates on the research and development of absorbable metals for biomedical applications. Prog Biomater. 2018;7:93-110.

[2] Y. F. Zheng, X. N. Gu, F. Witte. Biodegradable metals. Mater Sci Eng R Rep. 2014;77:1-34.

[3] Q. Peng, Y. Huang, L. Zhou, N. Hort, K. U. Kainer. Preparation and properties of high purity Mg–Y biomaterials. Biomaterials. 2010;31:398-403.

[4] D. Zhao, F. Witte, F. Lu, J. Wang, J. Li, L. Qin. Current status on clinical applications of magnesium-based orthopaedic implants: A review from clinical translational perspective. Biomaterials. 2017;112:287-302.

[5] T. Kraus, F. Moszner, S. Fischerauer, M. Fiedler, E. Martinelli, J. Eichler, F. Witte, E. Willbold, M. Schinhammer, M. Meischel, P. J. Uggowitzer, J. F. Löffler, A. Weinberg. Biodegradable Fe-based alloys for use in osteosynthesis: Outcome of an in vivo study after 52weeks. Acta Biomater. 2014;10:3346-3353.

[6] D. Pierson, J. Edick, A. Tauscher, E. Pokorney, P. Bowen, J. Gelbaugh, J. Stinson, H. Getty, C. H. Lee, J. Drelich, J. Goldman. A simplified in vivo approach for evaluating the bioabsorbable behavior of candidate stent materials. J Biomed Mater Res B Appl Biomater. 2012;100B:58-67.

[7] D. Andreas, H. Thomas, B. F. Wilhelm, P. Matthias. In vitro and in vivo corrosion properties of new iron–manganese alloys designed for cardiovascular applications. J Biomed Mater Res B Appl Biomater. 2015;103:649-660.

[8] L.-Y. Li, L.-Y. Cui, R.-C. Zeng, S.-Q. Li, X.-B. Chen, Y. Zheng, M. B. Kannan. Advances in functionalized polymer coatings on biodegradable magnesium alloys – A review. Acta Biomater. 2018;79:23-36.

[9] Y. Zheng, X. Xu, Z. Xu, J. Wang, H. Cai. Development of Fe-based degradable metallic biomaterials. Metallic Biomaterials: Wiley-VCH Verlag GmbH & Co. KGaA; 2017. p. 113-160.

[10] J. Venezuela, M. S. Dargusch. The influence of alloying and fabrication techniques on the mechanical properties, biodegradability and biocompatibility of zinc: A comprehensive review. Acta Biomater. 2019;87:1-40.

[11] G. Katarivas Levy, J. Goldman, E. Aghion. The prospects of zinc as a structural material for biodegradable Implants—a review paper. Metals. 2017;7:402.

[12] D. Zhu, I. Cockerill, Y. Su, Z. Zhang, J. Fu, K.-W. Lee, J. Ma, C. Okpokwasili, L. Tang, Y. Zheng, Y.-X. Qin, Y. Wang. Mechanical strength, biodegradation, and in vitro and in vivo biocompatibility of Zn biomaterials. ACS Appl Mater Interfaces. 2019.

[13] K. Falchuk. The biochemical basis of zinc physiology. Physiol Rev. 1993;73:79-118.

[14] C. J. Frederickson, J.-Y. Koh, A. I. Bush. The neurobiology of zinc in health and disease. Nat Rev Neurosci. 2005;6:449-462.

[15] X. Liu, J. Sun, K. Qiu, Y. Yang, Z. Pu, L. Li, Y. Zheng. Effects of alloying elements (Ca and Sr) on microstructure, mechanical property and in vitro corrosion behavior of biodegradable Zn–1.5Mg alloy. J Alloys Compd. 2016;664:444-452.

[16] P. K. Bowen, J. Drelich, J. Goldman. Zinc exhibits ideal physiological corrosion behavior for bioabsorbable stents. Adv Mater. 2013;25:2577-2582.

[17] L. Zhao, Z. Zhang, Y. Song, S. Liu, Y. Qi, X. Wang, Q. Wang, C. Cui. Mechanical properties and in vitro biodegradation of newly developed porous Zn scaffolds for biomedical applications. Mater Des. 2016;108:136-144.

[18] J. Niu, Z. Tang, H. Huang, J. Pei, H. Zhang, G. Yuan, W. Ding. Research on a Zn-Cu alloy as a biodegradable material for potential vascular stents application. Mater Sci Eng, C. 2016;69:407-413.

[19] X. Gu, Y. Zheng, Y. Cheng, S. Zhong, T. Xi. In vitro corrosion and biocompatibility of binary magnesium alloys. Biomaterials. 2009;30:484-498.

[20] Y. Qin, P. Wen, H. Guo, D. Xia, Y. Zheng, L. Jauer, R. Poprawe, M. Voshage, J. H. Schleifenbaum. Additive manufacturing of biodegradable metals: current research status and future perspectives. Acta Biomater. 2019.

[21] J. P. Kruth, L. Froyen, J. Van Vaerenbergh, P. Mercelis, M. Rombouts, B. Lauwers. Selective laser melting of iron-based powder. J Mater Process Technol. 2004;149:616-622.

[22] Y. Li, J. Zhou, P. Pavanram, M. A. Leeflang, L. I. Fockaert, B. Pouran, N. Tümer, K. U. Schröder, J. M. C. Mol, H. Weinans, H. Jahr, A. A. Zadpoor. Additively manufactured biodegradable porous magnesium. Acta Biomater. 2018;67:378-392.

[23] Y. Li, H. Jahr, K. Lietaert, P. Pavanram, A. Yilmaz, L. I. Fockaert, M. A. Leeflang, B. Pouran, Y. Gonzalez-Garcia, H. Weinans, J. M. C. Mol, J. Zhou, A. A. Zadpoor. Additively manufactured biodegradable porous iron. Acta Biomater. 2018;77:380-393.

[24] P. Wen, Y. Qin, Y. Chen, M. Voshage, L. Jauer, R. Poprawe, J. Henrich Schleifenbaum. Laser additive manufacturing of Zn porous scaffolds: shielding gas flow, surface quality and densification. J Mater Sci Technol. 2018.

[25] D. Carluccio, A. G. Demir, L. Caprio, B. Previtali, M. J. Bermingham, M. S. Dargusch. The influence of laser processing parameters on the densification and surface morphology of pure Fe and Fe-35Mn scaffolds produced by selective laser melting. J Manuf Process. 2019;40:113-121.

[26] Y. Li, H. Jahr, X. Y. Zhang, M. A. Leeflang, W. Li, B. Pouran, F. D. Tichelaar, H. Weinans, J. Zhou, A. A. Zadpoor. Biodegradation-affected fatigue behavior of additively manufactured porous magnesium. Addit Manuf. 2019;28:299-311.

[27] Y. Li, K. Lietaert, W. Li, X. Y. Zhang, M. A. Leeflang, J. Zhou, A. A. Zadpoor. Corrosion fatigue behavior of additively manufactured biodegradable porous iron. Corros Sci. 2019;156:106-116.

[28] K. Lietaert, B. Neirinck, J. Plas, J. Vleugels. Influence of unit cell architecture and of relative density on the mechanical properties of additively manufactured Zn scaffolds as biodegradable implant materials. Proceedings Euro PM 2017: International Powder Metallurgy Congress and Exhibition. Politecnico di Milano, Italy: The European Powder Metallurgy Association; 2017. p. 1-7.

[29] Y. Qin, P. Wen, M. Voshage, Y. Chen, P. G. Schückler, L. Jauer, D. Xia, H. Guo, Y. Zheng, J. H. Schleifenbaum. Additive manufacturing of biodegradable Zn-xWE43 porous scaffolds: Formation quality, microstructure and mechanical properties. Mater Des. 2019;181:107937.

[30] K. Lietaert, W. Baekelant, L. Thijs, J. Vleugels. Direct metal printing of zinc: from single laser tracks to high density parts. European Congress and Exhibition on Powder Metallurgy. European PM Conference Proceedings. Swerea KIMAB, Sweden: The European Powder Metallurgy Association; 2016. p. 1-6.

[31] A. Oyane, H.-M. Kim, T. Furuya, T. Kokubo, T. Miyazaki, T. Nakamura. Preparation and assessment of revised simulated body fluids. J Biomed Mater Res A. 2003;65A:188-195.

[32] F. Zhao, B. van Rietbergen, K. Ito, S. Hofmann. Flow rates in perfusion bioreactors to maximise mineralisation in bone tissue engineering in vitro. J Biomech. 2018;79:232-237.

[33] M. E. Gomes, V. I. Sikavitsas, E. Behravesh, R. L. Reis, A. G. Mikos. Effect of flow perfusion on the osteogenic differentiation of bone marrow stromal cells cultured on starch-based three-dimensional scaffolds. J Biomed Mater Res A. 2003;67A:87-95.

[34] J. R. Vetsch, D. C. Betts, R. Müller, S. Hofmann. Flow velocity-driven differentiation of human mesenchymal stromal cells in silk fibroin scaffolds: A combined experimental and computational approach. PLoS One. 2017;12:e0180781.

[35] Y. Xin, K. Huo, H. Tao, G. Tang, P. K. Chu. Influence of aggressive ions on the degradation behavior of biomedical magnesium alloy in physiological environment. Acta Biomater. 2008;4:2008-2015.

[36] Y. Chen, S. Zhao, B. Liu, M. Chen, J. Mao, H. He, Y. Zhao, N. Huang, G. Wan. Corrosion-Controlling and Osteo-Compatible Mg Ion-Integrated Phytic Acid (Mg-PA) Coating on Magnesium Substrate for Biodegradable Implants Application. ACS Appl Mater Interfaces. 2014;6:19531-19543.

[37] Y. Sheng, H. Zhou, Z. Li, L. Chen, X. Wang, X. Zhao, L. Wei. Improved blood compatibility and cyto-compatibility of Zn-1Mg via plasma electrolytic oxidation. Materialia. 2019;5:100244.

[38] L. Liu, Y. Meng, A. A. Volinsky, H.-J. Zhang, L.-N. Wang. Influences of albumin on in vitro corrosion of pure Zn in artificial plasma. Corros Sci. 2019;153:341-356.

4

[39] X. Liu, H. Yang, Y. Liu, P. Xiong, H. Guo, H.-H. Huang, Y. Zheng. Comparative studies on degradation behavior of pure zinc in various simulated body fluids. JOM. 2019;71:1414-1425.

[40] S. Champagne, E. Mostaed, F. Safizadeh, E. Ghali, M. Vedani, H. Hermawan. In vitro degradation of absorbable zinc alloys in artificial urine. Materials. 2019;12:295.

[41] M. Yazdimamaghani, M. Razavi, D. Vashaee, K. Moharamzadeh, A. R. Boccaccini, L. Tayebi. Porous magnesium-based scaffolds for tissue engineering. Mater Sci Eng, C. 2017;71:1253-1266.

[42] L.-E. Loh, C.-K. Chua, W.-Y. Yeong, J. Song, M. Mapar, S.-L. Sing, Z.-H. Liu, D.-Q. Zhang. Numerical investigation and an effective modelling on the Selective Laser Melting (SLM) process with aluminium alloy 6061. Int J Heat Mass Transfer. 2015;80:288-300.

[43] P. Wen, M. Voshage, L. Jauer, Y. Chen, Y. Qin, R. Poprawe, J. H. Schleifenbaum. Laser additive manufacturing of Zn metal parts for biodegradable applications: Processing, formation quality and mechanical properties. Mater Des. 2018;155:36-45.

[44] T. DebRoy, H. L. Wei, J. S. Zuback, T. Mukherjee, J. W. Elmer, J. O. Milewski, A. M. Beese, A. Wilson-Heid, A. De, W. Zhang. Additive manufacturing of metallic components – Process, structure and properties. Prog Mater Sci. 2018;92:112-224.

[45] J. Lévesque, H. Hermawan, D. Dubé, D. Mantovani. Design of a pseudo-physiological test bench specific to the development of biodegradable metallic biomaterials. Acta Biomater. 2008;4:284-295.

[46] N. T. Kirkland, N. Birbilis, M. P. Staiger. Assessing the corrosion of biodegradable magnesium implants: A critical review of current methodologies and their limitations. Acta Biomater. 2012;8:925-936.

[47] L. Liu, Y. Meng, C. Dong, Y. Yan, A. A. Volinsky, L.-N. Wang. Initial formation of corrosion products on pure zinc in simulated body fluid. J Mater Sci Technol. 2018;34:2271-2282.

[48] C. Shen, X. Liu, B. Fan, P. Lan, F. Zhou, X. Li, H. Wang, X. Xiao, L. Li, S. Zhao, Z. Guo, Z. Pu, Y. Zheng. Mechanical properties, in vitro degradation behavior, hemocompatibility and cytotoxicity evaluation of Zn–1.2Mg alloy for biodegradable implants. RSC Adv. 2016;6:86410-86419.

[49] H. F. Li, X. H. Xie, Y. F. Zheng, Y. Cong, F. Y. Zhou, K. J. Qiu, X. Wang, S. H. Chen, L. Huang, L. Tian, L. Qin. Development of biodegradable Zn-1X binary alloys with nutrient alloying elements Mg, Ca and Sr. Sci Rep. 2015;5:10719.

[50] K. Törne, M. Larsson, A. Norlin, J. Weissenrieder. Degradation of zinc in saline solutions, plasma, and whole blood. J Biomed Mater Res B Appl Biomater. 2016;104:1141-1151.

[51] P. Sotoudeh Bagha, S. Khaleghpanah, S. Sheibani, M. Khakbiz, A. Zakeri. Characterization of nanostructured biodegradable Zn-Mn alloy synthesized by mechanical alloying. J Alloys Compd. 2018;735:1319-1327.

[52] X. Liu, J. Sun, F. Zhou, Y. Yang, R. Chang, K. Qiu, Z. Pu, L. Li, Y. Zheng. Micro-alloying with Mn in Zn–Mg alloy for future biodegradable metals application. Mater Des. 2016;94:95-104.

[53] S. Zhao, C. T. McNamara, P. K. Bowen, N. Verhun, J. P. Braykovich, J. Goldman, J. W. Drelich. Structural characteristics and in vitro biodegradation of a novel Zn-Li alloy prepared by induction melting and hot rolling. Metall Mater Trans A. 2017;48:1204-1215.

[54] J. Cheng, B. Liu, Y. H. Wu, Y. F. Zheng. Comparative in vitro study on pure metals (Fe, Mn, Mg, Zn and W) as biodegradable metals. J Mater Sci Technol. 2013;29:619-627.

[55] E. Mostaed, M. Sikora-Jasinska, A. Mostaed, S. Loffredo, A. G. Demir, B. Previtali, D. Mantovani, R. Beanland, M. Vedani. Novel Zn-based alloys for biodegradable stent applications: Design, development and in vitro degradation. J Mech Behav Biomed Mater. 2016;60:581-602.

[56] Y. Yang, F. Yuan, C. Gao, P. Feng, L. Xue, S. He, C. Shuai. A combined strategy to enhance the properties of Zn by laser rapid solidification and laser alloying. J Mech Behav Biomed Mater. 2018;82:51-60.

[57] D. Vojtěch, J. Kubásek, J. Šerák, P. Novák. Mechanical and corrosion properties of newly developed biodegradable Zn-based alloys for bone fixation. Acta Biomater. 2011;7:3515-3522.

[58] Z. Tang, J. Niu, H. Huang, H. Zhang, J. Pei, J. Ou, G. Yuan. Potential biodegradable Zn-Cu binary alloys developed for cardiovascular implant applications. J Mech Behav Biomed Mater. 2017;72:182-191.

[59] M. Sikora-Jasinska, E. Mostaed, A. Mostaed, R. Beanland, D. Mantovani, M. Vedani. Fabrication, mechanical properties and in vitro degradation behavior of newly developed ZnAg alloys for degradable implant applications. Mater Sci Eng, C. 2017;77:1170-1181.

[60] A. Kafri, S. Ovadia, G. Yosafovich-Doitch, E. Aghion. In vivo performances of pure Zn and Zn–Fe alloy as biodegradable implants. J Mater Sci Mater Med. 2018;29:94.

[61] H. Yang, C. Wang, C. Liu, H. Chen, Y. Wu, J. Han, Z. Jia, W. Lin, D. Zhang, W. Li, W. Yuan, H. Guo, H. Li, G. Yang, D. Kong, D. Zhu, K. Takashima, L. Ruan, J. Nie, X. Li, Y. Zheng. Evolution of the degradation mechanism of pure zinc stent in the one-year study of rabbit abdominal aorta model. Biomaterials. 2017;145:92-105.

[62] A. J. Drelich, S. Zhao, R. J. Guillory, J. W. Drelich, J. Goldman. Long-term surveillance of zinc implant in murine artery: Surprisingly steady biocorrosion rate. Acta Biomater. 2017;58:539-549.

[63] P. K. Bowen, R. J. Guillory, E. R. Shearier, J.-M. Seitz, J. Drelich, M. Bocks, F. Zhao, J. Goldman. Metallic zinc exhibits optimal biocompatibility for bioabsorbable endovascular stents. Mater Sci Eng, C. 2015;56:467-472.

[64] S. Zhao, J.-M. Seitz, R. Eifler, H. J. Maier, R. J. Guillory, E. J. Earley, A. Drelich, J. Goldman, J. W. Drelich. Zn-Li alloy after extrusion and drawing: Structural, mechanical characterization, and biodegradation in abdominal aorta of rat. Mater Sci Eng, C. 2017;76:301-312.

[65] S. A. Arab, G. R. J. II, S. Daniel, G. Jeremy, D. J. W. Effect of PLLA coating on corrosion and biocompatibility of zinc in vascular environment. Surf Innov. 2017;5:211-220.

[66] Y. Zong, G. Yuan, X. Zhang, L. Mao, J. Niu, W. Ding. Comparison of biodegradable behaviors of AZ31 and Mg–Nd–Zn–Zr alloys in Hank's physiological solution. Mater Sci Eng, B. 2012;177:395-401.

[67] R. Wauthle, S. M. Ahmadi, S. Amin Yavari, M. Mulier, A. A. Zadpoor, H. Weinans, J. Van Humbeeck, J.-P. Kruth, J. Schrooten. Revival of pure titanium for dynamically loaded porous implants using additive manufacturing. Mater Sci Eng, C. 2015;54:94-100.

[68] R. Wauthle, J. van der Stok, S. Amin Yavari, J. Van Humbeeck, J.-P. Kruth, A. A. Zadpoor, H. Weinans, M. Mulier, J. Schrooten. Additively manufactured porous tantalum implants. Acta Biomater. 2015;14:217-225.

[69] G. Li, H. Yang, Y. Zheng, X.-H. Chen, J.-A. Yang, D. Zhu, L. Ruan, K. Takashima. Challenges in the use of zinc and its alloys as biodegradable metals: perspective from biomechanical compatibility. Acta Biomater. 2019.

[70] S. Wu, X. Liu, K. W. K. Yeung, C. Liu, X. Yang. Biomimetic porous scaffolds for bone tissue engineering. Materials Science and Engineering: R: Reports. 2014;80:1-36.

[71] P. Zhang, S. X. Li, Z. F. Zhang. General relationship between strength and hardness. Materials Science and Engineering: A. 2011;529:62-73.

[72] H.-S. Han, H.-K. Kim, Y.-C. Kim, H.-K. Seok, Y.-Y. Kim. Conventional and improved cytotoxicity test methods of newly developed biodegradable magnesium alloys. Met Mater Int. 2015;21:1108-1117.

[73] J. Wang, F. Witte, T. Xi, Y. Zheng, K. Yang, Y. Yang, D. Zhao, J. Meng, Y. Li, W. Li, K. Chan, L. Qin. Recommendation for modifying current cytotoxicity testing standards for biodegradable magnesium-based materials. Acta Biomater. 2015;21:237-249.

[74] Y. Su, I. Cockerill, Y. Wang, Y.-X. Qin, L. Chang, Y. Zheng, D. Zhu. Zinc-based biomaterials for regeneration and therapy. Trends Biotechnol. 2019;37:428-441.

[75] J. Fischer, M. H. Prosenc, M. Wolff, N. Hort, R. Willumeit, F. Feyerabend. Interference of magnesium corrosion with tetrazolium-based cytotoxicity assays. Acta Biomater. 2010;6:1813-1823.

[76] P. Li, C. Schille, E. Schweizer, F. Rupp, A. Heiss, C. Legner, U. E. Klotz, J. Geis-Gerstorfer, L. Scheideler. Mechanical characteristics, in vitro degradation, cytotoxicity, and antibacterial evaluation of Zn-4.0Ag alloy as a biodegradable material. Int J Mol Sci. 2018;19:755.

[77] J. Kubásek, D. Vojtěch, E. Jablonská, I. Pospíšilová, J. Lipov, T. Ruml. Structure, mechanical characteristics and in vitro degradation, cytotoxicity, genotoxicity and mutagenicity of novel biodegradable Zn–Mg alloys. Mater Sci Eng, C. 2016;58:24-35.

[78] C. Shuai, Y. Cheng, Y. Yang, S. Peng, W. Yang, F. Qi. Laser additive manufacturing of Zn-2Al part for bone repair: Formability, microstructure and properties. J Alloys Compd. 2019;798:606-615.

[79] H. Li, H. Yang, Y. Zheng, F. Zhou, K. Qiu, X. Wang. Design and characterizations of novel biodegradable ternary Zn-based alloys with IIA nutrient alloying elements Mg, Ca and Sr. Mater Des. 2015;83:95-102.

[80] H. R. Bakhsheshi-Rad, E. Hamzah, H. T. Low, M. Kasiri-Asgarani, S. Farahany, E. Akbari, M. H. Cho. Fabrication of biodegradable Zn-Al-Mg alloy: Mechanical properties, corrosion behavior, cytotoxicity and antibacterial activities. Mater Sci Eng, C. 2017;73:215-219.

[81] D. Zhu, Y. Su, M. L. Young, J. Ma, Y. Zheng, L. Tang. Biological Responses and Mechanisms of Human Bone Marrow Mesenchymal Stem Cells to Zn and Mg Biomaterials. ACS Appl Mater Interfaces. 2017;9:27453-27461.

[82] Y. Qiao, W. Zhang, P. Tian, F. Meng, H. Zhu, X. Jiang, X. Liu, P. K. Chu. Stimulation of bone growth following zinc incorporation into biomaterials. Biomaterials. 2014;35:6882-6897.

[83] J. Yu, L. Xu, K. Li, N. Xie, Y. Xi, Y. Wang, X. Zheng, X. Chen, M. Wang, X. Ye. Zinc-modified Calcium Silicate Coatings Promote Osteogenic Differentiation through TGF-β/Smad Pathway and Osseointegration in Osteopenic Rabbits. Sci Rep. 2017;7:3440.

[84] G. Cama, S. Nkhwa, B. Gharibi, A. Lagazzo, R. Cabella, C. Carbone, P. Dubruel, H. Haugen, L. Di Silvio, S. Deb. The role of new zinc incorporated monetite cements on osteogenic differentiation of human mesenchymal stem cells. Mater Sci Eng, C. 2017;78:485-494.

[85] J. Ma, N. Zhao, D. Zhu. Endothelial cellular responses to biodegradable metal zinc. ACS Biomater Sci Eng. 2015;1:1174-1182.

[86] E. R. Shearier, P. K. Bowen, W. He, A. Drelich, J. Drelich, J. Goldman, F. Zhao. In vitro cytotoxicity, adhesion, and proliferation of human vascular cells exposed to zinc. ACS Biomater Sci Eng. 2016;2:634-642.

[87] N. Z. Gammoh, L. Rink. Zinc in Infection and Inflammation. Nutrients. 2017;9:624.

4

Supplementary information
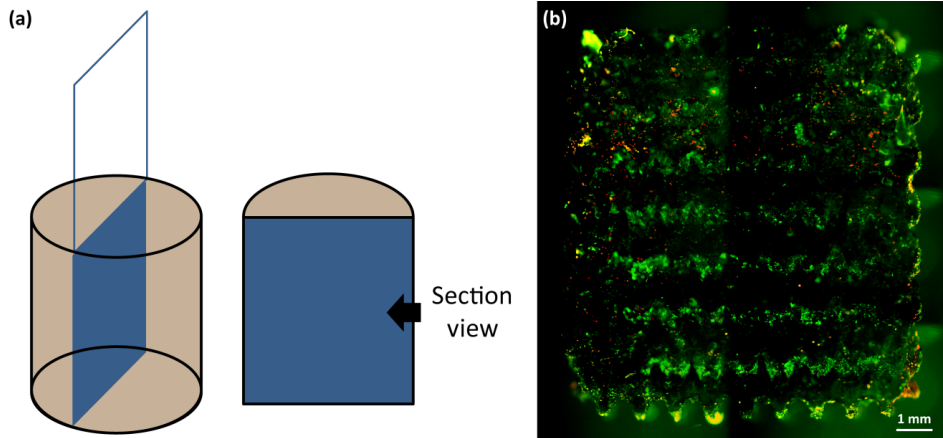
Figure S1. Schematic of cutting (a) and FOI image of cells on the section of AM Zn scaffolds (b) after 24 h.
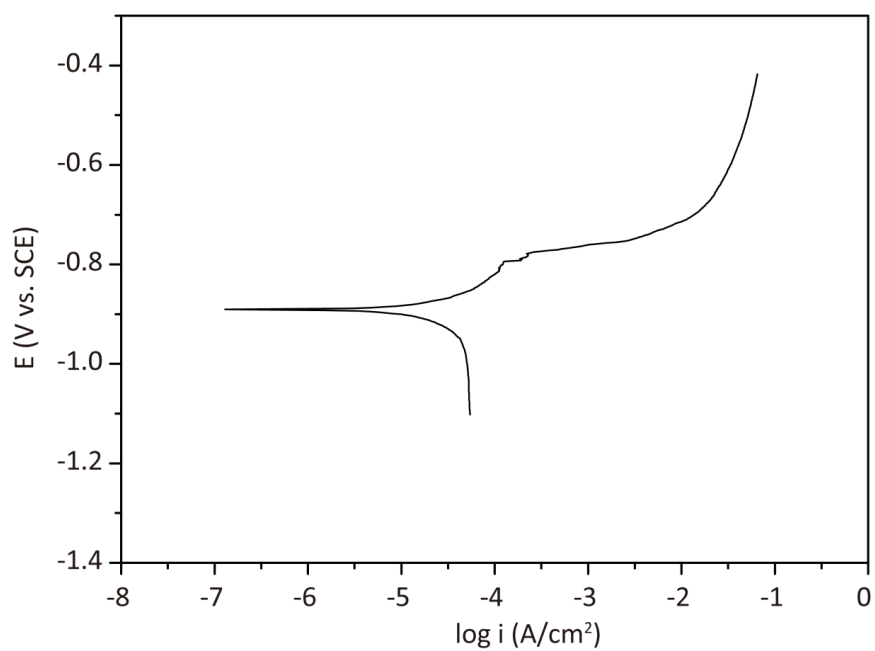
Figure S2. PDP curves of AM porous zinc.

4

5

Biodegradation-affected fatigue behavior of additively manufactured porous magnesium

We used selective laser melting (SLM) to fabricate porous magnesium alloy (WE43) scaffolds based on diamond unit cells. The microstructure of the resulting material was examined using electron back-scattered diffraction, scanning transmission electron microscopy, and X-ray diffraction. The fatigue behaviors of the material in air and in revised simulated body fluid (r-SBF) were evaluated and compared. Biodegradation decreased the fatigue strength of the porous material from 30% to 20% of its yield strength. Moreover, cyclic loading significantly increased its biodegradation rate. The mechanistic aspects of how biodegradation and cyclic loading interacted with each other on different scales were revealed as well. On the micro-scale, cracks initiated at biodegradation pits and propagated transgranularly. In addition, dislocations became more tangled after the fatigue tests. On the macro-scale, cracks preferred initiating at the strut junctions where tensile stress concentrations were present, as revealed by the finite element analysis of the porous material under compressive loading. Most of the cracks initiated in the struts were positioned on the periphery of the specimens.[1]

5.1. Introduction

Magnesium is widely recognized as one of the most promising biodegradable materials for orthopedic applications [1]. First, physical and mechanical properties of Mg, e.g., density (1.74-2.0 g/cm^3) and elastic modulus (41-45 GPa), are similar to those of human bones (1.8-2.1 g/cm^3 and 3-20 GPa, respectively) [2]. Secondly, Mg is an essential mineral crucial to bone health and can even stimulate new bone formation [3]. Thirdly, excessive Mg can be efficiently secreted through the urinary system [4]. The recent developments in additive manufacturing (AM) have provided a technological platform to develop biodegradable Mg scaffolds [5]. Biodegradable metallic scaffolds with complex, precisely controlled topologies that could be used to control their biodegradation profiles both temporally and spatially are highly sought after as one type of the candidates of the ideal bone substitute [5-7].

Despite the attractive properties of Mg, the application of Mg as a scaffold material has been hindered by its rapid biodegradation, which may cause the formation of hydrogen gas cavities and premature loss of mechanical integrity [8]. The focus of most studies on biodegradable Mg and its alloys has therefore been placed on reducing the degradation rate through the modifications of chemical composition, microstructure, and surface conditions [8-15]. In recent years, Mg-based materials with lower biodegradation rates have inspired surgeons to consider clinical applications [16]. For example, orthopedic devices or implants based on pure Mg, Mg-Y-Re-Zr, and Mg-Ca-Zn have been tested to fix fractures or bone flaps [17]. However, human body is not only an aqueous environment but also a severe environment with complex cyclic loading, which can cause fatigue failure of porous orthopedic implants as well. The fatigue behavior of AM topologically ordered porous biomaterials made from bioinert metals, such as pure titanium [18], titanium alloys [19-22], Co-Cr [23, 24], and tantalum [23, 25], have been extensively studied. It is motivated by the critical importance of the fatigue behavior in the design of load-bearing orthopedic implants that experience millions of loading cycles per year [20]. Understanding the fatigue behavior is even more critical in the case of biodegradable metals, as biodegradation is highly likely to shorten their fatigue life [26].

However, up till now, there have been only a few studies on the biodegradation-affected fatigue behavior of bulk WE43, high-purity Mg, and Mg-Zn-Ca alloys in simulated body fluid (SBF) [26-28]. Dong et al. [26], for example, found significantly accelerated corrosion and mechanical deterioration of Mg under cyclic loading in SBF. As compared to fatigue testing of bulk Mg in air, where crack initiated at microstructural defects, cracks nucleated at localized sites or pits [26, 28] when fatigue specimens were immersed in SBF. Jafari et al. [27] found that fatigue cracks could initiate at deformation twin boundaries in air, while biodegradation pits were the main

crack initiation sites in SBF. As the study on AM topologically ordered biodegradable porous Mg biomaterials have appeared only very recently [7]. There is yet virtually no information available in the literature regarding the response of these biomaterials to cyclic mechanical loading and how biodegradation affects that.

In this paper, we report for the first time how biodegradation affects the fatigue behavior of AM topologically ordered porous metallic biomaterials. We used the Mg alloy WE43, which is known to present a favorable biodegradation profile [29]. We hypothesized that (i) biodegradation of Mg in aggressive physiological environments and under cyclic loading would severely reduce its fatigue life and (ii) the mechanistic aspects of biodegradation-affected fatigue behavior of topologically ordered porous Mg alloys would be unique, i.e., not directly comparable with the more commonly observed corrosion fatigue behavior of bulk Mg alloys. To prove these hypotheses, we evaluated and compared the fatigue behaviors of the Mg scaffolds in air and in revised simulated body fluid (r-SBF). We designed and fabricated of a novel test setup that complemented our fatigue test machine and ensured that cyclic loading of the specimen could occur in r-SBF [30] under controlled conditions of temperature and atmosphere. Furthermore, we revealed the unique mechanistic aspects of how biodegradation and cyclic loading interacted with each other on different scales.

5.2. Material and methods

5.2.1. Scaffold manufacturing and post processing

Cylindrical WE43 magnesium alloy (containing 4% yttrium and 3% rare earths) samples (diameter: 10 mm and height: 11.2 mm) with diamond unit cells (strut size: 400 µm and pore size: 600 µm, Fig. 1a) were additively manufactured using a laboratory-scale selective laser melting (SLM) machine [7], in which argon was fed to maintain an inert atmosphere with oxygen content below 10 ppm. The optical system of the SLM machine consisted of a single-mode ytterbium fiber laser (IPG YLR-200) with a maximum output power of 230 W, a galvanometric scanner (SCANLAB hurrySCAN 20), and an f-theta focusing lens (SILL S4LFT 3254/126). The WE43 powder (4 wt% yttrium and 3 wt% rare earth elements) with a nearly spherical particle shape (Magnesium Elektron UK, Manchester, UK) was gas-atomized and sieved to a particle size range of 25 to 60 µm. Hatch vectors were used for scanning with 100 J/mm^3 energy density. The samples were built on an aluminum baseplate without preheating. To smoothen the strut surfaces, the samples were chemically polished in a solution composed of 5% (by volume) HCl, 5% HNO$_3$, and 90% C$_2$H$_5$OH for 2 min, followed by ultrasonic cleaning in C$_2$H$_5$OH for 2 min to wash out HCl and HNO$_3$.
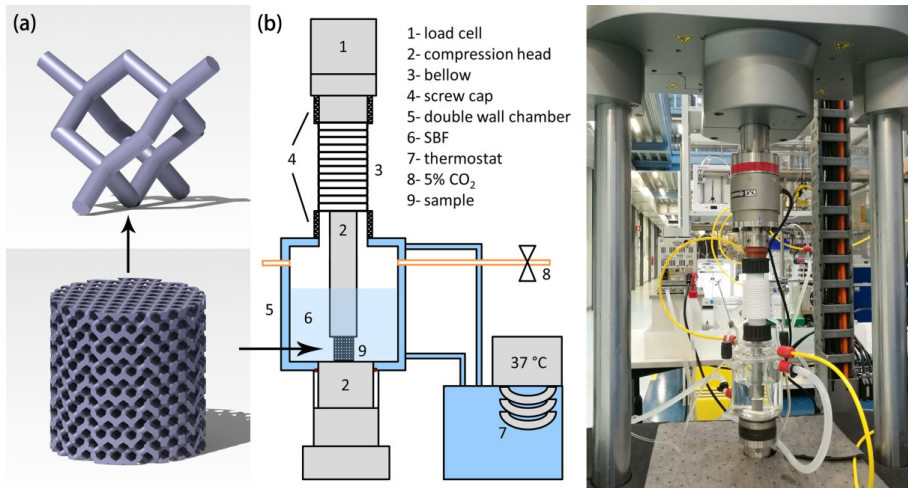
Figure 1 AM Mg alloy scaffold design: (a) diamond unit cell and unit cell-based scaffold; (b) biodegradation fatigue test set-up.

5.2.2. Microstructure characterization

The microstructure of WE43 samples was examined with a digital microscope (Keyence VHX5000). Samples for optical microstructural analysis were ground and polished to 1 μm, followed by 5 s chemical etching (5% Nital). Electron back-scattered diffraction (EBSD) data were collected at a step size of 200 nm, using a HKL Nordlys II detector attached to a JEOL JSM-6500F field emission gun scanning electron microscope (FEGSEM). Inverse pole figures (IPF) was reconstructed by using the TSL OIM® Analysis commercial software. Samples for EBSD analysis were prepared by grinding, mechanical polishing up to 1 μm diamond suspension, and mechanical polishing using 0.04 μm silica oxide. A scanning transmission electron microscope (STEM, FEI Tecnai STEM F20UT/STEM) was used to analyze the precipitates in the as-built samples and to compare dislocation densities and distributions before and after the fatigue tests. BF (bright field) images were made. For elemental mapping with energy dispersive X-ray spectroscopy (EDX, Oxford Instruments EDX detector X-MaxN 100TLE), spectrum was collected for each beam position in an STEM image. Samples for STEM analysis were embedded in a resin and mechanically thinned down to 30 μm. The slice was glued on a Cu ring of 3 mm (outer diameter). This ring was placed in a Gatan Ar ion mill and the sample was thinned down until a hole appeared. The edge of the hole was electron transparent. Phase identification was performed on the cross section using an X-ray diffractometer (XRD, Bruker D8 Advance diffractometer Bragg-Brentano geometry with a graphite monochromator and Vantec position sensitive detector),

operating at 45 kV and 35 mA with a step size of 0.035° and a counting time of 15 s per step using Co Ka radiation. XRD was also used to study the changes in microstructure and strain accumulation occurring during the fatigue tests. The top surface of the scaffold was aligned with the goniometer axis. The struts on the top were aligned with the direction of the X-ray beam. The full width at half maximum (FWHM) was determined using the "Create Area" function of the Bruker-Eva software.

5.2.3. Fatigue tests in air and in r-SBF

Compression-compression fatigue tests were performed at a minimum to maximum stress ratio of 0.1, a frequency of 15 Hz [31] and seven different stress levels: $0.2\sigma_y$, $0.3\sigma_y$, $0.4\sigma_y$, $0.5\sigma_y$, $0.6\sigma_y$, $0.7\sigma_y$ and $0.8\sigma_y$, where σ_y is the yield stress (=22 MPa [1]) using a dynamic testing machine (Instron E10000 ElectroPlus with a 10 kN load cell). The tests were stopped when specimens failed, unless failure did not occur until 3×10^6 loading cycles (2.3 days). Biodegradation fatigue tests were performed by using the same machine equipped with a double-wall specimen chamber designed and manufactured in-house (Fig. 1b). The specimen was immersed in revised simulated body fluid (r-SBF) [30] inside the chamber throughout the test. The temperature of r-SBF was held at 37 °C and purging of CO_2 at 5% was maintained during the test. The ratcheting strain rate per cycle was calculated as $d[(\varepsilon_{max} + \varepsilon_{min})/2]/dN$, where ε_{max} and ε_{min} are the maximum and minimum axial strains in a cycle, respectively, and N is the number of cycles.

5.2.4. Static immersion tests in r-SBF

For comparison, static immersion tests were carried out in r-SBF at 37 °C without any mechanical loading. The immersion time was in accordance with that of the biodegradation fatigue tests at three stress levels: $0.3\sigma_y$ (840 min), $0.5\sigma_y$ (50 min), and $0.8\sigma_y$ (6.5 min). Mg ion concentration (ρ_{Mg}) in the solution was determined using an inductively coupled plasma optical emission spectroscope (ICP-OES, iCAP 6500 Duo, Thermo Scientific). Then, the biodegradation rate was calculated based on the ion concentration data: $v_{cr}=(\rho_{Mg}\times V)/t$, where V is the volume of the r-SBF and t is the immersion time.

5.2.5. Morphological characterization

The as-polished samples and as-fatigue-tested specimens were scanned using micro-computed tomography (μCT) (Quantum FX, Perkin Elmer, USA) at a tube current of 180 μA and a tube voltage of 90 kV. Scanning time was 3 min. Voxel size was $30\times30\times30$ μm^3 when the whole specimen was studied and $10\times10\times10$ μm^3 when focus was placed on certain areas. To reduce beam-hardening artefacts, a thin tubular copper filter (thickness = 0.5 mm) was used. μCT images were automatically reconstructed and

converted into a series of 2D images using Analyze 11.0 (Perkin Elmer, USA). The images were then exported to AVIZO Fire. For higher resolution scanning, two different threshold ranges (50-100 and 100-255) were applied to segment the specimens with the lower value range incorporating most degradation products and the higher value range segmenting the degradation products apart from the Mg alloy.

5.2.6. Finite element (FE) analysis

To aid in understanding the response of the porous material to compressive loading, especially the stress distribution inside the material, simulations with the finite element method (FEM) were conducted using the commercial software package Abaqus (Dassault Systèmes Simulia Corp, France). Representative volume element (RVE) of a single diamond unit was developed. The RVE models were meshed using ten-node tetrahedral element (C3D10). The elastic and plastic properties were extracted from the stress-strain curves of the as-selectively laser melt WE43 alloy [32]. The density, elastic modulus and Poisson's ratio of the material was set at 1.8 g/cm^3, 44.8 GPa and 0.35, respectively. For the purpose of modeling the local premature yielding in stress concentration areas, before the plastic deformation data were put into the Abaqus software, the elastic deformation was removed from the stress strain curve. The element size was set at 0.05 and a total of 45936 elements were used in the FE models. The FE models were subjected to static compressive loading to $0.2\sigma_y$. Then, the contours of the first principal stresses of the RVE models were extracted to help infer the stress concentrations inside the porous material under compression.

5.2.7. Crack morphology characterization

The morphologies of the cracks appearing after the biodegradation fatigue tests were examined using a scanning electron microscope (SEM, JSM-IT100, JEOL). A Keyence VHX5000 digital microscope was used to observe the fatigue crack distribution on the cross-section of the entire specimen. EBSD analysis was performed to reveal the grain orientations around the cracks.

5.2.8. Statistical analysis

Differences in biodegradation rate between the groups with and without cyclic loading were analyzed using one-way analysis of variance (ANOVA), followed by post-hoc Turkey test. A p-value below 0.05 was assumed to indicate a statistically significant difference ($p < 0.05$, *; $n.s.$ = not significant).

5.3. Results

5.3.1. Microstructural features of SLM Mg alloy scaffolds

During SLM, melt pools were stacked on the top of the struts in the building direction (Fig. 2a). The melt lines were, however, not visible at the bottom of the struts (Fig. 2a). IPF mapping revealed that on the top of the struts, the melt pool boundaries were decorated with a thin layer of ultrafine grains, below which elongated grains were present between two melt lines (indicated by dash lines) (Fig. 2b). In addition, a number of abnormal larger grains were present on the top (Fig. 2b). At the bottom, equiaxed fine grains were dominant (Fig. 2a). The pole figure (PF) showed that the grains had a slightly preferred orientation tilted from the building direction (Fig. 2b). STEM revealed two types of precipitates: small round particles (box 1 in Fig. 2c) and Chinese script particles (box 2 in Fig. 2c). STEM EDX mapping suggested that the small particles in the size range of 30-60 nm were Zr-rich particles and those in the size range of 15-30 nm were Y-O-rich particles (Fig. 2c, EDX mapping 1), while Chinese script particles were rich in Mg, Nd, Y, and O (Fig. 2c, EDX mapping 2). XRD analysis indicated the presence of Y_2O_3, which was in agreement with the results of the STEM EDX analysis, and the presence of Mg_3Nd (Fig. 2d), which was most likely the Chinese script phase surrounded by the Y-O rich and Mg rich matrix (Fig. 2c).

5.3.2. Fatigue properties and degradation fatigue properties

Some levels of hysteresis were observed during the fatigue tests at two different stress levels (i.e., $0.5\sigma_y$ and $0.6\sigma_y$) (Fig. 3a). With increasing fatigue cycles, the hysteresis loops shifted towards higher strains (Fig. 3a). The slopes of the hysteresis loops decreased at 30,000 and 100,000 cycles for $0.6\sigma_y$ and $0.5\sigma_y$, respectively, as compared with those at lower cycles (Fig. 3a). Specimens tested at $0.6\sigma_y$ had faster strain accumulation and shorter fatigue lives than those tested at $0.5\sigma_y$ (Fig. 3b). The ratcheting strain rate curve (Fig. 3c) could be divided into two stages. At the first stage, the ratcheting strain rate per cycle was stable, followed by the second stage, during which the ratcheting strain rapidly increased, leading to fatigue failure (Fig. 3c). Specimens tested at the $0.5\sigma_y$ stress level had a longer duration of the first stage than those tested at $0.6\sigma_y$ (Fig. 3c).

5
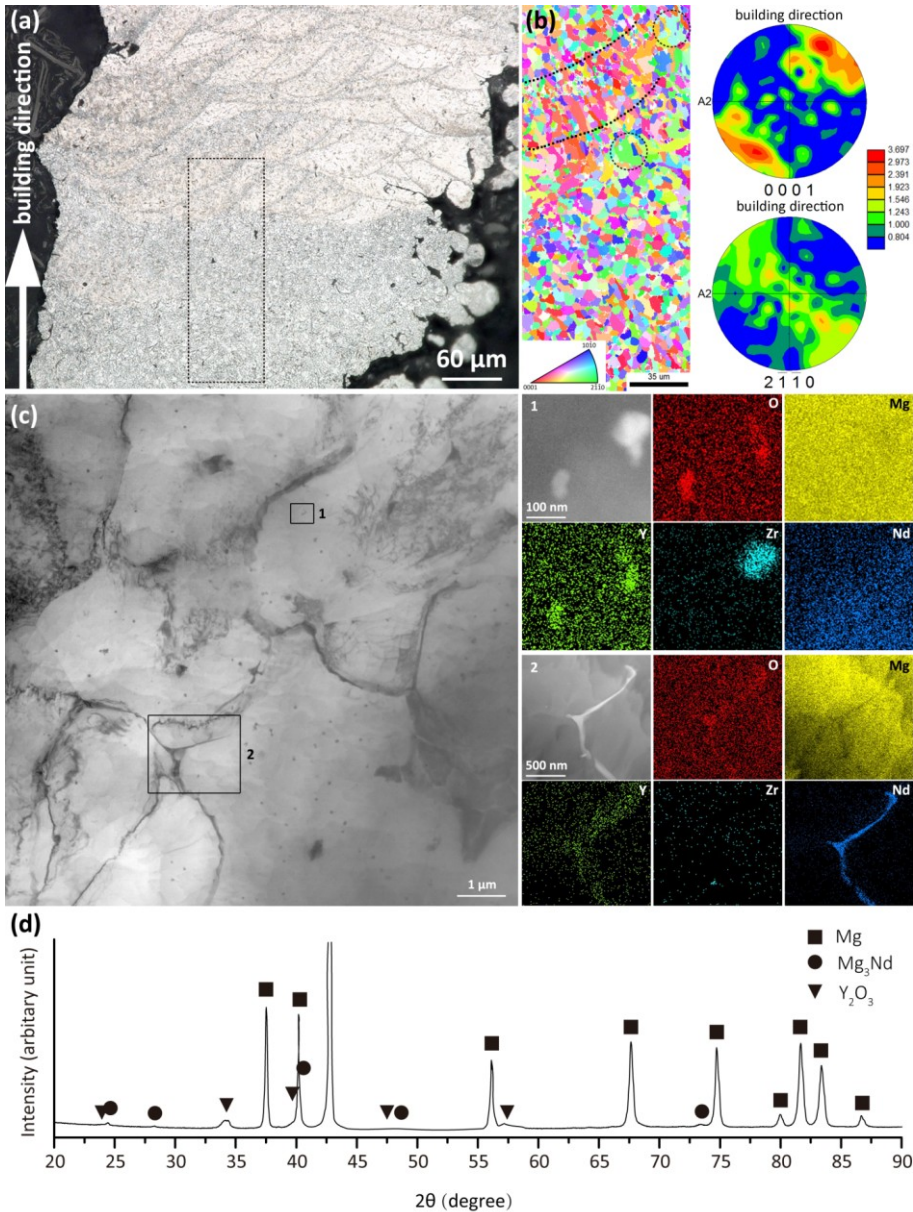
Figure 2 Microstructure, grain orientation and phase constituents of the SLM WE43 Mg alloy scaffolds: (a) optical microscope image showing the traces of melt pools inside struts (dashed box: area for IPF mapping); (b) IPF mapping (dashed lines: melt line, dashed circles: abnormal large grains) and PF showing grain sizes, morphologies and orientations; (c) STEM annular dark field images (grey scale) and EDX analysis showing precipitates and elemental distributions in areas similar to those in boxes 1 and 2; (d) XRD pattern showing the phases present in the as-built Mg alloy scaffolds.
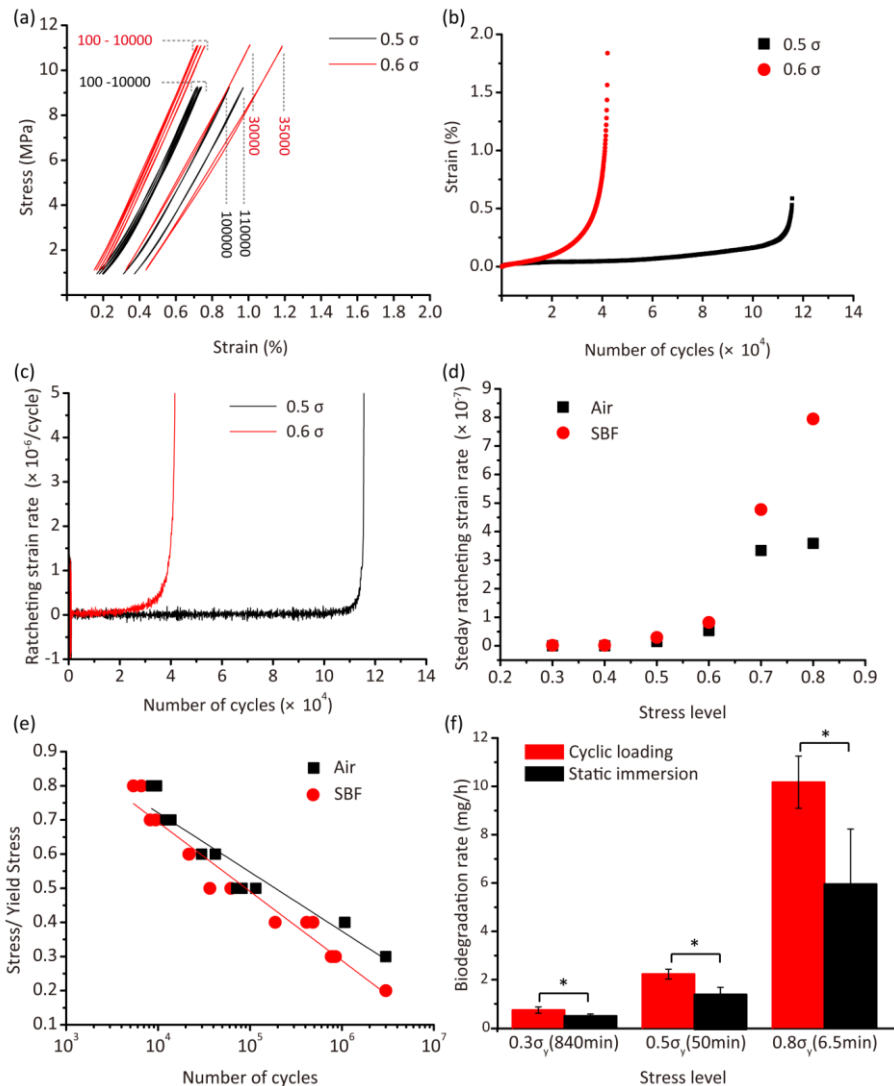
Figure 3 Fatigue behavior of the SLM WE43 Mg alloy scaffolds: (a) hysteresis loops; (b) strain accumulation; (c) ratcheting strain rate per cycle; (d) steady ratcheting strain rate of fatigue specimens in air and in r-SBF; (e) S-N curves; (f) biodegradation rates with and without cyclic loading in r-SBF.

For fatigue and biodegradation fatigue specimens tested at different stress levels, the ratcheting strain rate at the first stage increased with increasing stress level (Fig. 3d). At all the stress levels, the biodegradation fatigue specimens had a higher ratcheting strain rate than the fatigue specimens (Fig. 3d). Furthermore, the fatigue strength of AM magnesium scaffolds decreased from $0.3\sigma_y$ in air to $0.2\sigma_y$ in r-SBF (S-N curves, Fig. 3e).

The biodegradation rate of the specimens tested under cyclic loading significantly increased, as compared to that of the samples subjected to the static immersion tests (Fig. 3f). Moreover, the biodegradation rate increased as the stress level increased (Fig. 3f).

5.3.3. Fatigue failure mode at the macro-scale
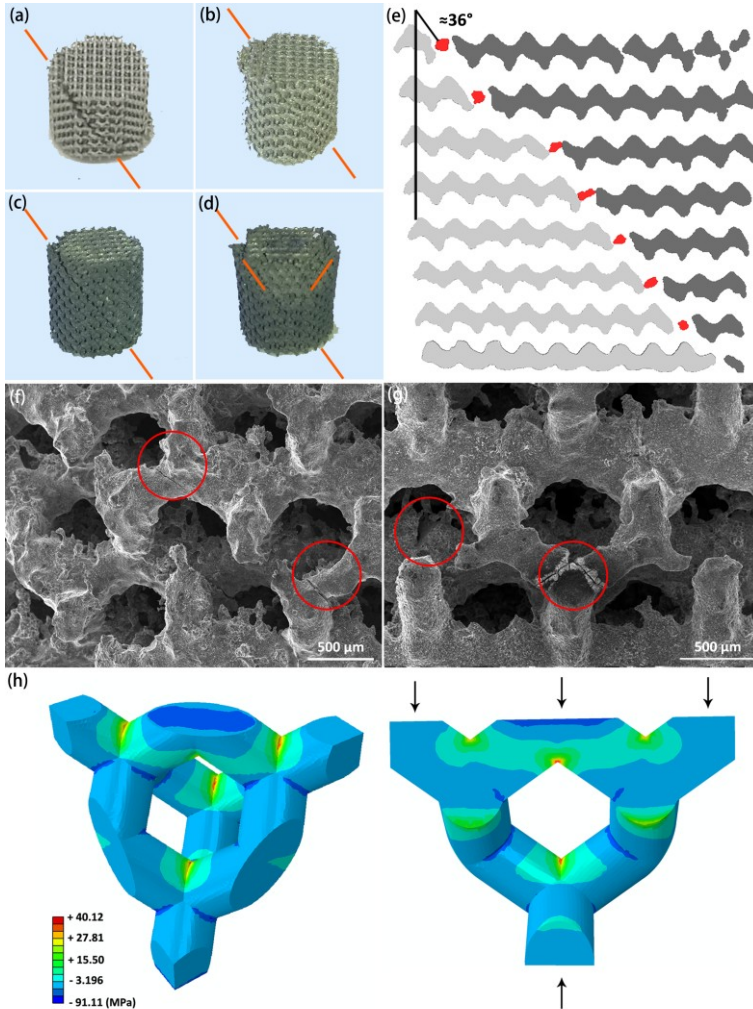
Figure 4 Fatigue failure mode on the macro scale: (a) specimen that failed at $0.8\sigma_y$ in air; (b) specimen that failed at $0.4\sigma_y$ in air; (c) specimen that failed at $0.8\sigma_y$ in r-SBF; (d) specimen that failed at $0.3\sigma_y$ in r-SBF; (e) cross section of fatigue specimen from μCT; (f) fatigue cracks in the specimen tested in air; (g) fatigue cracks in the specimen tested in r-SBF; (h) stress distributions in the diamond lattice structure under compressive load.

There was no visual difference between the specimens tested at $0.8\sigma_y$ (Fig. 4a) and those tested at $0.4\sigma_y$ (Fig. 4b) in air. The fracture plane was orientated at a certain angle ($\approx36^o$) with respect to the loading direction from the top to the bottom of the scaffolds (Fig. 4a,b). The biodegradation fatigue specimens tested at high stress levels exhibited a failure mode that was similar to that of the specimens tested in air (Fig. 4c). At low stress levels, however, small parts occasionally detached from the specimen before its total failure (Fig. 4d). Some parts of the struts (red parts) were found to have been detached but still hang between the separated parts of the specimen (Fig. 4d). Cracks occurred mostly at the strut junctions both for the specimens tested in air and those tested in r-SBF (Fig. 4f, g). Cracking was most likely caused by the tensile stresses that were concentrated at the strut junctions, while compressive stresses were present mostly in the body of the struts (Fig. 4h), as revealed by FE simulations under compressive load.

5.3.4. Fatigue crack distribution

After 350,000 loading cycles, cracks mostly occurred at the strut junctions (Fig. 5c) on the periphery of the scaffolds (Fig. 5a). After 800,000 cycles, cracks on the periphery propagated into larger sizes with several cracks even running through the whole struts (Fig. 5b). However, the crack propagation routes turned from their initial directions and sometimes became separated into two paths (Fig. 5d). In the center of the scaffolds, however, cracks could barely be found, while localized biodegradation was found after 800,000 cycles (Fig. 5b).

5
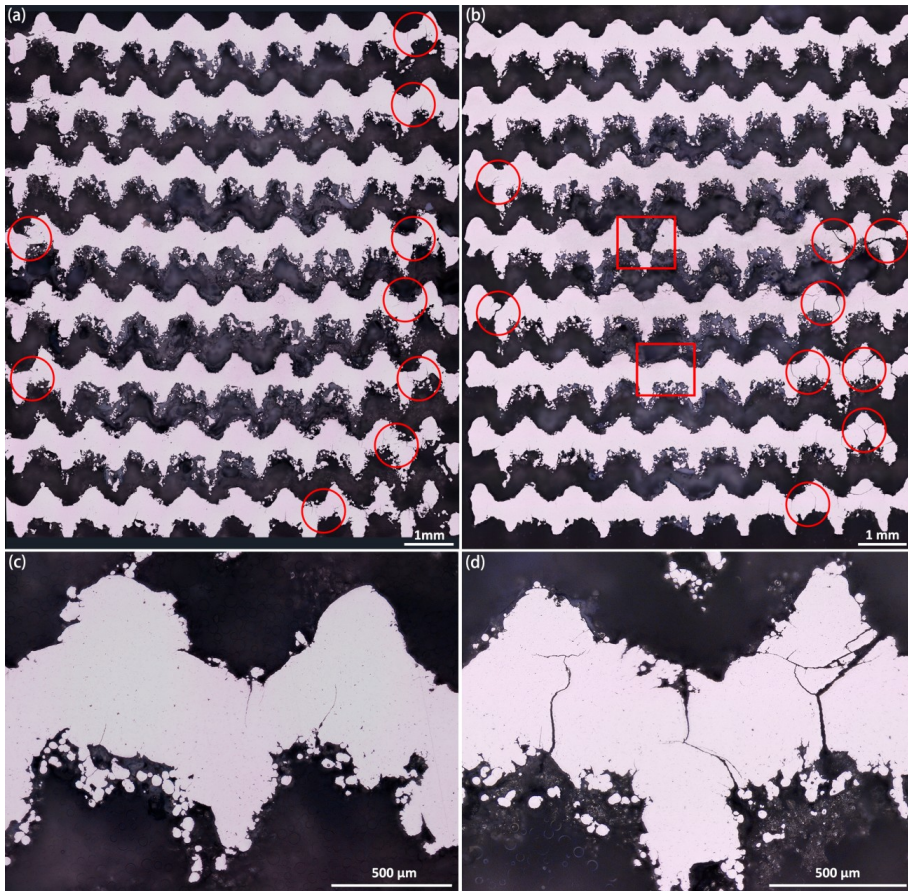
Figure 5 Fatigue crack distributions within the whole scaffold at $0.3\sigma_y$ in r-SBF: (a) (c) biodegradation fatigue specimen after 350,000 cycles (circle: cracks); (b) (d) biodegradation fatigue specimen after 800,000 cycles (circle: cracks, box: localized biodegradation).

5.3.5. Biodegradation pattern

The as-polished scaffolds were measured by means of µCT (threshold 2) to have an average strut size of 417 ± 0.3 µm (design value = 400 µm) and porosity of 65.5% ± 0.07% (design value = 67%). After 350,000 loading cycles, there were more biodegradation products formed in the central region of the specimens (Fig. 6b), as compared to their periphery (Fig. 6a). After 3,000,000 loading cycles, the center of the scaffold was almost full of biodegradation products (Fig. 6d). Some of the struts in the central region of the specimens were also degraded and replaced by biodegradation products (Fig. 6c,d).
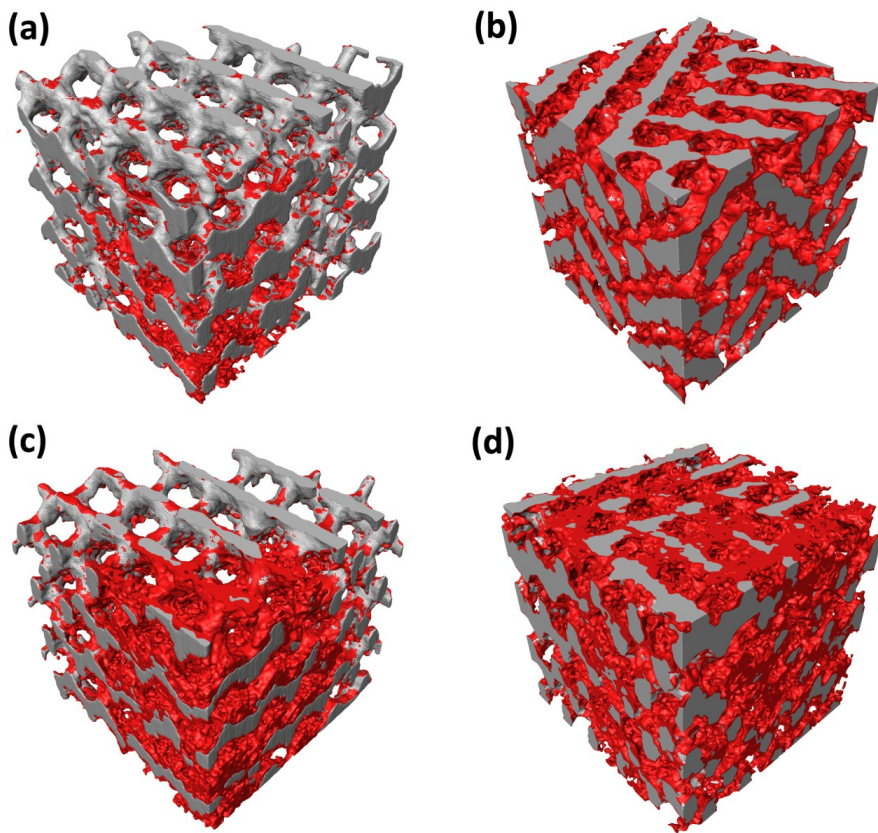
Figure 6 Biodegradation pattern of the scaffold after fatigue test at $0.2\sigma_y$ in r-SBF: (a) biodegradation products formed on the periphery and (b) in the center after 350,000 cycles; (c) biodegradation products formed on the periphery and (d) in the center after 3,000,000 cycles.

5.3.6. Fatigue crack morphology

Cracks initiated from the surface of the struts of the scaffold specimens tested in air and in r-SBF (Fig. 7a-d). For the specimens tested in air, the initiation zone was relatively flat, while the crack propagation zone had a pattern of striations on the fractured surface (Fig. 7a). For the specimens tested in r-SBF, the whole fracture surface was generally smoother than the specimens tested in air and without clear crack morphologies (Fig. 7c,d). Some fracture planes had two facets (Fig. 7b,d), which is consistent with the observations described in subsection 3.4 (Fig. 5d) that the cracks propagated from the top to the bottom (Fig. 7b,d) and then turned to another direction coming out of the figure (Fig. 7b,d). For the specimens tested in r-SBF, the cracks initiated at the

biodegradation pits were observed on the strut surface (Fig. 7d). Moreover, the crack propagation was transgranular (Fig. 7d). There was no preferred orientation of the cracks with respect to the grains (Fig. 7e).
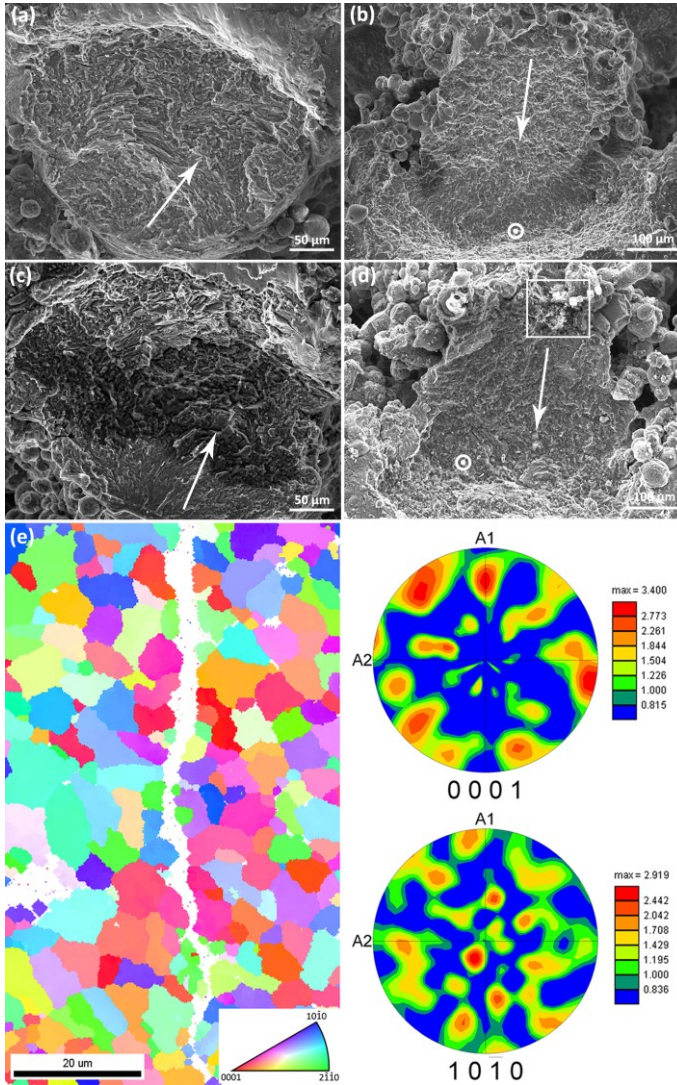
Figure 7 Fatigue crack morphology at $0.4\sigma_y$: (a) (b) specimen that failed in air (arrow: direction of crack propagation, circle with a dot inside: crack propagation route coming out from the figure); (c) (d) specimen that failed in r-SBF; (e) EBSD analysis.

5.4. Discussion

This study reports, for the first time ever, the fatigue behavior of topologically ordered biodegradable porous metallic biomaterials fabricated with AM both in r-SBF and in air. Biodegradation in r-SBF decreased the fatigue strength of the studied biomaterial from $0.3\sigma_y$ in air to $0.2\sigma_y$ in r-SBF. Detailed microstructural, morphological, and computational studies painted a clear picture of the fatigue crack initiation and growth mechanisms and how biodegradation influences them. Fatigue cracks preferably initiated at the strut junctions where finite element simulations showed clear patterns of stress concentration when the porous material was under compressive load. In r-SBF, biodegradation created pits, thereby giving rise to additional sites of crack initiation. Most of the strut cracks initiated on the periphery of the specimens. The biodegradation pattern was location-dependent, with more localized biodegradation occurring at the center of the specimens. This indicates that further improvements of the fatigue life of AM porous Mg scaffolds could be realized through topological optimization and microstructural improvement.

5.4.1. Microstructural features

Because of the high cooling rates experienced during the SLM process, the resulting grains are much finer than those originating from conventional manufacturing processes [33]. The grains on the top of the struts had varied sizes and morphologies, including ultrafine grains, columnar grains and abnormal large grains, while the grains at the bottom were mostly equiaxed. According to the classic theory of alloy solidification, the solid/liquid interface morphology may be planar, cellular, columnar, or equiaxed dendritic, depending on the ratio of thermal gradient at the solid-liquid interface (temperature gradient, G) as well as the kinetics of mass transfer (solidification rate velocity, R) [34]. As a result of the overlapping scan lines in SLM, the material at the bottom of the strut experiences more cycles of re-melting than that on the top, thereby producing a relatively moderate temperature gradient. It is likely that the moderate temperature gradient decreases the G/R ratios in the regions going through equiaxed dendritic solidification. On the top of the struts, however, higher temperature gradients results in equiaxed grains, elongated grains and columnar grains, depending on the local G and R values [35].

It is generally understood that the G/R ratios are lower near the surface of the melt pool as compared to the bottom [36]. The fine equiaxed grains are therefore more frequently observed near the melt pool surface [37]. At the melt pool boundary, thermal gradient is higher than that on the surface and heterogeneous nucleation can be induced when the previous layer is remelted. The grains there can, thus, grow epitaxially with the columnar solidification front (Fig. 2b). The slightly preferred orientation of the

grains may originate from the columnar grains (Fig. 2b). However, epitaxial growth can be restrained by the formation of equiaxed grains near the surface of the melt pool. If the depth of the equiaxed grains is larger than the re-melted depth, equiaxed grains may dominate the whole area [38]. Otherwise, a combination of fine equiaxed grains and columnar grains will be formed, which is probably the reason for the microstructural features observed within the melt pool on the top (Fig. 2b).

There are three types of precipitates (STEM, XRD results) in the SLM WE43 Mg alloy. The Y, O-rich and Nd-rich phases are likely Y_2O_3 and Mg_3Nd, respectively. XRD did not detect a Zr-rich phase, because of its low volume fraction.

These microstructure features can influence both the fatigue and the biodegradation behaviors of the porous material as a whole. Fine grains tend to improve mechanical strength according to the Hall-Petch relationship. In addition, fine grains may inhibit crack initiation and increase the number of barriers to early crack propagation [39]. Furthermore, grain refinement causes the presence of large grain boundaries that may act as effective physical barriers to biodegradation, as compared to coarse grains [40]. Moreover, a large fraction of grain boundaries is likely to accelerate the passivation kinetics and reduce the intensity of micro-galvanic coupling between grains and grain boundaries [11, 41].

Fine precipitates may cause precipitation strengthening in the SLM Mg alloy, thereby improving its fatigue strength. While the effect of precipitates on the short crack growth behavior is relatively small, they may strongly affect the fatigue strength by improving resistance to fatigue crack initiation [42, 43]. Furthermore, the homogeneously distributed precipitates in the grain interior favor the uniform biodegradation of grains [44, 45] and may act as barriers retarding corrosion development [46].

In short, the fine grains and precipitates in the SLM Mg alloy improve the fatigue and corrosion resistance at the same time. Since the grain morphology is not always equiaxed, the ductility and, thus, fatigue resistance may decrease. Inhomogeneous grain sizes may accelerate biodegradation [47]. Optimization of the SLM process parameters and appropriate post-treatments are needed to create homogeneous fine equiaxed grains in order to further enhance the fatigue life of the SLM porous Mg alloy.

5.4.2. Fatigue behavior in air

The fatigue life of a porous structure is determined not only by crack initiation and propagation but also by strain accumulation [21, 22]. In general, the fatigue behavior of the Mg alloy scaffolds at the early stage of fatigue testing was dominated by strain ratcheting (Fig. 3a-c). The strain ratcheting of the whole scaffold could be caused by the cyclic strain ratcheting of the unit cell [48, 49]. As cyclic loading proceeded, the elastic gradient of the porous Mg alloy gradually decreased, meaning that cyclic softening

started to contribute to the fatigue behavior. The cyclic softening could be attributed to crack initiation and propagation [21, 22, 50]. Finally, the elastic gradient of the porous Mg alloy dropped considerably (Fig. 3a) at the tip of the strain accumulation curve before failure (Fig. 3b), probably due to the failure of the struts. Consequently, the number of effective struts that could bear the load became smaller, leading to a decrease in scaffold stiffness. The adjacent struts then had to bear the load transferred from the struts that had already failed. This accelerated the failure of the entire specimen.

5.4.3. Effect of biodegradation on fatigue properties

Ratcheting strain rate is dependent on unit cell ratcheting, crack initiation and propagation. In the specimens tested in air, cracks were observed to initiate at the strut junctions on the surface, where tensile stress concentrations would occur. In the specimens tested in r-SBF, the corrosive medium could erode Mg alloy struts, thereby weakening the entire scaffold. These struts would then have to bear higher compressive stresses than those in air. Higher stresses led to higher ratcheting strain rates of unit cells. Furthermore, the biodegradation pits formed in r-SBF acted as preferred sites for crack initiation. Additionally, biodegradation could accelerate fatigue crack propagation, as crack planes were relatively fresher than the surrounding area and, thus, more sensitive to r-SBF. As a result, biodegradation decreased the fatigue life of the specimens. The influence of biodegradation on the fatigue strength could be evaluated by the reduction ratio of fatigue strength (RRFS) [28], i.e., $(\sigma_{Air} - \sigma_{CF})/\sigma_{Air}$, where σ_{Air} and σ_{CF} are the fatigue strengths in air and in the biodegradation environment, respectively. In this study, RRFS of the AM Mg alloy scaffolds is 0.33. The moderate RRFS value indicates that the effect of biodegradation on the fatigue behavior of the AM porous Mg alloy is less pronounced as compared to that of the solid counterpart (0.3-0.8) [28, 51, 52]. The topological design of the porous structure may modulate the effect of biodegradation on the fatigue behavior of the AM Mg alloy scaffolds.

5.4.4. Effect of cyclic loading on biodegradation

As the mechanical properties of the protective film formed on the Mg alloy during biodegradation are different from those of the Mg alloy itself, the protective film is unstable and may even peel off under tensile loading. The extrusion and intrusion of persistent slip bands during cyclic loading may break the protective film [28]. Mg will then be dissolved in the broken, unprotected area and act as anode, while the areas with the protective film will become the cathode, resulting in the formation of a pit [53]. If the breakdown of the protective film is large enough to allow the corrosive medium to attack the underlying Mg, crevice corrosion may occur [53].

5.4.5. Failure modes at the macro- and micro-scales

Based on all the results presented above, the fatigue failure mechanisms of the porous Mg were proposed and these are illustrated in a schematic diagram (Fig. 8). In air, some micro-scale defects might be present in the struts at the beginning of cyclic loading. The micro-cracks could only propagate in the areas experiencing tension. The non-uniform distributions of compressive and tensile stresses might result in crack deflection (Fig. 8a). This is supported by the observation that cracks deflected once they reached a certain length (Fig. 5d).

By contrast, in r-SBF, two different biodegradation-affected fatigue mechanisms operated from the periphery to the center of the scaffolds (Fig. 8b,c). At the beginning, both the center and periphery of the specimens experienced accelerated biodegradation (subsection 4.4). The struts on the periphery tended to degrade faster than those in the center. Cracks were therefore more likely to initiate on the periphery. In addition, pitting preferred to occur near the cracks. As a combined result, the cracks could propagate through the entire struts (Fig. 8b) and some struts on the periphery of the scaffolds fell off prior to the ultimate failure (Fig. 4d). In the center, however, almost no cracking occurred up to 800,000 loading cycles.

With the biodegradation fatigue tests going on, localized biodegradation occurred primarily in the center of the specimens (Fig. 6d, Fig. 8c). Cyclic loading accelerated the localized biodegradation, because localized biodegradation occurred to a great extent up to 3 million cycles over a time span of 2.3 days. Logically, the pH value of the r-SBF increased more in the center of the scaffolds, as compared to the periphery, because of limited inter-diffusion in the center. It could be inferred that, with a higher pH value in the center, biodegradation products could more easily form and reside there, thereby leading to reduced pore sizes. Decreased pore sizes would in turn result in decreased ion diffusion, which would favor the activation of crevice-like localized biodegradation. The progress of localized biodegradation would be even faster than crack initiation and propagation, which is why only biodegradation products and incomplete struts were observable in the center (Fig. 8c).
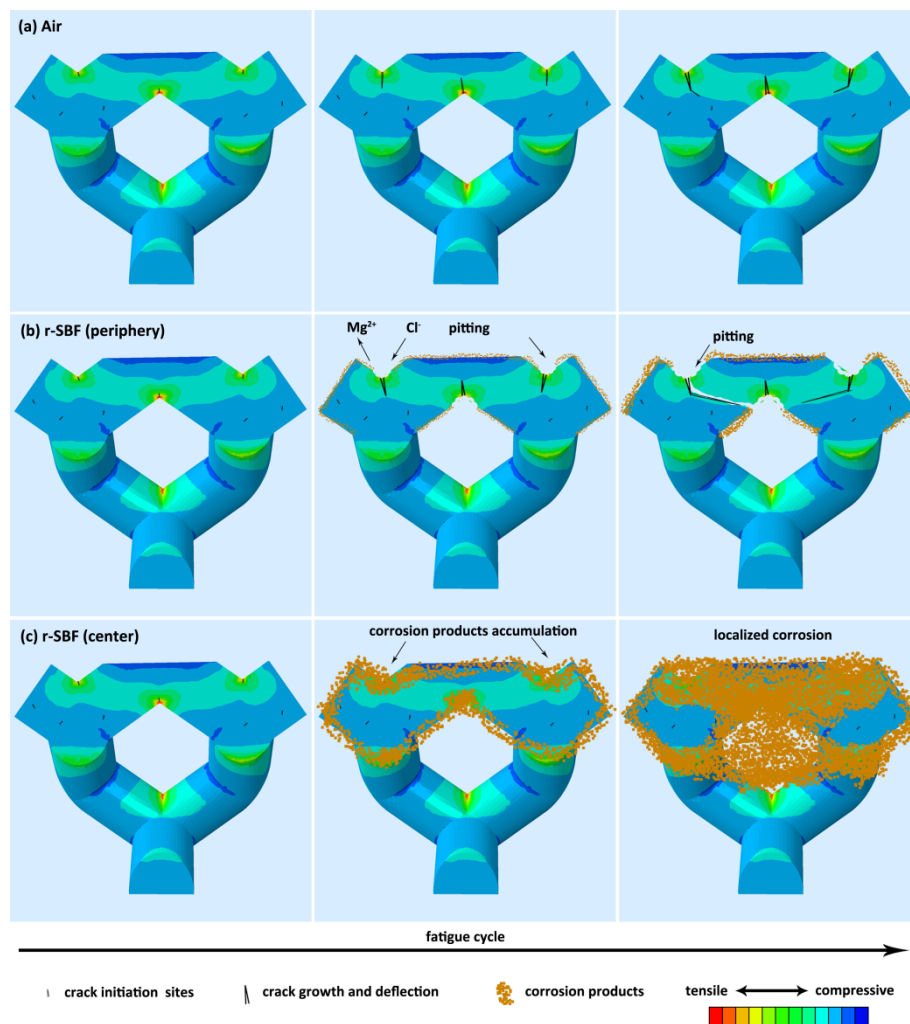
Figure 8 Schematic illustration of the fatigue mechanisms of AM Mg alloy scaffolds: (a) in air; (b) in r-SBF on the periphery; (c) in r-SBF in the center.

Twin boundaries [54], inner pores, and rough surfaces [55, 56] are believed to cause stress concentrations and favor crack initiation. For topologically ordered porous structures, stress distribution follows a certain pattern. The topological design could therefore play an important role in determining the fatigue behavior. IPF mapping of the microstructure around the short cracks showed transgranular fracture. Small grains formed during the SLM process could increase the number of barriers to early crack propagation [39]. However, no deformation twinning was observed even at a high stress level. The HCP crystal structure has only a limited number of slip systems, usually

causing twinning to occur under both tensile and compressive stresses [57]. In this study, however, it did not occur, perhaps because the strain was not large enough or that the loading direction was not appropriate for twinning. Deformation twins may have been suppressed also because of the fine grains and the precipitates [58]. No twinning may actually be beneficial for the fatigue life, as cracks may initiate at the twin boundaries [27].
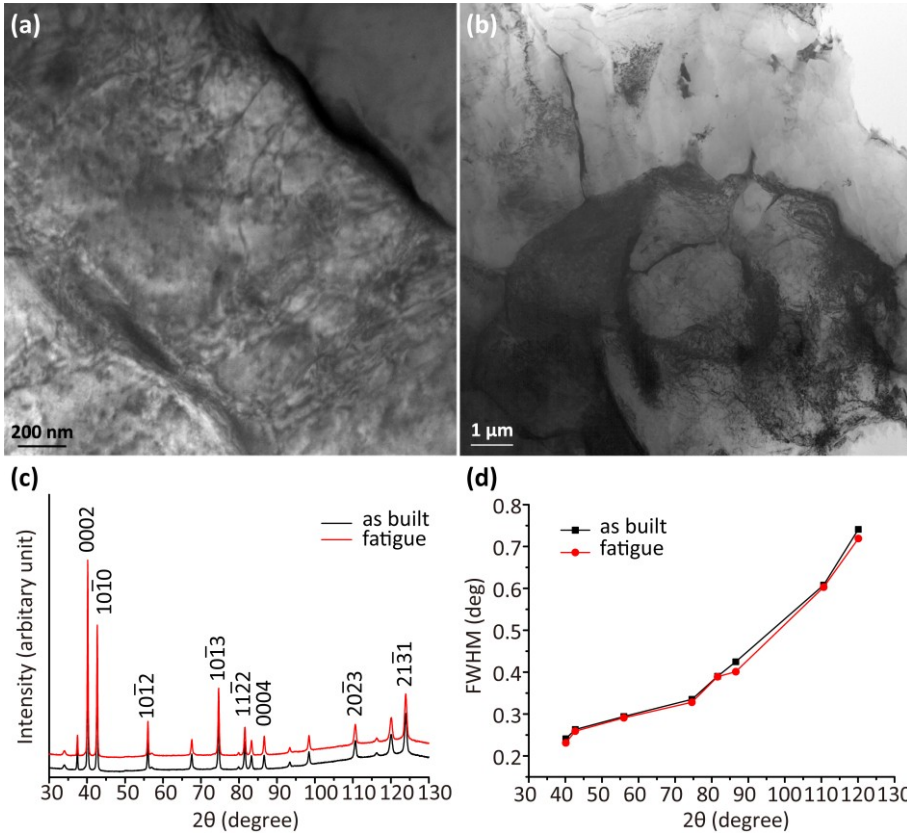
Figure 9 Dislocations in the struts of the Mg alloy scaffolds before and after the fatigue tests in air at $0.4\sigma_y$: (a) as-built sample; (b) fatigue specimen after failure; (c) XRD patterns of the as-built sample and fatigue sample after failure; (d) FWHM of the as-built sample and fatigue specimen after failure.

Dislocation densities were high in both specimens before and after the fatigue tests (Fig. 9a, b) and dislocations became more tangled after the fatigue tests. XRD did not show large differences in peak intensity or full FWHM between the specimens before and after the fatigue test (Fig. 9c, d). In general, the curvature of AM porous materials does not allow for accurate FWHM readings. Moreover, because of the limited ductility

of Mg, local stress concentrations may be released more likely by crack formation and propagation than by plastic deformation. Furthermore, plastic deformation is generally limited to the vicinity of crack tips, further decreasing the chance that the differences in intensity and FWHM can be detected by XRD.

There are two ways to improve the fatigue life of topologically ordered AM porous Mg. The first one is minimizing microstructural defects through the optimization of laser processing parameters, post-manufacturing heat treatments, and surface modification. The other way is optimizing their topological design, as it influences not only the fatigue resistance [19, 20, 23, 59] but also the biodegradation behavior of AM porous biomaterials [7, 60].

5.5. Conclusions

Biodegradation affected the fatigue resistance of the AM WE43 magnesium alloy scaffolds and reduced the fatigue strength from $0.3\sigma_y$ to $0.2\sigma_y$. Moreover, cyclic loading accelerated the biodegradation process in r-SBF. The pattern of biodegradation was location-dependent with the center of the scaffolds experiencing more localized biodegradation than the periphery. At the micro-scale, biodegradation pits acted as additional crack initiation sites. Fatigue crack propagation took place transgranularly. At the macro-scale, cracks preferred to generally initiate at the strut junctions where tensile stress concentration tended to occur. In particular, most of the cracks initiated in the struts positioned on the periphery of the specimens. The results of the present research pointed to the directions for further research to improve the biodegradation fatigue properties of porous magnesium by optimizing both the topological design of the porous structure and the laser-processing parameters that affect its microstructure to a great extent.

References

[1] F. Witte. The history of biodegradable magnesium implants: A review. Acta Biomater. 2010;6:1680-1692.

[2] R. K. Singh Raman, S. Jafari, S. E. Harandi. Corrosion fatigue fracture of magnesium alloys in bioimplant applications: A review. Eng Fract Mech. 2015;137:97-108.

[3] M. P. Staiger, A. M. Pietak, J. Huadmai, G. Dias. Magnesium and its alloys as orthopedic biomaterials: A review. Biomaterials. 2006;27:1728-1734.

[4] Y. Song, D. Shan, R. Chen, F. Zhang, E.-H. Han. Biodegradable behaviors of AZ31 magnesium alloy in simulated body fluid. Mater Sci Eng, C. 2009;29:1039-1045.

[5] Y. Li, H. Jahr, K. Lietaert, P. Pavanram, A. Yilmaz, L. I. Fockaert, M. A. Leeflang, B. Pouran, Y. Gonzalez-Garcia, H. Weinans, J. M. C. Mol, J. Zhou, A. A. Zadpoor. Additively manufactured biodegradable porous iron. Acta Biomater. 2018;77:380-393.

[6] P. Wen, Y. Qin, Y. Chen, M. Voshage, L. Jauer, R. Poprawe, J. Henrich Schleifenbaum. Laser additive manufacturing of Zn porous scaffolds: shielding gas flow, surface quality and densification. J Mater Sci Technol. 2018.

[7] Y. Li, J. Zhou, P. Pavanram, M. A. Leeflang, L. I. Fockaert, B. Pouran, N. Tümer, K. U. Schröder, J. M. C. Mol, H. Weinans, H. Jahr, A. A. Zadpoor. Additively manufactured biodegradable porous magnesium. Acta Biomater. 2018;67:378-392.

[8] B. Zberg, P. J. Uggowitzer, J. F. Loffler. MgZnCa glasses without clinically observable hydrogen evolution for biodegradable implants. Nat Mater. 2009;8:887-891.

[9] S. Shadanbaz, G. J. Dias. Calcium phosphate coatings on magnesium alloys for biomedical applications: A review. Acta Biomater. 2012;8:20-30.

[10] X. Li, X. Liu, S. Wu, K. W. K. Yeung, Y. Zheng, P. K. Chu. Design of magnesium alloys with controllable degradation for biomedical implants: From bulk to surface. Acta Biomater. 2016;45:2-30.

[11] M. Alvarez-Lopez, M. D. Pereda, J. A. del Valle, M. Fernandez-Lorenzo, M. C. Garcia-Alonso, O. A. Ruano, M. L. Escudero. Corrosion behaviour of AZ31 magnesium alloy with different grain sizes in simulated biological fluids. Acta Biomater. 2010;6:1763-1771.

[12] L. Dexue, D. Yutian, G. Tingbiao, Q. Xiaoqiong, G. Chenggong, Y. Shankun, L. Shengling. Influence of fine-grain and solid-solution strengthening on mechanical properties and in vitro degradation of WE43 alloy. Biomedical Materials. 2014;9:015014.

[13] X. Gu, Y. Zheng, Y. Cheng, S. Zhong, T. Xi. In vitro corrosion and biocompatibility of binary magnesium alloys. Biomaterials. 2009;30:484-498.

[14] X. Gu, Y. Zheng, S. Zhong, T. Xi, J. Wang, W. Wang. Corrosion of, and cellular responses to Mg-Zn-Ca bulk metallic glasses. Biomaterials. 2010;31:1093-1103.

[15] H.-J. Yu, J.-Q. Wang, X.-T. Shi, D. V. Louzguine-Luzgin, H.-K. Wu, J. H. Perepezko. Ductile Biodegradable Mg-Based Metallic Glasses with Excellent Biocompatibility. Adv Funct Mater. 2013;23:4793-4800.

[16] Y. F. Zheng, X. N. Gu, F. Witte. Biodegradable metals. Mater Sci Eng R Rep. 2014;77:1-34.

[17] D. Zhao, F. Witte, F. Lu, J. Wang, J. Li, L. Qin. Current status on clinical applications of magnesium-based orthopaedic implants: A review from clinical translational perspective. Biomaterials. 2017;112:287-302.

[18] R. Wauthle, S. M. Ahmadi, S. Amin Yavari, M. Mulier, A. A. Zadpoor, H. Weinans, J. Van Humbeeck, J.-P. Kruth, J. Schrooten. Revival of pure titanium for dynamically loaded porous implants using additive manufacturing. Mater Sci Eng, C. 2015;54:94-100.

[19] S. Amin Yavari, S. M. Ahmadi, R. Wauthle, B. Pouran, J. Schrooten, H. Weinans, A. A. Zadpoor. Relationship between unit cell type and porosity and the fatigue

5

behavior of selective laser melted meta-biomaterials. J Mech Behav Biomed Mater. 2015;43:91-100.

[20] F. Bobbert, K. Lietaert, A. Eftekhari, B. Pouran, S. Ahmadi, H. Weinans, A. Zadpoor. Additively manufactured metallic porous biomaterials based on minimal surfaces: A unique combination of topological, mechanical, and mass transport properties. Acta Biomater. 2017;53:572-584.

[21] S. J. Li, L. E. Murr, X. Y. Cheng, Z. B. Zhang, Y. L. Hao, R. Yang, F. Medina, R. B. Wicker. Compression fatigue behavior of Ti–6Al–4V mesh arrays fabricated by electron beam melting. Acta Mater. 2012;60:793-802.

[22] Y. J. Liu, H. L. Wang, S. J. Li, S. G. Wang, W. J. Wang, W. T. Hou, Y. L. Hao, R. Yang, L. C. Zhang. Compressive and fatigue behavior of beta-type titanium porous structures fabricated by electron beam melting. Acta Mater. 2017;126:58-66.

[23] S. M. Ahmadi, R. Hedayati, Y. Li, K. Lietaert, N. Tümer, A. Fatemi, C. D. Rans, B. Pouran, H. Weinans, A. A. Zadpoor. Fatigue performance of additively manufactured meta-biomaterials: The effects of topology and material type. Acta Biomater. 2018;65:292-304.

[24] B. V. Hooreweder, K. Lietaert, B. Neirinck, N. Lippiatt, M. Wevers. CoCr F75 scaffolds produced by additive manufacturing: Influence of chemical etching on powder removal and mechanical performance. J Mech Behav Biomed Mater. 2017;70:60-67.

[25] R. Wauthle, J. van der Stok, S. Amin Yavari, J. Van Humbeeck, J.-P. Kruth, A. A. Zadpoor, H. Weinans, M. Mulier, J. Schrooten. Additively manufactured porous tantalum implants. Acta Biomater. 2015;14:217-225.

[26] D. Bian, W. Zhou, Y. Liu, N. Li, Y. Zheng, Z. Sun. Fatigue behaviors of HP-Mg, Mg–Ca and Mg–Zn–Ca biodegradable metals in air and simulated body fluid. Acta Biomater. 2016;41:351-360.

[27] S. Jafari, R. K. S. Raman, C. H. J. Davies, J. Hofstetter, P. J. Uggowitzer, J. F. Loffler. Stress corrosion cracking and corrosion fatigue characterisation of MgZn1Ca0.3 (ZX10) in a simulated physiological environment. J Mech Behav Biomed Mater. 2017;65:634-643.

[28] X. N. Gu, W. R. Zhou, Y. F. Zheng, Y. Cheng, S. C. Wei, S. P. Zhong, T. F. Xi, L. J. Chen. Corrosion fatigue behaviors of two biomedical Mg alloys – AZ91D and WE43 – In simulated body fluid. Acta Biomater. 2010;6:4605-4613.

[29] H. Windhagen, K. Radtke, A. Weizbauer, J. Diekmann, Y. Noll, U. Kreimeyer, R. Schavan, C. Stukenborg-Colsman, H. Waizy. Biodegradable magnesium-based screw clinically equivalent to titanium screw in hallux valgus surgery: short term results of the first prospective, randomized, controlled clinical pilot study. BioMedical Engineering OnLine. 2013;12:62.

[30] A. Oyane, H.-M. Kim, T. Furuya, T. Kokubo, T. Miyazaki, T. Nakamura. Preparation and assessment of revised simulated body fluids. J Biomed Mater Res A. 2003;65A:188-195.

5

[31] Y. Duan, J. A. Griggs. Effect of loading frequency on cyclic fatigue lifetime of a standard-diameter implant with an internal abutment connection. Dent Mater. 2018.

[32] N. A. Zumdick, B. D. Zander. Microstructure and properties of WE43 manufactured via SLM. Symposium on Biodegradable Metals for biomedical Applications. 14 May 2016 - 17 May 2016, Montreal (Canada)2016.

[33] C. C. Ng, M. M. Savalani, M. L. Lau, H. C. Man. Microstructure and mechanical properties of selective laser melted magnesium. Appl Surf Sci. 2011;257:7447-7454.

[34] J. Dupont. Fundamentals of Weld Solidification. ASM Handbook.6:700.

[35] V. Manakari, G. Parande, M. Gupta. Selective Laser Melting of Magnesium and Magnesium Alloy Powders: A Review. Metals. 2016;7:2.

[36] F. Yan, W. Xiong, E. Faierson. Grain Structure Control of Additively Manufactured Metallic Materials. Materials. 2017;10:1260.

[37] Y. Zhu, D. Liu, X. Tian, H. Tang, H. Wang. Characterization of microstructure and mechanical properties of laser melting deposited Ti–6.5Al–3.5Mo–1.5Zr–0.3Si titanium alloy. Mater Des. 2014;56:445-453.

[38] T. Wang, Y. Y. Zhu, S. Q. Zhang, H. B. Tang, H. M. Wang. Grain morphology evolution behavior of titanium alloy components during laser melting deposition additive manufacturing. J Alloys Compd. 2015;632:505-513.

[39] Z. Zúberová, L. Kunz, T. T. Lamark, Y. Estrin, M. Janeček. Fatigue and Tensile Behavior of Cast, Hot-Rolled, and Severely Plastically Deformed AZ31 Magnesium Alloy. Metall Mater Trans A. 2007;38:1934-1940.

[40] N. N. Aung, W. Zhou. Effect of grain size and twins on corrosion behaviour of AZ31B magnesium alloy. Corros Sci. 2010;52:589-594.

[41] G. R. Argade, S. K. Panigrahi, R. S. Mishra. Effects of grain size on the corrosion resistance of wrought magnesium alloys containing neodymium. Corros Sci. 2012;58:145-151.

[42] J. F. Adams, J. E. Allison, J. W. Jones. The effects of heat treatment on very high cycle fatigue behavior in hot-rolled WE43 magnesium. Int J Fatigue. 2016;93:372-386.

[43] Y. Uematsu, K. Tokaji, M. Matsumoto. Effect of aging treatment on fatigue behaviour in extruded AZ61 and AZ80 magnesium alloys. Mater Sci Eng, A. 2009;517:138-145.

[44] A. Atrens, G.-L. Song, M. Liu, Z. Shi, F. Cao, M. S. Dargusch. Review of recent developments in the field of magnesium corrosion. Adv Eng Mater. 2015;17:400-453.

[45] G. v. Baril, C. Blanc, N. Pébère. AC impedance spectroscopy in characterizing time-dependent corrosion of AZ91 and AM50 magnesium alloys characterization with respect to their microstructures. J Electrochem Soc. 2001;148:B489.

[46] G. Song, A. Atrens. Understanding Magnesium Corrosion—A Framework for Improved Alloy Performance. Adv Eng Mater. 2003;5:837-858.

[47] S. Gollapudi. Grain size distribution effects on the corrosion behaviour of materials. Corros Sci. 2012;62:90-94.

5

[48] A. M. Harte, N. A. Fleck, M. F. Ashby. Fatigue failure of an open cell and a closed cell aluminium alloy foam. Acta Mater. 1999;47:2511-2524.

[49] McCullough, Fleck. The stress–life fatigue behaviour of aluminium alloy foams. Fatigue Fract Eng Mater Struct. 2000;23:199-208.

[50] J. Zhou, W. O. Soboyejo. Compression–compression fatigue of open cell aluminum foams: macro-/micro- mechanisms and the effects of heat treatment. Mater Sci Eng, A. 2004;369:23-35.

[51] M. S. Bhuiyan, Y. Mutoh, T. Murai, S. Iwakami. Corrosion fatigue behavior of extruded magnesium alloy AZ80-T5 in a 5% NaCl environment. Eng Fract Mech. 2010;77:1567-1576.

[52] S. Jafari, R. K. Singh Raman, C. H. J. Davies. Corrosion fatigue of a magnesium alloy in modified simulated body fluid. Eng Fract Mech. 2015;137:2-11.

[53] S. Z. B., M. Y., M. Y. Effects of humidity and temperature on the fatigue behaviour of an extruded AZ61 magnesium alloy. Fatigue Fract Eng Mater Struct. 2005;28:373-379.

[54] S. M. Yin, F. Yang, X. M. Yang, S. D. Wu, S. X. Li, G. Y. Li. The role of twinning–detwinning on fatigue fracture morphology of Mg–3%Al–1%Zn alloy. Mater Sci Eng, A. 2008;494:397-400.

[55] M. F. Horstemeyer, N. Yang, K. Gall, D. L. McDowell, J. Fan, P. M. Gullett. High cycle fatigue of a die cast AZ91E-T4 magnesium alloy. Acta Mater. 2004;52:1327-1336.

[56] P. Zhang, J. Lindemann. Influence of shot peening on high cycle fatigue properties of the high-strength wrought magnesium alloy AZ80. Scripta Mater. 2005;52:485-490.

[57] S. Hyuk Park, S.-G. Hong, B. Ho Lee, W. Bang, C. Soo Lee. Low-cycle fatigue characteristics of rolled Mg–3Al–1Zn alloy. Int J Fatigue. 2010;32:1835-1842.

[58] F. A. Mirza, D. L. Chen, D. J. Li, X. Q. Zeng. Low cycle fatigue of a rare-earth containing extruded magnesium alloy. Mater Sci Eng, C. 2013;575:65-73.

[59] S. Amin Yavari, R. Wauthle, J. van der Stok, A. C. Riemslag, M. Janssen, M. Mulier, J. P. Kruth, J. Schrooten, H. Weinans, A. A. Zadpoor. Fatigue behavior of porous biomaterials manufactured using selective laser melting. Mater Sci Eng, C. 2013;33:4849-4858.

[60] Y. Li, H. Jahr, K. Lietaert, P. Pavanram, A. Yilmaz, L. I. Fockaert, M. A. Leeflang, B. Pouran, Y. Gonzalez-Garcia, H. Weinans, J. M. C. Mol, J. Zhou, A. A. Zadpoor. Additively manufactured biodegradable porous iron. Acta Biomater. 2018.

5

5

6

Biodegradation-affected fatigue behavior of additively manufactured porous iron

The corrosion fatigue behavior of additively manufactured topologically ordered porous iron based on diamond unit cells was studied for the first time to understand its response to cyclic loading in a simulated physiological environment. The material exhibited high fatigue resistance with fatigue strengths being 70% and 65% of yield stress in air and revised simulated body fluid, respectively, mainly due to its slow degradation and excellent ductility. However, cyclic loading significantly increased biodegradation rate, especially at higher stress levels. The observed extraordinary fatigue strength, slow biodegradation and high ductility underline the importance of porous iron as a promising bone-substituting material.[1]

6.1. Introduction

The first reports of applying selective laser melting (SLM) to fabricate topologically ordered biodegradable porous metals, such as magnesium and iron [1, 2], have just appeared in the literature. The quasi-static mechanical properties of those topologically ordered AM porous metals have been found to remain in the range of the values reported for trabecular bone even after 4 weeks of *in vitro* biodegradation [1, 2]. Quasi-static mechanical properties alone are, however, not enough for understanding how biomaterials function under physiological load. Bone-substituting biomaterials including AM biodegradable porous metals are expected to undergo millions of cycles of mechanical loading [3, 4], and may therefore experience fatigue fracture, even when the maximum stress experienced by the material is less than its yield stress. In the case of biodegradable metals, the complexity of understanding the dynamic nature of the fatigue behavior is compounded by the fact that biodegradation and fatigue mutually affect each other. Moreover, both the topological design of the porous structure and material type affect the fatigue behavior of AM porous biomaterials, even for bio-inert metals [5]. Taken together, the isolated and coupled effects of all above-mentioned factors make for a complex multi-factorial biodegradation-, topology- and material-dependent fatigue phenomenon that requires a detailed systematic study to unravel. The research on the fatigue behavior of AM biodegradable porous metals has just begun with one single study on AM porous magnesium (the WE43 magnesium alloy) [6]. No comparable studies exist for AM porous iron or for any other type of biodegradable porous metals.

In this paper, we present the results of the first study ever on the fatigue behavior of AM porous iron. As the major mode of loading in orthopedic porous implant is compression [7], the compression-compression loading mode was chosen for this work. In particular, we carefully designed our study so as to understand some of the above-mentioned aspects regarding the fatigue behavior of AM biodegradable porous metals and to distinguish between the roles of different factors. The topological design was, for example, kept constant (*i.e.*, being similar to the previous study on magnesium) to decouple the effect of material type on corrosion-fatigue behavior from that of topological design. We performed all our experiments both in air and in revised simulated body fluid (r-SBF) using a novel test setup that complemented our fatigue test machine and ensured that cyclic loading on the specimen could occur in circulated r-SBF at 37 $^{\circ}$C [8]. This parallel design of the study allowed us to investigate the mutual effects of biodegradation and cyclic loading on each other.

6.2. Material and methods

6.2.1. Scaffold manufacturing and post processing

Iron scaffolds with diamond unit cells (a strut thickness of 200 µm and a unit cell size of 1 mm) were designed by using Magics (Materialise, Belgium) to have a height of 10.5 mm, a diameter of 10 mm and a relative density of 20% (Fig. 1a and b). A ProX DMP 320 machine (3D Systems, Belgium) with the DMP Suite software (3D Systems, Belgium) was used for direct metal printing of the samples using the selective laser melting (SLM) technique. We used a nitrogen gas atomized Fe powder (Material Technology Innovations Co., Ltd., China) (Fig. 1c) with the following characteristics: purity: 99.88%; particle sizes: D_{10}=32 µm, D_{50}=48 µm, and D_{90}=71 µm; morphology: spherical; apparent density: 4.09 g/cm^3; tap density: 4.88 g/cm^3; angle of repose: 157 °; carbon content: 0.0044%. The powder was deposited in layers of 30 µm thick. Only contours but no hatch vectors were used (0.33 W/mm energy density) during the printing process. The samples were built on a steel base plate and later on removed by means of electrical discharge machining (EDM). Powder particles entrapped in pores were removed through ultrasonic cleaning in 96 % ethanol for 20 min. Then, the samples were chemically cleaned in 50% HCl for 1 min to remove residuals from EDM and loose powder particles, followed by 5 min ultrasonic cleaning in 96% ethanol to wash out HCl. The bulk density of AM porous iron and the porosity within the struts were determined using the Archimedes' method.

6.2.2. Characterization of microstructure

Electron back-scattered diffraction (EBSD) data were collected using an HKL Nordlys II detector at a step size of 200 nm attached to a JEOL JSM-6500F field emission gun scanning electron microscope (FEGSEM). Image quality (IQ) and inverse pole figure (IPF) maps were reconstructed by using the commercial software TSL OIM® Analysis. Samples for EBSD analysis were prepared by grinding, mechanical polishing up to 1 µm diamond abrasives in liquid suspension, and further mechanical polishing using 0.04 µm silica oxide.

6.2.3. Fatigue tests in air and in r-SBF

Compression-compression fatigue tests were performed at a minimum to maximum stress ratio of 0.1, a frequency of 15 Hz, and six different stress levels (maximum stress): $0.65\sigma_y$, $0.7\sigma_y$, $0.75\sigma_y$, $0.8\sigma_y$, $0.85\sigma_y$ and $0.9\sigma_y$, where σ_y is the yield stress (=28 MPa [2]) using an electro-dynamic mechanical testing machine (Instron E10000 ElectroPlus with

a 10 kN load cell). The tests were stopped when specimens failed, unless failure did not occur until 3×10^6 loading cycles (which lasted 2.3 days). The stress applied without causing failure after 3×10^6 loading cycles is defined as fatigue strength. Corrosion fatigue tests were performed by using the same machine equipped with a double-wall specimen chamber designed and manufactured in-house (Fig. 1c). Corundum was used as the material of the compression head. The specimen was immersed in 300 ml circulated r-SBF [8] inside the chamber throughout the test. The temperature of r-SBF was held at 37 °C and the flow rate was controlled at 1.2 ml/min [9] with a peristaltic pump. Purging of CO_2 at 5% was maintained during the test. The ratcheting strain rate [10] per cycle was calculated as $d[(\varepsilon_{max} + \varepsilon_{min})/2]/dN$, where ε_{max} and ε_{min} are the maximum and minimum axial strains in a cycle, respectively, and N is the number of cycles. The influence of biodegradation on the fatigue strength was evaluated by the reduction ratio of fatigue strength (RRFS) [4], *i.e.*, $(\sigma_{Air} - \sigma_{SBF})/\sigma_{Air}$, where σ_{Air} and σ_{SBF} are the fatigue strength in air and in r-SBF, respectively. Iron (ρ_{Fe}), calcium and phosphate ion concentration in the r-SBF solution was determined using an inductively coupled plasma optical emission spectroscope (ICP-OES, iCAP 6500 Duo, Thermo Scientific). Then, the biodegradation rate was calculated based on the iron ion concentration data: $v_{br}=(\rho_{Fe}\times V)/t$, where V is the volume of the r-SBF and t the immersion time. All the tests were performed in triplicates for each stress level.
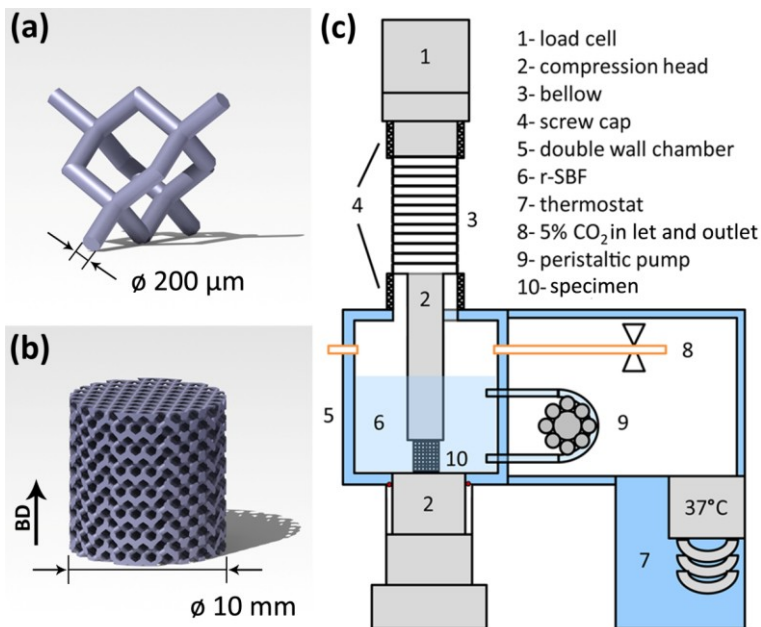

Figure 1. Iron scaffold design and corrosion fatigue test setup: (a) diamond unit cell; (b) scaffold; (c) corrosion fatigue test setup. BD: building direction.

6.2.4. Static immersion tests in r-SBF

Static immersion tests were carried out in 300 ml r-SBF at 37 °C without any mechanical loading for comparison purposes. The immersion time was in accordance with that of the corrosion fatigue tests at three stress levels: $0.65\sigma_y$ (55.5 h), $0.75\sigma_y$ (5.5 h), and $0.9\sigma_y$ (1 h). Ion concentration and biodegradation rate was determined similarly as mentioned above in section 2.3. All the tests were performed in triplicates for each immersion time.

6.2.5. Characterization of corrosion products

The morphologies and compositions of the corrosion products on the surface of the specimens after the biodegradation tests with and without cyclic loading were analyzed with a scanning electron microscope (SEM) equipped with energy-dispersive X-ray spectroscopy (EDS) (SEM, JSM-IT100, JEOL). An accelerating voltage of 15 kV was used for the EDS analyses.

6.2.6. Characterization of crack morphology and distribution

The morphologies of the cracks appearing after the corrosion fatigue tests were examined using a SEM (JSM-IT100, JEOL). EBSD analysis was performed to reveal the grain orientations around the cracks. The first nearest-neighbor Kernel Average Misorientation (KAM) maps, calculated from EBSD data, was chosen to represent the local misorientations.

After the fatigue tests, the specimens were mounted in resin and polished up to 1 μm diamond abrasives in liquid suspension. A Keyence VHX5000 digital microscope was used to observe fatigue crack distribution on the cross section of the entire specimen.

6.2.7. Finite element (FE) modeling

Simulations with the finite element method (FEM) were conducted using the commercial software package Abaqus (Dassault System Simulia Corp, France) to study the stress distribution in the fatigue specimens. Single diamond unit cell was developed as the representative volume elements (RVE) of the porous structure. The RVE models were subjected to a compressive load of $0.65\sigma_y$. The contours of the first principal stress of the RVE models were extracted to study stress concentrations.

6.2.8. Characterization of strain accumulation

X-ray diffraction (XRD) pattern was generated by using an X-ray diffractometer (Bruker D8 Advance diffractometer in Bragg-Brentano geometry). The diffractometer was equipped with a graphite monochromator and Vantec position sensitive detector and operated at 45 kV and 35 mA with a step size of 0.0214° and a dwell time of 3 s per step using Co Ka radiation. The top surface of the scaffold was aligned with the goniometer axis. The struts on the top were aligned with the direction of the X-ray beam. The full width at half maximum (FWHM) was determined using the "Create Area" function of the Bruker-Eva software. The XRD analysis was performed in triplicates.

6.2.9. Statistical analysis

Differences in biodegradation rate between the groups with and without cyclic loading were analyzed using one-way analysis of variance (ANOVA), followed by *post-hoc* Turkey test. A *p*-value below 0.05 was assumed to indicate a statistically significant difference ($p < 0.05$, *; *n.s.* = not significant).

6.3. Results

6.3.1. Porosity and microstructural features of the AM iron scaffolds

The bulk porosity of the AM iron scaffolds was 73.2 ± 0.1%. Th porosity within the struts was determined to be 0.8% ± 0.1%. Melt lines were not visible on the cross section of SLM iron scaffold struts (Fig. 2a). Only several elongated grains along the length of the strut were observable. The microstructures of the SLM iron scaffolds were featured by a combination of mostly equiaxed fine grains, several irregular large grains and ultra-fine grains. IPF mapping and pole figures (PF) showed that the grains had no preferred growth orientation (Fig. 2b and c).
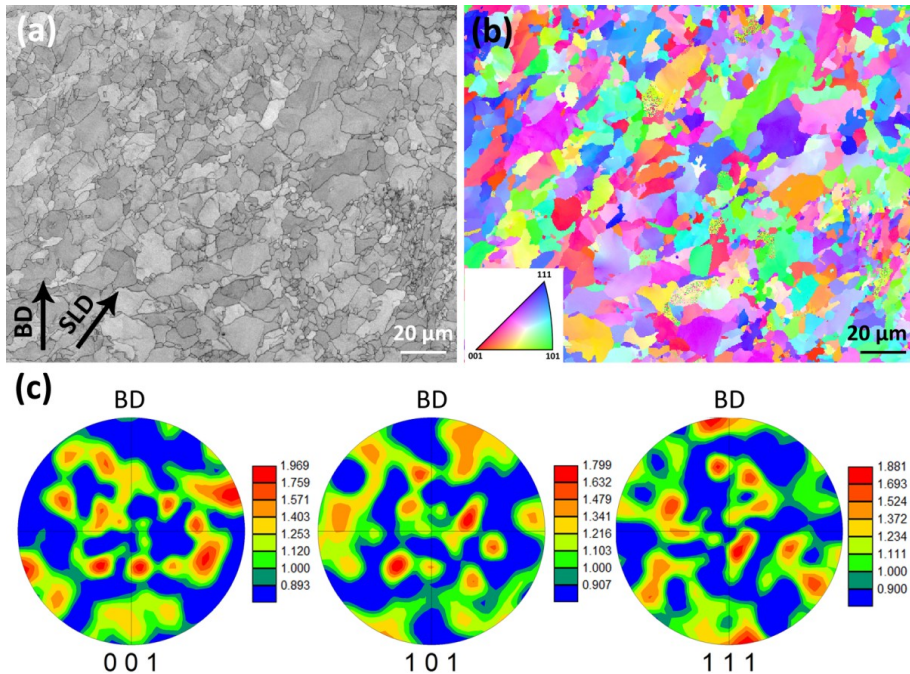
Figure 2. EBSD characterization of AM iron scaffold struts on the longitudinal section: (a) IQ map; (b) IPF map; (c) PF. BD: building direction; SLD: strut length direction.

6

6.3.2. Degradation-affected fatigue behavior

Strain ratcheting rate increased with increasing stress level both in air and in r-SBF (Fig. 3a). However, at the same stress level, the strain ratcheting rates of fatigue specimens in air and in r-SBF overlapped with each other. The S-N curves showed that the fatigue strength of the AM iron scaffolds decreases from $0.7\sigma_y$ in air to $0.65\sigma_y$ in r-SBF (Fig. 3b). Thus, the RRFS of the AM iron scaffolds was 0.08.

At the macro-scale, there were no visual differences between the fatigue specimens tested in air and in r-SBF (Fig. 3c). At 2% strain before failure, neither the specimens tested in air nor the ones tested in r-SBF showed any obvious visual changes (from outside). Even at 5% strain, no fracture plane was observable under either condition (Fig. 3c). Instead, the structure of the iron scaffolds slipped slightly sideways (Fig. 3c).

6.3.3. Fatigue-affected degradation behavior

The biodegradation rates of all specimens tested under cyclic loading increased as compared to those of the specimens subjected to static immersion tests (Fig. 3d). The increase was more significant at a higher stress level (compare the corrosion rates at *e.g.*,

$0.75\sigma_y$ and $0.9\sigma_y$). Moreover, the biodegradation rate increased with rising stress level (Fig. 3d).
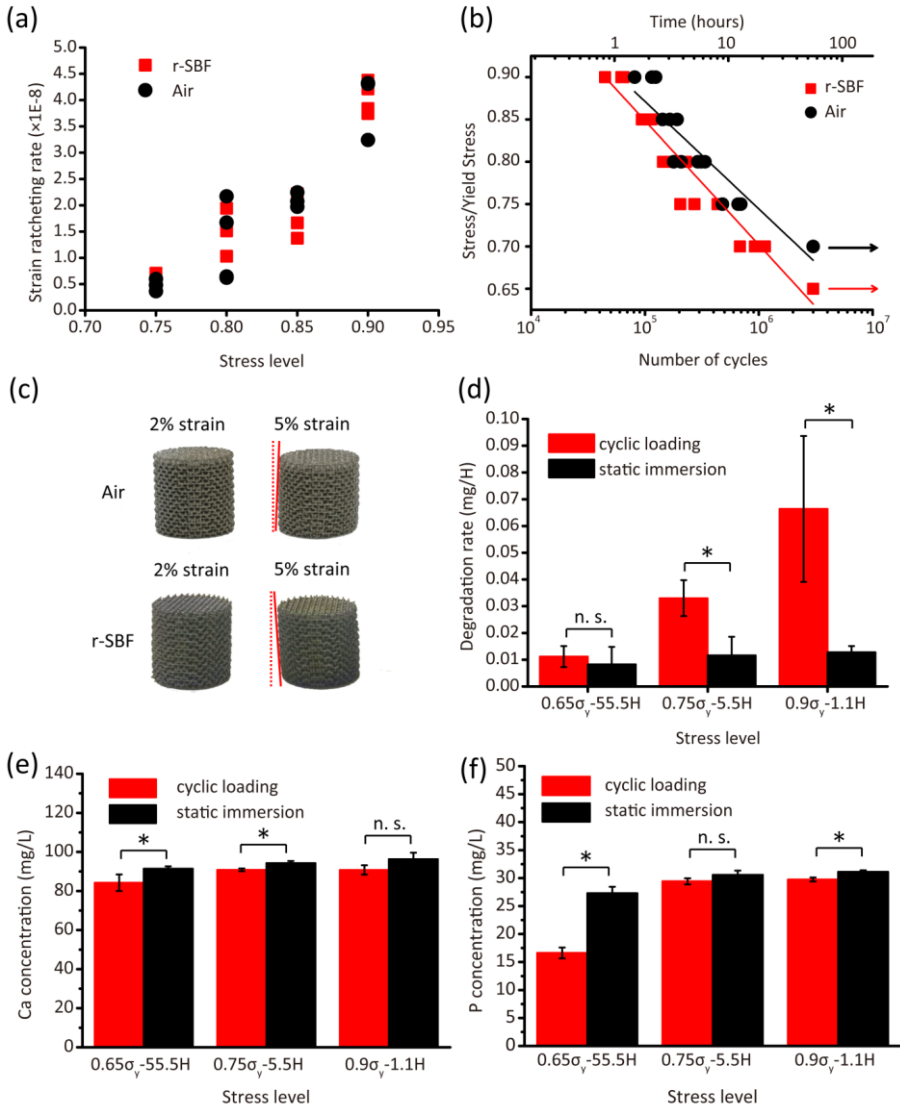

Figure 3. Fatigue behavior of the AM iron scaffold specimens in air and in r-SBF: (a) ratcheting rate; (b) S-N curve; (c) failure mode; (d) degradation rate; (e) Ca and (f) P ion concentrations.

Under cyclic loading, both Ca and P ion concentrations in r-SBF were lower than those in static immersion (Fig. 3e and f). For the Ca ion concentration, the differences were significant at $0.65\sigma_y$ and $0.75\sigma_y$, while for the P ion concentration, the differences were significant at $0.65\sigma_y$ and $0.9\sigma_y$.

EDS analysis revealed that the corrosion products all contained C, O, P, Ca and Fe elements. At the same immersion time, specimens under cyclic loading had higher P and Ca contents in their corrosion products (Fig. 4). Moreover, pits, as a result of localized degradation, were only found on iron scaffold struts subjected to cyclic loading (Fig. 4b, d and f), while the degradation of iron struts without mechanical loading occurred uniformly (Fig. 4a, c and e).

6.3.4.   Fatigue   crack   distribution   and characterization

Under $0.9\sigma_y$ cyclic loading, at 2% strain, cracks initiated mostly at the strut junctions and were distributed randomly within the whole scaffolds (Fig. 5a and b). There was no obvious increase in the number of cracks in the specimens tested in r-SBF as compared to that tested in air. At 5% strain, the cracks became wider and longer (Fig. 5c and d). However, no cracks that had propagated through the entire strut were found. The failure modes of the specimens tested in air and in r-SBF were similar. Under cycling loading, struts were still interconnected while several layers of struts in the middle of the specimens glided (Fig. 5c and d). At $0.65\sigma_y$, although the specimen did not fail after 3×10^6 loading cycles both in air and in r-SBF, cracks in the scaffolds had already initiated (Fig. 5e and f). Unlike fatigue tests at the highest stress level (i.e., $0.9\sigma_y$), more cracks had initiated in the specimens tested in r-SBF than those tested in air (compare Fig. 5e and f).

From the SEM images of crack morphology, it could be inferred that cracks preferentially initiated from the surface at the junction of struts both for the specimens tested in air and for those tested in r-SBF (Fig. 6). At $0.9\sigma_y$, cracks coexisted with pits that were formed as a result of localized degradation (Fig. 6f). At $0.65\sigma_y$, no cracks in the specimens tested in air were observed. In r-SBF, however, pits as a result of localized degradation near the cracks were found, being similar to the specimens subjected to cyclic loading at $0.9\sigma_y$ (Fig. 6i).

6
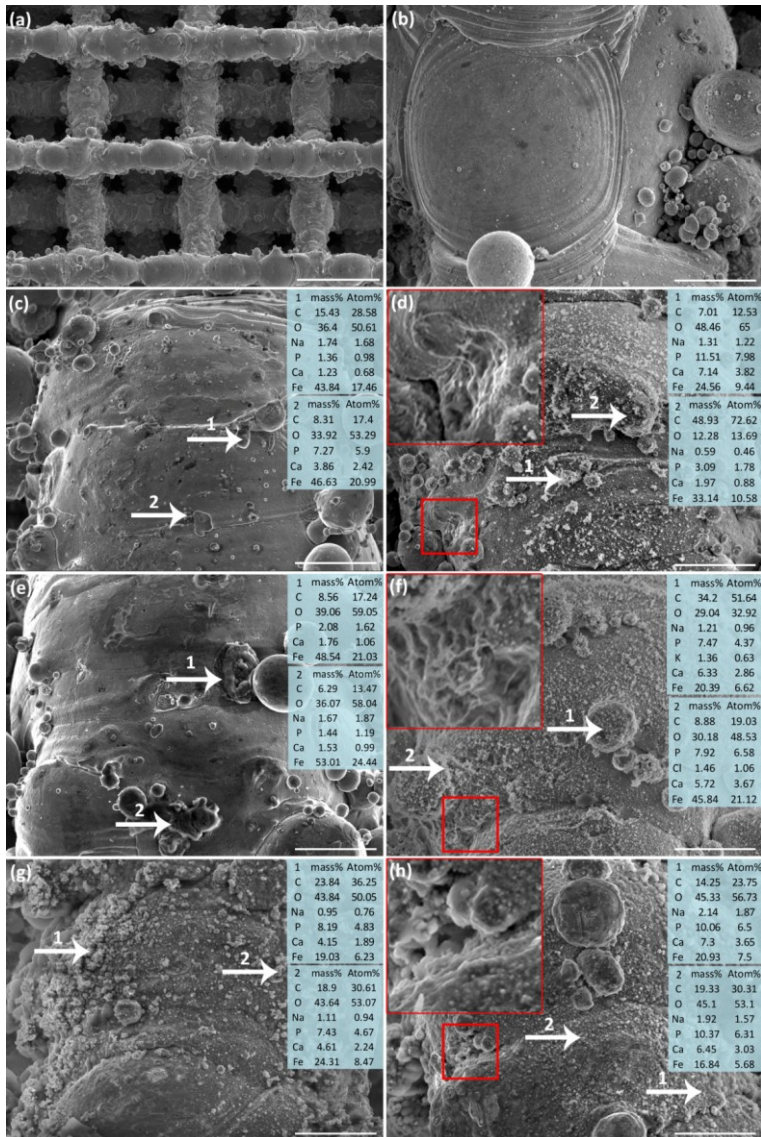
Figure 4. Corrosion products analysis: (a) (b) surface morphology of the as-built specimen; (c) (d) specimens after static immersion in r-SBF (c) and after fatigue test in r-SBF under $0.9\sigma_y$ dynamic loading (d); (e) (f) specimens after static immersion in r-SBF (e) and after fatigue test under $0.75\sigma_y$ dynamic loading (f); (g) (h) specimens after static immersion in r-SBF (g) and after fatigue test under $0.65\sigma_y$ dynamic loading (h). Arrow: EDS analysis points; red square: localized degradation and higher magnification overlay; scale bar: (a) 500 µm; (b-h) 50 µm.
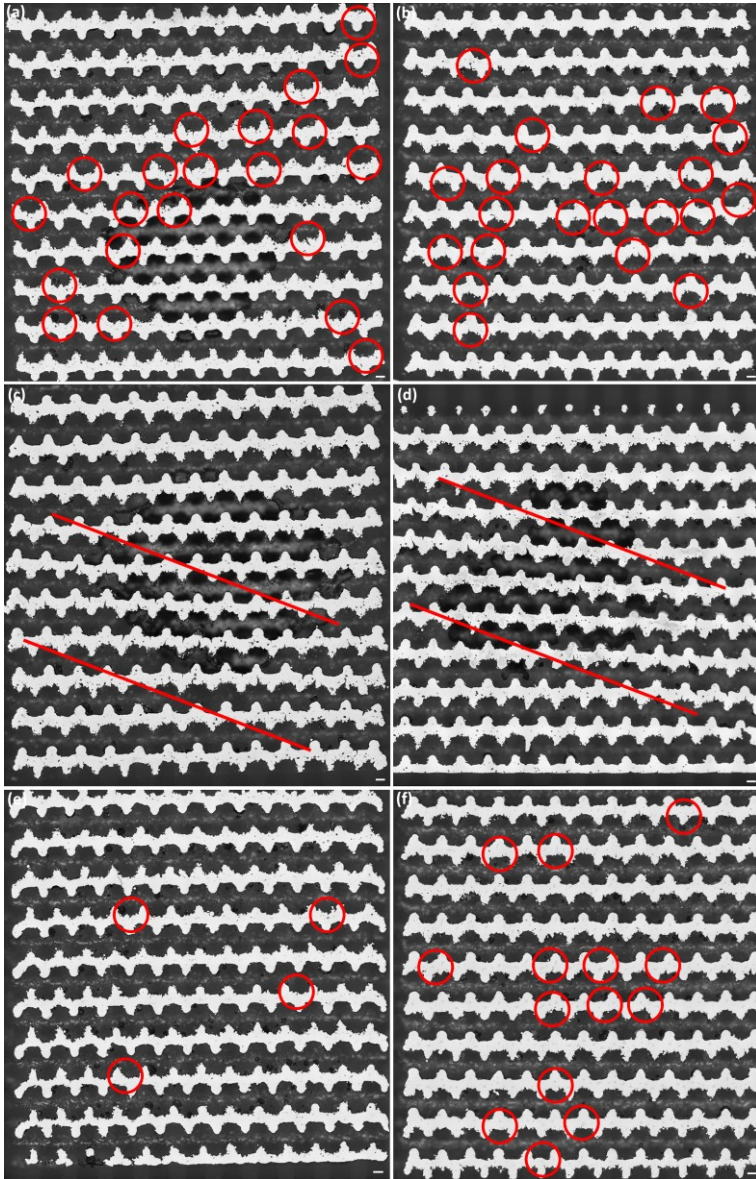
Figure 5. Fatigue crack distributions in the whole scaffold: (a) (b) specimens after fatigue test till 2% strain in air (a) and in r-SBF at $0.9\sigma_y$ (b); (c) (d) specimens after fatigue test till 5% strain in air (c) and in r-SBF at $0.9\sigma_y$ (d); (e) (f) specimens after 3×10^6 cycles of fatigue test at $0.65\sigma_y$ in air (e) and in r-SBF (f). Circles: cracks; area between two parallel lines: deformed struts; scale bar: 200 μm.

FE modeling indicated tensile stresses being concentrated at the strut junctions, while compressive stresses were present mostly in the body of the struts (Fig. 6j).
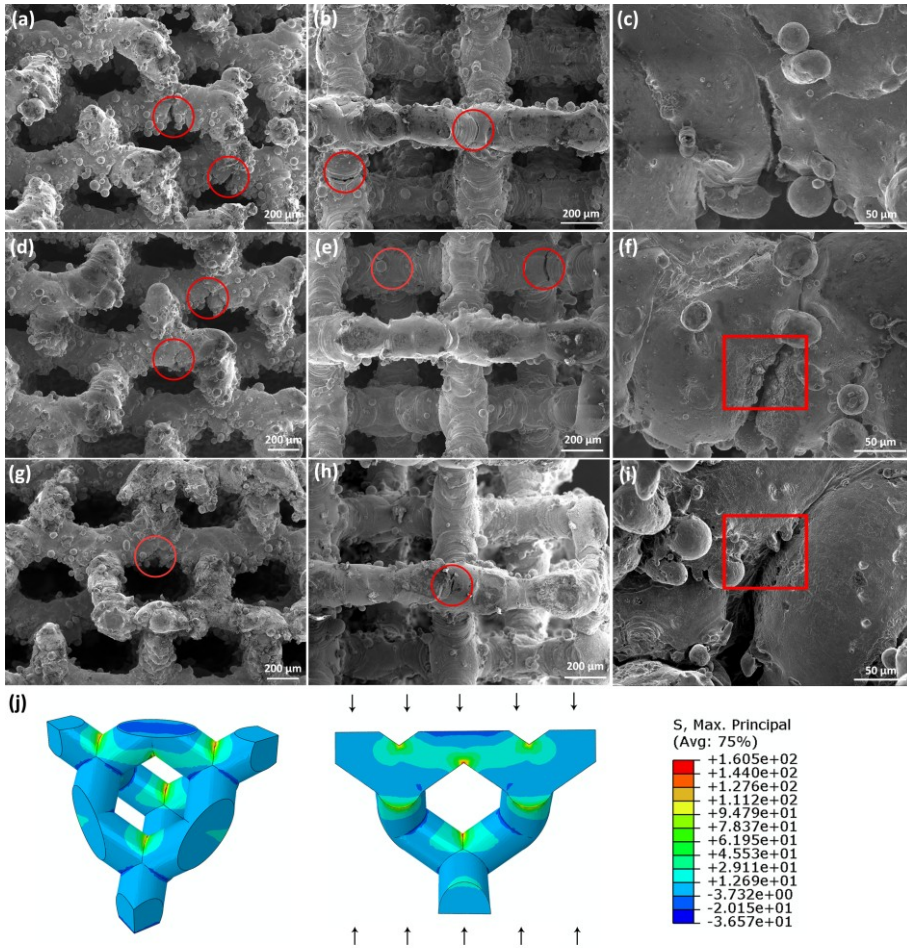
Figure 6. Fatigue crack morphologies: (a) (b) (c) specimen after fatigue test until 5% strain in air at $0.9\sigma_y$; (d) (e) (f) specimen after fatigue test until 5% strain in r-SBF at $0.9\sigma_y$; (g) (h) (i) specimen after 3×10^6 cycles of fatigue test in r-SBF at $0.65\sigma_y$; (j) stress distribution in a diamond unit cell under compressive loading. Circles: cracks; square: pitting.

EBSD analysis showed the crack propagation to be transgranular (Fig. 7a and b). Moreover, there were no preferred orientations of the cracks with respect to the grains (Fig. 7b). KAM maps indicated that there were more concentrations of maximum average intragranular misorientations around the cracks in the fatigue specimens tested

under $0.9\sigma_y$ cyclic loading than those subjected to $0.65\sigma_y$ cyclic loading and in the as-built specimens (Fig. 7c, d and e). Obviously, these disorientations did not develop to such an extent that grain splitting was activated.
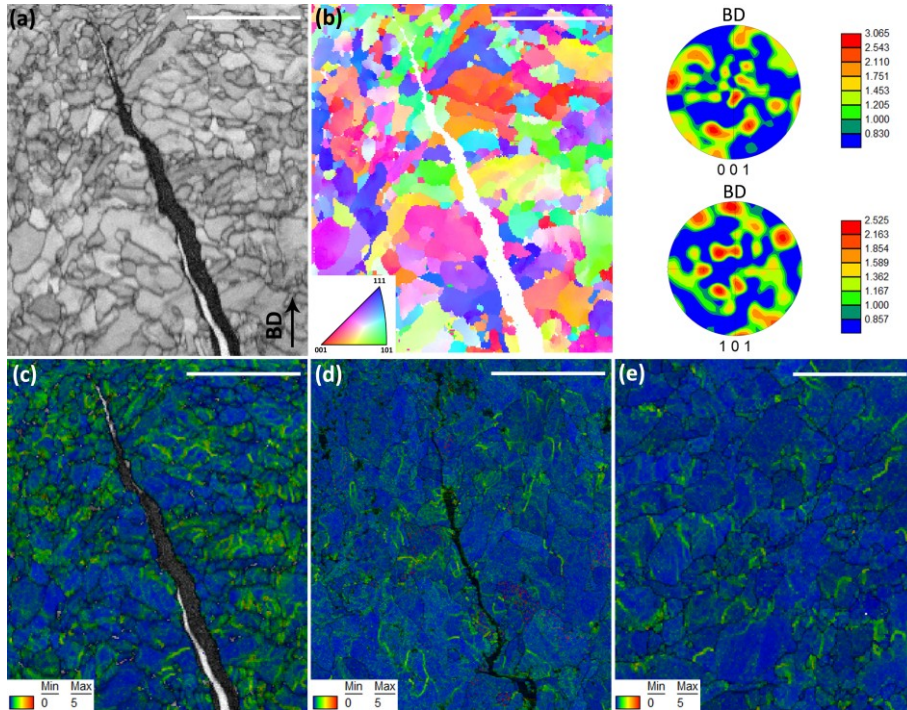
Figure 7. EBSD characterization of the fatigue crack track in air: (a) IQ map of the specimen tested at $0.9\sigma_y$; (b) IPF map of the specimen tested at $0.9\sigma_y$; (c) KAM map of the specimen tested at $0.9\sigma_y$; (d) KAM map of the specimen tested at $0.65\sigma_y$; (e) KAM map of the as-built sample. Scale bar: 25 μm.

6.3.5. FWHM of the iron scaffolds

XRD showed no marked differences in peak intensity between the specimens before and after the fatigue tests at 0.65 and $0.9\sigma_y$ (Fig. 8a). However, FWHM slightly increased after the fatigue test at $0.9\sigma_y$ (Fig. 8b), while at $0.65\sigma_y$, FWHM remained almost the same as the as-built specimen at low Bragg angles. Interestingly, the FWHM values even decreased at high Bragg angles (Fig. 8b).
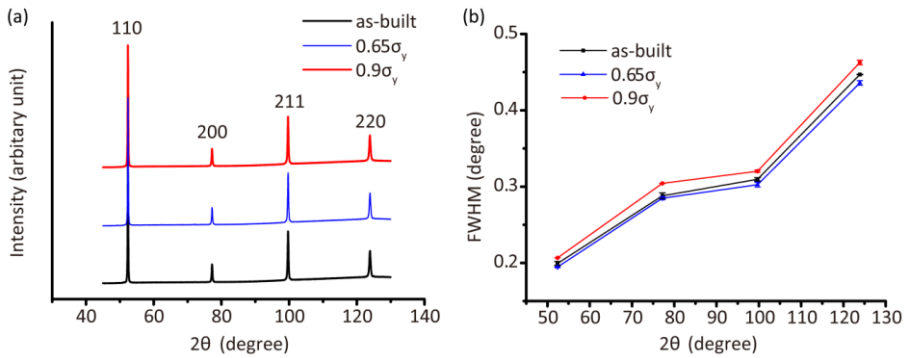
Figure 8. XRD analysis of the AM porous iron before and after the fatigue test in air at $0.9\sigma_y$: (a) XRD patterns; (b) FWHM.

6.4. Discussion

For the first time ever, we systematically studied the fatigue behavior of AM topologically ordered biodegradable porous iron both in r-SBF and in air. The parallel design of the study allowed us to unravel two novel aspects of this category of AM biomaterials: (i) the effect of material type on fatigue behavior and (ii) the mutual influences of biodegradation and cyclic loading. Interestingly, while biodegradation only slightly decreased the fatigue strength of porous iron from $0.7\sigma_y$ in air to $0.65\sigma_y$ in r-SBF, cyclic loading significantly increased its biodegradation rate, particularly at higher stress levels. This is very different from AM porous magnesium [6] both quantitatively and qualitatively. Quantitatively speaking, the fatigue strength of AM porous iron is about 2-3 times higher than that of AM porous magnesium both in air and in r-SBF. In qualitative terms, the effect of biodegradation on the fatigue life of the porous WE43 magnesium alloy was much stronger than that of porous iron. The effect of cyclic loading on the biodegradation rates of porous iron and WE43 magnesium was, however, quite significant and in that sense were not quite different. While some of these differences (*e.g.*, the effect of biodegradation on fatigue life) can be easily explained by the faster biodegradation of WE43 [1], explaining other observations (*e.g.*, higher fatigue strength in air) requires a more in-depth analysis. For one thing, the intrinsic mechanical properties of the material itself must be the main reason that pure iron is much more ductile than the WE43 magnesium alloy. For another, printing quality, e.g., the difference in surface morphology and defects, such as internal pores, can affect the fatigue performance of all AM metallic scaffolds to different extents [11]. Further morphological and microstructural examinations of fatigue-tested porous iron showed that fatigue cracks preferably initiated at the strut junctions of the specimens tested both in air and in r-SBF. In r-SBF, localized degradation accelerated by cyclic

loading may have promoted crack initiation. A higher degradation rate at a higher stress level could be contributed by higher internal stresses, according to EBSD and XRD analysis. Unlike titanium scaffolds [12], crack tips in the iron scaffolds were found to be blunt instead of being sharp, because of the good ductility of the latter. The cycle number that an implant needs to sustain in the first months after surgery is typically between 0.1×10^6 and 1×10^6 cycles [13]. The average patient's walking activity is around 2×10^6 cycles per year [14]. In this study, the SLM iron scaffolds did not fail at $0.65\sigma_y$ up to 3×10^6 cycles in r-SBF, making it qualified as a highly fatigue-resistant biodegradable porous biomaterial.

6.4.1. Effect of microstructure on biodegradation and fatigue behavior

Microstructure can influence both the biodegradation behavior and fatigue behavior of a material. SLM iron was found to have a higher degradation rate than the cold-rolled counterpart [2], as SLM led to the formation of fine grains. Generally, as SLM involves rapid solidification and high cooling rates, resulting grain sizes are usually much finer than those of conventionally manufactured counterparts. According to the classical solidification theory, grain morphology is determined by the ratio of thermal gradient, G, and solidification rate velocity, R [15]. On the top of the melt pool, the grains are more likely to be fine and equiaxed, because of low G/R ratios [16, 17]. At the bottom of the melt pool, however, the thermal gradient is greater than that on the top and heterogeneous nucleation may be induced when the previous layer is re-melted. Columnar grains may thus be formed at the bottom [18]. Moreover, unlike previously reported AM solid iron [19, 20], the AM porous scaffolds had only a limited number of elongated grains oriented in parallel with the length of the strut. This indicates that the effect of directional solidification would not be as strong as in the case of the solid counterpart. As the struts of the iron scaffolds were built in a tilted direction, the scanning contours were offset layer by layer, which could be the reason why some grains were elongated along the length of struts. Columnar grain growth may be restrained by the formation of equiaxed grains on the surface of the melt pool. When the re-melted depth is smaller than the equiaxed grains [21], a mixture of fine equiaxed grains and columnar grains will be formed. Furthermore, the microstructure of SLM porous iron being different from that of solid parts can also be caused by different thermal boundary conditions, as the melt pool is surrounded much more by a powder bed (with low thermal conductivity) when scanning a strut. Small grains increase the area of grain boundaries that are more reactive in the corrosive medium [22-24]. In fact, the increased biodegradation is beneficial, given the fact that the biodegradation rate of iron is normally considered to be too low [25, 26]. In terms of the fatigue behavior, fine grains are usually capable of inhibiting crack initiation and increasing the number of

barriers to early crack propagation [27]. Moreover, the good ductility of pure iron itself can improve the fatigue properties of AM iron scaffolds. As the stress concentration factor, K_t, and fatigue notch factor, K_f, are both important for the fatigue behavior, the notch sensitivity q, i.e. $(1- K_f)/(1- K_t)$, is frequently used to express the degree of difference between these two quantities. K_f is dependent not only on the specimen geometry but also on the material properties [28]. For a material with good ductility, as the plastic deformation in the vicinity of crack tips reduces the influence of stress concentration on crack growth, K_t is normally lower than K_f [29, 30]. The notch sensitivity, q, is therefore lower for ductile materials than brittle ones [30]. The failure mode of the iron scaffolds is different from that of the AM porous titanium reported in the literature [5]. There was no fracture plane through the iron scaffolds (Fig. 3c) and the cracks were blunting (Fig. 5c, Fig. 6c) instead of propagating sharply through the whole strut. As discussed above, this could be attributed to the high ductility of iron.

In addition, defects, such as pores caused by lack of fusion, may affect the fatigue behavior of AM iron as well. Internal pores and unmelted powder particles on the strut surface could both serve as stress concentration sites for fatigue crack initiation [5]. As the internal pore volume fraction was found to be negligibly low in the present AM iron scaffolds, it would be beneficial for their fatigue resistance.

6.4.2. Effect of cyclic loading on biodegradation

The corrosion products formed on the surface of scaffold struts could fall off under cyclic loading, as their mechanical properties are totally different from those of the iron substrate. Furthermore, the extrusion and intrusion of persistent slip bands during cyclic loading may break up the layer of corrosion products at the surface [4]. In addition, pitting potentials under cyclic loading are much smaller than those without stress, and the pitting potentials decrease with increasing stress level [31-34]. The acceleration of pitting degradation may promote intergranular degradation [31]. For topologically ordered porous structures, stress distribution follows a certain pattern. Taking the diamond unit cell lattice structure as an example, tensile stress tends to be concentrated at the strut junctions according to the results obtained from FE modeling (Fig. 6j). Concentrated tensile stress can cause micro residual stress and local strain, which can be seen in the KAM maps (Fig. 7c and d) and FWHM (Fig. 8b). KAM quantifies the average misorientation around a measurement point with respect to a defined set of nearest neighbor points [35]. It therefore provides a qualitative measurement of the distribution of micro residual stresses or local strains [36]. Local strains cause dislocations to slip and multiply in iron grains. Because of the barrier effect of grain boundaries, the slipped dislocations pile-up at these interfaces and normally this phenomenon is more obvious at higher cyclic stress levels [31]. FWHM is related to the dislocation density and the so-called type II micro residual stresses [37]. For the

specimens tested under the loading stress level of $0.9\sigma_y$, there were more obvious local strain concentrations around the cracks (Fig. 7c), leading to larger FWHM values (Fig. 8b) than those tested at $0.65\sigma_y$. However, as the curvature of AM porous materials does not allow for accurate FWHM readings, the increase of FWHM values is not obvious. The slip bands and dislocation pile-ups at the strut junctions are the preferred sites for cracks to initiate because of stress concentration [38]. Consequently, cyclic loading increased the degradation rate of the specimens in r-SBF. This increase was substantial at higher stress levels (Fig. 3d). The increased biodegradation rate was confirmed by the analysis of ion concentrations (Ca, P) in r-SBF (Fig. 3e and f). The faster biodegradation rate may favor the formation of corrosion products. The rise of pH value may facilitate the precipitation and deposition of phosphates, including $Mg_3(PO_4)_2$, $Ca_{10}(PO_4)_6(OH)_2$, and $Fe_3(PO_4)_2 \cdot 8H_2O$ [39]. Indeed, for the specimens in r-SBF under cyclic loading, the concentrations of Ca and P ions were lower in r-SBF, while more Ca and P contents were found in the corrosion products (Fig. 4).

6.4.3. Effect of biodegradation on fatigue properties

In addition to crack initiation and propagation, strain accumulation can affect the fatigue properties of a porous metallic structure [12, 40]. At the early stages of fatigue testing, the fatigue behavior of the iron scaffolds is controlled by strain ratcheting, which may be caused by the cyclic strain ratcheting of the unit cell [41, 42]. Higher stresses leads to higher ratcheting strain rates of the unit cells. As cyclic loading progresses, the cyclic softening of porous metallic structure starts to contribute to crack initiation and propagation as well [12, 40, 43]. In this study, the strain ratcheting rates of the iron scaffolds in air and in r-SBF were quite similar (Fig. 3a), probably because the overall amount of biodegradation was quite small. For example, under cyclic loading at $0.9\sigma_y$, only 0.07 ± 0.03 mg iron was lost from the specimen after fatigue testing (Fig. 3d). Such a slight mass loss would not substantially weaken the entire scaffold. However, according to the S-N curve, at the same stress levels, the fatigue strengths of the Fe scaffolds all decreased from those in air to those in r-SBF (Fig. 3b). The localized biodegradation occurring to the specimens in r-SBF could be the main reason behind this, as the pits created could act as the preferred sites for crack initiation (Fig. 6f and i) [44]. Furthermore, biodegradation could accelerate fatigue crack propagation, as anodic reaction or hydrogen embrittlement might occur at the crack tips [45].

In r-SBF, the above-mentioned slip bands and dislocation pile-ups (section 4.2) could increase the chemical and electrochemical potentials [31, 46]. Iron ion dissolution at or near dislocations and slip bands may form pits, which will in turn introduce higher stress concentrations [45]. Crack may then initiate as soon as the local stress concentration reaches a certain value. In addition, it has been reported that iron oxide could be easily formed on fresh slip bands due to its high chemical activity [45].

Subsequently, if the previously extruded slip bands intrude back, some hard iron oxides may be carried into the surface of the specimen. The corrosion products can impede the normal slipping of slip bands and, thus, may initiate cracks. At a high stress level, the mechanical damage may play a more important role than the corrosion attack in crack initial propagation [36]. This may be the reason why at $0.9\sigma_y$, crack initiation did not show clear differences between the specimens in r-SBF and in air, while at $0.65\sigma_y$, there were more cracks initiated at the strut junctions in the iron scaffolds tested in r-SBF, as compared to the specimens tested in air (Fig. 5e, f).

6.5. Conclusions

The AM porous iron exhibited extraordinarily high fatigue resistance, even when fatigue was accompanied and influenced by biodegradation in r-SBF. Indeed, biodegradation only reduced the fatigue strength of the SLM iron scaffolds from $0.7\sigma_y$ in air to $0.65\sigma_y$ in r-SBF. On the other hand, cyclic loading significantly accelerated the biodegradation rate, especially at higher stress levels. Cracks preferred to initiate at the strut junctions where tensile stresses were concentrated. Cyclic loading introduced micro strain-favored pit formation, which in turn promoted crack initiation. The extraordinarily high fatigue resistance and slow degradation rate make AM porous iron a promising biodegradable metallic material for bone substitution.

References

[1] Y. Li, J. Zhou, P. Pavanram, M. A. Leeflang, L. I. Fockaert, B. Pouran, N. Tümer, K. U. Schröder, J. M. C. Mol, H. Weinans, H. Jahr, A. A. Zadpoor. Additively manufactured biodegradable porous magnesium. Acta Biomater. 2018;67:378-392.

[2] Y. Li, H. Jahr, K. Lietaert, P. Pavanram, A. Yilmaz, L. I. Fockaert, M. A. Leeflang, B. Pouran, Y. Gonzalez-Garcia, H. Weinans, J. M. C. Mol, J. Zhou, A. A. Zadpoor. Additively manufactured biodegradable porous iron. Acta Biomater. 2018;77:380-393.

[3] A. P. Md Saad, A. Syahrom. Study of dynamic degradation behaviour of porous magnesium under physiological environment of human cancellous bone. Corros Sci. 2018;131:45-56.

[4] X. N. Gu, W. R. Zhou, Y. F. Zheng, Y. Cheng, S. C. Wei, S. P. Zhong, T. F. Xi, L. J. Chen. Corrosion fatigue behaviors of two biomedical Mg alloys – AZ91D and WE43 – In simulated body fluid. Acta Biomater. 2010;6:4605-4613.

[5] S. M. Ahmadi, R. Hedayati, Y. Li, K. Lietaert, N. Tümer, A. Fatemi, C. D. Rans, B. Pouran, H. Weinans, A. A. Zadpoor. Fatigue performance of additively manufactured meta-biomaterials: The effects of topology and material type. Acta Biomater. 2018;65:292-304.

[6] Y. Li, H. Jahr, X.-Y. Zhang, M. A. Leeflang, W. Li, B. Pouran, F. D. Tichelaar, H. Weinans, J. Zhou, A. A. Zadpoor. Biodegradation-affected fatigue behavior of additively manufactured porous magnesium.submitted.

[7] S. M. Ahmadi, R. Hedayati, Y. Li, K. Lietaert, N. Tümer, A. Fatemi, C. D. Rans, B. Pouran, H. Weinans, A. A. Zadpoor. Fatigue performance of additively manufactured meta-biomaterials: The effects of topology and material type. Acta Biomater. 2017.

[8] A. Oyane, H.-M. Kim, T. Furuya, T. Kokubo, T. Miyazaki, T. Nakamura. Preparation and assessment of revised simulated body fluids. J Biomed Mater Res A. 2003;65A:188-195.

[9] A. P. Md. Saad, N. Jasmawati, M. N. Harun, M. R. Abdul Kadir, H. Nur, H. Hermawan, A. Syahrom. Dynamic degradation of porous magnesium under a simulated environment of human cancellous bone. Corros Sci. 2016;112:495-506.

[10] Y. C. Lin, Z.-H. Liu, X.-M. Chen, J. Chen. Uniaxial ratcheting and fatigue failure behaviors of hot-rolled AZ31B magnesium alloy under asymmetrical cyclic stress-controlled loadings. Materials Science and Engineering: A. 2013;573:234-244.

[11] S. M. Ahmadi, R. Kumar, E. V. Borisov, R. Petrov, S. Leeflang, Y. Li, N. Tümer, R. Huizenga, C. Ayas, A. A. Zadpoor, V. A. Popovich. From microstructural design to surface engineering: A tailored approach for improving fatigue life of additively manufactured meta-biomaterials. Acta Biomater. 2019;83:153-166.

[12] S. J. Li, L. E. Murr, X. Y. Cheng, Z. B. Zhang, Y. L. Hao, R. Yang, F. Medina, R. B. Wicker. Compression fatigue behavior of Ti–6Al–4V mesh arrays fabricated by electron beam melting. Acta Mater. 2012;60:793-802.

[13] R. Hedayati, S. M. Ahmadi, K. Lietaert, N. Tümer, Y. Li, S. Amin Yavari, A. A. Zadpoor. Fatigue and quasi-static mechanical behavior of bio-degradable porous biomaterials based on magnesium alloys. J Biomed Mater Res A. 2018;106:1798-1811.

[14] F. Bobbert, K. Lietaert, A. Eftekhari, B. Pouran, S. Ahmadi, H. Weinans, A. Zadpoor. Additively manufactured metallic porous biomaterials based on minimal surfaces: A unique combination of topological, mechanical, and mass transport properties. Acta Biomater. 2017;53:572-584.

[15] J. Dupont. Fundamentals of Weld Solidification. ASM Handbook.6:700.

[16] F. Yan, W. Xiong, E. Faierson. Grain Structure Control of Additively Manufactured Metallic Materials. Materials. 2017;10:1260.

[17] Y. Zhu, D. Liu, X. Tian, H. Tang, H. Wang. Characterization of microstructure and mechanical properties of laser melting deposited Ti–6.5Al–3.5Mo–1.5Zr–0.3Si titanium alloy. Mater Des. 2014;56:445-453.

[18] V. Manakari, G. Parande, M. Gupta. Selective Laser Melting of Magnesium and Magnesium Alloy Powders: A Review. Metals. 2016;7:2.

[19] A. Simchi, H. Pohl. Effects of laser sintering processing parameters on the microstructure and densification of iron powder. Mater Sci Eng, A. 2003;359:119-128.

6

[20] B. Song, S. Dong, Q. Liu, H. Liao, C. Coddet. Vacuum heat treatment of iron parts produced by selective laser melting: Microstructure, residual stress and tensile behavior. Mater Des. 2014;54:727-733.

[21] T. Wang, Y. Y. Zhu, S. Q. Zhang, H. B. Tang, H. M. Wang. Grain morphology evolution behavior of titanium alloy components during laser melting deposition additive manufacturing. J Alloys Compd. 2015;632:505-513.

[22] C. S. Obayi, R. Tolouei, A. Mostavan, C. Paternoster, S. Turgeon, B. A. Okorie, D. O. Obikwelu, D. Mantovani. Effect of grain sizes on mechanical properties and biodegradation behavior of pure iron for cardiovascular stent application. Biomatter. 2016;6:e959874.

[23] M. Moravej, S. Amira, F. Prima, A. Rahem, M. Fiset, D. Mantovani. Effect of electrodeposition current density on the microstructure and the degradation of electroformed iron for degradable stents. Mater Sci Eng, B. 2011;176:1812-1822.

[24] P. K. Rai, S. Shekhar, K. Mondal. Development of gradient microstructure in mild steel and grain size dependence of its electrochemical response. Corros Sci. 2018;138:85-95.

[25] T. Kraus, F. Moszner, S. Fischerauer, M. Fiedler, E. Martinelli, J. Eichler, F. Witte, E. Willbold, M. Schinhammer, M. Meischel, P. J. Uggowitzer, J. F. Löffler, A. Weinberg. Biodegradable Fe-based alloys for use in osteosynthesis: Outcome of an in vivo study after 52weeks. Acta Biomater. 2014;10:3346-3353.

[26] M. Peuster, C. Hesse, T. Schloo, C. Fink, P. Beerbaum, C. von Schnakenburg. Long-term biocompatibility of a corrodible peripheral iron stent in the porcine descending aorta. Biomaterials. 2006;27:4955-4962.

[27] Z. Zúberová, L. Kunz, T. T. Lamark, Y. Estrin, M. Janeček. Fatigue and Tensile Behavior of Cast, Hot-Rolled, and Severely Plastically Deformed AZ31 Magnesium Alloy. Metall Mater Trans A. 2007;38:1934-1940.

[28] G. K. Haritos, T. Nicholas, D. B. Lanning. Notch size effects in HCF behavior of Ti–6Al–4V. Int J Fatigue. 1999;21:643-652.

[29] A. M. Sherman, R. G. Davies. The effect of martensite content on the fatigue of a dual-phase steel. Int J Fatigue. 1981;3:36-40.

[30] Z.-Z. Hu, S.-Z. Cao. Relationship between fatigue notch factor and strength. Eng Fract Mech. 1994;48:127-136.

[31] J. Xie, A. T. Alpas, D. O. Northwood. A mechanism for the crack initiation of corrosion fatigue of Type 316L stainless steel in Hank's solution. Mater Charact. 2002;48:271-277.

[32] J. Yang, Q. Wang, K. Guan. Effect of stress and strain on corrosion resistance of duplex stainless steel. Int J Pressure Vessels Piping. 2013;110:72-76.

[33] G. LÜ, H. Cheng, C. Xu, Z. He. Effect of Strain and Chloride Concentration on Pitting Susceptibility for Type 304 Austenitic Stainless Steel*. Chin J Chem Eng. 2008;16:314-319.

6

[34] B. T. Lu, Z. K. Chen, J. L. Luo, B. M. Patchett, Z. H. Xu. Pitting and stress corrosion cracking behavior in welded austenitic stainless steel. Electrochimica Acta. 2005;50:1391-1403.

[35] S. I. Wright, M. M. Nowell, D. P. Field. A Review of Strain Analysis Using Electron Backscatter Diffraction. Microsc Microanal. 2011;17:316-329.

[36] T. Zhao, Z. Liu, C. Du, C. Dai, X. Li, B. Zhang. Corrosion fatigue crack initiation and initial propagation mechanism of E690 steel in simulated seawater. Mater Sci Eng, A. 2017;708:181-192.

[37] I. Fernández Pariente, M. Guagliano. About the role of residual stresses and surface work hardening on fatigue ΔKth of a nitrided and shot peened low-alloy steel. Surf Coat Technol. 2008;202:3072-3080.

[38] D. Bian, W. Zhou, Y. Liu, N. Li, Y. Zheng, Z. Sun. Fatigue behaviors of HP-Mg, Mg–Ca and Mg–Zn–Ca biodegradable metals in air and simulated body fluid. Acta Biomater. 2016;41:351-360.

[39] R. Gorejová, L. Haverová, R. Oriňaková, A. Oriňak, M. Oriňak. Recent advancements in Fe-based biodegradable materials for bone repair. J Mater Sci. 2018.

[40] Y. J. Liu, H. L. Wang, S. J. Li, S. G. Wang, W. J. Wang, W. T. Hou, Y. L. Hao, R. Yang, L. C. Zhang. Compressive and fatigue behavior of beta-type titanium porous structures fabricated by electron beam melting. Acta Mater. 2017;126:58-66.

[41] A. M. Harte, N. A. Fleck, M. F. Ashby. Fatigue failure of an open cell and a closed cell aluminium alloy foam. Acta Mater. 1999;47:2511-2524.

[42] McCullough, Fleck. The stress–life fatigue behaviour of aluminium alloy foams. Fatigue Fract Eng Mater Struct. 2000;23:199-208.

[43] J. Zhou, W. O. Soboyejo. Compression–compression fatigue of open cell aluminum foams: macro-/micro- mechanisms and the effects of heat treatment. Mater Sci Eng, A. 2004;369:23-35.

[44] L. Chen, Y. Sheng, H. Zhou, Z. Li, X. Wang, W. Li. Influence of a MAO + PLGA coating on biocorrosion and stress corrosion cracking behavior of a magnesium alloy in a physiological environment. Corros Sci. 2019;148:134-143.

[45] W. Zhao, Y. Wang, T. Zhang, Y. Wang. Study on the mechanism of high-cycle corrosion fatigue crack initiation in X80 steel. Corros Sci. 2012;57:99-103.

[46] Y. Zheng, Y. Li, J. Chen, Z. Zou. Effects of tensile and compressive deformation on corrosion behaviour of a Mg–Zn alloy. Corros Sci. 2015;90:445-450.

6

6

7

Biodegradation-affected fatigue behavior of additively manufactured porous zinc

In this study, we compared the compression-compression fatigue behavior of AM porous zinc in air and in revised simulated body fluid (r-SBF). The fatigue strength of AM porous Zn was high in air (i.e., 70% of its yield strength) and even higher in r-SBF (i.e., 80% of its yield strength). SEM, EDS, and microhardness test showed that the formation of corrosion products around struts junctions and inside cracks could explain the higher fatigue strength of AM porous Zn in r-SBF. Furthermore, we compared the fatigue behavior of the uniform design with a functionally graded design. Regardless of the applied testing conditions, the functionally graded structure exhibited higher relative fatigue strengths as compared to the uniform structures, even though the latter had a higher relative density. Inspection of the fatigue crack distribution showed that the functionally graded design controls the sequence of crack initiation and propagation, leading to an early damage accumulation in the thicker struts, which over time moves towards the thinner struts. In conclusion, the favorable fatigue behavior of AM porous Zn further highlights its potential as a promising bone substituting biomaterial.[1]

7.1. Introduction

The recent progress in additive manufacturing (AM) technologies has provided unprecedented opportunities to tackle the dilemma between free-form design and manufacturing feasibility [1]. As far as non-biodegradable metals are considered, many types of AM porous metallic implants have been studied during the last few years with some variants already commercialized [2-4]. In contrast, AM biodegradable porous metals such as magnesium (Mg), iron (Fe), and zinc (Zn) have just appeared in the literature [5-10]. Among these metals, AM porous Zn has shown the most promising rate of biodegradation and degree of biocompatibility [7], making it the most likely candidate for future studies and eventual commercialization. However, the mechanical properties of biomedical-grade Zn are largely unstudied. That is the case even for traditionally manufactured bulk Zn material [11], let alone AM porous Zn. Even more unknown is the fatigue behavior of biodegradable of AM porous Zn. Indeed, there is no data whatsoever on the fatigue behavior of AM porous Zn and how it is affected by (while affecting) the biodegradation process of the scaffolds.

Our former studies on the biodegradation-affected fatigue behavior of AM porous Mg and Fe have shown that cyclic loading and biodegradation affect each other to a great extent [12, 13]. We, therefore, expect a similarly complex biodegradation-affected fatigue behavior for AM porous Zn. In fact, the mechanical behavior of Zn is expected to be even more complex, as Zn is reported to exhibit some special phenomenon, such as natural aging and creep that can affect its strength, ductility, and fatigue properties [14-18]. These phenomena could occur also at low temperatures. For example, the strength and ductility of Zn-0.08wt%Mg have been found to decrease at room temperature [16]. Furthermore, the creep properties of Zn at 37 °C have been shown to be a critical factor in the design of biodegradable Zn alloys [14].

Here, we report the first data ever on the biodegradation-affected fatigue behavior of AM porous Zn. We designed and directly printed one uniform and one functionally graded lattice structures using a powder bed fusion process (*i.e.*, selective laser melting) and investigated their compression-compression fatigue behavior in air and in revised simulated body fluid (r-SBF). We conducted a detailed analysis to reveal the mechanisms driving the fatigue behavior of these biomaterials and it interacts with the biodegradation process.

7.2. Material and methods

7.2.1. Manufacturing of porous Zn

Two different structures including one uniform structure (strut thickness: 0.4 mm, S04) and one functionally graded structure (strut thickness: radially graded from 0.4 to 0.2, S0402) were designed by Element (nTopology, USA) using a 1.4 mm diamond unit cell (Figure 1a, b). The specimens were produced using a powder bed fusion process known as direct metal printing or selective laser melting in the literature (equipment: ProX DMP 320 machine, 3D Systems, Belgium). The machine had a maximum laser power of 500 W and could reach oxygen levels below 50 ppm in the build chamber. A nitrogen-atomized Zn powder was used in this study [19]. The powder layer thickness was 60 μm while the energy density was 39.0 J/mm^3. The specimens were removed from the steel baseplate by wire electrical discharge machining.

7.2.2. Morphological characterization of AM porous Zn

The specimens were imaged using micro-computed tomography (micro-CT) (Phoenix Nanotom, GE Sensing Inspection Technologies GmbH, Germany) at a tube voltage of 130 kV and a tube current of 220 μA. The exposure time was 500 ms and the spatial resolution was 12 μm^3. A total of 1440 projections were acquired. The acquired data were then reconstructed and transformed to 2D images (DICOM stack) using Phoenix Datos|x 2.0 (GE Sensing & Inspection Technologies GmbH, Germany). To extract quantifiable data from these images, the following steps were taken. First, the images were imported to Fiji (NIH, US) and thresholded locally. Then, a series of circular regions of interest (ROIs) were created to calculate the porosity, strut size, and pore size using BoneJ (a plugin of Fiji) [6]. Besides, the porosity of the specimens was also determined using a weighing method [5]. 3D reconstruction of the images was done by Avizo Fire (VSG, France). The porosity within the struts was determined by using a method based on the Archimedes' principle [20].
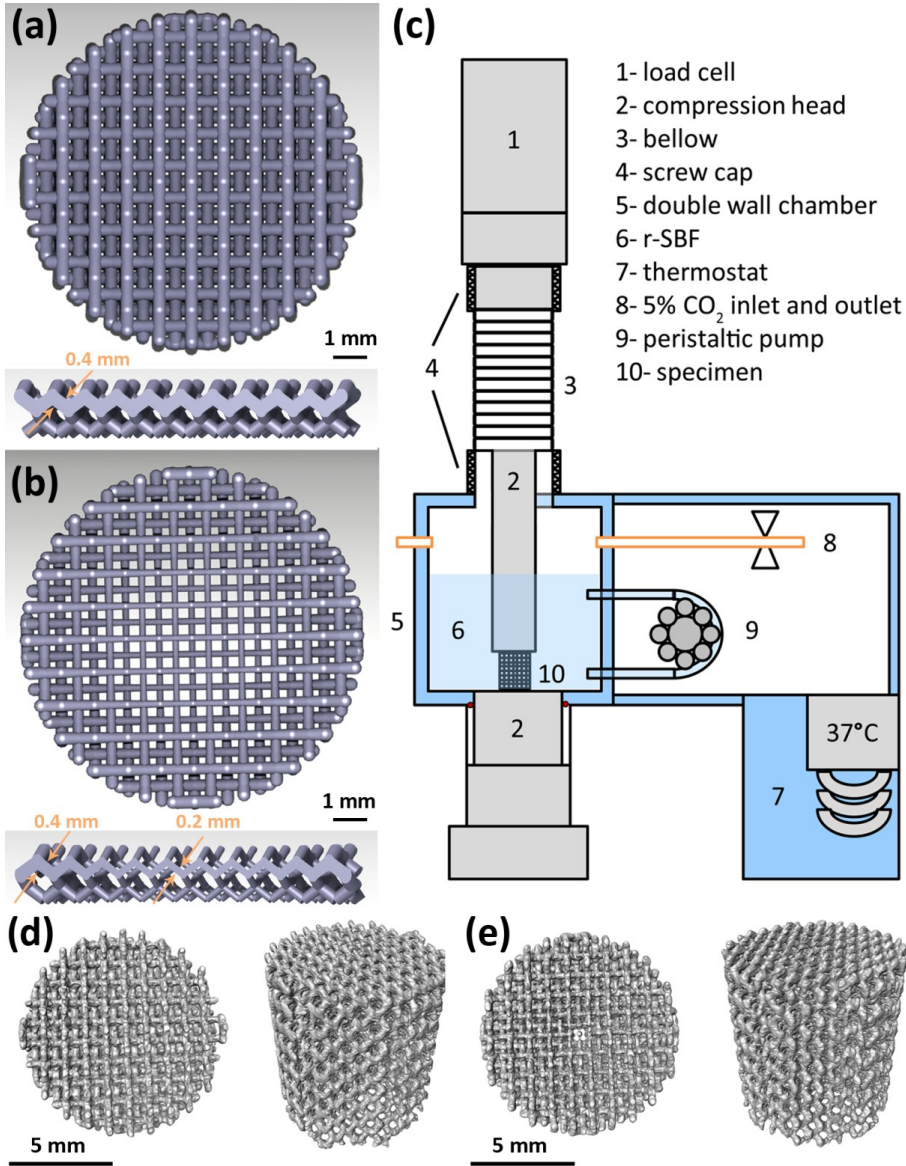
7

Figure 1. The design of AM porous Zn specimens and the corrosion fatigue test setup: (a) the uniform diamond structure; (b) a functionally graded diamond structure; (c) the corrosion fatigue test setup; (d) (e) the micro-CT reconstructions of AM porous Zn specimens from the S04 (d) and S0402 groups (e).

7.2.3. Fatigue tests in air and in r-SBF

Compression-compression fatigue tests were performed at 15 Hz with a 0.1 minimum-to-maximum stress ratio within a custom-made *in vitro* biodegradation chamber mounted on an electrodynamic mechanical testing machine (10 kN load cell, Instron E10000 ElectroPlus, USA) (Figure 1c). Different stress levels (maximum stress) between $0.7\sigma_y$ and $0.9\sigma_y$ were used from, where σ_y is the yield strength of AM porous Zn (10.8 MPa) [7]. The specimens were considered to have exhausted their load-bearing capacity when the displacement exceeded 0.5 mm. If a specimen did not fail until 3×10^6 cycles (55.5 h), the experiment was stopped and a run-out result was registered. The fatigue strength was defined as the maximum stress for which no failure occurred after 3×10^6 loading cycles. Corrosion fatigue tests were performed in 300 ml circulated r-SBF [21] at 1.2 ml/min [22] in the abovementioned chamber under physiological conditions (37 °C, 5% CO_2). The changes in the stiffness of the material were calculated using the loading and displacement data measured by the mechanical testing machine for each loading cycle. The ratcheting strain rate [23] per cycle was obtained as described before [12]. After corrosion fatigue tests, the concentrations of Zn, Ca, and P ions in the medium were determined using an inductively coupled plasma optical emission spectroscope (ICP-OES, iCAP 6500 Duo, Thermo Scientific). The weight change was recorded for the specimens after corrosion fatigue tests. For all stress levels, the experiments were performed in triplicates.

7.2.4. Characterization of crack morphology and corrosion products

After fatigue tests, the morphologies of the cracks were examined using a scanning electron microscope (SEM) (JSM-IT100, JEOL). The crack distributions on the cross sections of the specimens were inspected by a digital microscope (Keyence VHX5000, KEYENCE, Japan). For the corrosion fatigue specimens, the morphologies and compositions of the corrosion products on the strut surface were analyzed with the same SEM equipped with an energy-dispersive X-ray spectroscope (EDS). EDS mapping was also applied to analyze the cross sections of the corrosion products. The hardness values of AM Zn and corrosion products were measured in triplicates, respectively, by using a microhardness tester (DuraScan, G5, Austria) at an indentation load of 1 N.

7.2.5. Characterization of microstructure

An electron back-scattered diffraction (EBSD) analysis was performed at a step size of 200 nm using an HKL Nordlys II detector attached to a field emission gun scanning electron microscope (FEGSEM, JEOL JSM-6500F, Japan). Afterwards, inverse pole figure (IPF) and image quality (IQ) maps were reconstructed (TSL OIM® Analysis,

USA). The EBSD specimens were grinded and polished up to 1 μm with lubricants and further mechanically polished using 0.04 μm silica oxide.

7.2.6. Statistical analysis

The ratcheting rate, fatigue life, Zn ion concentration, and hardness were analyzed using one-way analysis of variance (ANOVA). A p-value less than 0.05 was assumed to indicate a statistically significant difference ($p < 0.05$, *)

7.3. RESULTS

7.3.1. Morphology of as-built porous Zn

The actual porosities of the AM Zn scaffolds were 4-5% lower than the design values (Table 1). The strut sizes of the S04 specimens were found to be 42 μm higher and the pore sizes were 50 μm smaller than their design values (Table 1). The average strut size and pore size of the S0402s specimen fell between the minimum and maximum values of the functionally graded design (Table 1). The 3D models reconstructed from the micro-CT images (Figure 1d, e) showed that the struts were uniform for S04 specimens, while the S0402 specimens had graded struts. The relative density of the struts was measured to be 93.6 ± 0.7% and 92.4% ± 1.0% for S04 and S0402 specimens, respectively. The difference between these two groups was statistically not significant ($p = 0.149$).

Table 1- Morphological properties of AM porous Zn specimens.

AM porous Zn	Porosity (%)		Strut size (μm)		Pore size (μm)	
	μCT	Design	μCT	Design	μCT	Design
S04	62.0±2.5	67.4	442±1	400	550±38	600
S0402	68.5±2.3	74.3	357±18	400-200	589±69	600-800

7.3.2. Fatigue behavior of AM porous Zn

The yield strengths of S04 and S0402 specimens were 10.8 ± 0.2 and 6.3 ± 0.1 MPa, respectively. Progressive strain accumulation was observed in the displacement vs. cycle number curves obtained for AM porous Zn (Figure 2a). At 0.8σy, the curves typically showed three stages for the experiments performed in air. In the first stage, rapid displacement accumulation was observed at the beginning of the fatigue test (Figure 2a). This was followed by a second stage, where large numbers of cycles caused only limited strain accumulation (Figure 2a). The speed of displacement accumulation remained more or less constant (Figure 2a). In the final stage, the displacement

accumulation of the specimens dramatically increased and continued until the failure of the specimen (Figure 2a). The corrosion fatigue specimens had much longer second stages as compared to their counterparts in air and showed no third stage even after 3 million cycles of loading (Figure 2a). All the specimens held their structural integrity after failure, with only slight expansions in the radial direction (Figure 2b).

For the experiments performed at $0.8\sigma_y$ in air, the stiffness of the AM porous Zn specimens gradually declined in the second stage and rapidly dropped after a critical number of cycles in the third stage (Figure 2c). On the contrary, the corrosion fatigue specimens showed a constant stiffness, which even increased after 3 million cycles of loading (Figure 2c). In the experiments performed at $0.9\sigma_y$, the stiffness of all specimens gradually decreased regardless of the test conditions (i.e., in air or in r-SBF) (Figure 2d). However, the corrosion fatigue specimens exhibited a slower rate of decline as compared to the specimens tested in air (Figure 2d).

For both types of testing conditions, the ratcheting rate was proportional to the stress level (Figure 2e). At $0.8\sigma_y$, the S04 and S0402 specimens showed significantly lower ratcheting rate in r-SBF than in air. At $0.9\sigma_y$, the S04 specimens exhibited (a statistically insignificantly) higher ratcheting rate in r-SBF than in air, while the S0402 specimens showed no large differences between both testing conditions (Figure 2e). Among different designs, the S0402 specimens significantly lower ratcheting rates than the S04 specimens tested at $0.8\sigma_y$ and $0.85\sigma_y$ (Figure 2e).

The normalized fatigue strengths of the corrosion fatigue specimens were higher than those tested in air (Figure 2f). Moreover, the S0402 specimens showed better fatigue strength than S04 specimens, regardless of the testing conditions (Figure 2f), while the difference in the fatigue life between both groups at the same stress level were statistically insignificant.

7

7
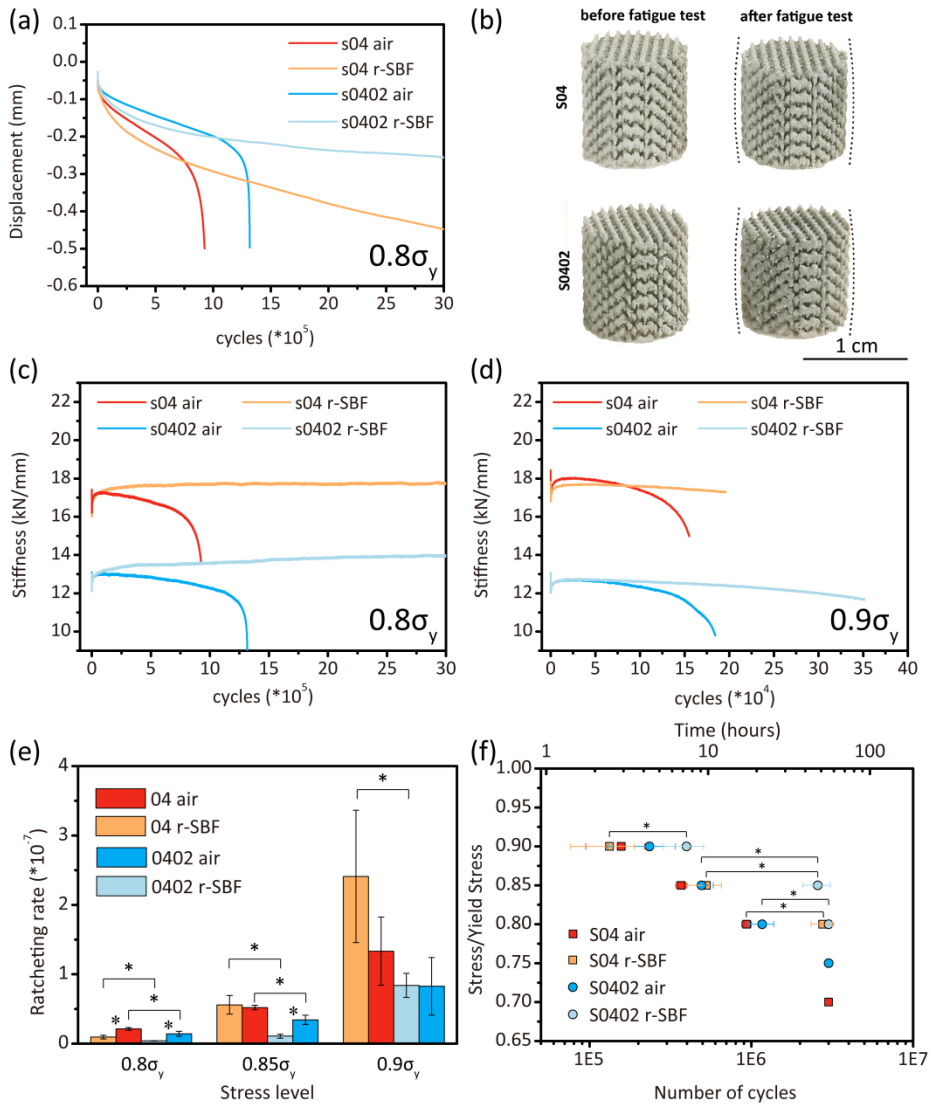
Figure 2. The fatigue performance of AM porous Zn specimens in air and in r-SBF: (a) the displacement of the specimens under $0.8\sigma_y$ cyclic loading; (b) the shapes of specimens before and after the fatigue tests; (c) the variation of stiffness at $0.8\sigma_y$ with the cycle number; (d) the variation of the stiffness at $0.9\sigma_y$ with the cycle number; (e) the ratcheting rates at different loading levels and (f) S-N curves.

7.3.3. Characterization of fatigue cracks and corrosion products

Regardless of the testing conditions, almost all the fatigue cracks were found at the junction between two struts (Figure 3a-d). EDS analysis showed that the as-built specimens contained mainly Zn (>80%) with small percentages of O (≈10%) and C (≈6%) on the surface (Figure 3b). For the corrosion fatigue specimens, the corrosion products mostly formed around the cracks that contained more O (>30%) with extra P and Ca detected (Figure 3d). Accumulation of the corrosion products were also found at strut junctions of AM porous Zn, where Zn, O, and C were mainly indexed with a small amount of P (Figure 3e, f).

Furthermore, we checked the crack morphology and corrosion products on the cross section of the specimens after corrosion fatigue tests (Figure 4). Cracks were found to initiate from the corrosion products (Figure 4a). Zn, O, C, P, and Ca inside the cracks were detected in EDS point analysis (Figure 4a) and the corrosion products filled the cracks. EDS mapping confirmed the presence of Zn, O and C inside the cracks (Figure 4b-d).

ICP analysis showed that the degradation rate of S0402 specimens was higher than that of the S04 specimens, especially at $0.8\sigma_y$ (Figure 4e). Moreover, the degradation rates of both of the groups were higher at $0.8\sigma_y$ than at $0.8\sigma_y$. The concentrations of Ca and P ions decreased from the initial values after the corrosion fatigue experiments (Figure 4f). The S04 and S0402 specimens had 30.6 ± 8.7 mg and 19.5 ± 5.3 mg weight gain, respectively, at $0.8\sigma_y$.

The microhardness tests showed that the corrosion products had an average hardness value of 205±16 HV, which was almost 5 times higher than that of AM Zn (42±3 HV) (Figure 5a, b). After indentation tests at the interface, the cracks appeared to have not propagated along the zinc/corrosion product interface, but across the interface (Figure 5c, d).

7
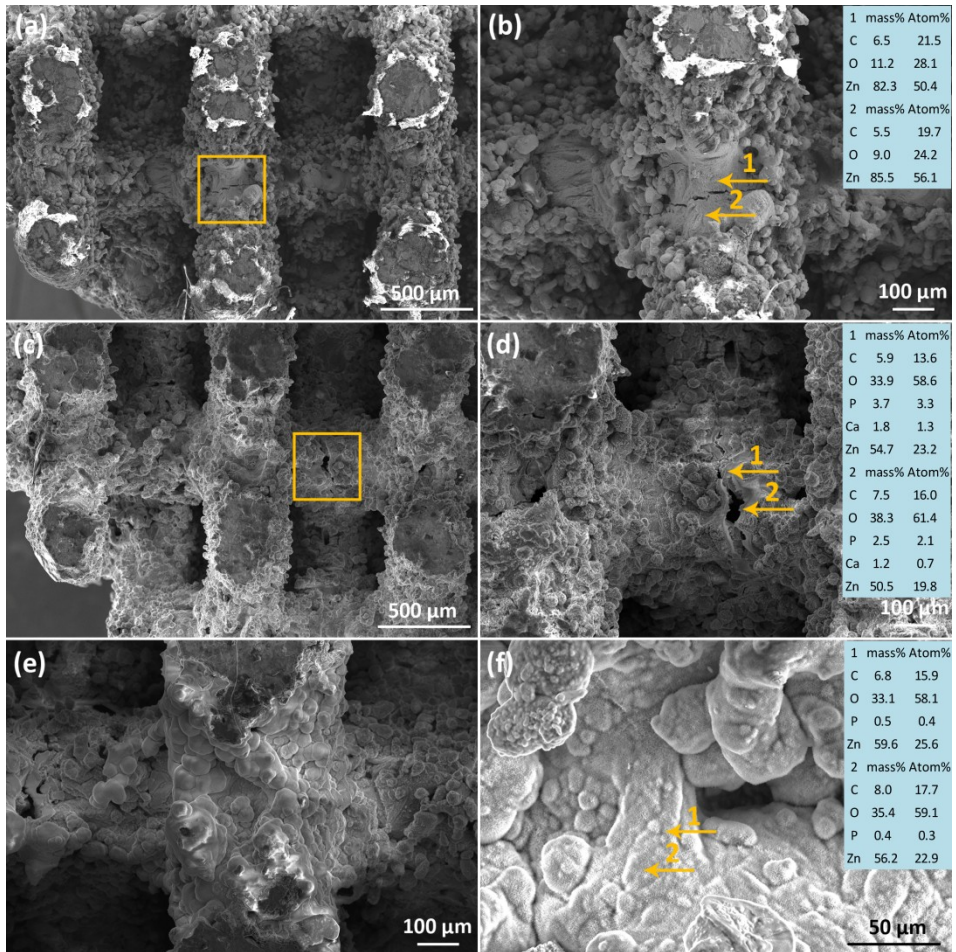
Figure 3. The morphology of AM porous Zn specimens after fatigue tests: (a) low- and (b) higher-magnification views of crack morphology after the fatigue tests in air; (c) low- and (d) higher-magnification crack views of morphology after the corrosion fatigue tests; (e) low- and (f) higher-magnification views of the corrosion products. Orange square: cracks.
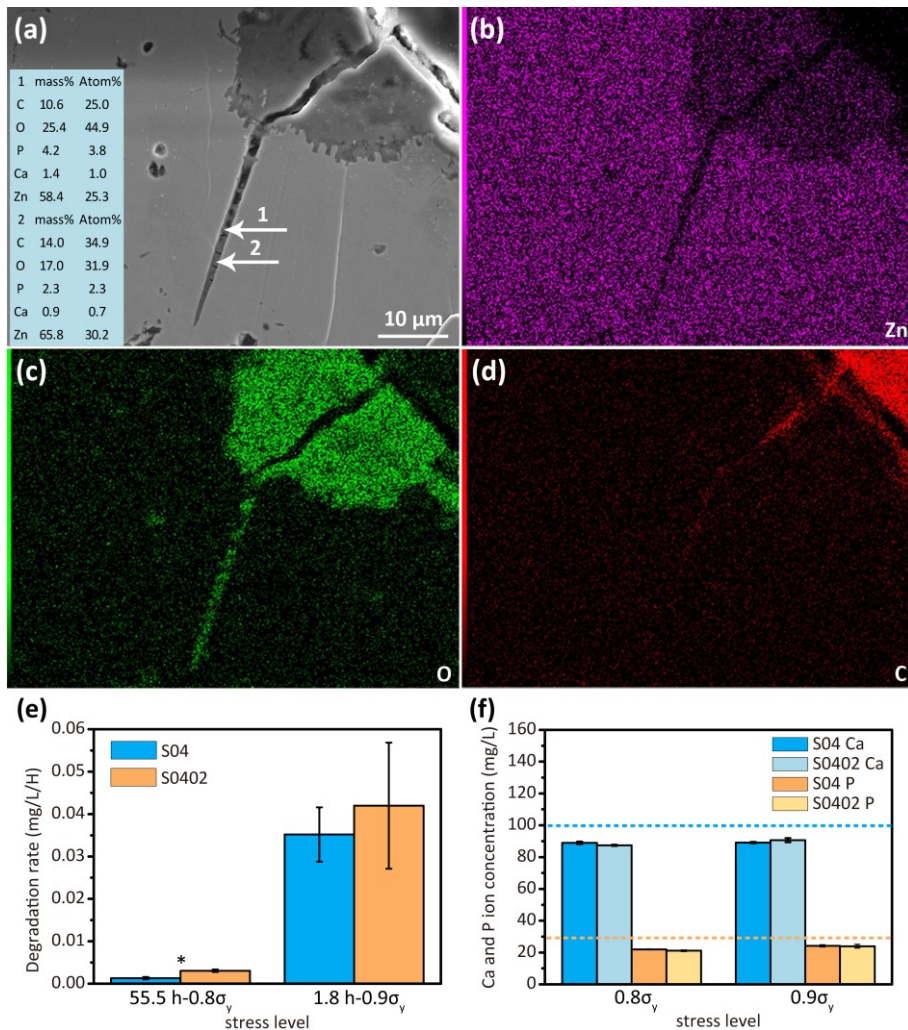
Figure 4. The characteristics of the corrosion products on the cross-section of the specimens and the ion concentrations of the immersion medium: (a) the crack morphology and EDS point analyses of the corrosion products inside the crack; (b-d) EDS mapping; (e) the degradation rates (corrosion fatigue test duration at $0.8\sigma_y$: 55 h; corrosion fatigue test duration at $0.9\sigma_y$: 1.8 h) and (f) Ca and P ion concentrations of the medium after the corrosion fatigue tests. The blue and orange dash lines in (f): the starting concentrations of Ca and P ions of the medium, respectively.
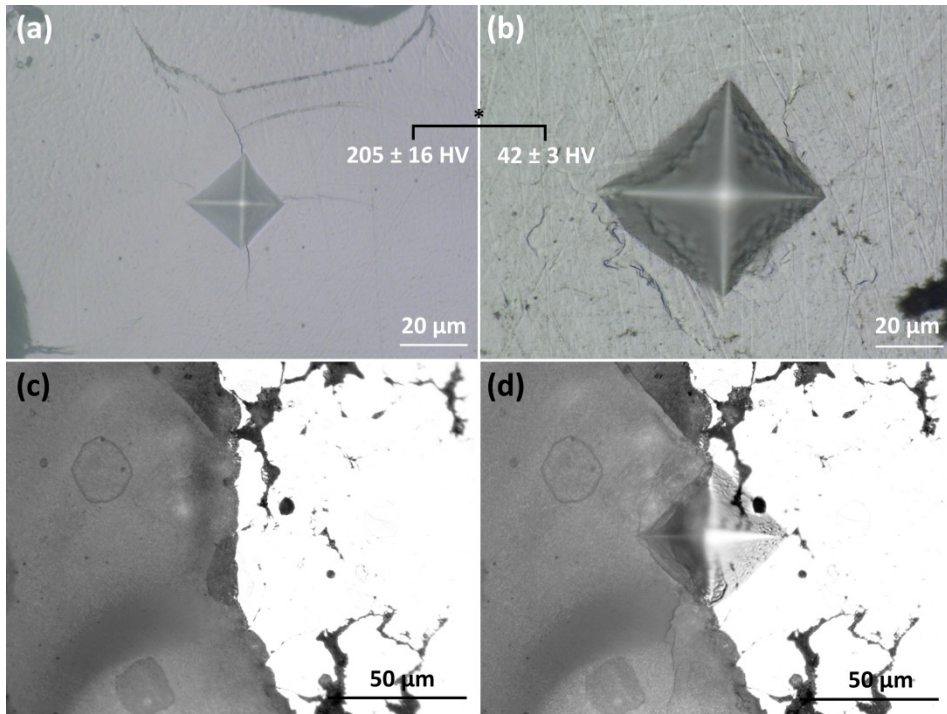
Figure 5. The indentations on the corrosion products (a), Zn (b), and at the corrosion product/Zn interface (c) (d).

7.3.4. Fatigue cracks distribution

In order to check the distribution of fatigue cracks within the AM porous Zn specimens, they were cut along their longitudinal section (Figure 6a). For the specimens tested in air, the cracks already initiated after 300,000 cycles (Figure 6b, e). The cracks seemed to initiate randomly in the S04 specimens (Figure 6b), while more cracks were found in the thicker struts than thinner ones for the S0402 specimens (Figure 6e). As the fatigue tests progressed, the cracks propagated and grew in size and width for the S04 specimen (Figure 6c). For the S0402 specimens, the cracks seemed to form gradually from the thicker struts towards the thinner ones (Figure 6e, f). In contrast, the corrosion fatigue specimens exhibited smaller numbers of cracks than the specimens tested in air even after 3 million cycles (Figure 6c, g).

7.3.5. Microstructural characterization after fatigue tests

According to our EBSD analysis, the fatigue cracks propagated transgranularlly for both types of the testing conditions (Figure 7). At lower cycle numbers, some low-angle boundaries were observed around the cracks both for the specimens tested in air and

those exposed to biodegradation in r-SBF (Figure 7a, c). After larger numbers of fatigue cycles, IPF and IQ maps showed some high-angle boundaries along the cracks (Figure 7b, d).

7.4. DISCUSSION

We reported the first data ever on the fatigue behavior of AM porous Zn in air and in r-SBF. Interestingly, and opposite to AM porous Mg and Fe [12, 13], AM porous Zn showed increased fatigue strength in r-SBF as compared to dry testing conditions (*i.e.*, in air). According to the SEM observations, EDS measurements, and microhardness analysis, the formation of corrosion products contributes to the improvement the fatigue resistance of AM porous Zn. Another notable observation was that functionally graded AM porous Zn structures exhibit better fatigue performance as compared to the uniform ones. Functionally graded designs could, therefore, serve as an effective tool to improve the fatigue resistance of AM porous biodegradable metals.
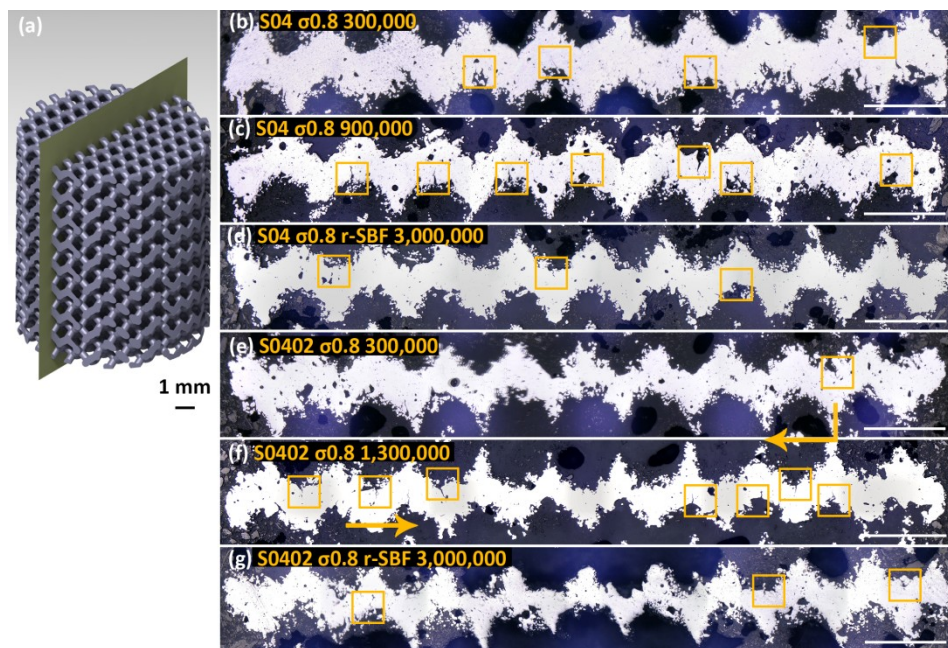
Figure 6. The distributions of fatigue cracks in the AM Zn specimens: (a) a schematic diagram of the longitudinal cross-section; (b-d) the S04 specimens after the fatigue tests: (b) 300,000 cycles in air, (c) 900,000 cycles in air, and (d) 3,000,000 cycles in r-SBF at $0.8\sigma_y$; (e-g) the S0402 specimens after fatigue test: (e) 300,000 cycles in air, (f) 1,300,000 cycles in air, and (g) 3,000,000 cycles in r-SBF at $0.8\sigma_y$. Orange squares: cracks; scale bar in (b-g): 1mm. The arrows indicate the direction of crack formation from thicker struts to thinner ones.
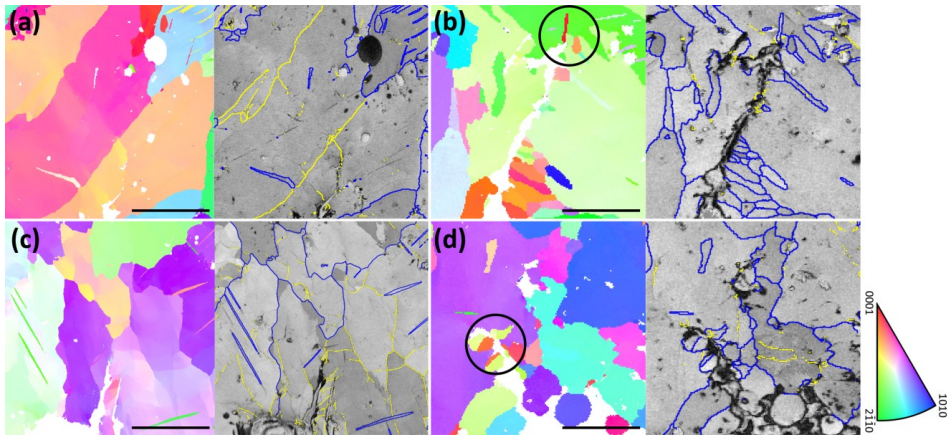
Figure 7. The IPF and IQ maps of the fatigue crack track: (a) a specimen tested at $0.8\sigma_y$ for 300,000 cycles (in air); (b) a specimen tested at $0.8\sigma_y$ for 900,000 cycles (in air); (c) a specimen tested at $0.8\sigma_y$ for 300,000 cycles (in r-SBF); (d) a specimen tested at $0.8\sigma_y$ for 3,000,000 cycles (in r-SBF). Scale bar: 60 μm; Black square: recrystallization; blue lines: high-angle boundaries (> 15 °); yellow lines in: low-angle boundaries (< 15 °).

7.4.1. Mechanisms of corrosion fatigue behavior

For the fatigue tests in air, the displacement vs. cycle numbers plots measured for AM porous Zn showed three stages. This three-stage behavior is similar to what has been measured for some other types of porous metallic materials [24]. The abrupt strain accumulation in the first stage is probably caused by the failure of weak struts or the flattening of rough surfaces at the top or bottom of the cylindrical specimens (Figure 2a). In the second stage, the strain increased at a constant rate, which can be attributed to not only the cyclic ratcheting of the unit cells but also to the initiation and propagation of cracks, as is evidenced by cyclic softening of the specimens (*i.e.*, the gradual loss of stiffness) (Figure 2c, d). According to Mccullough *et al.* [25], cyclic ratcheting may originate from the ratcheting (*i.e.*, plastic deformation) of the cell, which is analogous to creep [26]. This phenomenon is also observed in many bulk materials, such as Mg alloys and steel [23]. Cyclic ratcheting is believed to be related to several intrinsic mechanisms including dislocation and slip characteristics, stacking fault energy, microstructural evolution, and cyclic softening behavior [27]. After fatigue, the specimens showed only small deformations in the radial direction, which is similar to the behavior exhibited by AM porous Fe and different from the catastrophic, sudden failure observed in the case of AM porous Mg (Figure 2b) [12, 13]. The good ductility of pure Zn could explain this. Furthermore, as evidenced by the EBSD analysis (Figure 7), small grains were found adjacent to the crack tips. IQ maps showed that these grains all had high-angle boundaries. As Zn is known for its low recrystallization temperature

[14], recrystallization may have occurred in the vicinity of crack tips, where high stresses are concentrated. The recrystallized small grains can then retard the propagation of fatigue cracks.

As a representative measure of fatigue performance, the accumulated ratcheting strain per cycle can be calculated as [25]:

$$\frac{d\varepsilon}{dN} = C(1-R)^p \frac{0.6}{n+2} \left[\frac{1.7(2n+1)}{n} \frac{|\sigma|_{max}}{\sigma_0} \right]^n \bar{\rho}^{(3n+1)/2} \qquad (1)$$

where C, p, n, and σ_0 are material constants, R is the stress ratio, $|\sigma|_{max}$ is the maximum loading stress, and $\bar{\rho}$ is the relative density of the porous structure. If we consider the fatigue limit is achieved when the accumulated strain equals the yield strain ε_y of the whole porous structure, the fatigue life N_f can be determined by integrating Equation (1) [25]:

$$\frac{1}{N_f} = \frac{C(1-R)^p}{\varepsilon_y} \frac{0.6}{n+2} \left[\frac{1.7(2n+1)}{n} \frac{|\sigma|_{max}}{\sigma_0} \right]^n \bar{\rho}^{(3n+1)/2} \qquad (2)$$

When both cyclic ratcheting strain and cyclic plastic strain are considered, the cyclic damage can be determined as [27]:

$$\frac{dD}{dN} = \frac{1}{\varepsilon_f} \left\{ C_1(1-R)^p \frac{0.6}{n+2} \left[\frac{1.7(2n+1)}{n} \frac{|\sigma|_{max}}{\sigma_0} \right]^n \bar{\rho}^{(3n+1)/2} + C_2 \varepsilon_y \left(\frac{\bar{\rho}^2}{\sigma} \right)^{-\alpha/\beta} \right\} \qquad (3)$$

where ε_f is the ductility of the material, while C_2, α, and β are three material constants. Recently, Yang *et al.* [28] have suggested that instead of using the maximum loading stress $|\sigma|_{max}$, the local maximum stress should be applied to analyze the cyclic damage, as stresses are distributed differently in a porous structure due to the effects of geometrical design. According to Equation (3), the fatigue life is proportional to the ductility of the material and is inversely proportional to the loading stress, which is consistent with this work (Figure 2) and our former study on the fatigue behavior of AM porous Mg and Fe [12, 13].

Surprisingly, AM porous Zn showed a better fatigue performance in air than in r-SBF (Figure 2f). This could be attributed to the constant or even increased stiffness of the specimens tested in r-SBF (Figure 2c, d). AM porous Zn releases Zn into the medium (Figure 4e, f), thereby decreasing its stiffness. The only plausible explanation for the increased stiffness of the specimens after corrosion fatigue tests is the formation of corrosion products (Figure 3e, f). According the EDS and SEM analysis (Figure 3, 4), corrosion products may improve the fatigue behavior of AM porous Zn in two ways. First, corrosion products were found to have been accumulated around strut junctions,

7

where the peaks of the tensile stress normally occur for a diamond structure [12, 13] (Figure 3e, f). This additional material may reduce the tensile stress peaks, thereby reducing the possibility of crack initiation and the rate of crack propagation. Moreover, AM porous Zn can be considered as a composites material that contains both metallic (*i.e.*, Zn) and ceramic (*i.e.*, corrosion products) constituents. This effect is particularly important given the fact that the corrosion products were found to be almost 5 times harder than the metal itself (Figure 5). The indentation at the interface of Zn and corrosion products suggested a good interface bonding, as cracks propagated into the corrosion products but not along the interface [29]. Although corrosion fatigue led to a loss of Zn from the AM porous Zn specimens and cracks could initiate from the localized corrosion sites, the contributions of the corrosion products to the load-bearing capability of the porous structures more than compensated for the effects of the material loss, as shown by the weight gains of the AM porous Zn specimens. Second, the corrosion products were found to have been formed both along fatigue cracks (Figure 3d) as well as inside them (Figure 4c). The accumulation of the corrosion products could reduce the further corrosion of the freshly exposed crack surface.

7.4.2. Effects of topological design

As reported by other researchers [26, 27, 30], the relative fatigue strength can be decreased by increasing the porosity of the porous structure, although Mccullough *et al.* [25] stated that Equation (2) is not sufficient to make the conclusion. Li *et al.* [27] found that dislocation generation was more obvious in AM porous titanium specimens with higher densities, which could pin the movement of the interface and, thus, retard cyclic ratcheting. In this study, even though S04 specimens had higher porosities than those of the S0402 specimens, the S0402 specimens showed higher relative fatigue strengths than the S04 specimens (Figure 2f). In the present study, even though the S04 specimens had a higher relative density than the S0402 specimens, the S0402 specimens showed higher relative fatigue strengths than the S04 specimens in air and in r-SBF (Figure 2f). Similar results have been reported by Zhao *et al.* [31] in a study on three different uniform porous structures with different buckling components. It can be inferred that topological design can be used to improve the fatigue performance of the AM porous structures.

As can be seen in the fatigue crack distribution of the S0402 specimens (Figure 6), fatigue cracks have initiated from the thicker struts on the periphery of the specimens at early cycles and transferred to the thinner struts in the center of the specimens as cyclic loading has progressed. In the case of the S04 group, however, the cracks were randomly distributed. Given that the unit cell size was constant in all cases, the unit cells with thicker struts had higher relative densities and, thus, higher stiffness values than those with thinner ones. For the same level of applied strain, the thicker struts will, therefore, experience higher stresses as compared to the thinner ones. This explanation

has been also confirmed by our former studies using finite element models [32, 33]. Consequently, cracks preferably initiate in the thicker struts in the early stages of the fatigue experiments. As cyclic loading continues, the initiation of an increasing number of cracks and their propagation decreases the stiffness of the thicker struts on the periphery of the specimens. The stress carried by the thicker struts, therefore, decreases while the adjacent thinner struts start to bear more loads. As a result, crack propagation in the thicker struts start to slow down while cracks start to initiate in the thinner struts. Over time, the cracks initiation and propagation transfers towards the center of the specimens until the scaffolds fail.

In order to predict the fatigue life of the functionally graded structures, Zhao *et al.* [31] have proposed a model of the fatigue life of a dual-layer structure with a hard core (L_1) and a soft shell (L_2) :

$$N = \frac{\varepsilon_{R1}C_1}{\sigma^{m_1}}\left(f_1 + \frac{E_2}{E_1}f_2\right)^{m_1} + \frac{(\varepsilon_{R2}-\varepsilon_{R1})C_2}{\sigma^{m_2}}\left(\frac{E_1'}{E_2}f_1 + f_2\right)^{m_2} \tag{4}$$

where ε_{R1} and ε_{R2} are the crack initiation strains of the porous structures L_1 and L_2, respectively, $C_1, m_1, C_2,$ and m_2 are material constants related to L_1 and L_2, E_1 and E_2 are the stiffness values of L_1 and L_2, respectively, and f_1 and f_2 are the volume fractions of L_1 and L_2, respectively. When the stiffness of L_1 is higher than that of L_2 (i.e., $E_1 > E_2$), it can be deduced from Equation (4) that the fatigue life of the functionally graded structure can be improved by increasing the volume fraction of E_1 (f_1). Since we have a graded strut thickness (*i.e.*, graded stiffness) here, the dual-layer model cannot be directly applied. However, a simplified version of the problem could be considered in which the S0402 specimens are made of three uniform structures with three different strut thicknesses ($s_1 > s_2 > s_3$) and their corresponding relative densities ($d_1 > d_2 > d_3$). If the volume fractions of these three structures are respectively given as $v_1, v_2,$ and v_3, the apparent density, d_a, of the whole structure can be determined as:

$$d_a = d_1v_1 + d_2v_2 + d_3v_3 = d_1v_1 + d_2v_2 + d_3(1 - v_1 - v_2) \tag{5}$$

It is easy to deduce that there are many solutions to improve the volume fraction of the thicker struts, d_1, while keeping the same apparent density, d_a. For a continuously graded structure, there will be even more ways to increase the volume fraction of the thicker struts by tuning the variation function of the strut thickness. Consequently, in addition to adjusting the percentage of bending- and stretch-dominated structures [31], the fatigue life of AM porous structures could be increased through the optimization of functionally graded designs.

7.4.3. Future outlook

Many studies have shown that the mechanical response of Zn is highly strain rate sensitive [15, 16, 34, 35]. In general, the flow stress increases with the strain rate whereas the elongation decreases [11]. Given such a significant degree of strain rate sensitivity, the loading frequency used for the fatigue experiments may play a major role in determining the S-N curves. As only 15 Hz was used in this study, it is interesting to compare the results obtained here with those measured for lower loading frequencies, such as 5 or even 1 Hz. Furthermore, lower frequencies also lead to longer immersion times of the specimens in the medium, which is closer to the *in vivo* conditions experienced in the human body [36]. Different *in vitro* physiological environments [37] may also have an impact on the corrosion fatigue behavior of AM porous Zn. Furthermore, to better mimic the *in vivo* loading conditions, the experiments may need to be repeated in some other types of loading regimens, such as compression-tension, bending, and torsion.

7.5. CONCLUSIONS

AM porous Zn showed high relative fatigue strengths (0.7) in air, which further increased to 0.8 in r-SBF. The increased fatigue strength in r-SBF could be attributed to the accumulation of the corrosion products that reinforce the strut junctions and fill fatigue cracks. At $0.8\sigma_y$, the stiffness of the scaffolds remained constant and even increased because of the accumulation of the corrosion products. Furthermore, topological design was found to play an important role on the fatigue behavior of AM porous Zn. Functionally graded specimens showed increased values of normalized fatigue strength as compared to uniform designs, although the later had a higher relative density. This favorable fatigue performance underscores the potential of AM porous Zn as a promising load-bearing bone substituting biomaterial. Moreover, further improvement of the fatigue resistance of AM porous biodegradable metals maybe achieved by optimizing their topological design.

REFERENCES

[1] L. Zhang, G. Yang, B. N. Johnson, X. Jia. Three-dimensional (3D) printed scaffold and material selection for bone repair. Acta Biomater. 2019;84:16-33.

[2] S. M. Ahmadi, R. Hedayati, Y. Li, K. Lietaert, N. Tümer, A. Fatemi, C. D. Rans, B. Pouran, H. Weinans, A. A. Zadpoor. Fatigue performance of additively manufactured meta-biomaterials: The effects of topology and material type. Acta Biomater. 2018;65:292-304.

[3] S. M. Ahmadi, R. Kumar, E. V. Borisov, R. Petrov, S. Leeflang, Y. Li, N. Tümer, R. Huizenga, C. Ayas, A. A. Zadpoor, V. A. Popovich. From microstructural design to surface engineering: A tailored approach for improving fatigue life of additively manufactured meta-biomaterials. Acta Biomater. 2019;83:153-166.

[4] M. Lowther, S. Louth, A. Davey, A. Hussain, P. Ginestra, L. Carter, N. Eisenstein, L. Grover, S. Cox. Clinical, industrial, and research perspectives on powder bed fusion additively manufactured metal implants. Addit Manuf. 2019;28:565-584.

[5] Y. Li, H. Jahr, K. Lietaert, P. Pavanram, A. Yilmaz, L. I. Fockaert, M. A. Leeflang, B. Pouran, Y. Gonzalez-Garcia, H. Weinans, J. M. C. Mol, J. Zhou, A. A. Zadpoor. Additively manufactured biodegradable porous iron. Acta Biomater. 2018;77:380-393.

[6] Y. Li, J. Zhou, P. Pavanram, M. A. Leeflang, L. I. Fockaert, B. Pouran, N. Tümer, K. U. Schröder, J. M. C. Mol, H. Weinans, H. Jahr, A. A. Zadpoor. Additively manufactured biodegradable porous magnesium. Acta Biomater. 2018;67:378-392.

[7] Y. Li, P. Pavanram, J. Zhou, K. Lietaert, P. Taheri, W. Li, H. San, M. A. Leeflang, J. M. C. Mol, H. Jahr, A. A. Zadpoor. Additively manufactured biodegradable porous zinc. Submitted.

[8] P. Wen, Y. Qin, Y. Chen, M. Voshage, L. Jauer, R. Poprawe, J. Henrich Schleifenbaum. Laser additive manufacturing of Zn porous scaffolds: shielding gas flow, surface quality and densification. J Mater Sci Technol. 2018.

[9] Y. Qin, P. Wen, M. Voshage, Y. Chen, P. G. Schückler, L. Jauer, D. Xia, H. Guo, Y. Zheng, J. H. Schleifenbaum. Additive manufacturing of biodegradable Zn-xWE43 porous scaffolds: Formation quality, microstructure and mechanical properties. Mater Des. 2019;181:107937.

[10] A. Kopp, T. Derra, M. Müther, L. Jauer, J. H. Schleifenbaum, M. Voshage, O. Jung, R. Smeets, N. Kröger. Influence of design and postprocessing parameters on the degradation behavior and mechanical properties of additively manufactured magnesium scaffolds. Acta Biomater. 2019.

[11] G. Li, H. Yang, Y. Zheng, X.-H. Chen, J.-A. Yang, D. Zhu, L. Ruan, K. Takashima. Challenges in the use of zinc and its alloys as biodegradable metals: perspective from biomechanical compatibility. Acta Biomater. 2019.

[12] Y. Li, H. Jahr, X. Y. Zhang, M. A. Leeflang, W. Li, B. Pouran, F. D. Tichelaar, H. Weinans, J. Zhou, A. A. Zadpoor. Biodegradation-affected fatigue behavior of additively manufactured porous magnesium. Addit Manuf. 2019;28:299-311.

[13] Y. Li, K. Lietaert, W. Li, X. Y. Zhang, M. A. Leeflang, J. Zhou, A. A. Zadpoor. Corrosion fatigue behavior of additively manufactured biodegradable porous iron. Corros Sci. 2019;156:106-116.

[14] S. Zhu, C. Wu, G. Li, Y. Zheng, J.-F. Nie. Creep properties of biodegradable Zn-0.1Li alloy at human body temperature: implications for its durability as stents. Mater Res Lett. 2019;7:347-353.

[15] W. Bednarczyk, J. Kawałko, M. Wątroba, P. Bała. Achieving room temperature superplasticity in the Zn-0.5Cu alloy processed via equal channel angular pressing. Mater Sci Eng, A. 2018;723:126-133.

7

[16] H. Jin, S. Zhao, R. Guillory, P. K. Bowen, Z. Yin, A. Griebel, J. Schaffer, E. J. Earley, J. Goldman, J. W. Drelich. Novel high-strength, low-alloys Zn-Mg (<0.1wt% Mg) and their arterial biodegradation. Mater Sci Eng, C. 2018;84:67-79.

[17] J. Woodthorpe, R. Pearce. Microstructural observations on the frequency effect in the fatigue behaviour of superplastic Zn-Al eutectoid. Met Sci. 1977;11:103-108.

[18] Y. Chen, Z. P. Sun, X. Q. Yan, J. L. Huang, W. M. Long, S. X. Liu. Analysis on embrittlement phenomenon of flux cored Zn–Al wire. Mater Sci Technol. 2013;29:1017-1019.

[19] K. Lietaert, W. Baekelant, L. Thijs, J. Vleugels. Direct metal printing of zinc: from single laser tracks to high density parts. European Congress and Exhibition on Powder Metallurgy. European PM Conference Proceedings. Swerea KIMAB, Sweden: The European Powder Metallurgy Association; 2016. p. 1-6.

[20] R. Wauthle, J. van der Stok, S. Amin Yavari, J. Van Humbeeck, J.-P. Kruth, A. A. Zadpoor, H. Weinans, M. Mulier, J. Schrooten. Additively manufactured porous tantalum implants. Acta Biomater. 2015;14:217-225.

[21] A. Oyane, H.-M. Kim, T. Furuya, T. Kokubo, T. Miyazaki, T. Nakamura. Preparation and assessment of revised simulated body fluids. J Biomed Mater Res A. 2003;65A:188-195.

[22] A. P. Md. Saad, N. Jasmawati, M. N. Harun, M. R. Abdul Kadir, H. Nur, H. Hermawan, A. Syahrom. Dynamic degradation of porous magnesium under a simulated environment of human cancellous bone. Corros Sci. 2016;112:495-506.

[23] Y. C. Lin, Z.-H. Liu, X.-M. Chen, J. Chen. Uniaxial ratcheting and fatigue failure behaviors of hot-rolled AZ31B magnesium alloy under asymmetrical cyclic stress-controlled loadings. Mater Sci Eng, A. 2013;573:234-244.

[24] M. Kolluri, M. Mukherjee, F. Garcia-Moreno, J. Banhart, U. Ramamurty. Fatigue of a laterally constrained closed cell aluminum foam. Acta Mater. 2008;56:1114-1125.

[25] McCullough, Fleck. The stress–life fatigue behaviour of aluminium alloy foams. Fatigue Fract Eng Mater Struct. 2000;23:199-208.

[26] A. M. Harte, N. A. Fleck, M. F. Ashby. Fatigue failure of an open cell and a closed cell aluminium alloy foam. Acta Mater. 1999;47:2511-2524.

[27] S. J. Li, L. E. Murr, X. Y. Cheng, Z. B. Zhang, Y. L. Hao, R. Yang, F. Medina, R. B. Wicker. Compression fatigue behavior of Ti–6Al–4V mesh arrays fabricated by electron beam melting. Acta Mater. 2012;60:793-802.

[28] L. Yang, C. Yan, W. Cao, Z. Liu, B. Song, S. Wen, C. Zhang, Y. Shi, S. Yang. Compression-compression fatigue behaviour of Gyroid-type Triply Periodic Minimal Surface porous structures fabricated by Selective Laser Melting. Acta Mater. 2019.

[29] J. M. Gomez-Vega, E. Saiz, A. P. Tomsia, T. Oku, K. Suganuma, G. W. Marshall, S. J. Marshall. Novel Bioactive Functionally Graded Coatings on Ti6Al4V. Adv Mater. 2000;12:894-898.

7

[30] N. W. Hrabe, P. Heinl, B. Flinn, C. Korner, R. K. Bordia. Compression-compression fatigue of selective electron beam melted cellular titanium (Ti-6Al-4V). J Biomed Mater Res B Appl Biomater. 2011;99:313-320.

[31] S. Zhao, S. J. Li, S. G. Wang, W. T. Hou, Y. Li, L. C. Zhang, Y. L. Hao, R. Yang, R. D. K. Misra, L. E. Murr. Compressive and fatigue behavior of functionally graded Ti-6Al-4V meshes fabricated by electron beam melting. Acta Mater. 2018;150:1-15.

[32] Y. Li, H. Jahr, P. Pavanram, F. S. L. Bobbert, U. Puggi, X. Y. Zhang, B. Pouran, M. A. Leeflang, H. Weinans, J. Zhou, A. A. Zadpoor. Additively manufactured functionally graded biodegradable porous iron. Acta Biomater. 2019;96:646-661.

[33] X.-Y. Zhang, G. Fang, S. Leeflang, A. A. Zadpoor, J. Zhou. Topological design, permeability and mechanical behavior of additively manufactured functionally graded porous metallic biomaterials. Acta Biomater. 2019;84:437-452.

[34] M. Sikora-Jasinska, E. Mostaed, A. Mostaed, R. Beanland, D. Mantovani, M. Vedani. Fabrication, mechanical properties and in vitro degradation behavior of newly developed ZnAg alloys for degradable implant applications. Mater Sci Eng, C. 2017;77:1170-1181.

[35] P. Guo, F. Li, L. Yang, R. Bagheri, Q. Zhang, B. Q. Li, K. Cho, Z. Song, W. Sun, H. Liu. Ultra-fine-grained Zn-0.5Mn alloy processed by multi-pass hot extrusion: Grain refinement mechanism and room-temperature superplasticity. Mater Sci Eng, A. 2019;748:262-266.

[36] Q. Chen, G. A. Thouas. Metallic implant biomaterials. Mater Sci Eng R Rep. 2015;87:1-57.

[37] L. Liu, Y. Meng, A. A. Volinsky, H.-J. Zhang, L.-N. Wang. Influences of albumin on in vitro corrosion of pure Zn in artificial plasma. Corros Sci. 2019;153:341-356.

7

7

8

Additively manufactured functionally graded biodegradable porous iron

Here, we present the first ever report on AM functionally graded biodegradable porous metallic biomaterials. We made use of a diamond unit cell for the topological design of four different types of porous structures including two functionally graded structures and two reference uniform structures. Specimens were then fabricated from pure iron powder using selective laser melting (SLM), followed by experimental and computational analyses of their permeability, dynamic biodegradation behavior, mechanical properties, and cytocompatibility. It was found that the topological design with functional gradients controlled the fluid flow, mass transport properties and biodegradation behavior of the AM porous iron specimens, as up to 4-fold variations in permeability and up to 3-fold variations in biodegradation rate were observed for the different experimental groups. After 4 weeks of in vitro biodegradation, the AM porous scaffolds lost 5-16% of their weight. This falls into the desired range of biodegradation rates for bone substitution and confirms our hypothesis that topological design could indeed accelerate the biodegradation of otherwise slowly degrading metals, like iron. Even after 4 weeks of biodegradation, the mechanical properties of the specimens (i.e., E = 0.5-2.1 GPa, σ_y = 8-48 MPa) remained within the range of the values reported for trabecular bone. Design-dependent cell viability did not differ from gold standard controls for up to 48 h.[1]

8.1. Introduction

The emergence of additive manufacturing (AM) techniques has provided unprecedented opportunities for the fabrication of porous metallic bone substitutes with promising bone regeneration capabilities [1-3]. The topological design of AM porous biomaterials can be precisely controlled and customized [4] with the aim of mimicking the mechanical properties of bone [5], facilitating cell proliferation and differentiation, and ultimately enhancing bone tissue regeneration [6]. During the last few years, a large number of AM porous metallic biomaterials have been investigated including those made from titanium alloys [7-9], stainless steel [10], cobalt-chromium alloys [11], and tantalum [12]. Most of these porous biomaterials possess complex, yet highly ordered micro-architectures that are made of regular unit cells designed through polyhedral arrangements of multiple struts (*i.e.*, beam-like structural elements). This leads to a homogeneous distribution of material properties throughout the entire porous structure [13]. A homogenous distribution of material properties is, however, not consistent with what is found in human bone where highly graded and non-uniform micro-architectures are present [14]. All types of human bones (i.e., long, short, flat or irregular) show a gradual change in porosity from a compact outer cortical shell towards the spongy inner cancellous tissue. Other examples are the relative porosity and direction of trabecular structures in long bones (e.g., femoral head and neck region or distal radius), which are both highly graded and dependent on the local values of mechanical stimuli (*e.g.*, strain energy density) [15-19]. It is therefore imperative that AM porous biomaterials mimic the natural gradual structures of human bones, particularly given the fact that they will be eventually surrounded by pockets of bony tissue with gradual micro-architecture [20] and biomechanical performance [21]. Furthermore, meeting the incompatible and sometimes contradictory design requirements of bone substitutes is often impossible without allowing for graded designs. For example, recent studies have clearly indicated that bone substitutes need to possess a high level of porosity (and, thus, permeability) to facilitate nutrient perfusion and cell viability [22]. However, highly porous scaffolds usually exhibit inadequate mechanical strength and low cell seeding efficiency [23]. Reconciling these contradictory design requirements limits the application of uniform topologies and calls for graded designs [24].

In addition to the above-mentioned advantages, functionally graded porous structures exhibit higher strength, ductility, and energy absorption capacity as compared to those of uniform porous structures [21, 24-26]. The deformation behavior of functionally graded porous structures has been found to be smooth and continuous (during compression) without the formation of diagonal shear bands [21, 27]. Finally, AM graded porous scaffolds have been found to result in high cell seeding efficiency [22, 23, 28] and to accelerate bone defect regeneration [29, 30].

Although graded designs of AM porous biomaterials made from non-biodegradable metals such as titanium or cobalt-chrome alloys can improve the short-term performance of bone substitutes, they may hinder full regeneration of bony defects, given that part of the mechanical load will be permanently carried by the implant. Moreover, foreign objects, such as metallic implants, may elicit constant physical irritation and chronic local inflammation [31], which may necessitate revision surgery. Finally, non-biodegradable implants inflict the perpetual risk of incurring usually recurrent and difficult-to-treat implant-associated infections upon patients [32].

AM porous biomaterials made from biodegradable metals could solve the above-mentioned problems. However, only a few reports of direct printing of topologically ordered porous biodegradable metals are available. The first papers on this topic have appeared very recently [33-38], with direct metal printing (i.e., selective laser melting) being used for the fabrication of AM porous magnesium alloys, iron, iron-based alloys and zinc. AM of functionally graded, biodegradable metals has, however, not yet been reported.

Here, for the first time, we report the direct printing of a functionally graded biodegradable porous metal (*i.e.*, pure iron) using selective laser melting (SLM). Among biodegradable metals, inexpensive pure iron is a promising material and as it does not release hydrogen during biodegradation [39]. While a number of animal studies have shown good biocompatibility of iron-based biomaterials [40, 41], their low *in vivo* degradation rate [41] is a clear disadvantage. However, AM porous metallic biomaterials generally have much larger surface areas as compared to their solid counterparts [42], which would be an important advantage for the materials that otherwise degrade too slowly, such as iron and its alloys. Moreover, as the biodegradation behavior of AM porous iron is topology-dependent, the presence of a functional gradient opens up new opportunities for adjusting the biodegradation behavior of porous iron. We, therefore, designed and additively manufactured four groups of AM porous iron specimens, namely two types of functionally graded porous specimens and two uniform (*i.e.*, reference) porous specimens. We then performed a comprehensive study on the mechanical behavior, permeability, biodegradation behavior, and cytocompatibility of these four groups using computational and experimental approaches.

8.2. Material and methods

8.2.1. Scaffold manufacturing and post processing

Four different types of specimens (Figure 1a, b) based on a 1.4 mm diamond unit cell were designed using the software Element (nTopology, USA). The experimental groups included a uniform structure with a 0.2 mm strut thickness (S0.2), a functionally graded

porous structure with a strut thickness changing from 0.2 mm on the periphery to 0.4 mm in the center (Dense-in), a functionally graded porous structure with strut thickness starting from 0.4 mm on the periphery and decreasing to 0.2 mm in the center (Dense-out), and a uniform porous structure with a strut thickness of 0.4 mm (S0.4) (Figure 1a). Specimens were produced with a ProX DMP 320 machine (3D Systems, Belgium). The iron powder employed was gas atomized in nitrogen (Material Technology Innovations Co., Ltd., China) and had the following characteristics: purity: 99.88%; particle sizes: D10 = 32 μm, D50 = 48 μm, and D90 = 71 μm; morphology: spherical; apparent density: 4.09 g/cm^3; tap density: 4.88 g/cm^3; angle of repose: 157 °; carbon content: 0.0044%. The specimens were built employing a layer thickness of 30 μm on a steel baseplate. Contour and hatch vectors were used as the scanning strategy (energy densities: 0.33 W/mm and 0.65 W/mm, respectively) for most of the specimen, except for the specimens with 0.2 mm thick struts, in which case only contour was needed. Specimen removal was performed by means of electrical discharge machining (EDM). Powder particles entrapped in pores were removed through ultrasonic cleaning in 96% ethanol for 20 min. Then, the specimen were chemically cleaned in 50% HCl for 1 min to remove residuals from EDM and loose powder particles, followed by 5 min ultrasonic cleaning in 96% ethanol to wash the residual HCl out.

8.2.2. Morphological characterization

The iron scaffolds were imaged using micro-computed tomography (micro-CT) (Quantum FX, Perkin Elmer, USA) at a tube current of 180 μA, a tube voltage of 90 kV, a scan time of 3 min, and a resolution of (30 μm)^3 with a total of 3600 projections. Micro-CT images were automatically reconstructed and converted into a series of 2D images using Analyze 11.0 (Perkin Elmer, USA). The images were subsequently exported to FIJI (NIH, Bethesda, MD, USA) and locally thresholded using the Bernsen algorithm (radius = 20). This allowed for accurate segmentation of the scaffolds and capturing their morphological features. Afterwards, a number of circular regions of interest (ROIs) with a diameter of 10 mm were created on the cross-section of the scaffolds. The porosity (defined as the ratio of the void volume to the scaffold volume), average strut thickness (Tb.Th), and average strut spacing (Tb.Sp) (*i.e.*, pore size), were then calculated using BoneJ (a plugin of FIJI).

In addition, a weighing method was used to determine the porosity of the specimens of the four groups based on the following equation: *Porosity* $= 1 - (W_{iron}/V_{bulk})/\rho_{iron}$, where W_{iron} is the weight of the specimen, V_{bulk} the bulk volume of the scaffold, and ρ_{iron} the theoretical density of pure iron.
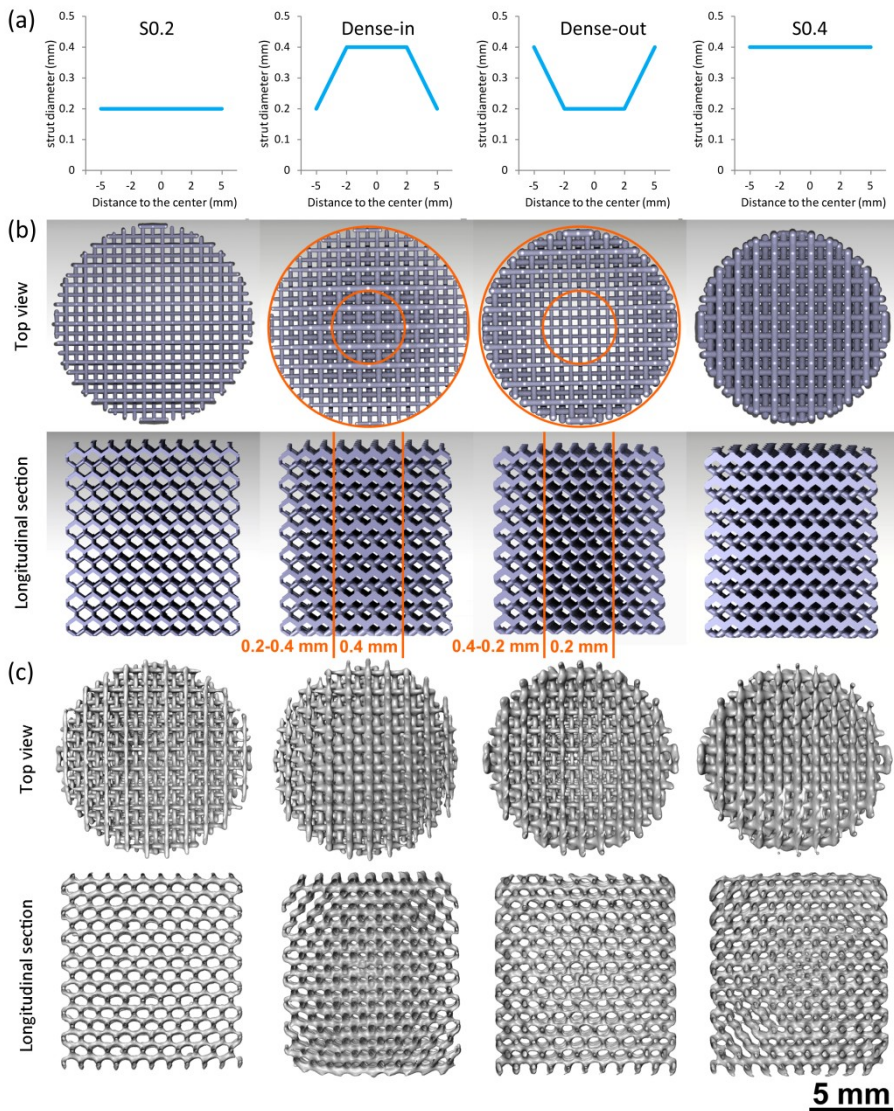
Figure 1. The four different topological designs of the specimens from the S0.2, Dense-in, Dense-out, and S0.4 groups: (a) strut size distribution, (b) top view and longitudinal cross-section of the CAD models, and (c) the micro-CT reconstructions of the AM porous iron specimens.

8.2.3. Microstructural characterization

The microstructures of both thin and thick struts of the as-built specimens were examined using a digital optical microscope (Keyence VHX5000) after etching by a 5%

Nital reagent (5 ml HNO$_3$ per 100 ml C$_2$H$_5$OH). The average grain size was measured using the line intercept method (based on three randomly chosen lines).

8.2.4. Permeability measurements

The falling head method was used, where a standpipe provided the water head and a pressure gauge measured the water pressure at the bottom of the standpipe. We used a vacuum pump to fill the standpipe with water, a chamber to host the scaffold, and a reservoir for water collection (Figure 2a). The water pressure was measured just above the porous biomaterial and registered every two seconds in LabView (v.11.0). The measured pressure corresponded to the momentary height of the water column. Three specimens from each of the four experimental groups were used for permeability measurements. The permeability, k, was calculated using the following equation [43]:

$$k = \frac{a}{A}\frac{L}{t}In\frac{H_1}{H_2}\frac{\mu}{\rho g} = \frac{B}{A}\Big/t$$

where a and A are, respectively, the cross-sectional areas of the standpipe and the specimen, L is the height of the specimen, H_1 and H_2 are the water levels at time points t_0 and t_i, respectively, t equals to $t_i - t_0$, and μ and ρ are the dynamic viscosity and density of water, respectively. B/A was plotted against time and extrapolated using a power function until the velocity of water approached zero. Then, the slope of this graph was used to calculate the permeability coefficient. As Darcy's law is only applicable when the Reynold's number is below 10, the slope was only taken in the region where the Reynolds number was between 1 and 10.
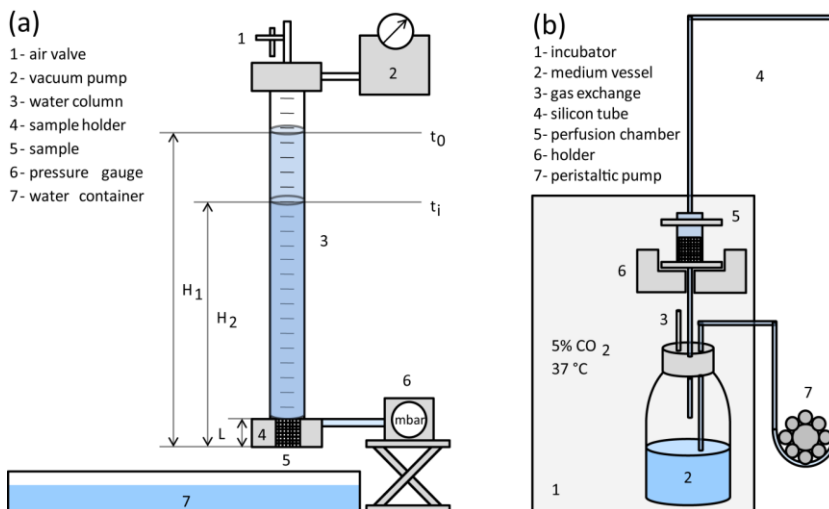

Figure 2. Setups used for permeability measurements (a) and dynamic biodegradation tests (b).

Computer simulations were performed on AM porous iron models using the computational fluid dynamics (CFD) solver of Abaqus (Dassault System Simulia Corp, France). Steady-state Navier-Stokes equations were used to describe the flow problem. A velocity of 0.0125 m/s was applied to the inlet to ensure that fluid flow remained laminar throughout the scaffold, and an outlet pressure of 0 Pa was defined. A no-slip wall condition was set for the material/fluid interface areas. Water (density = 1000 kg/m^3 and viscosity = 0.001 Pa·s) was considered to be the working fluid. The average pressure at the inlet region was extracted to be used in Darcy's equation to determine the permeability coefficient.

8.2.5. Dynamic biodegradation tests

Dynamic *in vitro* biodegradation tests were conducted for up to 28 days in a custom-built bioreactor (Figure 2b) using pre-equilibrated (5% CO_2, 20% O_2, 37 °C) revised simulated body fluid (r-SBF) [44] at a flow rate of 0.3 ml/min to mimic moderate physiological fluid movement in bone [45-47]. Upon removing specimens from the r-SBF solution, weight loss was determined after ultrasonic cleaning with 99% acetone and 96% ethanol, for 30 min each, and air-drying at room temperature (dry weight with an accuracy of 0.1 mg). Medium pH values (accuracy: ± 0.002) were registered after 28 days *in vitro* (InLab Expert Pro-ISM, METTLER TOLEDO). Concentrations of Fe, Ca, and P ions in the solution were analyzed using an inductively coupled plasma optical emission spectroscope (ICP-OES, iCAP 6500 Duo, Thermo Scientific).

8.2.6. Characterization of biodegradation products

Phase identification of the biodegradation products was performed using an X-ray diffractometer (XRD, Bruker D8 Advance diffractometer in Bragg-Brentano geometry). The diffractometer was equipped with a graphite monochromator and a Vantec position-sensitive detector and operated at 45 kV and 35 mA with a step size of 0.035° and a dwell time of 10 s per step using Co Ka radiation. The morphologies and compositions of the biodegradation products on the surface of the specimens after the biodegradation tests were analyzed with a scanning electron microscope equipped with an energy-dispersive X-ray spectroscope (EDS) (SEM, JSM-IT100, JEOL). In addition to observing the biodegradation products, the specimens were ultrasonically cleaned in ethanol and cut to observe the morphologies of the struts both at the periphery and in the center.

8.2.7. Mechanical characterization

Compression tests at a crosshead speed of 2 mm/min were carried out using an Instron mechanical testing machine equipped with a 10 kN load cell. The mechanical properties of the AM porous iron specimens before and after the biodegradation tests were

8

determined according to ISO 13314:2011 and the quasi-elastic gradient (hereafter referred to as the elastic modulus) and yield strength were obtained. The elastic moduli of the porous structures were determined as the slope of the initial linear part of the stress-strain curve using linear fitting in the software Origin (OriginLab Corporation, USA). The initial linear part of the stress-strain curve was offset by 0.2% and its intersection with the stress-strain curve was taken to calculate the yield strength. The tests were performed in triplicate per specimen design and the mean values of the elastic modulus and yield strength were calculated as well as their standard deviations.

Simulations with the finite element method (FEM) were conducted using the commercial software package Abaqus (Dassault System Simulia Corp, France) to study the stress distributions in the specimens. Quarter-symmetric discretized models were built using a tetrahedron element (C3D10). The symmetry boundary conditions were defined on the longitudinal sections of the quarter-symmetric model. The top surface of the model was compressed to a displacement of 0.4 mm. The contours of the von Mises stress of the models were extracted to study the stress concentrations.

8.2.8. Cytocompatibility

The human osteoblast-like cell line MG-63 (ATCC, CRL-1427) was used for cytocompatibility analysis. Cells were cultured in Dulbecco's modified Eagle's medium with low glucose (100 mg/L, DMEM LG) (Sigma) with 10% fetal calf serum (PAN Biotech) (DMEM LG+) at 37 °C, 20% O_2, 5% CO_2 and 95% humidity (physiological conditions). Cells were passaged at 80% confluency. After cleaning, all the scaffolds were sterilized for 30 min by immersion in 100% isopropanol (Merck; Darmstadt, Germany). All specimens were extracted at 37°C for up to 72 h (EN ISO 10993-12 mod.) and extracts (10×) were compared to extracts (1×) from Ti6Al4V control scaffolds [34]. For cytotoxicity testing, extracts were sterile filtered (0.2 µm) and the MTS assay was described in detail in our earlier publication [34], using Dimethyl sulfoxide (DMSO) (20%) as positive control [48]. Two million MG-63 cells in 600 µL DMEM LG were seeded per specimen. After 15 min, 10 ml of fresh DMEM LG+ was added and specimens incubated under physiological conditions for another 4 h. Cell-seeded scaffolds were then cut along their sagittal axis to access their central region and fluorescent staining was performed as described previously by us [34]. For SEM analysis, cell-seeded scaffolds were rinsed with 1× phosphate buffered saline and fixed for 1 h in 3% glutaraldehyde (Agar Scientific, Wetzlar, Germany) in 0.1 M Soerensen's phosphate buffer (Merck, Darmstadt, Germany) at room temperature. Fixed scaffolds were dehydrated in 30, 50, 70, 90 and 100% ethanol, for 10 min each (last step twice). Samples were then air-dried at room temperature and the sagittal cut surface of the central region sputter-coated (Sputter Coater EM SCD500, Leica, Wetzlar, Germany)

with 12.5 nm of gold-palladium and imaging at 10 kV in SEM (ESEM XL 30 FEG, FEI, Eindhoven, The Netherlands).

8.2.9. Statistical analysis

The optical density data (*i.e.*, MTS assay data) were normalized with respect to their corresponding controls. The obtained values of the relative cytotoxicity were then analyzed using a two-way ANOVA test ($\alpha = 0.05$) followed by a post-hoc test (*i.e.*, Tukey's multiple comparisons test, $\alpha = 0.05$). Statistical significance is indicated as $p < 0.0001$, ****; $p < 0.001$, ***; $p < 0.01$, **; $p < 0.05$, *; *n.s.* = not significant.

8.3. Results

8.3.1. Morphological characteristics

The porosity values measured by using micro-CT and weighing were similar to each other (Table 1). All the specimens had 6-9% less porosity than their nominal (*i.e.*, designed) values. As compared to the design values, the strut sizes were about ≈50 µm larger and the pore sizes were ≈50 µm smaller (Table 1). Reconstructed 3D models from micro-CT images confirmed that the strut thickness was radially graded for the specimens of the Dense-in and Dense-out groups, while the strut thickness remained uniform for the specimens of the S0.2 and S0.4 groups (Figure 1c). The graded struts can be clearly observed in SEM image (Figure S1).

Table 1- Topological characteristics of AM iron scaffolds.

AM iron scaffold	Strut size(µm)		Pore size (µm)		Porosity (%)		
	Design	µCT	Design	µCT	Design	µCT	Weight
S0.2	200	257±3	800	755±2	90.9	84.8±0.1	84.6±0.4
Dense-in	200-400	387±1	800-600	609±11	79.5	70.6±0.4	69.7±0.2
Dense-out	400-200	386±5	600-800	635±1	79.5	71.0±0.2	70.3±0.5
S0.4	400	461±4	600	506±11	67.0	58.4±2.0	58.9±0.3

8.3.2. Microstructure of the scaffolds

The AM iron had fine grains with an average size of 12 ± 0.3 µm (Figure 3a) for the 0.4 m struts and 10.8 ± 1.4 µm for the 0.2 mm struts (Figure 3b).
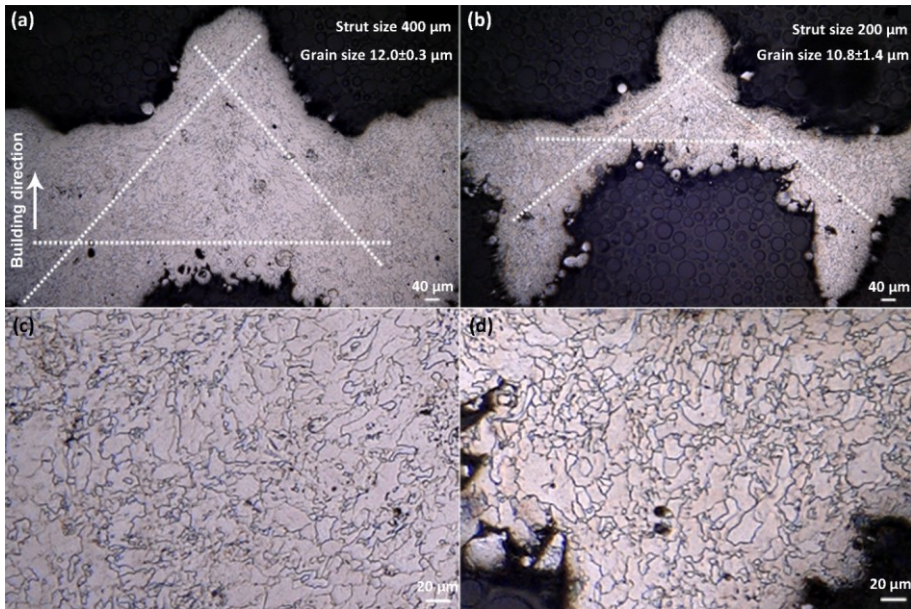
Figure 3. Microstructures of the AM iron scaffolds with struts having a diameter of 400 μm (a, c) and 200 μm (b, d).

8.3.3. Permeability and velocity distribution

The order from the highest permeability of the AM iron specimens to the lowest was as follows: S0.2, S0.4, Dense-in, and Dense-out (Figure 4a). Although the permeability values predicted by the CFD simulations were generally higher than the experimental results, they were well correlated to each other (R^2 =0.84) (Figure 4b). The flow velocity distribution showed that the fluid velocity was homogeneous inside the specimens of the S0.2 and S0.4 groups (Figure 4c). As for the functionally graded designs, the Dense-in specimens exhibited higher velocities at the periphery than at the center, while the opposite was true for the Dense-out specimens. Flow velocities values higher than the input velocity (*i.e.*, 0.0125 m/s) were also observed in the specimens (Figure 4c).
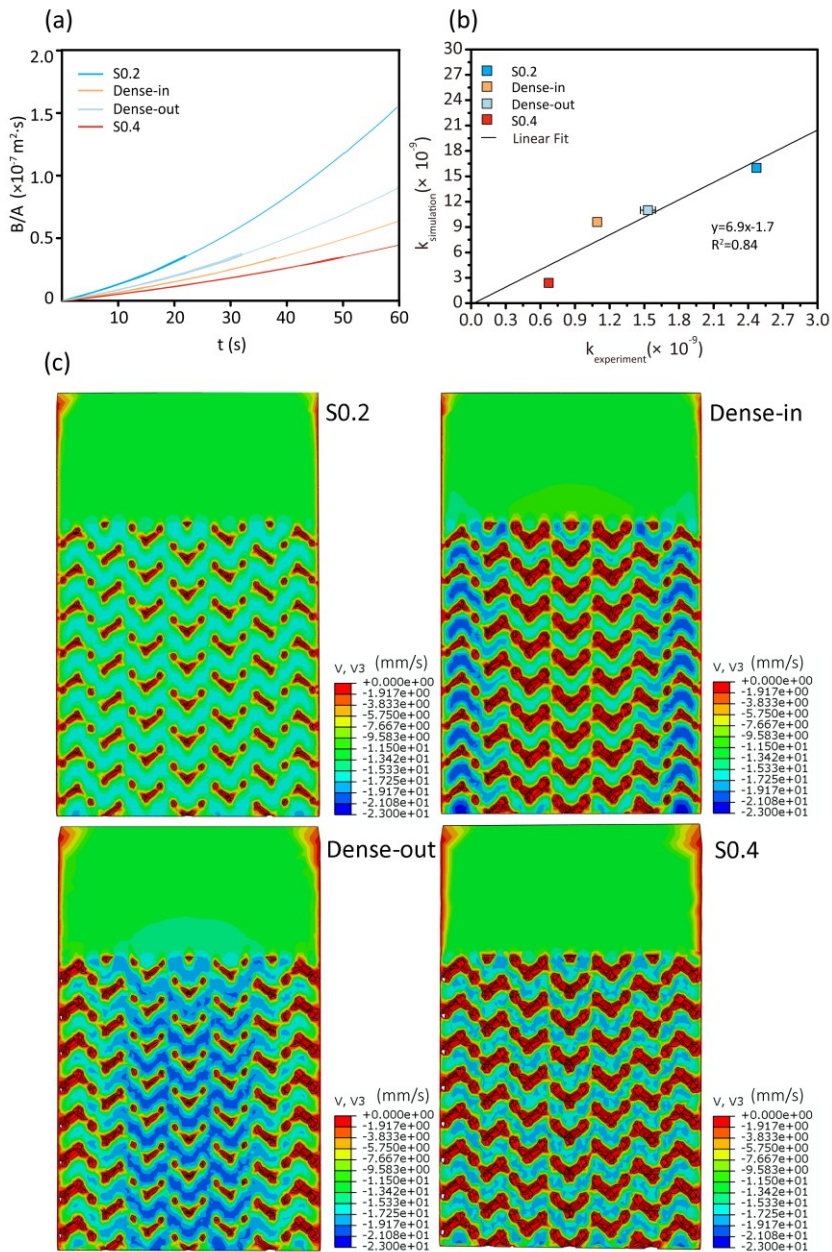
Figure 4. Results from the permeability tests and CFD simulations of the AM porous iron scaffolds with the different topological designs: experimental results (a), permeability values (b), and velocity distributions predicted by the CFD models (c).

8.3.4. In vitro dynamic biodegradation behavior
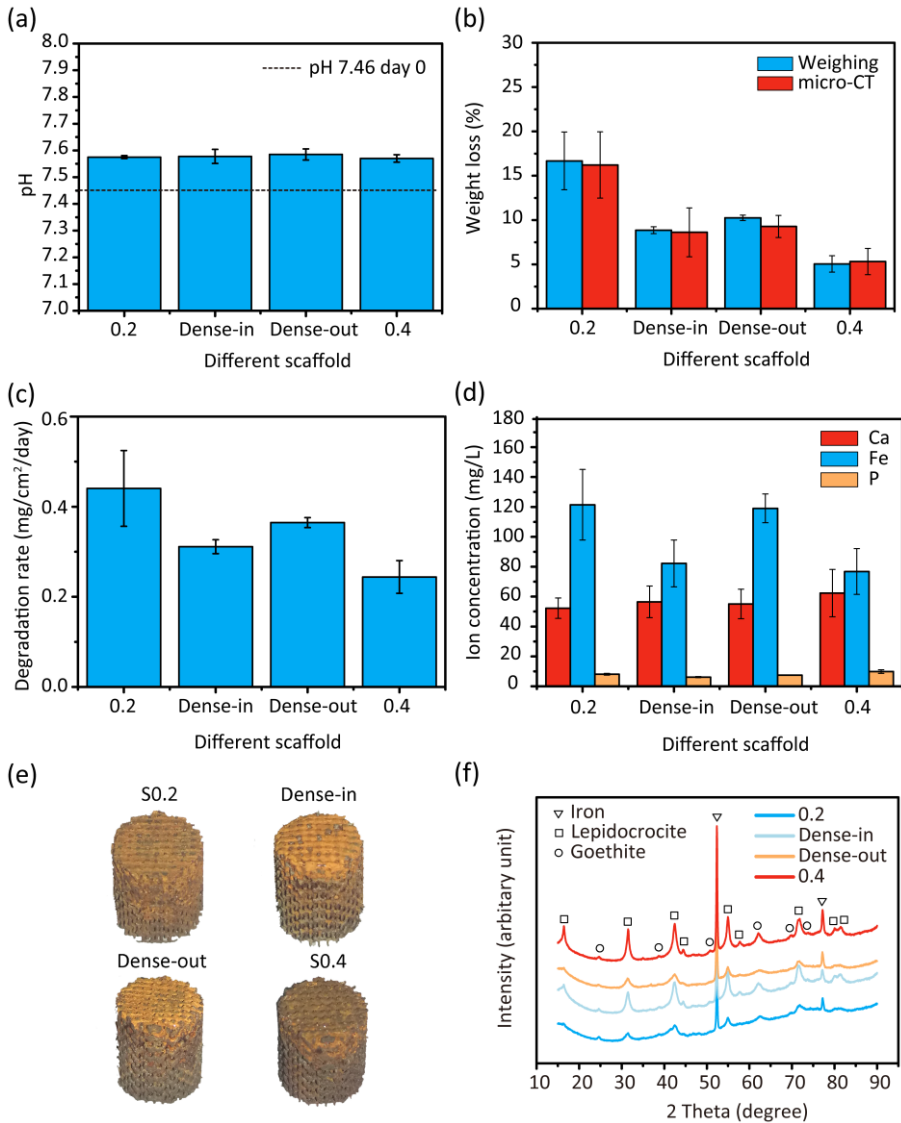
Figure 5. Results from the dynamic biodegradation tests for 28 days: pH value (a), weight loss (b), biodegradation rate (c), ion concentration (d), the appearance of the specimens (e), and XRD patterns (f).

After 28 days of dynamic immersion, the pH values of the r-SBF solution increased marginally from 7.5 to around 7.6. There were no large differences between the pH values observed for the specimens of the different groups (Figure 5a). The specimens of

the S0.2 group exhibited a weight loss of 16.7 ± 3.3%, which was the highest among all the experimental groups (Figure 5b). The specimens of the group S0.4 had the lowest values of weight loss (*i.e.*, 5.1 ± 0.9%), which was about one-third of the maximum value (Figure 5b). The weight loss of the specimens of the Dense-in and Dense-out groups lay between the extreme values, with the Dense-out specimens showing somewhat a higher value of weight loss (*i.e.*, 10.3 ± 0.3%) than the Dense-in specimens (*i.e.*, 8.9 ± 0.4%) (Figure 5b). After normalizing the biodegradation rate by the surface area of the specimen, the ranking of the biodegradation rate was the same as that based on weight reduction (Figure 5c). The specimens of the S0.2 group had a higher Fe ion concentration in the r-SBF than those of the S0.4 group, while the Dense-out specimens had a higher Fe ion concentration than the Dense-in ones (Figure 5d). After 28 days, the concentrations of Ca and P ions decreased from the initial values of 100 mg/L and 31 mg/L, respectively, to around 50 mg/L and 10 mg/L, respectively (Figure 5d).

8.3.5. Characterization of biodegradation products
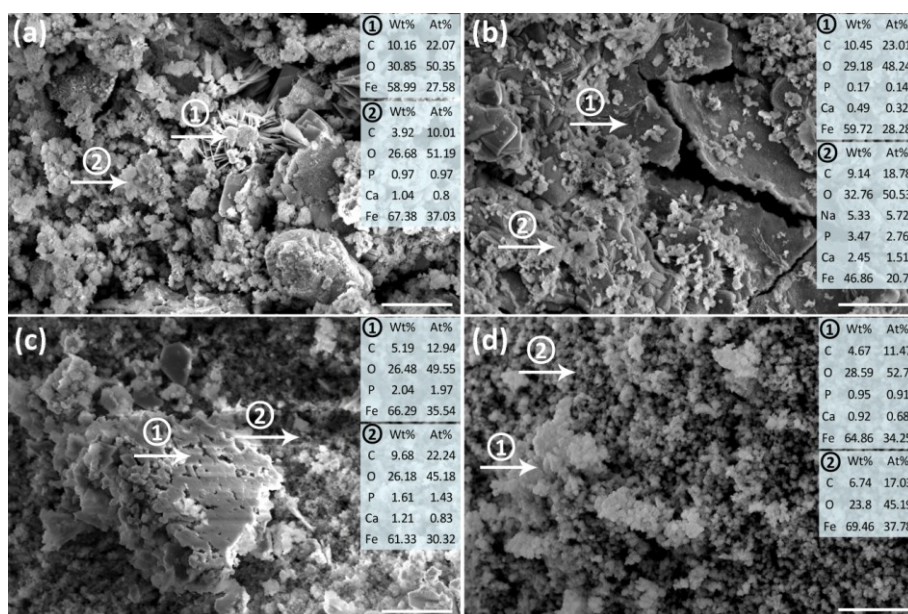
Figure 6. Morphologies and chemical compositions of the biodegradation products formed on the AM porous iron specimens after 28 days: (a) S0.2 (b) Dense-in (c) Dense-out, and (d) S0.4. Scale bar: 10 μm.

Brownish biodegradation products accumulated on the surfaces of all the specimens after 28 days of biodegradation (Figure 5e). The biodegradation products contained lepidocrocite [*i.e.*, γ-FeO(OH)] and goethite [*i.e.*, α-FeO(OH)] (Figure 5f). However,

the intensity peaks of these biodegradation products in the XRD patterns were relatively low. SEM analysis of external struts showed that, after 28 days of immersion, two types of biodegradation products were formed on the surface: grey earth-cracking-like layers at the bottom and pockets of white loose compounds on the top (Figure 6). EDS analysis indicated that the grey biodegradation products contained C, O, and Fe, while the white biodegradation products contained P, Ca (Figure 6), and sometimes Na (Figure 6b).
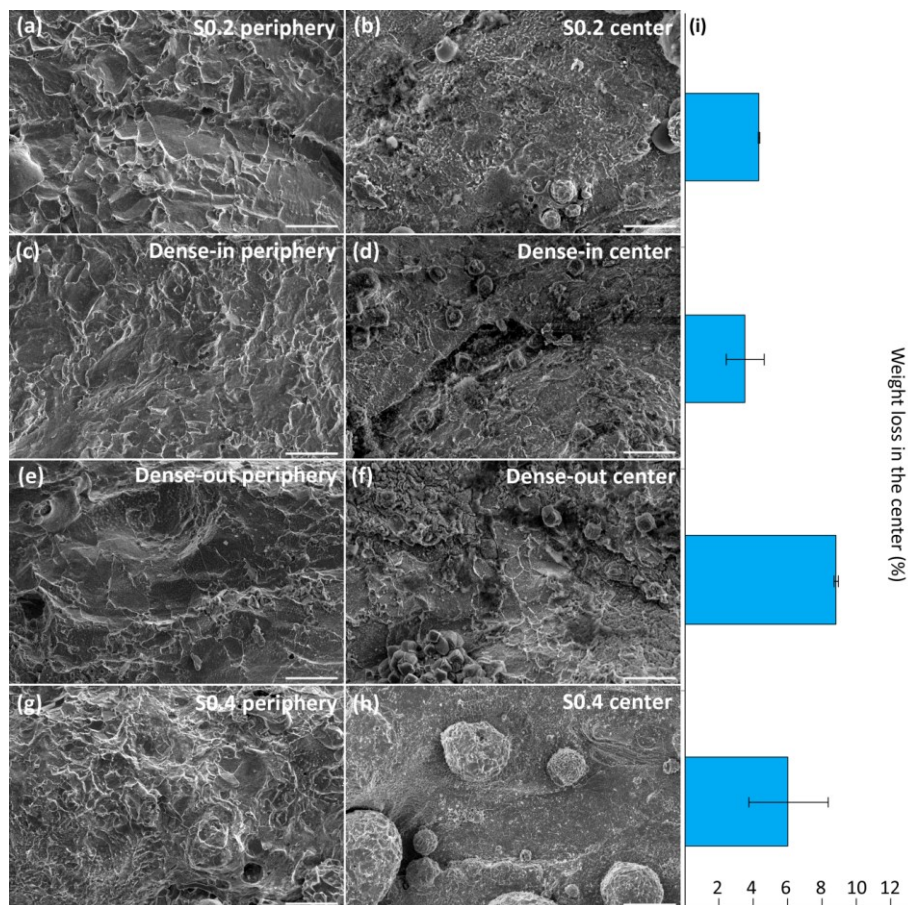
Figure 7. Morphologies of the biodegraded AM porous iron specimens after cleaning on the periphery (left) and in the center (right): S0.2 (a, b), Dense-in group (c, d), Dense-out group (e, f), S0.4 group (g, h), and the weight losses of the specimens of the different groups in the center (i) after immersion for 28 days. Scale bar: 10 μm.

Different biodegradation behaviors were observed from the center to the periphery of the specimens (Figure 7). After disintegrated degradation products on the struts were

removed, the grain boundaries became clearly visible. In the case of the specimens from the S0.2, S0.4, and Dense-in groups, the grain structure turned out to be better definable on the periphery of the specimens (Figure 7a, c, and g) than in their center (Figure 7b, d, and h). Moreover, the center of all the specimens contained some remnants of the biodegradation products even after cleaning (Figure 7b, d, f, h). We further assessed the volume losses of the specimens in the center using micro-CT and found that the Dense-out specimens had a larger weight reduction than the S0.2 specimens, even though their geometry were exactly the same in the center (Figure 7i). The specimens of the S0.4 group degraded faster than the Dense-in specimens, although they had the same geometry in the center (Figure 7i).

8.3.6. Mechanical properties
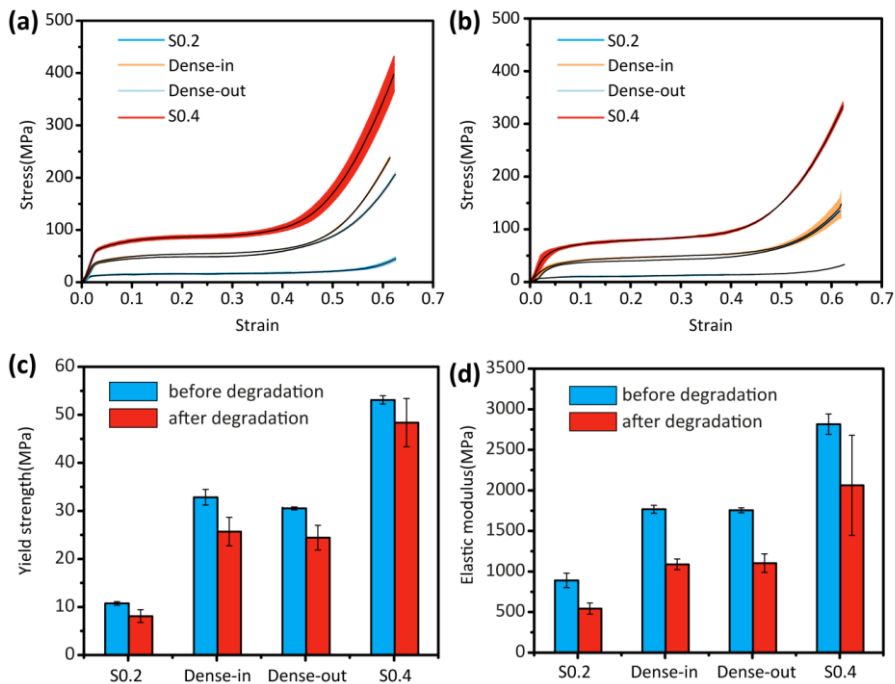
Figure 8. Mechanical properties of the AM porous iron specimens before and after biodegradation for 28 days: (a) stress-strain curves before biodegradation, (b) stress-strain curves after biodegradation, (c) yield strengths, and (d) elastic moduli.

Under uniaxial compression, all the specimens exhibited smooth stress-strain curves without sudden fluctuations after yielding, both before (Figure 8a) and after (Figure 8b) biodegradation tests. All the stress-strain curves followed similar patterns, starting with

a linear elastic region and continuing with a rapidly decreasing slope until a plateau stage with almost no fluctuations was reached (Figure 8a, b). A densification phase ultimately resulted in a rapid increase in stress (Figure 8a, b). Among all the experimental groups, the S0.4 group possessed the largest values of yield strength (53.1 ± 0.9 MPa) and elastic modulus (2815.9 ± 126.6 MPa), while the S0.2 group exhibited the lowest values of yield strength (10.7 ± 0.4 MPa) and elastic modulus (891.6 ± 89.7 MPa) (Figure 8c, d). The mechanical properties of the functionally graded groups fell between those of the S0.4 and S0.2 groups (Figure 8c, d). The Dense-in scaffolds had somewhat higher values of yield strength (32.9 ± 1.6 MPa) and elastic modulus (1767.3 ± 48.5 MPa) than the Dense-out specimens (30.5 ± 0.3 MPa & 1754.4 ± 30.8 MPa) (Figure 8c, d). Yield strengths and elastic moduli of all the specimens decreased after 4 weeks of biodegradation (Figure 8c, d).
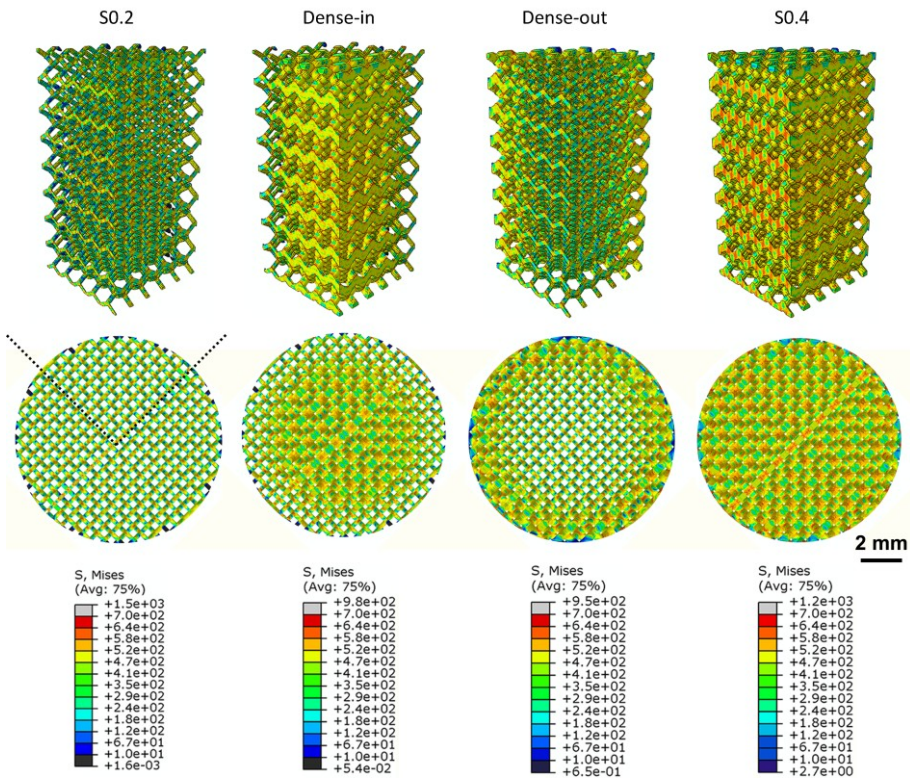

Figure 9. Distributions of the von Mises stress in the AM porous iron specimens at 0.4 mm displacement under compression predicted by FE modeling.

FEM simulations showed that von Mises stresses were uniformly distributed in the S0.2 and S0.4 specimens (Figure 9), while the Dense-in and Dense-out specimens had

more stress concentrations in their thicker struts. Moreover, at the same level of displacement, the Dense-in and Dense-out specimens showed lower values of the maximum von Mises stress than those observed for the S0.2 and S0.4 specimens.

8.3.7. Cytocompatibility

To evaluate the potential of AM porous pure iron specimens for biomedical applications, we performed biocompatibility testing (Figure 10). Relative cellular activity of human osteoblast-like MG-63 cells in extracts from the different types of iron scaffolds (a-d) was compared to that of control extracts from bio-inert Ti-6Al-4V. Cell viable in 24 h-extracts was >75% for all iron specimens, independent of their structural differences: 77.8% (S0.2), 79.2% (Dense-in), 82.2% (Dense-out) and 86.5% (S0.4). Interestingly, while the cell viability in extracts from other specimen types gradually decreased in an extraction time-dependent manner, cell viability in S0.4 extracts remained at almost 70% even after 48 h of extraction and did not significantly differ from Ti-6Al-4V controls (Figure 10d). MG-63 viability in extended, long-term extracts (72 h) of iron specimens dropped to below 50%, while Ti-6Al-4V extracts did not reveal significant cytotoxicity.

Direct cytocompatibility assessment revealed fluorescently labeled adhered cells at the periphery as well as in the center of the scaffolds. However, when comparing specimens of the different groups no design-specific cell distribution pattern could be identified (Figure 10e). Gradients in strut thickness (i.e., dense-in vs. dense-out) did not obviously influence regional cell seeding density. SEM images of MG-63 cells, 24 h after seeding, revealed a well-spread polygonal cell morphology with cytoplasmic projections attached to the surfaces of the iron scaffolds (Figure 10f, box).

8.4. Discussion

AM porous metallic biomaterials should meet multiple contradictory design criteria that are often difficult to reconcile without sacrificing one or the other to some extent. Here, we report for the first time how functional gradients can be used to meet these design requirements through directly printing a biodegradable porous iron biomaterial. The biodegradation of iron *in vivo* is generally slow, meaning that we should try to exploit topological design to increase the biodegradation rate of AM porous iron while ensuring sufficient mechanical support and proper nutrient transport. Our results clearly show that with the aid of topological design ideas in general and functional gradients in particular, the biodegradation rate and mass transport properties (*i.e.*, permeability) of AM porous iron can be increased while maintaining the bone-mimicking mechanical properties of these biomaterials.

8
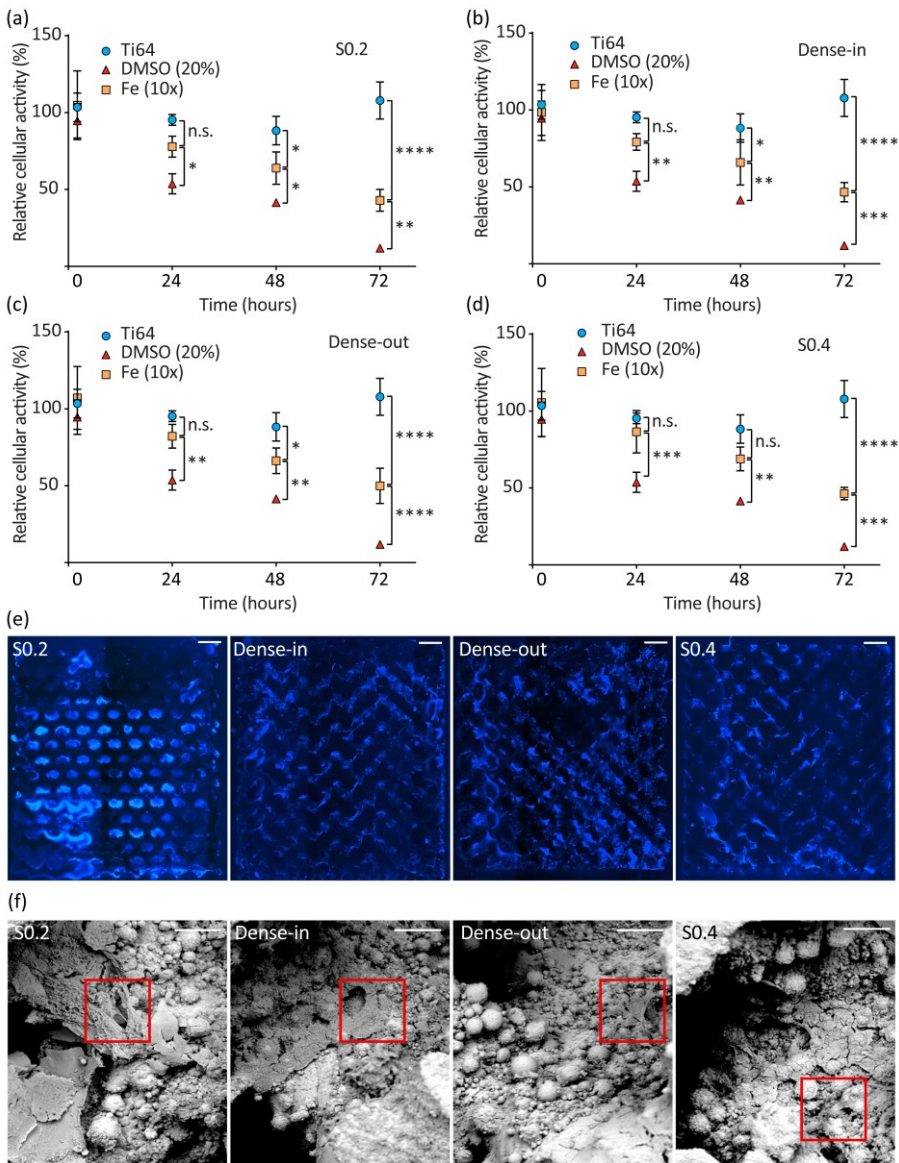
Figure 10. Cell distribution and cytocompatibility. Relative cytocompatibility (%) of different groups of iron specimens was assessed against titanium controls: S0.2 group (a), Dense-in group (b), Dense-out group (c), and S0.4 group (d). Fluorescently stained MG-63 cells on different AM porous iron specimens (e), and SEM analysis (f), respectively. Scale bar: 1 mm (e) and 100 μm (f). *n.s.,* not significant; *, $p < 0.05$; **, $p < 0.01$; ***, $p < 0.001$; ****, $p < 0.0001$.

8.4.1. Morphology and microstructure

All the topological designs of porous iron could be directly printed with the morphological parameters that were close to the design values. Due to thickened struts, the actual porosities were slightly lower than the design values for all the groups. As a strut thickness of 200 μm is quite thin, the actual strut diameter was nearly 60 μm larger than the design value, even when the contour scanning strategy was used. On the other hand, under the printing conditions used, the reproducibility of the scaffolds was high (with a standard deviation of 5% or lower).

As to the microstructure, micro melt pools formed during SLM [49], leading to high cooling rates (10^3-10^8 K/s) [50], which resulted in a non-equilibrium solidification process and refined grains (*i.e.*, 10-12 μm, in this study). As no large differences between the grain sizes of thick and thin struts were found, the different biodegradation behaviors of the different experimental groups were unlikely caused by their microstructures, but rather by their porous architectural features. Moreover, unlike previously reported AM solid iron [51, 52], our AM porous iron specimens did not exhibit obvious elongated grains along the build direction, which can also be seen by Electron Back-Scattered Diffraction (EBSD) analysis in our former paper [38]. This suggests that the effects of any directional solidification processes were not as strong as in the case of solid counterparts, particularly given that the struts of our scaffolds were built in a tilted orientation. The reason for this could be that there was limited overlap between the melt pools of different layers during the SLM process when the strut was tilted (Figure S2).

8.4.2. Permeability

As expected, permeability was highly dependent on the porosity of the specimen and influenced by porosity distribution on the transverse section. According to the Kozeny-Carman equation, the relationship between the permeability, k, porosity, φ, and the specific surface area, S_V, (*i.e.*, surface to volume ratio) of a porous structure is given by: $k = C_K\,\varphi^3/S_V^2$, where C_K is an empirical constant [53]. A higher porosity, therefore, results in a much higher permeability value. Interestingly, although the functionally graded Dense-in and Dense-out specimens had similar overall porosities, the Dense-out specimens showed higher permeability values than those of the Dense-in group. This may be due to the different C_K values for these two structures, as C_K is strongly dependent on pore geometry [54]. It may thus be concluded that, in addition to porosity, permeability can be also adjusted through topological design and the spatial distribution of repeating unit cells.

CFD simulations could help us to reveal the flow behavior of the scaffolds. Although the permeability values calculated from the simulations were higher than the

8

experimental values, they were well correlated to each other (Figure 4b). The discrepancies between the measured and predicted values could be attributed to the following factors. First, the CAD models had lower porosity and surface roughness than the actual values of the AM iron specimens. These differences might have caused an overestimation of the permeability. Furthermore, as can be seen from the velocity distribution (Figure 4c), even though we chose a slow inlet velocity, the actual velocity inside the scaffolds could be higher, which means that turbulent flow might occur. This phenomenon has also been observed by other researchers and appears to be caused by obstacles on the fluid path [55]. Turbulent flow might decrease the permeability of the scaffolds during the tests. It was also interesting to observe how the geometry could guide the flow behavior in the functionally graded scaffolds. For the Dense-in and Dense-out specimens, the higher porosity region always had a higher flow velocity (Figure 4c). A higher flow velocity can facilitate nutrient and oxygen transport to the cells residing inside the center of a scaffold [56].

8.4.3. Biodegradation behavior

The weight losses of the specimens were strongly dependent on their topological designs. Optimizing the topological design of the porous structure could, therefore, be an effective means to adjust the biodegradation behavior of AM porous iron. In general, the higher the porosity, the faster the weight loss. Furthermore, as the specimens from the different groups had different surface areas, we normalized the biodegradation rate to the surface area. The ranking of the different experimental groups in terms of biodegradation rate remained the same with or without normalization. As the biodegradation rate is directly related to the fluid flow inside the porous structure, topological design may influence the biodegradation behavior of AM iron scaffolds also through its effects on fluid velocity and permeability (subsection 4.2).

Visual inspection revealed that under dynamic biodegradation, brownish corrosion products formed both at the periphery and in the center of the specimens (Figure 5). EDS analysis indicated that the corrosion layer of the external struts contained Ca and P elements (Figure 6) after 28 days of immersion. Combined with ICP results (Figure 5d), these observations suggested that the Ca and P elements on the corrosion layer originated from the r-SBF medium. To better understand the different biodegradation mechanisms, we inspected the surface morphologies of degraded struts after ultrasonic cleaning (Figure 7). Biodegradation occurred both at the periphery and in the center of the specimens and grain boundaries became clearly visible on the surfaces of the struts (Figure 7). This was different from our previous study on 'uniform' AM porous iron, where struts in the center of the specimens remained almost intact after 28 days of immersion [34]. It could be explained by dynamic flow. In order to find out how topological design could be used to adjust the biodegradation behavior of the AM iron

scaffolds, the central regions of the AM iron specimens were inspected by micro-CT. Although the specimens of the S0.2 and Dense-out groups had exactly the same geometry in the center (Figure 1), the weight loss of the Dense-out specimens in the center was higher than that of the S0.2 specimens. This is counter-intuitive, given that the S0.2 specimens had higher permeability values than the specimens of the Dense-out group (Figure 7i). However, the velocity distribution predicted by CFD simulations (Figure 4c) suggests that the Dense-out scaffolds had higher flow velocities in the center than on the periphery. As the inlet flow velocity was constant in our dynamic biodegradation tests, there was a higher medium volume flow in the center of the Dense-out specimens. Similar results were observed for the S0.4 and Dense-in specimens. The Dense-out specimens degraded more slowly than the S0.4 specimens in the center, although the Dense-out specimens had generally higher permeability values than the S0.4 group. Once again, velocity distribution of the Dense-in specimens showed that the fluid velocity was higher at the periphery than in the center, leading to less medium volume flowing through the center of these specimens.

After 28 days of dynamic immersion, all the specimens lost more weight (*i.e.*, 5-16%) than the 'uniform' AM iron scaffolds under static immersion conditions (i.e., 3%) used in our earlier study [34]. It is well known that the *in vitro* test environment can affect the biodegradation rate of biodegradable metals. Others reported higher biodegradation rates of iron in dynamic immersion tests [57] as well. Furthermore, maintaining the CO_2 content at 5% means that the pH of the medium remains constant around 7.6. This would increase the biodegradation rate as well. The human body is a buffered system with a pH range of 7.38-7.42 [58]. Moreover, a flow rate of 0.012-1.67 ml/min [59] continuously occurs inside the (intra) medullary cavities that are home to the bone marrow and the progenitor cells of osteoblasts and osteoclasts. The dynamic biodegradation setup used in this research can, therefore, better mimic the *in vivo* conditions.

The biodegradation rates of the AM porous iron scaffolds observed here are higher than those reported for the pure iron fabricated using conventional manufacturing techniques (*i.e.*, 0.04-0.06 mg/cm^{-2}/day^{-1}) [48, 57], similar to those of cross-rolled pure iron (*i.e.*, 0.24-0.29 mg/cm^{-2}/day^{-1} [60]), and lower than those of electroformed pure iron (*i.e.*, 1.39 mg/cm^{-2}/day^{-1} [61, 62]). This is consistent with the order of the grain sizes obtained from using these different fabrication techniques. Conventionally manufactured iron has grain sizes in a range of 180-400 μm [48, 57], while the grain sizes of cross-rolled and electroformed iron are 16-19 μm [60] and 4 μm [61, 62], respectively. The AM porous iron specimens printed here had an average grain size of 10-12 μm, which is close to that of cross-rolled iron. Indeed, the specific solidification process experienced during AM creates smaller grains, which in turn increases the grain boundary area with defects in the crystal structure and high internal energy [63]. Larger areas of grain boundary are expected to cause higher chemical activity in a corrosive

8

medium [64, 65]. This clearly shows the advantage of the refined microstructure resulting from the SLM process in increasing the biodegradation rate of slowly degrading metals such as iron. Of course, other microstructural features such as texture and dislocation density may also affect the corrosion rate [60].

The actual weight reduction could be even higher than those measured here, because usual sample cleaning methods and weight loss measurements for solid samples cannot easily be applied to a porous specimen. For solid specimens, it is feasible to remove all the corrosion products with minimum attack to the sample itself. In the case of highly porous scaffolds, however, it is difficult to remove all the corrosion products, especially those in the center of the specimens (Figure 7b, d, f, h). Others have used acids or alkalis to remove corrosion products [66-69], but this may result in further erosion of the struts, particularly at the periphery. ICP-OES analysis showed even less iron release into the r-SBF medium as compared to the expectation from the weight loss measurements. This might be because iron ions participated in the formation of corrosion products (EDS results, Figure 6).

Although AM porous irons showed a sufficient rate of biodegradation in this study that should result in full biodegradation of the specimens within 1-2 years [68], the *in vivo* tests of AM porous iron should be performed in the future. In the case of bulk iron, a number of animal studies have shown that the *in vivo* degradation rates may be significantly lower than those measured *in vitro* [38, 39, 69]. It is, therefore, of great interest to determine the biodegradation rate of AM porous iron *in vivo* to better determine the potential of these biomaterials for future clinical application.

8.4.4. Mechanical behavior

The mechanical properties of all the AM porous iron specimens remained within the range of values reported for trabecular bone (*i.e.*, $E = 0.5\text{-}20$ GPa [70], $\sigma_y = 0.2\text{-}80$ MPa [71]) even after 28 days of biodegradation. Unlike other AM porous structures based on a diamond unit cell that were made from other materials [11, 72], the AM porous iron specimens studied here showed smooth stress-strain curves during uniaxial compression tests without fluctuations after the maximum stress (Figure 8a). In addition, no sudden failures occurred. This could be explained by the high ductility of pure iron [34]. Similar behavior has been observed for other highly ductile porous materials, such as AM porous structures made of pure titanium and tantalum [12, 73]. In the case of the functionally graded designs, the shape of the struts gradually and continuously changed so as to minimize the discontinuity of the stress at the interface between dissimilar layers [24]. The stress-strain curves remained smooth after the *in vitro* immersion tests and showed similar patterns to those of the non-biodegraded specimens (Figure 8b). Among the different designs, the yield strengths and elastic moduli of the AM iron specimens were strongly affected by porosity: a higher porosity resulted in lower values

of yield strength and elastic modulus. The mechanical properties of functionally graded structures could be predicted, based on the weighted average of the mechanical properties of each constituent using the Voight model [21]. Based on this model, the elastic modulus and strength of the functionally graded scaffolds are given by: $P_g = \sum_{i=1}^{n} f_i P_i$, where P_g represents the elastic modulus or strength of the functionally graded structure and f_i is the volume fraction of P_i. However, we find that such a weighted average cannot fully predict the mechanical properties of the functionally graded specimens designed in this study. For example, even though the Dense-in and Dense-out groups had similar porosities, both the yield strength and elastic modulus of the Dense-in specimens were slightly higher than those of the Dense-out group. The results from FE modeling of the specimens under compression could explain this trend. Given that stress was more concentrated in thicker struts, they carried more loads than thinner ones. Although both functionally graded groups had similar porosities (*i.e.*, the same volume of thick struts), the thickest struts were located at the periphery of the Dense-out group specimens, meaning that the thickest struts were generally open (*i.e.*, dangling) and did not contribute to the load-bearing capacity of the specimens.

Functionally graded structures have been reported to exhibit better failure performance than their uniform counterparts. For example, an axisymmetric deformation mechanism and long plateau stage have been observed for functionally graded specimens during compression tests, instead of abrupt failure accompanied by shear band formation [21, 24-26]. As thicker struts are the primary load-bearing elements of functionally graded structures, deformation occurs primarily in these struts, resulting in trumpet-like specimens after compression [21]. Functional gradients have been also found to increase the fatigue resistance of AM porous structure [25], as the cracks initiate layer by layer, instead of randomly initiating everywhere in the scaffolds at the same time. However, the results available for functionally graded AM porous metallic biomaterials in the literature usually refer to Ti-6Al-4V, which is a brittle alloy if no post-AM treatment is performed. As we used pure iron here, functional gradients did not alter the failure mode of the AM iron scaffolds, as the uniform designs exhibited smooth stress-strain curves themselves.

The structure of the human bone is generally highly heterogeneous and anisotropic with different stiffness and strength values in different directions [4]. At the same time, bone has sufficient permeability to facilitate the transfer of cells and nutrients. Bone-substituting porous implants should, therefore, combine a tailor-made distribution of mechanical properties with certain ranges of permeability, while taking biodegradation into account. The designs that we used in this study attempted to achieve these goals to the extent that was possible with linearly and radially graded porous structures. Of course, to fully address the above-mentioned design criteria regarding the mechanical, physical, and biological properties, further research attempts are needed. Topological optimization may be used to aid in achieving the desired properties while satisfying

8

certain prescribed constraints. Indeed, Hollister [74, 75] has advocated the adjustment of both stiffness and diffusive transport properties using topology optimization when designing scaffolds.

8.4.5. Cytocompatibility

To evaluate the biomedical application potential of our novel AM porous pure iron specimens, we applied latest ISO 10993 modifications to meet the special requirements for absorbable biomaterials [76, 77]. To this end, we used an MTS assay, which is the current state-of-the-art for extract-based *in vitro* evaluation of cytotoxicity [78]. In addition, using a medium containing serum allows to extract both polar and non-polar substances and supports cellular growth (ISO 10993-5, 2009) [78]. Of note, within the physiological range of 37 ºC, 24 h and 72 h are both specifically acceptable extraction conditions according to ISO 10993 (2009), with 72 h being the relatively harsher extraction regime [78]. Accordingly, in 24 h-extracts, cell activities in all iron extracts ranged between 77.8% (S0.2, the lowest) and 86.5% (S0.4, the highest), respectively, and can be classified as non-cytotoxic (*i.e.*, cytotoxicity grade 1; 75-99% viability) [79]. Upon 48 h-extraction, all conditioned media revealed $\geq 63\%$ remaining cellular activity, corresponding to being slightly cytotoxic (i.e., grade 2, 50-74%). Of note, under these conditions, the S0.4 group was still not significantly more cytotoxic than the titanium control, while Ti-6Al-4V controls remained non-toxic (grade 1) throughout. Only upon harsh 72 h-extractions, 75% of the samples have to be classified as moderately cytotoxic (*i.e.*, grade 3, < 49%). In line with our data, cytotoxicity was earlier reported to be inversely proportional to the iron ion concentration [66, 80]. Iron is an essential transition metal and nutritional requirement in cell culture, having both beneficial and toxic properties. The loss of ferric iron due to precipitation and its reduction to ferrous iron are equally undesirable events in the extracellular milieu. Ferric iron is the stable oxidative state of iron in aerobic conditions, and the normal oxidative state used by cells. In a solution at physiologic pH, ferric iron that is not bound by a chelator or carrier molecule will form ferric hydroxide complexes that are virtually insoluble. While the chemistry is quite complex, ferric iron can be reduced to ferrous iron which is free to participate in Fenton chemistry, to become a major source of oxidative stress in media due to the creation of hydroxyl free radical [81]. Pure iron showed good biocompatibility during long term implantation as biodegradable stents or pins [40, 41, 82, 83], which is in agreement with our *in vitro* results using the mild extraction regime. Unlike the *in vitro* situation where released iron ions can accumulate locally to high concentrations in a culture dish, released ions are usually rapidly diluted *in vivo* and will ultimately be secreted from the body [84]. This difference may point towards important limitations of the currently used static methods to evaluate cytocompatibility as they may tend to overestimate cytotoxic effects.

Fluorescent staining revealed relatively uniform cell seeding throughout the iron scaffolds without apparent design-specific differences (Figure 10e). This is in agreement with a recent study where human mesenchymal stromal cells were analyzed in 3D scaffolds with gradient pore sizes [85] and a study using pre-osteoblasts in gradient Ti-6Al-4V scaffolds [27]. The latter authors concluded that the degree of cell attachment was similar for various strut thicknesses. However, we expected that relatively more cell would adhere to thicker struts as compared to thinner ones, as these struts provide larger surface area to cells (and thus interfacial force). Logically, this might lead to more interactions with the material surface before the cells slip through the pores [22, 59]. Our analyses of cell distribution between Dense-In and Dense-Out groups did not reveal obvious differences in support of this former notion. Of note, our iron specimens were spatially graded instead of axially graded along the z-axis, as reported by others [20, 22, 23]. Axially grading could result in "sieve effects" during cell seeding and may account for differences between the studies. In addition, fluorescent labeling in porous, but otherwise light-dense, 3D structures has some limitations: subtle differences in cell distribution were hard to quantify due to large quantities of interfering iron biodegradation products. Such artefacts are absent in titanium scaffolds, facilitating quantification when using inert materials. Furthermore, the minimum and maximum pore sizes of our gradient scaffolds were 0.6 mm and 0.8 mm, respectively. This difference may not be large enough to affect cell seeding and qualifying both types as scaffolds of higher porosity [13]. Altogether, this may explain why we observed a rather uniform distribution in our gradient and non-gradient scaffolds. However, further decreasing the minimum pore size in smartly designed functionally graded porous scaffolds might hold potential to control cell distribution.

8.5. Conclusions

We demonstrated for the first time how SLM could be used for direct printing of functionally graded porous iron. The specimens of all the groups (*i.e.*, two functionally graded groups and two uniform groups) possessed precisely controlled topologies and fully interconnected porous structures. The topological design not only affected the permeability of the specimens of these groups but also changed the fluid flow inside the specimens. Consequently, the topological design controlled the biodegradation behavior of the AM porous iron scaffolds. For example, different biodegradation rates were found in the center of the AM porous iron specimens with and without functional gradients, even though they had the same local geometry. Taken together, our results suggest that topological design in general, and functional gradients in particular can be used as an important tool for adjusting the biodegradation behavior of AM porous metallic biomaterials. This holds especially for otherwise slowly degrading metals, such

as iron, to reach values desired for bone substitutes. Over a period of 28 days of dynamic immersion tests, the elastic modulus and yield strength of the porous iron remained in the range of the values reported for trabecular bone. Depending on the topological design of the specimens, AM porous iron appears to be widely cytocompatible. The observations reported here underline the importance of proper topological design in the development of AM porous biodegradable metals and suggest AM porous iron may be a highly attractive candidate for the development of future bone substitutes.

References

[1] A. A. Zadpoor, J. Malda. Additive manufacturing of biomaterials, iissues, and organs. Ann Biomed Eng. 2017;45:1-11.

[2] L. Murr, S. Gaytan, F. Medina, H. Lopez, E. Martinez, B. Machado, D. Hernandez, L. Martinez, M. Lopez, R. Wicker. Next-generation biomedical implants using additive manufacturing of complex, cellular and functional mesh arrays. Philos Trans Royal Soc A. 2010;368:1999-2032.

[3] A. A. Zadpoor. Mechanical performance of additively manufactured meta-biomaterials. Acta Biomater. 2019;85:41-59.

[4] X. Wang, S. Xu, S. Zhou, W. Xu, M. Leary, P. Choong, M. Qian, M. Brandt, Y. M. Xie. Topological design and additive manufacturing of porous metals for bone scaffolds and orthopaedic implants: A review. Biomaterials. 2016;83:127-141.

[5] A. A. Zadpoor. Mechanics of additively manufactured biomaterials. J Mech Behav Biomed Mater. 2017;70:1-6.

[6] A. H. Yusop, A. A. Bakir, N. A. Shaharom, M. R. Abdul Kadir, H. Hermawan. Porous biodegradable metals for hard tissue scaffolds: a review. Int J Biomater. 2012;2012:10.

[7] S. M. Ahmadi, R. Hedayati, Y. Li, K. Lietaert, N. Tümer, A. Fatemi, C. D. Rans, B. Pouran, H. Weinans, A. A. Zadpoor. Fatigue performance of additively manufactured meta-biomaterials: The effects of topology and material type. Acta Biomater. 2018;65:292-304.

[8] F. Bobbert, K. Lietaert, A. Eftekhari, B. Pouran, S. Ahmadi, H. Weinans, A. Zadpoor. Additively manufactured metallic porous biomaterials based on minimal surfaces: A unique combination of topological, mechanical, and mass transport properties. Acta Biomater. 2017;53:572-584.

[9] S. M. Ahmadi, R. Kumar, E. V. Borisov, R. Petrov, S. Leeflang, Y. Li, N. Tümer, R. Huizenga, C. Ayas, A. A. Zadpoor, V. A. Popovich. From microstructural design to surface engineering: A tailored approach for improving fatigue life of additively manufactured meta-biomaterials. Acta Biomater. 2019;83:153-166.

8

[10] C. Yan, L. Hao, A. Hussein, P. Young, D. Raymont. Advanced lightweight 316L stainless steel cellular lattice structures fabricated via selective laser melting. Mater Des. 2014;55:533-541.

[11] R. Hedayati, S. M. Ahmadi, K. Lietaert, B. Pouran, Y. Li, H. Weinans, C. D. Rans, A. A. Zadpoor. Isolated and modulated effects of topology and material type on the mechanical properties of additively manufactured porous biomaterials. J Mech Behav Biomed Mater. 2018;79:254-263.

[12] R. Wauthle, J. van der Stok, S. Amin Yavari, J. Van Humbeeck, J.-P. Kruth, A. A. Zadpoor, H. Weinans, M. Mulier, J. Schrooten. Additively manufactured porous tantalum implants. Acta Biomater. 2015;14:217-225.

[13] L. J. Gibson. Cellular Solids. MRS Bull. 2011;28:270-274.

[14] X. Miao, D. Sun. Graded/Gradient Porous Biomaterials. Materials. 2009;3:26-47.

[15] A. A. Zadpoor, G. Campoli, H. Weinans. Neural network prediction of load from the morphology of trabecular bone. Appl Math Model. 2013;37:5260-5276.

[16] J. Hazrati Marangalou, K. Ito, B. van Rietbergen. A novel approach to estimate trabecular bone anisotropy from stress tensors. Biomech Model Mechanobiol. 2015;14:39-48.

[17] D. M. Geraldes, A. T. M. Phillips. A comparative study of orthotropic and isotropic bone adaptation in the femur. Int J Numer Method Biomed Eng. 2014;30:873-889.

[18] P. Christen, K. Ito, I. Knippels, R. Müller, G. H. van Lenthe, B. van Rietbergen. Subject-specific bone loading estimation in the human distal radius. J Biomech. 2013;46:759-766.

[19] G. Campoli, H. Weinans, A. A. Zadpoor. Computational load estimation of the femur. J Mech Behav Biomed Mater. 2012;10:108-119.

[20] K. Nune, A. Kumar, R. Misra, S. Li, Y. Hao, R. Yang. Osteoblast functions in functionally graded Ti-6Al-4 V mesh structures. J Biomater Appl. 2016;30:1182-1204.

[21] X.-Y. Zhang, G. Fang, S. Leeflang, A. A. Zadpoor, J. Zhou. Topological design, permeability and mechanical behavior of additively manufactured functionally graded porous metallic biomaterials. Acta Biomater. 2019;84:437-452.

[22] K. C. Nune, A. Kumar, R. D. K. Misra, S. J. Li, Y. L. Hao, R. Yang. Functional response of osteoblasts in functionally gradient titanium alloy mesh arrays processed by 3D additive manufacturing. Colloids Surf, B. 2017;150:78-88.

[23] J. M. Sobral, S. G. Caridade, R. A. Sousa, J. F. Mano, R. L. Reis. Three-dimensional plotted scaffolds with controlled pore size gradients: Effect of scaffold geometry on mechanical performance and cell seeding efficiency. Acta Biomater. 2011;7:1009-1018.

[24] S. Li, S. Zhao, W. Hou, C. Teng, Y. Hao, Y. Li, R. Yang, R. D. K. Misra. Functionally Graded Ti-6Al-4V Meshes with High Strength and Energy Absorption. Adv Eng Mater. 2016;18:34-38.

8

[25] S. Zhao, S. J. Li, S. G. Wang, W. T. Hou, Y. Li, L. C. Zhang, Y. L. Hao, R. Yang, R. D. K. Misra, L. E. Murr. Compressive and fatigue behavior of functionally graded Ti-6Al-4V meshes fabricated by electron beam melting. Acta Mater. 2018;150:1-15.

[26] C. Han, Y. Li, Q. Wang, S. Wen, Q. Wei, C. Yan, L. Hao, J. Liu, Y. Shi. Continuous functionally graded porous titanium scaffolds manufactured by selective laser melting for bone implants. J Mech Behav Biomed Mater. 2018;80:119-127.

[27] E. Onal, J. Frith, M. Jurg, X. Wu, A. Molotnikov. Mechanical Properties and In Vitro Behavior of Additively Manufactured and Functionally Graded Ti6Al4V Porous Scaffolds. Metals. 2018;8:200.

[28] A. Di Luca, K. Szlazak, I. Lorenzo-Moldero, C. A. Ghebes, A. Lepedda, W. Swieszkowski, C. Van Blitterswijk, L. Moroni. Influencing chondrogenic differentiation of human mesenchymal stromal cells in scaffolds displaying a structural gradient in pore size. Acta Biomater. 2016;36:210-219.

[29] E. Damien, K. Hing, S. Saeed, P. A. Revell. A preliminary study on the enhancement of the osteointegration of a novel synthetic hydroxyapatite scaffold in vivo. J Biomed Mater Res A. 2003;66A:241-246.

[30] C. Erisken, D. M. Kalyon, H. Wang. Functionally graded electrospun polycaprolactone and β-tricalcium phosphate nanocomposites for tissue engineering applications. Biomaterials. 2008;29:4065-4073.

[31] M. Moravej, D. Mantovani. Biodegradable metals for cardiovascular stent application: interests and new opportunities. Int J Mol Sci. 2011;12:4250.

[32] R. O. Darouiche. Treatment of Infections Associated with Surgical Implants. New Engl J Med. 2004;350:1422-1429.

[33] Y. Li, J. Zhou, P. Pavanram, M. A. Leeflang, L. I. Fockaert, B. Pouran, N. Tümer, K. U. Schröder, J. M. C. Mol, H. Weinans, H. Jahr, A. A. Zadpoor. Additively manufactured biodegradable porous magnesium. Acta Biomater. 2018;67:378-392.

[34] Y. Li, H. Jahr, K. Lietaert, P. Pavanram, A. Yilmaz, L. I. Fockaert, M. A. Leeflang, B. Pouran, Y. Gonzalez-Garcia, H. Weinans, J. M. C. Mol, J. Zhou, A. A. Zadpoor. Additively manufactured biodegradable porous iron. Acta Biomater. 2018;77:380-393.

[35] P. Wen, Y. Qin, Y. Chen, M. Voshage, L. Jauer, R. Poprawe, J. Henrich Schleifenbaum. Laser additive manufacturing of Zn porous scaffolds: shielding gas flow, surface quality and densification. J Mater Sci Technol. 2018.

[36] D. Carluccio, A. G. Demir, L. Caprio, B. Previtali, M. J. Bermingham, M. S. Dargusch. The influence of laser processing parameters on the densification and surface morphology of pure Fe and Fe-35Mn scaffolds produced by selective laser melting. J Manuf Process. 2019;40:113-121.

[37] Y. Li, H. Jahr, X. Y. Zhang, M. A. Leeflang, W. Li, B. Pouran, F. D. Tichelaar, H. Weinans, J. Zhou, A. A. Zadpoor. Biodegradation-affected fatigue behavior of additively manufactured porous magnesium. Addit Manuf. 2019;28:299-311.

8

[38] Y. Li, K. Lietaert, W. Li, X. Y. Zhang, M. A. Leeflang, J. Zhou, A. A. Zadpoor. Corrosion fatigue behavior of additively manufactured biodegradable porous iron. Corros Sci. 2019;156:106-116.

[39] J. He, F.-L. He, D.-W. Li, Y.-L. Liu, Y.-Y. Liu, Y.-J. Ye, D.-C. Yin. Advances in Fe-based biodegradable metallic materials. RSC Adv. 2016;6:112819-112838.

[40] M. Peuster, C. Hesse, T. Schloo, C. Fink, P. Beerbaum, C. von Schnakenburg. Long-term biocompatibility of a corrodible peripheral iron stent in the porcine descending aorta. Biomaterials. 2006;27:4955-4962.

[41] T. Kraus, F. Moszner, S. Fischerauer, M. Fiedler, E. Martinelli, J. Eichler, F. Witte, E. Willbold, M. Schinhammer, M. Meischel, P. J. Uggowitzer, J. F. Löffler, A. Weinberg. Biodegradable Fe-based alloys for use in osteosynthesis: Outcome of an in vivo study after 52weeks. Acta Biomater. 2014;10:3346-3353.

[42] I. A. J. van Hengel, M. Riool, L. E. Fratila-Apachitei, J. Witte-Bouma, E. Farrell, A. A. Zadpoor, S. A. J. Zaat, I. Apachitei. Selective laser melting porous metallic implants with immobilized silver nanoparticles kill and prevent biofilm formation by methicillin-resistant Staphylococcus aureus. Biomaterials. 2017;140:1-15.

[43] F. Pennella, G. Cerino, D. Massai, D. Gallo, G. Falvo D'Urso Labate, A. Schiavi, M. A. Deriu, A. Audenino, U. Morbiducci. A Survey of Methods for the Evaluation of Tissue Engineering Scaffold Permeability. Ann Biomed Eng. 2013;41:2027-2041.

[44] A. Oyane, H.-M. Kim, T. Furuya, T. Kokubo, T. Miyazaki, T. Nakamura. Preparation and assessment of revised simulated body fluids. J Biomed Mater Res A. 2003;65A:188-195.

[45] F. Zhao, B. van Rietbergen, K. Ito, S. Hofmann. Flow rates in perfusion bioreactors to maximise mineralisation in bone tissue engineering in vitro. J Biomech. 2018;79:232-237.

[46] M. E. Gomes, V. I. Sikavitsas, E. Behravesh, R. L. Reis, A. G. Mikos. Effect of flow perfusion on the osteogenic differentiation of bone marrow stromal cells cultured on starch-based three-dimensional scaffolds. J Biomed Mater Res A. 2003;67A:87-95.

[47] J. R. Vetsch, D. C. Betts, R. Müller, S. Hofmann. Flow velocity-driven differentiation of human mesenchymal stromal cells in silk fibroin scaffolds: A combined experimental and computational approach. PLoS One. 2017;12:e0180781.

[48] T. Huang, J. Cheng, Y. F. Zheng. In vitro degradation and biocompatibility of Fe–Pd and Fe–Pt composites fabricated by spark plasma sintering. Mater Sci Eng, C. 2014;35:43-53.

[49] B. Song, X. Zhao, S. Li, C. Han, Q. Wei, S. Wen, J. Liu, Y. Shi. Differences in microstructure and properties between selective laser melting and traditional manufacturing for fabrication of metal parts: A review. Front Mech Eng. 2015;10:111-125.

[50] L.-E. Loh, C.-K. Chua, W.-Y. Yeong, J. Song, M. Mapar, S.-L. Sing, Z.-H. Liu, D.-Q. Zhang. Numerical investigation and an effective modelling on the Selective Laser

Melting (SLM) process with aluminium alloy 6061. Int J Heat Mass Transfer. 2015;80:288-300.

[51] A. Simchi, H. Pohl. Effects of laser sintering processing parameters on the microstructure and densification of iron powder. Mater Sci Eng, A. 2003;359:119-128.

[52] B. Song, S. Dong, Q. Liu, H. Liao, C. Coddet. Vacuum heat treatment of iron parts produced by selective laser melting: Microstructure, residual stress and tensile behavior. Mater Des. 2014;54:727-733.

[53] S. Truscello, G. Kerckhofs, S. Van Bael, G. Pyka, J. Schrooten, H. Van Oosterwyck. Prediction of permeability of regular scaffolds for skeletal tissue engineering: A combined computational and experimental study. Acta Biomater. 2012;8:1648-1658.

[54] H. Montazerian, M. Zhianmanesh, E. Davoodi, A. S. Milani, M. Hoorfar. Longitudinal and radial permeability analysis of additively manufactured porous scaffolds: Effect of pore shape and porosity. Mater Des. 2017;122:146-156.

[55] D. Ali, S. Sen. Finite element analysis of mechanical behavior, permeability and fluid induced wall shear stress of high porosity scaffolds with gyroid and lattice-based architectures. J Mech Behav Biomed Mater. 2017;75:262-270.

[56] F. P. W. Melchels, B. Tonnarelli, A. L. Olivares, I. Martin, D. Lacroix, J. Feijen, D. J. Wendt, D. W. Grijpma. The influence of the scaffold design on the distribution of adhering cells after perfusion cell seeding. Biomaterials. 2011;32:2878-2884.

[57] B. Liu, Y. F. Zheng. Effects of alloying elements (Mn, Co, Al, W, Sn, B, C and S) on biodegradability and in vitro biocompatibility of pure iron. Acta Biomater. 2011;7:1407-1420.

[58] J. C. Atherton. Acid–base balance: maintenance of plasma pH. Anaesth Intens Care. 2009;10:557-561.

[59] A. P. Md. Saad, N. Jasmawati, M. N. Harun, M. R. Abdul Kadir, H. Nur, H. Hermawan, A. Syahrom. Dynamic degradation of porous magnesium under a simulated environment of human cancellous bone. Corros Sci. 2016;112:495-506.

[60] C. S. Obayi, R. Tolouei, C. Paternoster, S. Turgeon, B. A. Okorie, D. O. Obikwelu, G. Cassar, J. Buhagiar, D. Mantovani. Influence of cross-rolling on the micro-texture and biodegradation of pure iron as biodegradable material for medical implants. Acta Biomater. 2015;17:68-77.

[61] M. Moravej, F. Prima, M. Fiset, D. Mantovani. Electroformed iron as new biomaterial for degradable stents: Development process and structure–properties relationship. Acta Biomater. 2010;6:1726-1735.

[62] M. Moravej, A. Purnama, M. Fiset, J. Couet, D. Mantovani. Electroformed pure iron as a new biomaterial for degradable stents: In vitro degradation and preliminary cell viability studies. Acta Biomater. 2010;6:1843-1851.

8

[63] F. Witte, N. Hort, C. Vogt, S. Cohen, K. U. Kainer, R. Willumeit, F. Feyerabend. Degradable biomaterials based on magnesium corrosion. Curr Opin Solid State Mater Sci. 2008;12:63-72.

[64] C. S. Obayi, R. Tolouei, A. Mostavan, C. Paternoster, S. Turgeon, B. A. Okorie, D. O. Obikwelu, D. Mantovani. Effect of grain sizes on mechanical properties and biodegradation behavior of pure iron for cardiovascular stent application. Biomatter. 2016;6:e959874.

[65] M. Moravej, S. Amira, F. Prima, A. Rahem, M. Fiset, D. Mantovani. Effect of electrodeposition current density on the microstructure and the degradation of electroformed iron for degradable stents. Mater Sci Eng, B. 2011;176:1812-1822.

[66] E. Zhang, H. Chen, F. Shen. Biocorrosion properties and blood and cell compatibility of pure iron as a biodegradable biomaterial. J Mater Sci Mater Med. 2010;21:2151-2163.

[67] J. Čapek, Š. Msallamová, E. Jablonská, J. Lipov, D. Vojtěch. A novel high-strength and highly corrosive biodegradable Fe-Pd alloy: Structural, mechanical and in vitro corrosion and cytotoxicity study. Mater Sci Eng, C. 2017;79:550-562.

[68] W. Lin, L. Qin, H. Qi, D. Zhang, G. Zhang, R. Gao, H. Qiu, Y. Xia, P. Cao, X. Wang, W. Zheng. Long-term in vivo corrosion behavior, biocompatibility and bioresorption mechanism of a bioresorbable nitrided iron scaffold. Acta Biomater. 2017;54:454-468.

[69] P. Mariot, M. A. Leeflang, L. Schaeffer, J. Zhou. An investigation on the properties of injection-molded pure iron potentially for biodegradable stent application. Powder Technol. 2016;294:226-235.

[70] J. Parthasarathy, B. Starly, S. Raman, A. Christensen. Mechanical evaluation of porous titanium (Ti6Al4V) structures with electron beam melting (EBM). J Mech Behav Biomed Mater. 2010;3:249-259.

[71] M. Yazdimamaghani, M. Razavi, D. Vashaee, K. Moharamzadeh, A. R. Boccaccini, L. Tayebi. Porous magnesium-based scaffolds for tissue engineering. Mater Sci Eng, C. 2017;71:1253-1266.

[72] S. Ahmadi, S. Yavari, R. Wauthle, B. Pouran, J. Schrooten, H. Weinans, A. Zadpoor. Additively Manufactured Open-Cell Porous Biomaterials Made from Six Different Space-Filling Unit Cells: The Mechanical and Morphological Properties. Materials. 2015;8:1871.

[73] R. Wauthle, S. M. Ahmadi, S. Amin Yavari, M. Mulier, A. A. Zadpoor, H. Weinans, J. Van Humbeeck, J.-P. Kruth, J. Schrooten. Revival of pure titanium for dynamically loaded porous implants using additive manufacturing. Mater Sci Eng, C. 2015;54:94-100.

[74] S. J. Hollister. Scaffold Design and Manufacturing: From Concept to Clinic. Adv Mater. 2009;21:3330-3342.

8

[75] S. J. Hollister. Porous scaffold design for tissue engineering. Nature Materials. 2005;4:518-524.

[76] J. Fischer, D. Pröfrock, N. Hort, R. Willumeit, F. Feyerabend. Reprint of: Improved cytotoxicity testing of magnesium materials. Mater Sci Eng, B. 2011;176:1773-1777.

[77] J. Wang, F. Witte, T. Xi, Y. Zheng, K. Yang, Y. Yang, D. Zhao, J. Meng, Y. Li, W. Li, K. Chan, L. Qin. Recommendation for modifying current cytotoxicity testing standards for biodegradable magnesium-based materials. Acta Biomater. 2015;21:237-249.

[78] X. Liu, D. P. Rodeheaver, J. C. White, A. M. Wright, L. M. Walker, F. Zhang, S. Shannon. A comparison of in vitro cytotoxicity assays in medical device regulatory studies. Regul Toxicol Pharmacol. 2018;97:24-32.

[79] H. Meng, X. Zhang, Q. Chen, J. Wei, Y. Wang, A. Dong, H. Yang, T. Tan, H. Cao. Preparation of poly (aspartic acid) superabsorbent hydrogels by solvent-free processes. J Polym Eng. 2015;35:647-655.

[80] S. Zhu, N. Huang, L. Xu, Y. Zhang, H. Liu, H. Sun, Y. Leng. Biocompatibility of pure iron: In vitro assessment of degradation kinetics and cytotoxicity on endothelial cells. Mater Sci Eng, C. 2009;29:1589-1592.

[81] R. S. Britton, K. L. Leicester, B. R. Bacon. Iron Toxicity and Chelation Therapy. Int J Hematol. 2002;76:219-228.

[82] A. Francis, Y. Yang, S. Virtanen, A. R. Boccaccini. Iron and iron-based alloys for temporary cardiovascular applications. J Mater Sci Mater Med. 2015;26:138.

[83] M. Peuster, P. Wohlsein, M. Brügmann, M. Ehlerding, K. Seidler, C. Fink, H. Brauer, A. Fischer, G. Hausdorf. A novel approach to temporary stenting: degradable cardiovascular stents produced from corrodible metal—results 6–18 months after implantation into New Zealand white rabbits. Heart. 2001;86:563-569.

[84] D. Andreas, H. Thomas, B. F. Wilhelm, P. Matthias. In vitro and in vivo corrosion properties of new iron–manganese alloys designed for cardiovascular applications. J Biomed Mater Res B Appl Biomater. 2015;103:649-660.

[85] A. Di Luca, B. Ostrowska, I. Lorenzo-Moldero, A. Lepedda, W. Swieszkowski, C. Van Blitterswijk, L. Moroni. Gradients in pore size enhance the osteogenic differentiation of human mesenchymal stromal cells in three-dimensional scaffolds. Sci Rep. 2016;6:22898.
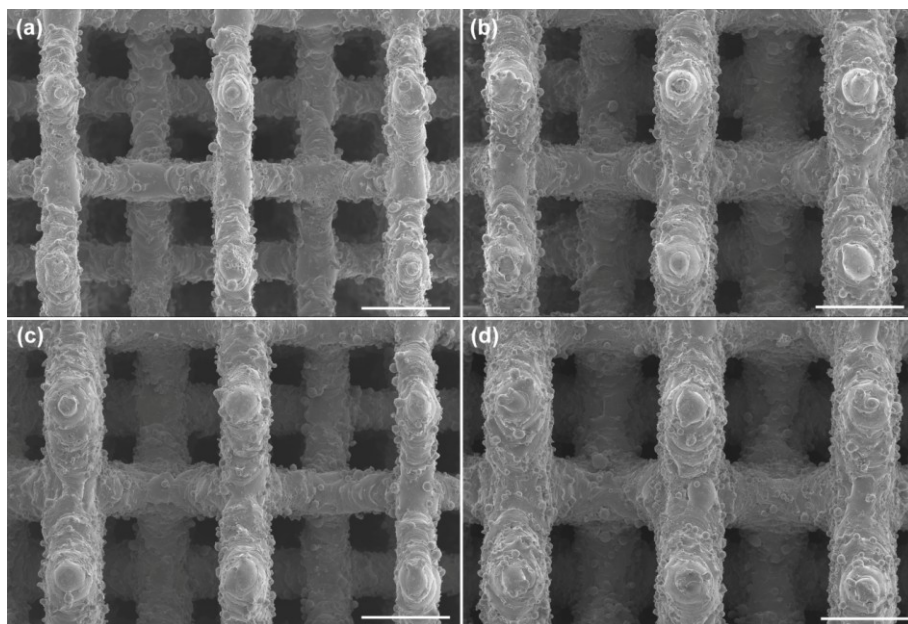
8

Supplementary information

Figure S1. The surface morphologies of our AM iron scaffolds: (a) S0.2, (b) Dense-in, (c) Dense-out, and (d) S0.4. Scale bar: 500 μm.
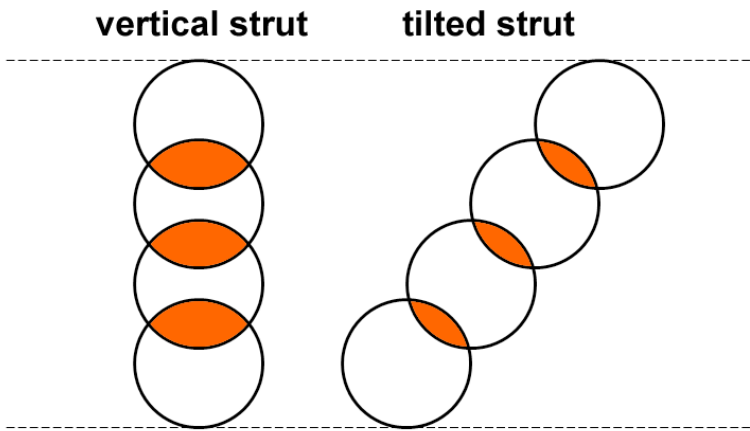
8

Figure S2. A schematic illustration of the melt pools overlapping along vertical and tilted struts.

9

Additively manufactured functionally graded biodegradable porous zinc

Here, we studied one functionally graded and two uniform AM porous Zn designs with diamond unit cell. Cylindrical specimens were fabricated from pure Zn powder by using a powder bed fusion technique, followed by a comprehensive study on their static and dynamic biodegradation behaviors, mechanical properties, permeability, and biocompatibility. Topological design, indeed, affected the biodegradation behavior of the specimens, as evidenced by 150% variations in biodegradation rate between the three different designs. After in vitro dynamic immersion for 28 days, the AM porous Zn had weight losses of 7-12%, relying on the topological design. The mechanical properties of the biodegraded specimens of all the groups maintained within the range of those of cancellous bone. After 28 days of in vitro biodegradation, the yield strengths of the specimens of all the groups (σ_y = 7-14 MPa) increased consistently, as compared to those of the as-built specimens (σ_y = 4-11 MPa). Moreover, AM porous Zn showed excellent biocompatibility, given that the cellular activities in none of the groups differed from the Ti controls for up to 72 h. Using topological design of AM porous Zn for controlling its mechanical properties and degradation behavior is thus clearly promising, thereby rendering flexibility to the material to meet a variety of clinical requirements. [1]

9

---

[1] The chapter is based on a scientific paper: Y. Li, P. Pavanram, J. Zhou, K. Lietaert, F.S.L Bobbert, Yusuke Kubo, M.A. Leeflang, H. Jahr, A.A. Zadpoor. Additively manufactured functionally graded biodegradable porous zinc. *Biomaterials Science* (in press)

9.1. Introduction

Recently, several studies on directly printed topologically ordered porous biodegradable magnesium (Mg) and iron (Fe) have been reported [1, 2] and these studies addressed some of the most important challenges faced in designing such biomaterials. For Mg- and Fe-based biomaterials, the most important challenge is the biodegradation rate, which is too high for Mg [3], but too low for Fe [4]. AM facilitates the production of porous Fe with greatly increased surface area and this can increase its biodegradation rate (0.2 mm/year [5]) to the desired range (0.2-0.5 mm/year [6]). However, according to *in vivo* tests with pure Fe, voluminous biodegradation products often form and remain in the human body even until 9 months after implantation [7].

Some researchers have tried to adjust the biodegradation rates of Mg and Fe through the development of new alloys and functional coatings [8, 9]. However, only limited adjustments in biodegradation rate are possible through these approaches. An alternative approach that has recently received a lot of attention is the use of other biodegradable metals. Within this paradigm, Zn and Zn-based alloys are considered promising candidates for orthopedic applications, as they are capable of tackling some of the fundamental challenges associated with using biodegradable Mg or Fe as an implant material [10]. Zn offers multiple advantages over Mg, Fe, and their alloys. First, as the chemical potential of Zn falls between the chemical potential values of Mg and Fe, it is expected to exhibit an intermediate rate of biodegradation, as compared to the extreme cases of Mg and Fe [11, 12]. Second, the biodegradation process of Zn does not generate hydrogen gas. Finally, similar to Mg but unlike Fe, the biodegradation products of Zn are biocompatible [13]. A few research groups, including ours, have recently been successful in directly printing AM porous Zn [14-16]. In a previous study, we assessed the biodegradation behavior, mechanical properties, and cytocompatibility of an AM porous Zn biomaterial with a regular and uniform porous structure [17].

Now, the next step is to go beyond the uniform lattice structure and fully exploit the advantages of topological design and free-form fabrication offered by AM to meet the design requirements of biodegradable porous metals aimed at applications as bone substitutes. Functionally graded designs are particularly interesting in this context, as they enable meeting conflicting design requirements in a single piece of material. Indeed, a recent study has shown that functional gradients could be used to adjust the biodegradation profile as well as the mechanical properties of AM porous Fe [5] to meet otherwise conflicting design requirements regarding biodegradation rate, mechanical properties, and permeability of such a biomaterial. It is therefore interesting to investigate if topological design can also tune the properties of other AM biodegradable porous metals.

Here, we designed and directly printed three experimental groups of AM porous Zn specimens, including one group with a functionally graded design and two groups with uniform designs to investigate the influence of topological design on the static and dynamic biodegradation behaviors, mechanical properties, permeability, and cytocompatibility of pure Zn prepared by using a powder bed fusion (PBF) technique. To put this into perspective, the porosity of the functionally graded porous structure design falls within the porosities of the two uniform porous structure designs.

9.2. Material and methods

9.2.1. AM of the specimens

Element (nTopology, USA) was used to design three different types of specimens (Figure 1) all with a 1.4 mm diamond unit cell, which included two uniform structures (strut thicknesses: 0.3 and 0.4 mm, hereafter called S03 and S04, respectively), and a functionally graded porous structure (strut thickness: linearly and radially varied from 0.4 mm to 0.2 mm) (S0402) (Figure 1). Specimens were fabricated using a ProX DMP 320 machine (3D Systems, Belgium) with a maximum laser power of 500 W and < 50 ppm oxygen levels in its build chamber. A nitrogen-atomized Zn powder was used in this study, as described previously [18]. The powder layer thickness and energy density were 60 µm and 39.0 J/mm^3, respectively. The specimens were removed from the steel baseplate through wire electrical discharge machining (WEDM). 96% ethanol was used to ultrasonically clean the unmelted powders stuck in the pores of the specimens for 20 min. Subsequently, the specimens were cleaned chemically for 2 min in 5% (by volume) HCl, 5% HNO$_3$, and 90% C$_2$H$_5$OH to further remove loose powder particles. Afterwards, residual HCl on the specimens were washed out by 5 min ultrasonic cleaning in 96% ethanol.
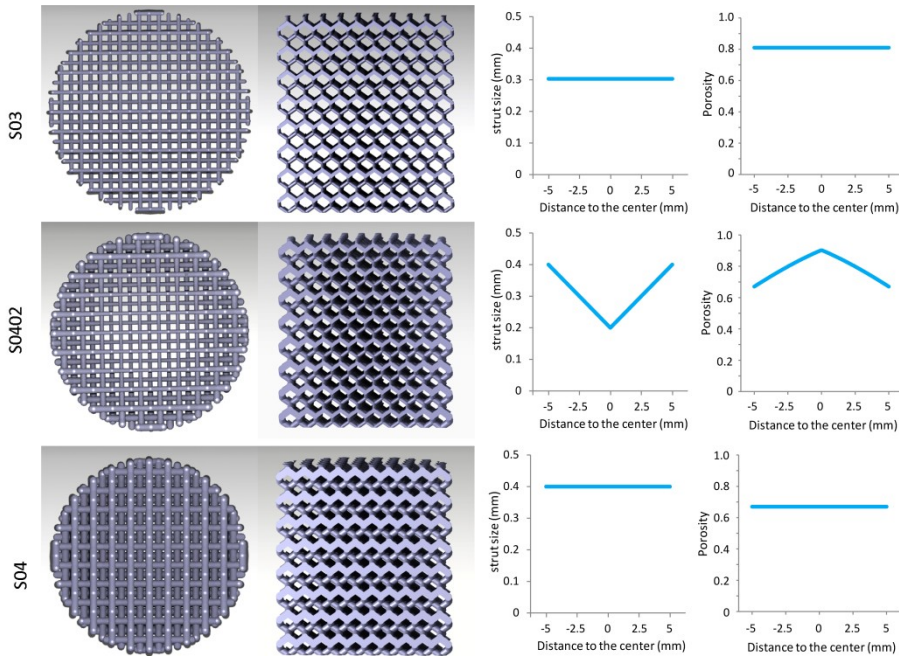
9

Figure 1. Topological designs of the AM porous zinc specimens of the three experimental groups.

9.2.2. Morphological characterization of the as-built specimens

The specimens were imaged using micro-computed tomography (micro-CT) (Phoenix Nanotom, GE Sensing Inspection Technologies GmbH, Germany) at a tube voltage of 130 kV and a tube current of 220 μA. The exposure time was 500 ms and the spatial resolution was 12 μm^3. 1440 projections were acquired. The acquired data were then reconstructed and transformed to 2D images (DICOM stack) using Phoenix Datos|x 2.0 (GE Sensing & Inspection Technologies GmbH, Germany). To extract quantifiable data from these images, the following steps were taken. First, the images were imported to the Fiji software (NIH, US) and thresholded locally over a range of 107 to 255. Then, a series of circular regions of interest (ROIs) were created and porosity, strut size, and pore size were calculated using BoneJ (a plugin of Fiji) [2]. Besides, the porosity of the specimens was also determined by using the weighing method [1].

9.2.3. Static and dynamic biodegradation tests

A standard cell culture incubator (20% O_2, 5% CO_2, 37 °C) was used for static *in vitro* biodegradation tests in revised simulated body fluid (r-SBF) [19], for up to 28 days. In

addition, dynamic *in vitro* biodegradation was performed at a flow rate of 0.3 ml/min, for the same period and also at cell culture conditions, using a custom-built bioreactor and pre-equilibrated r-SBF. Medium pH values were registered (InLab Expert Pro-ISM, METTLER TOLEDO, Switzerland) after static and dynamic biodegradation. An inductively coupled plasma optical emission spectroscope (ICP-OES, iCAP 6500 Duo, Thermo Scientific, USA) was used to analyze the concentrations of Zn, P, and Ca ions.

9.2.4. Characterization of the biodegradation products

Scanning electron microscope (SEM) and energy-dispersive X-ray spectroscope (EDS) (JSM-IT100, JEOL, Japan) was used to analyze the morphologies and compositions of the biodegradation products. X-ray diffractometer (XRD, Bruker D8 Advance diffractometer in Bragg-Brentano geometry, Germany) was used for the identification of the phases in the biodegradation products. XRD was operated at 45 kV and 35 mA using Co Ka radiation (step size: 0.035° and dwell time: 4 s).

9.2.5. Morphological characterization of specimens after biodegradation

After the biodegradation tests, ranges of 45–107 and 107–255 were applied to segment the biodegradation products and Zn, respectively, from the micro-CT images. After segmentation in Fiji, the volume of metallic specimen (*i.e.,* Zn) and the volume of the biodegradation products were calculated with BoneJ (a plugin of Fiji). The images were then imported to Avizo Fire (VSG, France) for 3D reconstruction.

9.2.6. Mechanical characterization

Compression tests were carried out at a crosshead speed of 2 mm/min, using a material testing machine with a 10 kN load cell (Instron, Germany). Yield strengths and quasi-elastic gradients (elastic modulus) of the specimens were obtained according to ISO 13314:2011. The slope of the starting linear part of the stress-strain curve equals to the elastic modulus of the porous specimen. The initial linear part was offset by 0.2% to find the intersection for yield strength. All the tests were performed in triplicate.

9.2.7. Permeability

The falling head method was used to measure the permeability of the specimens [5]. The specimens were placed in a chamber below a standpipe. Water fell in the standpipe, during which the pressure at the bottom of the standpipe was measured by a pressure gauge. Water pressure was registered in LabView (v.11.0, National Instruments, US) every two seconds. The instantaneous level of the water corresponded to the measured pressure. The following equation was used to calculate permeability, *k*:

9

$$k = \frac{a}{A}\frac{L}{t} In \frac{H_1}{H_2}\frac{\mu}{\rho g}$$

where a and A are the areas of the cross-section for the standpipe and specimen, respectively, L is the specimen height, H_1 and H_2 are the momentary level of water at two different time points, t is the interval between these two time points, μ is the dynamic viscosity, and ρ is the density of water. The tests were performed in triplicate for each of the groups.

9.2.8. Cell culture assays

Cleaned Zn scaffolds ($n = 3$) were sterilized in 100% isopropanol (Merck; Darmstadt, Germany) for 30 min and placed in non-tissue culture treated 48-well plates so as to achieve diminished adhesion and proliferation of cells on the surface of the wells. Cell suspension (500 μl with $3x10^6$ cells) of MG-63 was prepared and added dropwise to the scaffolds. After 30 min of incubation, 1 ml of additional medium was slowly added and the specimens were further incubated for 6 h under static physiological conditions, thus, ensuring complete cell attachment. After 6 h, the scaffolds were moved to a fresh 48-well plate and a counting chamber method was used to count the remaining cells in each well [20]. The equation below was used to calculate the cell seeding efficiency:

$$Cell\ seeding\ efficiency = \frac{(initial\ cells\ added\ to\ scaffold - remaining\ cells\ in\ wells)}{initial\ cells\ added\ to\ scaffold}$$

9.2.9. Cytocompatibility

9.2.9.1. Cell culture

Human osteoblast-like cells (MG-63, ATCC, CRL-1427) were cultured in Dulbecco's Modified Eagle Medium (DMEM) with low (1 g/L) glucose (DMEM LG; Sigma-Aldrich Chemie GmbH, Munich, Germany), containing 10% fetal calf serum (DMEM LG+, PAN-Biotech, Aidenbach, Germany), in the incubator (37 ˚C, 20% O_2, 5% CO_2, and 95% humidity).

9.2.9.2. Cytocompatibility testing

Specimens were cleaned as reported in subsection 2.1, and then sterilized in 100% isopropanol (Merck; Darmstadt, Germany) for 30 min. The biocompatibility of the AM porous Zn specimens was subsequently evaluated through direct cell seeding and indirect extract-based cytotoxicity tests.

(a) Direct cell seeding: The cleaned and sterilized specimens were seeded with 3×10^6 MG-63 cells and incubated for 24 h in DMEM LG+ medium under physiological conditions. The specimens after cell seeding were then cut longitudinally to evaluate cell viability in their core region using Live and Dead Dye from Live and Dead Cell

Assay kit (ab115347, Abcam, UK). Briefly, a 5X concentrated dye solution was added to the cell-seeded specimens and then incubated for 10 min at room temperature, prior to fluorescent optical imaging of living cells. After rinsing in 1X phosphate buffered saline, the scaffolds were fixed, dehydrated, and air-dried at room temperature as described before [1]. SEM (ESEM XL 30 FEG, FEI, Eindhoven, The Netherlands) was used to observe the cells.

(b) Indirect, extract-based cytocompatibility: The methodology for extract preparation and the MTS assay were both previously reported by us [6]. Briefly, extracts were prepared at 0.2 g Zn/ml in DMEM LG+ for 72 h under physiological conditions as recommended by EN ISO standards 10993-5 and 10993-12. The sterile filtered (0.2 µm) extracts from Zn specimens and those from identically designed Ti-6Al-4V specimens as gold standard, were compared to cytotoxic Dimethyl sulfoxide (DMSO, 20% v/v): MG-63 cells were seeded on regular bioplastics and DMEM LG+ was replaced with 10X extracts prior to further incubation for 0, 24, 48 and 72 h. Relative cellular activity was determined using CellTiter 96® AQueous One Solution Cell Proliferation Assay (Promega Corp., Mannheim, Germany) as described by us before [2].

9.2.10. Statistical analysis

One-way ANOVA tests ($\alpha = 0.05$), followed by the Turkey multiple comparison test ($\alpha = 0.05$), were performed to analyze biodegradation and permeability data. Two-way ANOVA tests ($\alpha = 0.05$), followed by the Turkey multiple comparison test ($\alpha = 0.05$), were used to analyze cytotoxicity data ($p < 0.0001$, ****; $p < 0.001$, ***; $p < 0.01$, **; $p < 0.05$, *; n.s. = not significant).

9.3. Results

9.3.1. Morphological characteristics of the as-built specimens

Table 1- Morphological characterization of AM porous Zn.

AM porous Zn	Porosity (%)		Strut size (µm)		Pore size (µm)	
	µCT	Design	µCT	Design	µCT	Design
S03	72.6±2.3	81.1	349±9	300	612±3	700
S0402	68.5±2.3	74.3	357±18	400-200	589±69	600-800
S04	62.0±2.5	67.4	442±1	400	550±38	600

9

The strut sizes of the AM Zn scaffolds were 40-50 µm thicker, while the pore sizes were 50-80 µm narrower than the design values (Table 1). The measured porosities were similar from µCT and the weighing method, which were 5-9% lower than the design values (Table 1). The 3D models reconstructed from the micro-CT (Figure 2a-c) and SEM images (Figure 2d-i) showed uniform strut thickness of the S03 and S04 groups, while the strut thickness of the S0402 group was graded. There were unmelted powder particles on the surface of the as-built specimens (Figure 2d-f). After chemical polishing, the surfaces of the specimens were relatively smooth (Figure 2g-i).
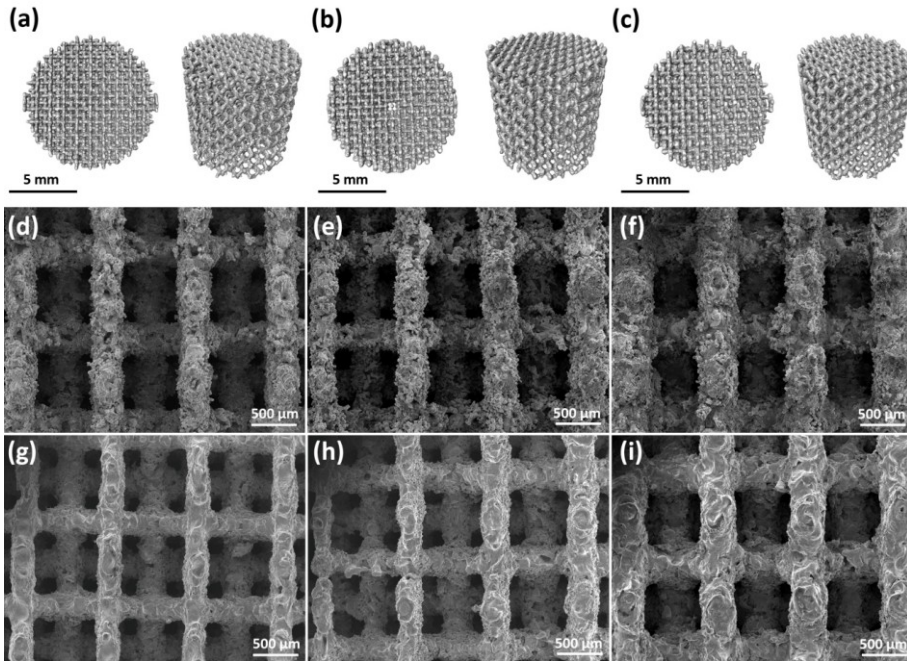
Figure 2. Morphologies of AM porous zinc: (a-c) micro-CT reconstructions of AM porous zinc S03 (a), S0402 (b), and S04 (c), (d-f) strut morphologies of the as-built AM porous zinc S03 (d), S0402 (e), and S04 (f), (g-i) strut morphologies of the as-cleaned AM porous zinc S03 (g), S0402 (h), and S04 (i).

9.3.2. *In vitro* biodegradation behavior

During both the static and dynamic immersion tests, white biodegradation products formed gradually on the struts surfaces of the scaffolds of all the three experimental groups (Figure 3a). The dynamic biodegradation appeared to produce more biodegradation products than the static one. Furthermore, the biodegradation products mainly formed at the bottom of the specimens (attached to the beaker) under the static

condition, but at the top of the specimens (*i.e.,* outlet side of the medium flow) under the dynamic condition (Figure 3a).
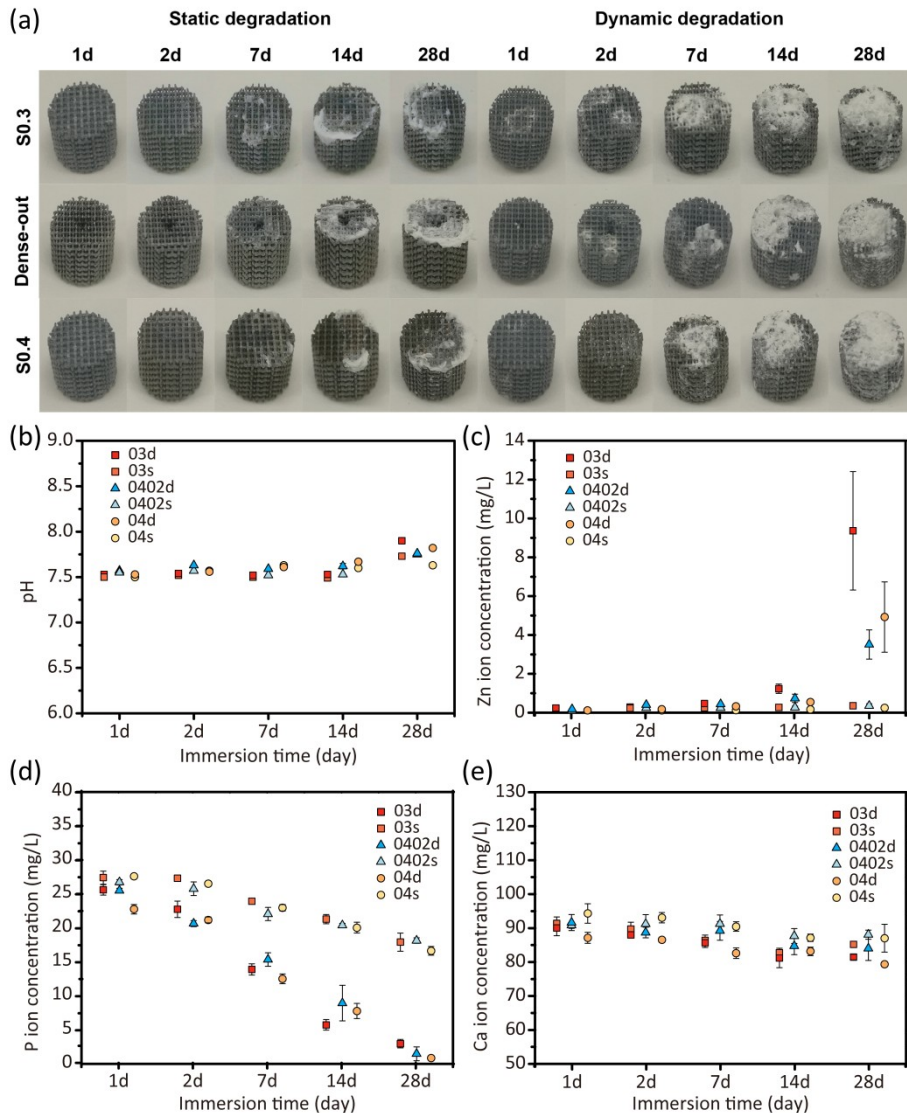

Figure 3. Biodegradation behavior of AM porous zinc: (a) a visual inspection of the as-degraded specimens under the static and dynamic conditions, (b) pH variation with the immersion time, (c-e) the changes in Zn (c), P (d), and Ca (e) ion concentrations with immersion time.

The pH values slightly increased from 7.5 to 7.9 in r-SBF solution during 28 days of immersion (Figure 3b). The dynamic tests resulted in higher pH values, as compared to the static ones, especially at day 28 (Figure 3b). pH value did not vary much between the solutions with the specimens of the different groups (Figure 3b). The static testing resulted in low Zn ion concentrations (around 0.3 mg/L) in all the three groups, even after 28 days of immersion (Figure 3c). In contrast, the dynamic testing greatly increased the released Zn ion concentrations after day 7 (Figure 3c). As compared to the S04 and S0402 groups, specimens of the group S03 released more Zn ions into r-SBF (Figure 3c). After 28 days, P and Ca ion concentrations gradually decreased, respectively, to 2 mg/L and 80 mg/L (Figure 3d, e). Similarly, the concentrations of P and Ca ions reduced to different extents under the static and dynamic conditions, with the dynamic tests always exhibiting lower P and Ca ion concentrations in the medium (Figure 3d, e). After 28 days, specimens of the group S04 showed a lower P concentration as compared to the specimens of the groups S03 and S0402, while the variations in Ca ion concentration with immersion time did not show clear differences between the experimental groups (Figure 3e).

9.3.3. Characteristics of the biodegradation products

For all the three groups, after 28 day static or dynamic degradation, four types of biodegradation products were found on the surfaces of the Zn scaffolds (Figure 4a-f). Clusters of small particles (Figure 4c) were mainly found on the biodegraded surfaces and contained Zn, O, C, P, and Ca. The morphological features of the other biodegradation products were: dome-like biodegradation products (Figure 4d) that had Zn, C, O, and P, needle-like biodegradation products (Figure 4e) that contained Zn, O, Ca, and P, and flake-like biodegradation products (Figure 4f) that contained Zn, O, Cl, and C. XRD analysis showed the presence of ZnO, $Zn_5(CO_3)_2(OH)_6$, $Ca_3(PO_4)_2$, and $Zn_5(OH)_6Cl_6H_2O$ after both static and dynamic immersion tests, with elevated intensity levels of these biodegradation products under the dynamic condition (Figure 4g).
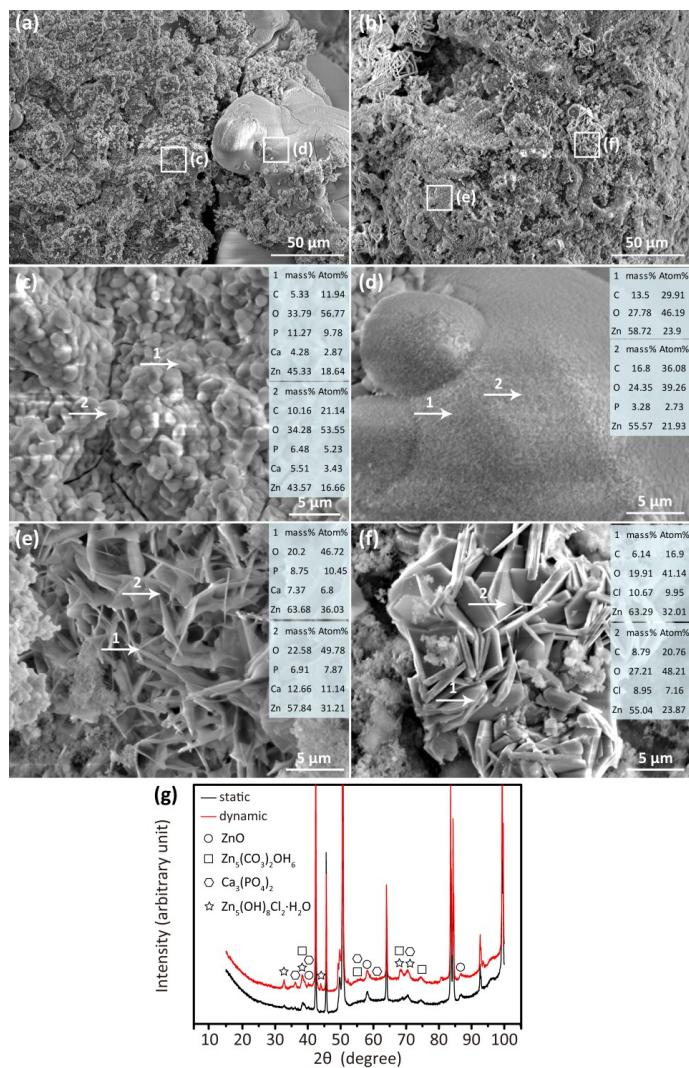
9

Figure 4. Biodegradation products of AM porous Zn at lower (a-b) and higher (c-f) magnification: (c) particle-like biodegradation products, (d) dome-like biodegradation products, (e) needle-like biodegradation products, (f) flake-like biodegradation products, and (g) XRD analysis.

9

9.3.4. Reconstructed morphologies of the specimens after biodegradation

Under the static condition, the specimens underwent more localized biodegradation (Figure 5a, yellow circles) than those under the dynamic one during the same period of 28 days. Interestingly, for the group S0402, the struts in the center seemed to experience more local biodegradation during the dynamic tests. In contrast, more biodegradation was found at the periphery of the specimens during the static tests. Furthermore, larger volumes of biodegradation products (Figure 5a, red) formed during the dynamic immersion tests than during the static tests. The biodegradation products appeared to have mostly formed on a specific side of the specimens, which was further dependent on the testing condition (Figure 5a). Under the static condition, the biodegradation products mainly formed at the bottom side of the specimens, which was in contact with the beaker (Figure 5a). Under the dynamic condition, however, the biodegradation products were found mostly on the top side of the specimens, which was the outlet side of the r-SBF flow (Figure 5a). After 28 days of dynamic biodegradation, specimens of the groups S03 and S04 exhibited the highest ($11.9\% \pm 0.6\%$) and lowest ($7.1\% \pm 0.3\%$) values of volume reduction, respectively (Figure 5b). The volume loss of the specimens of the group S0402 was in-between those extreme values ($7.9\% \pm 0.6\%$) (Figure 5b). As compared to the dynamic biodegradation tests, the static ones resulted in considerably lower values of volume loss in all the groups (Figure 5b). The dynamic tests resulted in about twice as much biodegradation product volumes (*i.e.,* volume gain) in all the three experimental groups, as compared to the static tests (Figure 5c).
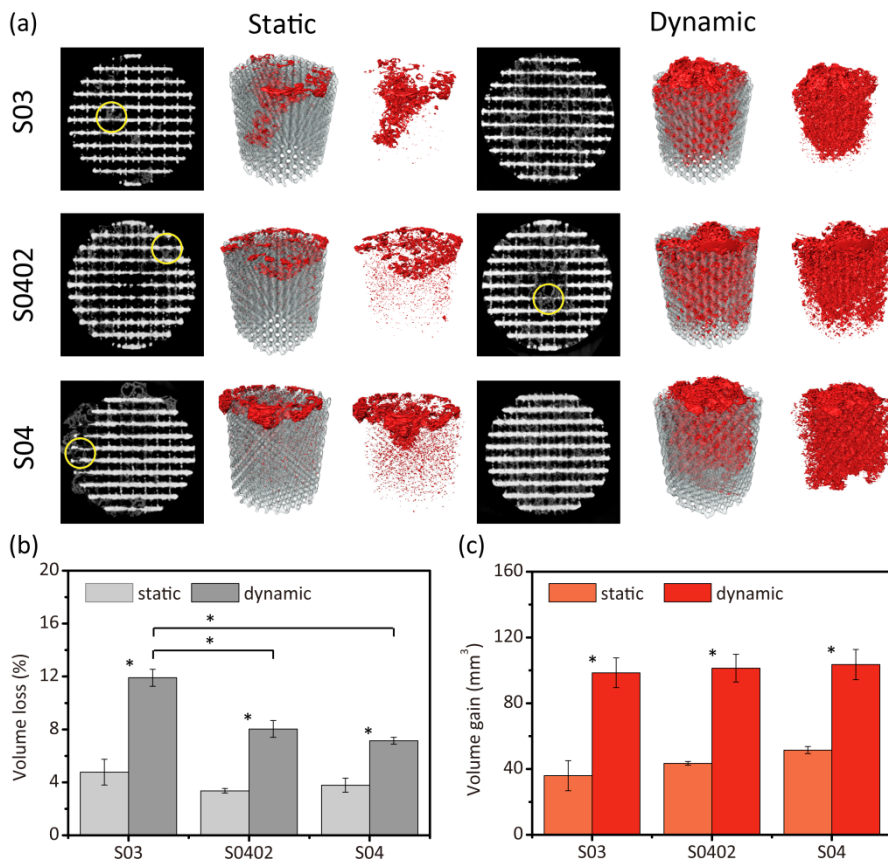
9

Figure 5. Micro-CT analysis of AM porous zinc after 28 days of biodegradation: (a) 3D reconstructions, (b) volume losses of AM porous zinc, and (c) volume gains due to the formation of the biodegradation products shown in Figure 4. Grey: zinc. Red: biodegradation products. Circle: localized biodegradation.

9.3.5. Mechanical properties

The specimens from all the experimental groups exhibited smooth stress-strain curves under compression, even after *in vitro* biodegradation for 28 days (Figure 6a, b). The stress-strain curves of the three groups all exhibited a linear elastic region at early stage, followed by a gradually decreasing slope until a plateau stage, and rapidly increased stresses towards the end (Figure 6a, b).

Among the as-built specimens, those of the S04 group possessed the highest elastic modulus (785.7 ± 72.1 MPa) and yield strength (10.8 ± 0.2 MPa), whereas the S03 group showed the lowest elastic modulus (399.8 ± 32.3 MPa) and yield strength (4.2 ± 0.1 MPa) (Figure 6c, d). Functionally graded group specimens (S0402) had the mechanical properties in between those of the S03 and S0.4 groups (Figure 6c, d). After

1 day of biodegradation, the elastic moduli and yield strengths of the specimens of all the groups increased (Figure 6c, d). Thereafter, all the groups showed fluctuations in elastic modulus (Figure 6c), while their yield strengths gradually increased with immersion time (Figure 6d). All the groups showed higher yield strengths at day 28 as compared to those of the corresponding as-built specimens (Figure 6d). In addition, the specimens that had undergone dynamic biodegradation exhibited higher yield strengths, as compared to those exposed to the static condition (Figure 6d).
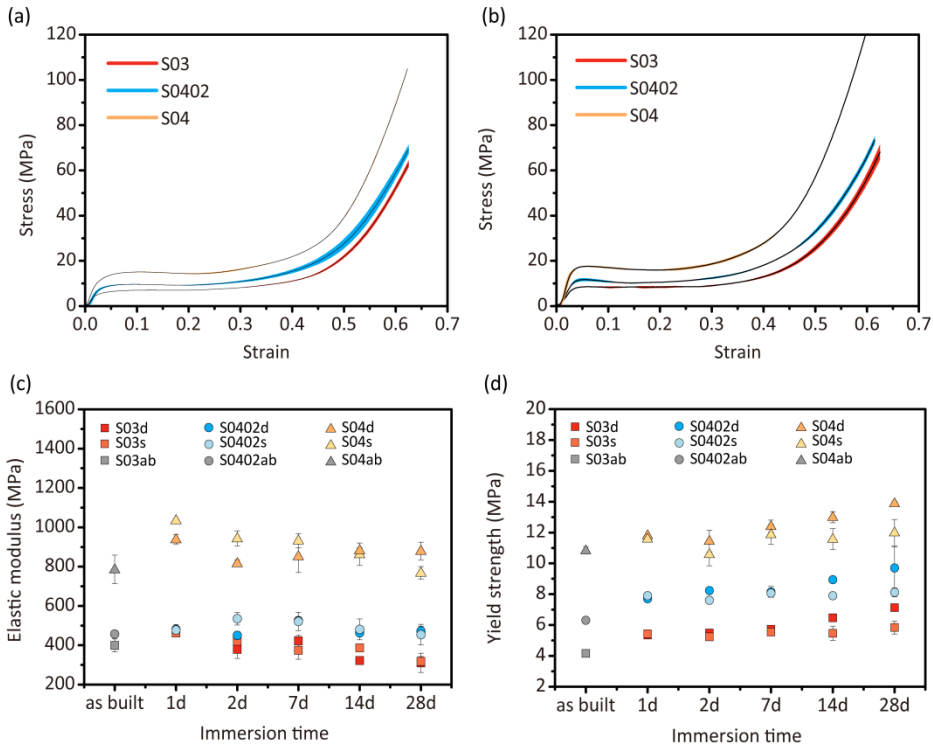

Figure 6. Compressive stress-strain curves of the AM porous zinc specimens before (a) and after (b) 28 days of degradation as well as the changes in elastic modulus (c) and yield strength (d) with immersion time.

9.3.6. Permeability and cell seeding efficiency

The order of the AM porous Zn specimens from the highest permeability to the lowest value was as follows: S03, S0402, and S04 (Figure 7a). The cell seeding efficiencies (Figure 7b) measured for all the experimental groups were above 70%: S03 (75.2%), S0402 (74.35%), and S04 (87.85%) (Figure 7b). Interestingly, specimens of the group S04 showed a 12% increase in cell seeding efficiency in comparison to those of the S03

group, while the seeding efficiency of the functionally graded structure (S0402) did not significantly differ from that of the group S03 (Figure 7b).
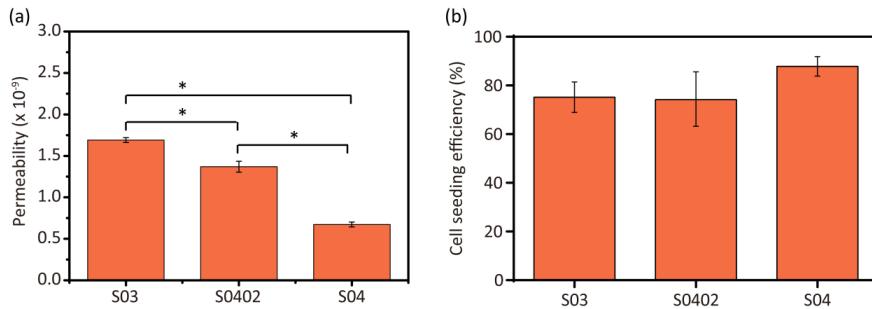

Figure 7. Permeability (a) and cell seeding efficiency (b) of the AM porous zinc specimens of all the three experimental groups.

9.3.7. Direct evaluation of cytocompatibility

The assessment of direct contact cytocompatibility by live-dead staining revealed that most of MG-63 cells were viable (fluorescing green) and only a few cells exhibited evidence of a compromised cell membrane integrity (fluorescing yellow-red) after 24 h of direct contact with the AM porous Zn specimens (Figure 8a-f). Adhered cells were observed at the periphery as well as at the center of the Zn specimens (Figure 8d-f), as is evident from these cross-sectional images. S04 and S0402 specimens appeared to contain more cells as compared to S03 specimen (Figure 8a-f). The functional gradient in strut thickness (*i.e.,* S0402 group) did not seem to influence the regional distribution of cells within the scaffold (Figure 8d-f).

9.3.8. Indirect biocompatibility *in vitro*

Cytocompatibility of the novel Zn specimens was assessed quantitatively using standardized extracts, and compared to that of the Ti-6Al-4V control, as recommended by ISO 10993. Cell viability in the 24 h-extracts was higher than 95% for all the porous Zn specimens, regardless of the topological design: 99.08% (S03), 96.78% (S0402), and 97.83% (S04) (Figure 8h-i). At all tested time points, up to harsh 72 h evaluation, the cell viability values found for the porous Zn groups were not significantly different from those found for the gold standard material (*i.e.,* Ti-6Al-4V) (Figure 8h-i).
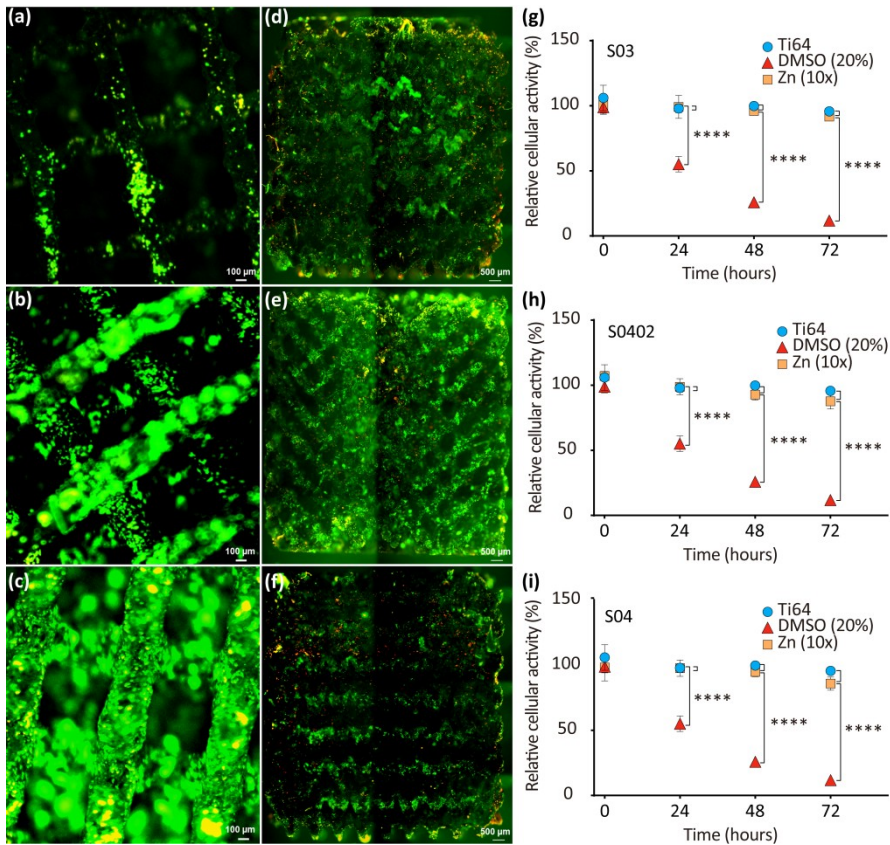
9

Figure 8. Cytocompatibility of AM porous zinc: images of fluorescent cells attached on top of specimens from group S03 (a), S0402 (b), and S04 (c), respectively, next to cell distribution in cross-sections of the respective specimens S03 (d), S0402 (e), and S04 (f) to demonstrate homogenous seeding in the specimen's core. Relative cellular activities of MG-63 cells *in vitro* upon exposure to zinc scaffolds S03 (g), S0402 (h), and S04 (i) (*n=5*). Randomly chosen scaffolds per group were analyzed in at least technical triplicates (zinc, *n=5*; Ti-6Al-4V, *n=3*).

9.4. DISCUSSION

Topological designs hold great promise for tuning the biodegradation behavior and mechanical properties of AM porous biodegradable metallic biomaterials. Here, we studied, for the first time ever, how topological design including a functional gradient can be applied to AM porous Zn. After biodegradation for 28 days, the volume losses of the AM porous Zn specimens varied between 7% to 12% (*i.e.,* 0.13-0.17 mm/year), depending on the topological design, suggesting that we could exploit the topological

design to achieve a desired value of biodegradation rate. Interestingly and being contrary to other AM porous biodegradable metals [5, 6], the yield strengths of the specimens of all the groups increased after 28 days of immersion. Furthermore, the specimens of all the groups showed excellent cytocompatibility, regardless of the topological design. The results demonstrate that AM porous Zn, with appropriate design, holds great potential to fulfill the multiple and often conflicting requirements that are laid out for an ideal bone substitute.

9.4.1. Biodegradation behavior

Based on the SEM/EDS analysis, the flake-like biodegradation products could be $Zn_5(OH)_8Cl_2 \cdot H_2O$ (Figure 4f) [21], while the dome-like biodegradation products were most likely $Zn_5(CO_3)_2(OH)_6$ (Figure 4d) [22]. Higher percentages of Ca and P elements were found in the clusters of small particles (Figure 4c), which could be hydroxyapatite or a combination of ZnO and $Ca_3(PO_4)_2$ [23]. This confirmed the results of the ICP analysis, showing that the concentrations of P and Ca ions gradually decreased with immersion time, as these ions were involved in the growth of the biodegradation products (Figure 3d-e). Furthermore, at all immersion time points and for all the experimental groups, the specimens that had undergone dynamic biodegradation exhibited higher Zn ion concentrations, but lower P and Ca ion concentrations in the immersion medium, as compared to the specimens exposed to the static biodegradation testing. This can be attributed to more biodegradation products formed under the dynamic testing condition (Figure 3a). Under the dynamic condition, the surface of the AM porous Zn specimens was constantly washed by the medium. The flow of the medium over the surface of the specimen inhibited the increase of local pH, thereby increasing the rate of biodegradation [24] and the rate of the formation of the biodegradation products. The human body has a constant pH around 7.4 [25]. Furthermore, the interstitial fluid flows through the (intra) medullary cavities at a rate of 0.012-1.67 ml/min [26]. Therefore, the dynamic biodegradation setup used in this research can mimic some aspects of the *in vivo* environment.

Under the static condition, no large differences were found between the three experimental groups with respect to Zn ion release into the medium (Figure 3c). In contrast, the dynamic tests showed that, after 28 days, a higher Zn ion concentration was found for the specimens of the group S03 than those of the groups S04 and S0402. Moreover, the pH value of the group S03 was slightly higher compared to the other two groups (Figure 3b). Micro-CT results confirmed that the volume losses of the AM porous Zn relied strongly on the topological design, with the group S03 exhibiting the largest volume loss. Topological design changed the permeability (i.e., the fluid flow inside the scaffolds) and thus influenced the biodegradation profile of the AM porous Zn. Generally, a higher porosity leads to a higher permeability and a higher rate of material loss during the *in vitro* immersion tests. Therefore, the biodegradation behavior

of AM Zn scaffolds can be effectively tuned by modifying the topological design of the porous structures.

Besides the commonly observed biodegradation behavior of AM porous Zn, micro-CT analysis suggested that the specimens experienced more localized biodegradation under the static condition (Figure 5a). Moreover, localized biodegradation mainly occurred at the bottom of the specimens. This phenomenon was likely caused by the stagnant flow of r-SBF entrapped in the narrow gap between the specimens and the beaker. Cl^- likely accumulated at these locations and may form a local passive layer inside those narrow spaces [27]. Pitting or crevice-like biodegradation would then take place. On the contrary, dynamic flow prevented the adsorption of Cl^- on the surface of the degraded layer, thereby ensuring the homogeneity of the biodegradation process [24, 28]. Interestingly, under the dynamic condition, localized biodegradation occurred at the core of the S0402 specimens, which could be related to the velocity distribution introduced by the gradient design. According to the computational fluid dynamics (CFD) simulations reported in a previous paper of the present authors [5], the S0402 specimens have a relatively higher flow velocity at the center than on the periphery. It can then be inferred that varied biodegradation rates within one single scaffold can be achieved simultaneously by tuning the local porosity (i.e., the permeability). Under the static condition, however, the group S0402 experienced more localized biodegradation at the periphery, where the struts were thicker and pores were smaller. The smaller pores in the graded structure may increase the possibility for localized degradation to occur. The differences between the static and dynamic conditions in terms of biodegradation rate and biodegradation mechanism observed at different locations within the specimens underscore the fact that, besides the choice of the biomaterial, the topological design of the porous structure plays a crucial role in controlling the biodegradation profile of the resulting implants.

The rates of Zn biodegradation found in this research are comparable (*i.e.*, 0.06-0.07 mm/year under the static condition and 0.13-0.17 mm/year under the dynamic condition) with the biodegradation rates reported by others (*i.e.*, 0.011-0.084 mm/year under static conditions [23, 29, 30]). Furthermore, it is interesting to note that, for pure Zn, the results from *in vitro* biodegradation tests are largely consistent with those found *in vivo* (i.e., 0.010-0.065 mm/year) [31-37]. It should, however, be noted that in most *in vivo* tests, pure Zn wires or stents that were used for those measurements were implanted in the abdominal aorta. Based on these considerations, AM porous Zn exhibited a moderate biodegradation rate that corresponds to complete degradation within 1-2 years [38]. However, in the future, animal experiments with AM porous Zn should be performed to determine its, possibly implantation site-specific, real *in vivo* biodegradation rate in order to better predict its potential as a bone substituting material and its local tissue responses.

9

9.4.2. Mechanical behavior

All the AM Zn scaffolds, even after 28 days of biodegradation, still had the mechanical properties within the scope of those of cancellous bone (E = 0.01-2 GPa, σ_y = 0.2-80 MPa [2]) (Figure 6). Similarly to AM porous Fe, titanium, and tantalum [1, 5, 39, 40], the AM porous Zn specimens had smooth stress-strain curves a plateau stage (Figure 6a, b), which could be attributed to the high ductility of pure Zn [14]. Regarding the functionally graded design (S0402), as the struts thickness continuously and gradually changed, abrupt changes in stress at the boundary between different struts could be minimized [41]. In the case of the three different groups, porosity strongly affected the elastic modulus and yield strengths of the AM Zn specimens: lower porosity resulted in a higher elastic modulus and yield strength. As the porosity of the group S0402 fell between the porosities of the S03 and S04 groups, their mechanical properties were also in between those of the S03 and S04 groups. Generally, human bone has a highly anisotropic and heterogeneous structure, leading to different strength and stiffness values in different directions and at different locations [42]. Meanwhile, bone has a sufficient permeability in order to transfer nutrients and cells. Therefore, biodegradable porous bone-substituting implants should also have a tailored distribution of mechanical properties and a certain range of permeability values. In this study, with a linearly and radially graded design, we attempted to show that it was possible to achieve those goals to some extent.

After one day of *in vitro* biodegradation, specimens of all the three groups showed improved mechanical properties as compared to those of their as-built counterparts. Although similar results were found at the early stages of the biodegradation of AM porous Mg and Fe [1, 2], the mechanical properties of the biodegraded specimens S0402 and S04 were higher than those of their as-built counterparts, even after *in vitro* biodegradation for 28 days (Figure 6c, d). Interestingly, the specimens subjected to dynamic biodegradation had higher yield strengths as compared to those under the static condition. The increases in the mechanical properties of the biodegradable metal with immersion time could be attributed to the contributions of the biodegradation products. AM porous Zn may behave like a composite material consisting of Zn and the biodegradation products. While progressing biodegradation deteriorated the mechanical properties of Zn, the formation of large amounts of biodegradation products under the dynamic condition could help in retaining, or even improving its mechanical properties. Under the static condition, however, a smaller volume of biodegradation products was less effective in playing this role and more localized biodegradation led to decreases in yield strength.

These observations, together with the bone-mimicking mechanical properties suggest that AM porous Zn is a promising candidate for orthopedic implants. Of course, animal experiments will still be required to see how far the here reported changes in

9

mechanical properties *in vitro* can be translated into the *in vivo* situation. Of note, the mechanical properties of AM porous Zn may also change as a result of bone tissue regeneration [43]. These two effects (*i.e.*, Zn biodegradation vs. bone tissue neoformation) should be simultaneously considered when studying the evolution of the mechanical properties of such biomaterials with time. Moreover, no information is available yet concerning the fatigue behavior of these biomaterials. Given the fact that both topological design and material category significantly affect both the static and dynamic mechanical behaviors of AM porous metallic biomaterials [44-47], there is a need for a thorough study on the dynamic mechanical responses of these porous structures [48].

9.4.3. Cytocompatibility

The ISO10993-recommended MTS assay, which is a sensitive and quantitative method to colorimetrically identify viable cells, revealed no significant differences in cellular activities of MG-63 indicator cells between the three different structures (i.e., S03, S0402, and S04). All the three groups revealed a good cytocompatibility. While Zn ions at low concentrations hold potential to enhance cell viability, adhesion, proliferation, and migration [49], at high concentrations they may stimulate oxidative stress pathways, inducing cell apoptosis and necrosis [50]. However, *in vivo* the body's vasculature facilitates the removal of Zn ions and respective biodegradation products, which helps prevent detrimental local ion overloads. Therefore, we used recently recommended modification to the ISO 10993 standards to make them applicable for absorbable biomaterials [51]. Using the suggested 10X diluted extracts in indirect cytotoxicity assays, the group S04 revealed 85% cellular activity, which was the lowest among all the groups, while the S03 specimens showed the highest (i.e., 91%) cellular activity, after relatively harsh 72 h incubation. Of note, during more frequently reported 24 to 48 h incubation times, cellular activities remained >90% in all the tested extracts. Thus, the Zn extracts from all the three experimental groups may be considered to be non-toxic (*i.e.*, 75-99% viability; cytotoxicity grade 1). Although a higher porosity normally increases permeability, thereby resulting in greater ion release into extracts [20, 40, 68], the outcome of our study did not indicate such differences between the three experimental groups. However, while our cytocompatibility testing regime was in line with current ISO 10993 recommendations, even our longest immersion time might have been too short to fully appreciate such increases in ion release, which may require weeks to occur.

To better appreciate any cell to biomaterial contact-mediated cytocompatibility issues, we additionally performed cell seeding experiments with all the three different AM porous Zn scaffolds using semi-quantitative fluorescent live/dead imaging. 24 h after seeding, majority of MG-63 cells remained viable and appeared well attached to the specimen surfaces. Interestingly, Zn-based biomaterials have been shown to support,

among others, cell viability and proliferation, because Zn ions are important cofactors in a variety of metabolic processes [52]. From surface visualization and cross-sectional imaging, MG-63 cells appeared to be evenly distributed along the periphery as well as within the core region of the specimens, without showing any obvious design-related differences. It is in agreement with the results obtained by other researchers who analyzed pre-osteoblasts in graded Ti-6Al-4V scaffolds [53], in comparison with cell distribution in graded polymer 3D scaffolds [54]. Of note, cell seeding efficiency was above 70% (i.e., 70% cells attached to the Zn surface) for all the three porous Zn scaffold designs, but a slightly higher efficacy in the group S04 was noticed, as compared to S03. Fluorescent images also showed that S04 and S0402 specimens appeared to contain more attached cells as compared to S03 specimen (Figure 8a-f). A general expectation may be that a smaller pore size provides a larger strut surface area for cell-surface interactions before cells pass through the pores. In addition, pore-clogging may result in increased cell accumulation within the scaffold [55]. However, with fluorescence it was hard to quantify cells objectively and the AM Zn scaffolds did not show significant differences in cell seeding efficiency between the different groups. A possible explanation might be that the scaffolds designed in the present study were graded along the radial direction (i.e., along the x and y axes), instead of the axial direction (z-axis), as in other studies [55-57]. Axial gradation could create a "sieve effect" during cell seeding and may account for increased cell seeding efficiencies. Another likely reason is that the pore/strut size differences between the scaffolds in our study were not large enough to significantly influence cell seeding efficiency. Moreover, fluorescent imaging has its limitations and is difficult to quantify within opaque metal 3D structures, which is a limitation of the present study.

9.5. CONCLUSIONS

We demonstrated that functionally graded porous Zn with precisely controlled topology can be fabricated by using PBF and the biodegradation behavior and mechanical properties of AM porous Zn can be tuned through topological design. The topological design changed the permeability by up to 3-fold and altered the biodegradation rate by up to 1.5-fold between the 3 groups of the AM porous Zn. Of note, the biodegradation rates of all the groups of AM porous Zn were rather moderate, with 7.1%-11.9% volume losses after 28 days of dynamic *in vitro* biodegradation. Elastic modulus (400-786 MPa) and yield strengths (4-11 MPa) of the specimens of all the three groups remained within the scope of those of human cancellous bone. Regardless of the topological design, the AM porous Zn exhibited good biocompatibility *in vitro*. The results highlighted that proper topological design plays an important role in developing AM biodegradable porous metals. AM porous Zn holds great potential for bone substitution in the future.

9

REFERENCES

[1] Y. Li, H. Jahr, K. Lietaert, P. Pavanram, A. Yilmaz, L. I. Fockaert, M. A. Leeflang, B. Pouran, Y. Gonzalez-Garcia, H. Weinans, J. M. C. Mol, J. Zhou, A. A. Zadpoor. Additively manufactured biodegradable porous iron. Acta Biomater. 2018;77:380-393.

[2] Y. Li, J. Zhou, P. Pavanram, M. A. Leeflang, L. I. Fockaert, B. Pouran, N. Tümer, K. U. Schröder, J. M. C. Mol, H. Weinans, H. Jahr, A. A. Zadpoor. Additively manufactured biodegradable porous magnesium. Acta Biomater. 2018;67:378-392.

[3] Y. F. Zheng, X. N. Gu, F. Witte. Biodegradable metals. Mater Sci Eng R Rep. 2014;77:1-34.

[4] D. Andreas, H. Thomas, B. F. Wilhelm, P. Matthias. In vitro and in vivo corrosion properties of new iron–manganese alloys designed for cardiovascular applications. J Biomed Mater Res B Appl Biomater. 2015;103:649-660.

[5] Y. Li, H. Jahr, P. Pavanram, F. S. L. Bobbert, U. Puggi, X. Y. Zhang, B. Pouran, M. A. Leeflang, H. Weinans, J. Zhou, A. A. Zadpoor. Additively manufactured functionally graded biodegradable porous iron. Acta Biomater. 2019.

[6] C. Gao, M. Yao, S. Li, P. Feng, S. Peng, C. Shuai. Highly biodegradable and bioactive Fe-Pd-bredigite biocomposites prepared by selective laser melting. Journal of Advanced Research. 2019;20:91-104.

[7] D. Pierson, J. Edick, A. Tauscher, E. Pokorney, P. Bowen, J. Gelbaugh, J. Stinson, H. Getty, C. H. Lee, J. Drelich, J. Goldman. A simplified in vivo approach for evaluating the bioabsorbable behavior of candidate stent materials. J Biomed Mater Res B Appl Biomater. 2012;100B:58-67.

[8] L.-Y. Li, L.-Y. Cui, R.-C. Zeng, S.-Q. Li, X.-B. Chen, Y. Zheng, M. B. Kannan. Advances in functionalized polymer coatings on biodegradable magnesium alloys – A review. Acta Biomater. 2018;79:23-36.

[9] Y. Zheng, X. Xu, Z. Xu, J. Wang, H. Cai. Development of Fe-based degradable metallic biomaterials. Metallic Biomaterials: Wiley-VCH Verlag GmbH & Co. KGaA; 2017. p. 113-160.

[10] J. Venezuela, M. S. Dargusch. The influence of alloying and fabrication techniques on the mechanical properties, biodegradability and biocompatibility of zinc: A comprehensive review. Acta Biomater. 2019;87:1-40.

[11] L. Zhao, Z. Zhang, Y. Song, S. Liu, Y. Qi, X. Wang, Q. Wang, C. Cui. Mechanical properties and in vitro biodegradation of newly developed porous Zn scaffolds for biomedical applications. Mater Des. 2016;108:136-144.

[12] J. Niu, Z. Tang, H. Huang, J. Pei, H. Zhang, G. Yuan, W. Ding. Research on a Zn-Cu alloy as a biodegradable material for potential vascular stents application. Mater Sci Eng, C. 2016;69:407-413.

9

[13] X. Wang, X. Shao, T. Dai, F. Xu, J. G. Zhou, G. Qu, L. Tian, B. Liu, Y. Liu. In vivo study of the efficacy, biosafety, and degradation of a zinc alloy osteosynthesis system. Acta Biomater. 2019;92:351-361.

[14] Y. Qin, P. Wen, M. Voshage, Y. Chen, P. G. Schückler, L. Jauer, D. Xia, H. Guo, Y. Zheng, J. H. Schleifenbaum. Additive manufacturing of biodegradable Zn-xWE43 porous scaffolds: Formation quality, microstructure and mechanical properties. Mater Des. 2019;181:107937.

[15] P. Wen, Y. Qin, Y. Chen, M. Voshage, L. Jauer, R. Poprawe, J. Henrich Schleifenbaum. Laser additive manufacturing of Zn porous scaffolds: shielding gas flow, surface quality and densification. J Mater Sci Technol. 2018.

[16] K. Lietaert, B. Neirinck, J. Plas, J. Vleugels. Influence of unit cell architecture and of relative density on the mechanical properties of additively manufactured Zn scaffolds as biodegradable implant materials. Proceedings Euro PM 2017: International Powder Metallurgy Congress and Exhibition. Politecnico di Milano, Italy: The European Powder Metallurgy Association; 2017. p. 1-7.

[17] Y. Li, P. Pavanram, J. Zhou, K. Lietaert, P. Taheri, W. Li, H. San, M. A. Leeflang, J. M. C. Mol, H. Jahr, A. A. Zadpoor. Additively manufactured biodegradable porous zinc. Submitted.

[18] K. Lietaert, W. Baekelant, L. Thijs, J. Vleugels. Direct metal printing of zinc: from single laser tracks to high density parts. European Congress and Exhibition on Powder Metallurgy. European PM Conference Proceedings. Swerea KIMAB, Sweden: The European Powder Metallurgy Association; 2016. p. 1-6.

[19] A. Oyane, H.-M. Kim, T. Furuya, T. Kokubo, T. Miyazaki, T. Nakamura. Preparation and assessment of revised simulated body fluids. J Biomed Mater Res A. 2003;65A:188-195.

[20] K. Shimizu, A. Ito, H. Honda. Enhanced cell-seeding into 3D porous scaffolds by use of magnetite nanoparticles. J Biomed Mater Res B Appl Biomater. 2006;77B:265-272.

[21] M. M. Alves, L. M. Marques, I. Nogueira, C. F. Santos, S. B. Salazar, S. Eugénio, N. P. Mira, M. F. Montemor. In silico, in vitro and antifungal activity of the surface layers formed on zinc during this biomaterial degradation. Appl Surf Sci. 2018;447:401-407.

[22] K. Törne, A. Örnberg, J. Weissenrieder. Influence of strain on the corrosion of magnesium alloys and zinc in physiological environments. Acta Biomater. 2017;48:541-550.

[23] L. Liu, Y. Meng, C. Dong, Y. Yan, A. A. Volinsky, L.-N. Wang. Initial formation of corrosion products on pure zinc in simulated body fluid. J Mater Sci Technol. 2018;34:2271-2282.

9

[24] J. Lévesque, H. Hermawan, D. Dubé, D. Mantovani. Design of a pseudo-physiological test bench specific to the development of biodegradable metallic biomaterials. Acta Biomater. 2008;4:284-295.

[25] J. C. Atherton. Acid–base balance: maintenance of plasma pH. Anaesth Intens Care. 2009;10:557-561.

[26] A. P. Md Saad, A. Syahrom. Study of dynamic degradation behaviour of porous magnesium under physiological environment of human cancellous bone. Corros Sci. 2018;131:45-56.

[27] H. Wu, C. Zhang, T. Lou, B. Chen, R. Yi, W. Wang, R. Zhang, M. Zuo, H. Xu, P. Han, S. Zhang, J. Ni, X. Zhang. Crevice Corrosion – A Newly Observed Mechanism of Degradation in Biomedical Magnesium. Acta Biomater. 2019.

[28] Y. Zong, G. Yuan, X. Zhang, L. Mao, J. Niu, W. Ding. Comparison of biodegradable behaviors of AZ31 and Mg–Nd–Zn–Zr alloys in Hank's physiological solution. Mater Sci Eng, B. 2012;177:395-401.

[29] X. Liu, J. Sun, F. Zhou, Y. Yang, R. Chang, K. Qiu, Z. Pu, L. Li, Y. Zheng. Micro-alloying with Mn in Zn–Mg alloy for future biodegradable metals application. Mater Des. 2016;94:95-104.

[30] M. Sikora-Jasinska, E. Mostaed, A. Mostaed, R. Beanland, D. Mantovani, M. Vedani. Fabrication, mechanical properties and in vitro degradation behavior of newly developed ZnAg alloys for degradable implant applications. Mater Sci Eng, C. 2017;77:1170-1181.

[31] P. K. Bowen, J. Drelich, J. Goldman. Zinc exhibits ideal physiological corrosion behavior for bioabsorbable stents. Adv Mater. 2013;25:2577-2582.

[32] A. Kafri, S. Ovadia, G. Yosafovich-Doitch, E. Aghion. In vivo performances of pure Zn and Zn–Fe alloy as biodegradable implants. J Mater Sci Mater Med. 2018;29:94.

[33] H. Yang, C. Wang, C. Liu, H. Chen, Y. Wu, J. Han, Z. Jia, W. Lin, D. Zhang, W. Li, W. Yuan, H. Guo, H. Li, G. Yang, D. Kong, D. Zhu, K. Takashima, L. Ruan, J. Nie, X. Li, Y. Zheng. Evolution of the degradation mechanism of pure zinc stent in the one-year study of rabbit abdominal aorta model. Biomaterials. 2017;145:92-105.

[34] A. J. Drelich, S. Zhao, R. J. Guillory, J. W. Drelich, J. Goldman. Long-term surveillance of zinc implant in murine artery: Surprisingly steady biocorrosion rate. Acta Biomater. 2017;58:539-549.

[35] P. K. Bowen, R. J. Guillory, E. R. Shearier, J.-M. Seitz, J. Drelich, M. Bocks, F. Zhao, J. Goldman. Metallic zinc exhibits optimal biocompatibility for bioabsorbable endovascular stents. Mater Sci Eng, C. 2015;56:467-472.

[36] S. Zhao, J.-M. Seitz, R. Eifler, H. J. Maier, R. J. Guillory, E. J. Earley, A. Drelich, J. Goldman, J. W. Drelich. Zn-Li alloy after extrusion and drawing: Structural, mechanical characterization, and biodegradation in abdominal aorta of rat. Mater Sci Eng, C. 2017;76:301-312.

9

[37] S. A. Arab, G. R. J. II, S. Daniel, G. Jeremy, D. J. W. Effect of PLLA coating on corrosion and biocompatibility of zinc in vascular environment. Surf Innov. 2017;5:211-220.

[38] G. Jia, C. Chen, J. Zhang, Y. Wang, R. Yue, B. J. C. Luthringer - Feyerabend, R. Willumeit-Roemer, H. Zhang, M. Xiong, H. Huang, G. Yuan, F. Feyerabend. In vitro degradation behavior of Mg scaffolds with three-dimensional interconnected porous structures for bone tissue engineering. Corros Sci. 2018;144:301-312.

[39] R. Wauthle, J. van der Stok, S. Amin Yavari, J. Van Humbeeck, J.-P. Kruth, A. A. Zadpoor, H. Weinans, M. Mulier, J. Schrooten. Additively manufactured porous tantalum implants. Acta Biomater. 2015;14:217-225.

[40] R. Wauthle, S. M. Ahmadi, S. Amin Yavari, M. Mulier, A. A. Zadpoor, H. Weinans, J. Van Humbeeck, J.-P. Kruth, J. Schrooten. Revival of pure titanium for dynamically loaded porous implants using additive manufacturing. Mater Sci Eng, C. 2015;54:94-100.

[41] X.-Y. Zhang, G. Fang, S. Leeflang, A. A. Zadpoor, J. Zhou. Topological design, permeability and mechanical behavior of additively manufactured functionally graded porous metallic biomaterials. Acta Biomater. 2019;84:437-452.

[42] X. Wang, S. Xu, S. Zhou, W. Xu, M. Leary, P. Choong, M. Qian, M. Brandt, Y. M. Xie. Topological design and additive manufacturing of porous metals for bone scaffolds and orthopaedic implants: A review. Biomaterials. 2016;83:127-141.

[43] R. Hedayati, S. Janbaz, M. Sadighi, M. Mohammadi-Aghdam, A. A. Zadpoor. How does tissue regeneration influence the mechanical behavior of additively manufactured porous biomaterials? J Mech Behav Biomed Mater. 2017;65:831-841.

[44] Y. Li, H. Jahr, X. Y. Zhang, M. A. Leeflang, W. Li, B. Pouran, F. D. Tichelaar, H. Weinans, J. Zhou, A. A. Zadpoor. Biodegradation-affected fatigue behavior of additively manufactured porous magnesium. Addit Manuf. 2019;28:299-311.

[45] Y. Li, K. Lietaert, W. Li, X. Y. Zhang, M. A. Leeflang, J. Zhou, A. A. Zadpoor. Corrosion fatigue behavior of additively manufactured biodegradable porous iron. Corros Sci. 2019;156:106-116.

[46] R. Hedayati, S. M. Ahmadi, K. Lietaert, B. Pouran, Y. Li, H. Weinans, C. D. Rans, A. A. Zadpoor. Isolated and modulated effects of topology and material type on the mechanical properties of additively manufactured porous biomaterials. J Mech Behav Biomed Mater. 2018;79:254-263.

[47] S. M. Ahmadi, R. Hedayati, Y. Li, K. Lietaert, N. Tümer, A. Fatemi, C. D. Rans, B. Pouran, H. Weinans, A. A. Zadpoor. Fatigue performance of additively manufactured meta-biomaterials: The effects of topology and material type. Acta Biomater. 2018;65:292-304.

[48] G. Li, H. Yang, Y. Zheng, X.-H. Chen, J.-A. Yang, D. Zhu, L. Ruan, K. Takashima. Challenges in the use of zinc and its alloys as biodegradable metals: perspective from biomechanical compatibility. Acta Biomater. 2019.

9

[49] J. Ma, N. Zhao, D. Zhu. Bioabsorbable zinc ion induced biphasic cellular responses in vascular smooth muscle cells. Sci Rep. 2016;6:26661.

[50] G. Katarivas Levy, J. Goldman, E. Aghion. The prospects of zinc as a structural material for biodegradable Implants—a review paper. Metals. 2017;7:402.

[51] J. Wang, F. Witte, T. Xi, Y. Zheng, K. Yang, Y. Yang, D. Zhao, J. Meng, Y. Li, W. Li, K. Chan, L. Qin. Recommendation for modifying current cytotoxicity testing standards for biodegradable magnesium-based materials. Acta Biomater. 2015;21:237-249.

[52] D. Zhu, Y. Su, M. L. Young, J. Ma, Y. Zheng, L. Tang. Biological Responses and Mechanisms of Human Bone Marrow Mesenchymal Stem Cells to Zn and Mg Biomaterials. ACS Appl Mater Interfaces. 2017;9:27453-27461.

[53] E. Onal, J. Frith, M. Jurg, X. Wu, A. Molotnikov. Mechanical Properties and In Vitro Behavior of Additively Manufactured and Functionally Graded Ti6Al4V Porous Scaffolds. Metals. 2018;8:200.

[54] A. Di Luca, B. Ostrowska, I. Lorenzo-Moldero, A. Lepedda, W. Swieszkowski, C. Van Blitterswijk, L. Moroni. Gradients in pore size enhance the osteogenic differentiation of human mesenchymal stromal cells in three-dimensional scaffolds. Sci Rep. 2016;6:22898.

[55] K. C. Nune, A. Kumar, R. D. K. Misra, S. J. Li, Y. L. Hao, R. Yang. Functional response of osteoblasts in functionally gradient titanium alloy mesh arrays processed by 3D additive manufacturing. Colloids Surf, B. 2017;150:78-88.

[56] Q. Zhang, H. Lu, N. Kawazoe, G. Chen. Pore size effect of collagen scaffolds on cartilage regeneration. Acta Biomater. 2014;10:2005-2013.

[57] S. H. Oh, I. K. Park, J. M. Kim, J. H. Lee. In vitro and in vivo characteristics of PCL scaffolds with pore size gradient fabricated by a centrifugation method. Biomaterials. 2007;28:1664-1671.

9

10

General conclusions, discussion, and recommendations

10

10.1. General conclusions

In this thesis work, we used, for the first time, AM to fabricate biodegradable porous Mg, Fe, and Zn and investigate their *in vitro* performances. We started with topologically ordered homogeneous designs and conducted comprehensive studies on the as-built microstructures, geometrical characteristics, electrochemical behavior, biodegradation behavior, quasi-static mechanical properties, fatigue behavior, and cytocompatibility of these novel biomaterials. Then, we adopted functionally graded designs to differentiate the materials of different structural designs in biodegradation behavior and mechanical properties. Our results showed that AM biodegradable porous metals have the potential to satisfy all the basic functional requirements regarding an ideal bone substituting biomaterial. Therefore, with a proper scaffold design and alloying, AM biodegradable porous metals could be a new generation of functional biomaterials that are particularly useful in orthopedic applications where the treatment of large bony defects remains a major challenge. The most significant findings from this research are summarized here:

1. Biodegradable porous metals with a fully interconnected, topologically ordered, and precisely controlled porous structure can be fabricated through SLM.

2. The mechanical properties of AM biodegradable porous metals are high enough to provide proper mechanical support in the early stages of bone regeneration process. These properties fall within the range of the values reported for the trabecular bone even after 4 weeks of *in vitro* biodegradation. For the same geometrical design, AM porous Fe had the highest elastic modulus and yield strength, while AM porous Zn showed the lowest mechanical properties. After four weeks of *in vitro* biodegradation, the elastic modulus and yield strength of the porous iron specimens decreased insignificantly, *i.e.* by 7% and 5%, respectively, whereas the yield strength of AM porous Mg reduced by 35%. Surprisingly, AM porous Zn showed even higher mechanical properties as compared to the as-built material after four weeks of *in vitro* biodegradation.

3. The biodegradation rates of AM biodegradable porous metals largely varied. Among the materials studied here, Mg had the highest biodegradation rate (*i.e.*, 20% volume loss after 4 weeks), while AM porous iron exhibited only 3.1% of weight reduction. The biodegradation rate of AM porous zinc was moderate with 3.6% volume loss after four weeks of static *in vitro* biodegradation. Dynamic flow increased the biodegradation rate of AM porous iron and zinc.

10

4. AM Zn showed the best *in vitro* biocompatibility results both in direct and indirect cytotoxicity tests. Although direct contact between MG-63 cells and AM Mg scaffolds revealed instant cytotoxicity in static cell culture, the fraction of unviable cells determined according to ISO 10993 was less than 25%. AM iron exhibited markedly lower degrees of biocompatibility as compared with both other metals, although its degradation rate was the lowest.

5. Biodegradation and fatigue affected each other to a great extent. AM Fe and Zn both had excellent fatigue resistance in r-SBF, with AM Zn showing even a higher fatigue strength in r-SBF ($0.8\sigma_y$) than in air ($0.7\sigma_y$). In contrast, AM Mg showed only $0.3\sigma_y$ fatigue strength in air, which decreased to $0.2\sigma_y$ in r-SBF. On the other hand, cyclic loading accelerated the biodegradation process in r-SBF.

6. Biodegradation mechanisms were found to be location-dependent for all the AM porous metals considered here. Topological design in general and functional gradients in particular were found to be effective tools for adjusting the biodegradation behavior, mechanical properties, and fatigue performance of these AM porous metals.

10.2. General discussion

In this dissertation, for the first time, three different types of biodegradable metals, namely a Mg-based alloy, pure Fe, and pure Zn, were additively manufactured through SLM. We also performed comprehensive studies on the as-built microstructures, quasi-static mechanical properties, electrochemical performance, biodegradation behavior, and biocompatibility of these biomaterials. AM biodegradable porous metals showed unique microstructures that resulted in biodegradation and electrochemical behaviors that were different from those of their traditionally manufactured counterparts. Dependent on the type of the underlying material, AM biodegradable porous metals with exactly the same geometrical design exhibited different mechanical properties, biodegradation rates, and cell responses. According to our *in vitro* cell culture experiments, AM porous Mg, Fe, and Zn had different levels of cytocompatibility. As the main applications of AM biodegradable porous metals are as load-bearing orthopedic implants, we also performed corrosion fatigue tests to evaluate the response of these materials to dynamic loading. Biodegradation and cyclic loading were found to influence each other to a great extent. Moreover, the corrosion fatigue behavior of AM biodegradable porous metals significantly differed from each other despite having the same geometrical design. All the studies performed confirmed the importance of the choice of the material used for the fabrication of AM biodegradable porous metals. With the performance of these metals understood, we turned our attention to the use of

10

topological design in adjusting the properties of AM porous biodegradable metals. Indeed, the biodegradation behavior of such materials were already found to be strongly location-dependent for all the three types of materials, suggesting that topological design could serve as an important tool for adjusting the biodegradation behavior of AM biodegradable porous metals. Our studies showed that topological design in general and functionally graded structures in particular has significant effects on the mechanical properties and biodegradation behavior of AM biodegradable porous metals and allow them to meet contradictory design requirements. In summary, AM biodegradable porous metals showed promising properties that can fulfill the requirements as an ideal bone implant, which include: fully interconnected pores with precisely controlled geometries, high enough mechanical properties that match those of the human trabecular bone, tunable biodegradation rates, and good biocompatibility. Some specific issues with respect to material processing, alloying, topological design, and *in vitro* test conditions are discussed below.

10.2.1. Material processing

The AM biodegradable porous metals studied here had precisely controlled geometries, which were close to the designed geometries, suggesting that SLM is an apprpriate technique to fabricate complex biodegradable metallic scaffolds. Rapid cooling rates occurring during the laser melting process resulted in fine grains in these three biodegradable metals [1]. It is well known that the grain size can affect not only the mechanical properties but also the biodegradation rate of metallic biomaterials [2]. AS compared with traditionally manufactured ones, AM biodegradable metals showed improved yield strengths, which can be attributed to their refined grain sizes [3]. AM biodegradable porous iron showed a significantly increased biodegradation rate as compared to cold rolled iron, because of the larger areas of grain boundaries [4]. On the contrary, grain refinement led to the increased corrosion resistance of the Mg-based alloy [2, 5]. Accelerated passivation kinetics was considered as the main reason for that observation. No information is available yet concerning the influence of grain size on the performance of AM Zn-based porous biomaterials. It is, therefore, important to study AM biodegradable metals with different grain sizes. Moreover, as can be seen in the case of AM porous Mg and Zn, the grain sizes and morphologies are inhomogeneous along the building direction [6, 7], further complicating the optimization of the microstructures of such biomaterials. In the future, with the flexibilies of tuning the laser power input and scanning strategy, it can be envisaged that, in addition to the geometrical design, the microstructures of AM biodegradable porous metals could be customized.

10

After AM, we used only chemical polishing to remove powder particles adhered to the surface. The procedure was effective on the periphery of the AM scaffolds, but powder particles still remained in the center. Since surface roughness can influence the fatigue and biodegradation behavior of metallic biomaterials [8, 9], more appropriate cleaning solutions need to be developed. For instance, sandblasting has been found to be an effective tool to smoothen the surface of AM titanium samples [8]. It can also induce compressive stresses and nano-crystallized zones on the surface, which will be beneficial for enhancing the fatigue behavior of AM porous metals [10]. Heat treatment is another post-processing procedure that may impact the properties of AM biodegradable porous metals. For example, hot isostatic pressing (HIP) can be used to improve the fatigue behavior of the AM porous metal by closing the internal pores present in the bulk of the struts constituting the porous structures [8].

10.2.2. Alloying

The mechanical properties of AM biodegradable porous metals were within the range of the values reported for the human trabecular bone (*i.e.*, E = 500-2,000 MPa [11], σ_y = 0.2-80 MPa [12]). However, if we would like to further improve their mechanical properties to match the mechanical properties of the cortical bone (i.e., E = 2,000-30,000 MPa, $\sigma_y \approx$ 200 MPa [13]), pure Fe and pure Zn need to be alloyed with proper elements. Fe-Mn alloys, for example, tend to exhibit much higher yield strengths than pure Fe at a level that is even comparable with 316L steel [14]. Such high values allow for the introduction of porosity through AM. Similarly, Zn shows much higher values of the yield strength when alloyed with Mg or Ag [15-17]. The strengthening mechanisms include grain refinement, solid solution strengthening, and precipitation strengthening. Moreover, alloying can be used to adjust the biodegradation rates of AM biodegradable metals. Fe-Co and Fe-Mn alloys, for example, show higher biodegradation rates as compared with pure iron, while Fe-Ni and Fe-Cr significantly increase the corrosion resistance of metallic biomaterials [18]. Zn-Ag alloys usually increase the biodegradation rates of Zn-based biomaterials due to the presence of galvanic corrosion [15]. Another advantage of alloying Fe with Mn is that Fe-Mn alloys possess an austenitic phase, which can enhance the compatibility with magnetic resonance imaging (MRI). Furthermore, the selection of alloying elements needs to consider the cytocompatibilty of the resulting biomaterials. As for Mg, although biodegradable stents and bone screws made from WE43 have been already launched into market [19], the biodegradation rate of AM porous WE43 is on the high side. New Mg alloys that are suitable for SLM still need to be developed. Considering the rapid solidification rates involved in SLM, Mg-based metallic glasses may possibly be fabricated through SLM. MgZnCa glasses have been reported as a proper candidate

10

[20]. Furthermore, alloying has the ability to make AM biodegradable metals more biofunctional. Mg-Nd-Zn-Zr, for example, has been found to show improved antibacterial activity as a result of adding Zn and Zr [21]. Adding Ag to pure Zn prevents bacteria from adhering to the surface of the implants. Ag ions have been also reported to kill bacteria [22]. Other elements, such as Sr can also be added, as they inhibit bone resorption and stimulate bone formation [23].

10.2.3. Topological design

As the human bone is a highly hierarchical structure, it is widely believed that the geometry of AM biodegradable porous metal should mimic that of the human bone [13]. The design of AM biodegradable metals should not only make sure of the match of their mechanical properties with the surrounding tissue, it should also possess fully interconnected pores and sufficient porosity to facilitate the transport of nutrients and cells [4, 7]. The surface of porous implants should facilitate cell adhesion and proliferation as well. Porosity and pore shape play a major role in determining the mechanical properties of porous structures. Stretching-dominated unit cells have higher elastic moduli and yield strengths than bending-dominated structures, while the latter have a better energy absorption ability [24]. Porosity is inversely related to the mechanical properties of porous metals. In addition to alloying, topological design can be another tool to improve the mechanical properties of AM biodegradable porous metals. However, lower porosity also means lower permeability, which may not be favorable for cells in the center of the scaffolds. These contradicting design requirements call for functionally graded designs. As observed in the case of functionally graded Fe or Zn, the periphery of AM scaffolds can be designed to have a lower porosity for load bearing, while the inner part of the scaffolds can be highly porous for sufficient mass transportation. In the studies presented in this dissertation, we only used the diamond unit cell, because all the struts of the diamond unit cell are tilted at the same angle along the building direction, thus excluding the verities that come from the AM process. The combination of different types of unit cells can be developed in the future. Furthermore, as topological design was also found to affect the biodegradation rates of AM porous Fe and Zn, it would be interesting to investigate its influence on AM porous Mg. More systematic studies are needed to build the relationship between topological design and biodegradation rate. More importantly, topological features, such as pore shape, pore size, and porosity, can all affect the cell adhesion and proliferation [25]. For example, it has been found that 300-1000 μm pore sizes are optimal for bone tissue regeneration [26]. Therefore, further optimization of AM biodegradable porous metal requires a better understanding of the complex relationships between topological design, mechanical properties, biodegradation behavior, and cell responses.

10

10.3. Recommendations

In this section, some general recommendations for potentially interesting future work are presented.

1. From the materials viewpoint, AM needs to be further optimized and investigated in order to obtain materials with the desired properties. Machine learning including deep learning algorithms may be used to build the relationships between composition of the underlying material, the geometry of lattice structures, processing parameters, microstructure, and the mechanical properties of AM materials. The materials "genome" should be established to guide the development of new materials instead of pursuing a trial and error approach.

2. From the design viewpoint, the influence of topological design on the mechanical properties, biodegradation behavior, cell adhesion, and cell proliferation should be systematically investigated using both experimental and numerical approaches.

3. There is still a big gap between *in vitro* and *in vivo* results for biodegradable biomaterials. *In vivo* tests are, therefore, required to evaluate the performance of AM biodegradable porous metals in their actual service conditions.

In addition to the general recommendations presented above, I have also formulated a number of specific recommendations as follows:

Material-related:

1. It would be interesting to explore the potential of AM Mg-based porous metallic glasses and their relevant processing parameters. This approach could result in materials that simultaneously improve the biodegradation resistance and mechanical properties of AM Mg-based porous biomaterials.

2. Alloying of pure iron with other elements should be considered for both improving the mechanical properties and further increasing the biodegradation rate of AM Fe-based porous biomaterials.

3. The mechanical properties of Zn-based AM porous biomaterials should be increased. This could be achieved by alloying Zn with other elements particularly Mg and Ca.

Process-related:

10

4. Better surface polishing solutions need to be developed for AM biodegradable porous metals.

5. Functional coatings can be applied to improve both the biodegradation resistance and biocompatibility of AM porous Mg.

6. The fatigue behavior of AM porous Mg can be further improved by optimizing both the topological design of the porous structure and the laser processing parameters that affect its microstructure to a great extent.

Property-related:

7. The cytotoxicity of AM Fe-based materials need to be systematically studied *in vitro,* as the current results are still debatable. Round-robin test may be a better solution for that purpose.

8. Creep and aging of AM Zn-based biomaterials and their relationship with the performance of such biomaterials need to be further investigated.

9. Different loading regimens, such as compression-tension, tension-tension, bending, and torsion, should be applied to the fatigue tests of AM biodegradable porous metals.

10. The effects of microstructure including the grain size on the biodegradation behavior of AM biodegradable metals should be investigated.

Function-related:

11. In addition to bone implants, AM biodegradable metals could be used for some other types of implantable diagnostic and therapeutic electronic devices.

References

[1] C. C. Ng, M. M. Savalani, M. L. Lau, H. C. Man. Microstructure and mechanical properties of selective laser melted magnesium. Appl Surf Sci. 2011;257:7447-7454.
[2] M. Alvarez-Lopez, M. D. Pereda, J. A. del Valle, M. Fernandez-Lorenzo, M. C. Garcia-Alonso, O. A. Ruano, M. L. Escudero. Corrosion behaviour of AZ31

magnesium alloy with different grain sizes in simulated biological fluids. Acta Biomater. 2010;6:1763-1771.

[3] M. Montani, A. G. Demir, E. Mostaed, M. Vedani, B. Previtali. Processability of pure Zn and pure Fe by SLM for biodegradable metallic implant manufacturing. Rapid Prototyp J. 2017;23:514-523.

[4] Y. Li, H. Jahr, K. Lietaert, P. Pavanram, A. Yilmaz, L. I. Fockaert, M. A. Leeflang, B. Pouran, Y. Gonzalez-Garcia, H. Weinans, J. M. C. Mol, J. Zhou, A. A. Zadpoor. Additively manufactured biodegradable porous iron. Acta Biomater. 2018;77:380-393.

[5] G. R. Argade, S. K. Panigrahi, R. S. Mishra. Effects of grain size on the corrosion resistance of wrought magnesium alloys containing neodymium. Corros Sci. 2012;58:145-151.

[6] Y. Li, P. Pavanram, J. Zhou, K. Lietaert, P. Taheri, W. Li, H. San, M. A. Leeflang, J. M. C. Mol, H. Jahr, A. A. Zadpoor. Additively manufactured biodegradable porous zinc. Submitted.

[7] Y. Li, J. Zhou, P. Pavanram, M. A. Leeflang, L. I. Fockaert, B. Pouran, N. Tümer, K. U. Schröder, J. M. C. Mol, H. Weinans, H. Jahr, A. A. Zadpoor. Additively manufactured biodegradable porous magnesium. Acta Biomater. 2018;67:378-392.

[8] S. M. Ahmadi, R. Kumar, E. V. Borisov, R. Petrov, S. Leeflang, Y. Li, N. Tümer, R. Huizenga, C. Ayas, A. A. Zadpoor, V. A. Popovich. From microstructural design to surface engineering: A tailored approach for improving fatigue life of additively manufactured meta-biomaterials. Acta Biomater. 2019;83:153-166.

[9] R. Walter, M. B. Kannan, Y. He, A. Sandham. Effect of surface roughness on the in vitro degradation behaviour of a biodegradable magnesium-based alloy. Appl Surf Sci. 2013;279:343-348.

[10] L. Yang, C. Yan, W. Cao, Z. Liu, B. Song, S. Wen, C. Zhang, Y. Shi, S. Yang. Compression-compression fatigue behaviour of Gyroid-type Triply Periodic Minimal Surface porous structures fabricated by Selective Laser Melting. Acta Mater. 2019.

[11] J. Parthasarathy, B. Starly, S. Raman, A. Christensen. Mechanical evaluation of porous titanium (Ti6Al4V) structures with electron beam melting (EBM). J Mech Behav Biomed Mater. 2010;3:249-259.

[12] M. Yazdimamaghani, M. Razavi, D. Vashaee, K. Moharamzadeh, A. R. Boccaccini, L. Tayebi. Porous magnesium-based scaffolds for tissue engineering. Mater Sci Eng, C. 2017;71:1253-1266.

[13] X. Wang, S. Xu, S. Zhou, W. Xu, M. Leary, P. Choong, M. Qian, M. Brandt, Y. M. Xie. Topological design and additive manufacturing of porous metals for bone scaffolds and orthopaedic implants: A review. Biomaterials. 2016;83:127-141.

[14] M. Schinhammer, A. C. Hänzi, J. F. Löffler, P. J. Uggowitzer. Design strategy for biodegradable Fe-based alloys for medical applications. Acta Biomater. 2010;6:1705-1713.

10

[15] C. Shuai, L. Xue, C. Gao, Y. Yang, S. Peng, Y. Zhang. Selective laser melting of Zn–Ag alloys for bone repair: microstructure, mechanical properties and degradation behaviour. Virtual and Physical Prototyping. 2018;13:146-154.

[16] Y. Yang, F. Yuan, C. Gao, P. Feng, L. Xue, S. He, C. Shuai. A combined strategy to enhance the properties of Zn by laser rapid solidification and laser alloying. J Mech Behav Biomed Mater. 2018;82:51-60.

[17] Y. Qin, P. Wen, M. Voshage, Y. Chen, P. G. Schückler, L. Jauer, D. Xia, H. Guo, Y. Zheng, J. H. Schleifenbaum. Additive manufacturing of biodegradable Zn-xWE43 porous scaffolds: Formation quality, microstructure and mechanical properties. Mater Des. 2019;181:107937.

[18] B. Liu, Y. F. Zheng. Effects of alloying elements (Mn, Co, Al, W, Sn, B, C and S) on biodegradability and in vitro biocompatibility of pure iron. Acta Biomater. 2011;7:1407-1420.

[19] H. Windhagen, K. Radtke, A. Weizbauer, J. Diekmann, Y. Noll, U. Kreimeyer, R. Schavan, C. Stukenborg-Colsman, H. Waizy. Biodegradable magnesium-based screw clinically equivalent to titanium screw in hallux valgus surgery: short term results of the first prospective, randomized, controlled clinical pilot study. Biomed Eng Online. 2013;12:62.

[20] B. Zberg, P. J. Uggowitzer, J. F. Loffler. MgZnCa glasses without clinically observable hydrogen evolution for biodegradable implants. Nat Mater. 2009;8:887-891.

[21] H. Qin, Y. Zhao, Z. An, M. Cheng, Q. Wang, T. Cheng, Q. Wang, J. Wang, Y. Jiang, X. Zhang, G. Yuan. Enhanced antibacterial properties, biocompatibility, and corrosion resistance of degradable Mg-Nd-Zn-Zr alloy. Biomaterials. 2015;53:211-220.

[22] Y. Xie, L. Zhao, Z. Zhang, X. Wang, R. Wang, C. Cui. Fabrication and properties of porous Zn-Ag alloy scaffolds as biodegradable materials. Mater Chem Phys. 2018;219:433-443.

[23] H. F. Li, X. H. Xie, Y. F. Zheng, Y. Cong, F. Y. Zhou, K. J. Qiu, X. Wang, S. H. Chen, L. Huang, L. Tian, L. Qin. Development of biodegradable Zn-1X binary alloys with nutrient alloying elements Mg, Ca and Sr. Sci Rep. 2015;5:10719.

[24] J. Kadkhodapour, H. Montazerian, A. C. Darabi, A. P. Anaraki, S. M. Ahmadi, A. A. Zadpoor, S. Schmauder. Failure mechanisms of additively manufactured porous biomaterials: Effects of porosity and type of unit cell. J Mech Behav Biomed Mater. 2015;50:180-191.

[25] A. A. Zadpoor. Additively manufactured porous metallic biomaterials. J Mater Chem B. 2019;7:4088-4117.

[26] F. S. L. Bobbert, A. A. Zadpoor. Effects of bone substitute architecture and surface properties on cell response, angiogenesis, and structure of new bone. J Mater Chem B. 2017;5:6175-6192.

10

CURRICULUM VITAE

1989.04.01 born in Shanxi Province, China

Education/Working experiences

2016.06– current   Ph.D. in Dept. of Biomechanical Engineering
Delft University of Technology, Delft, The Netherlands

2013.03–2015.06   Project Engineer in R&D Department
WKW (Beijing) Automotive Parts co. ltd., Beijing, China

2010.09–2013.01   M.Sc. in Dept. of Materials Science and Engineering
University of Science and Technology Beijing, Beijing, China

2006.09–2010.07   B.Sc. in Dept. of Materials Science and Engineering
Taiyuan University of Technology, Shanxi, China

More information

LIST OF PUBLICATIONS

1. **Y. Li**, W. Li, F.S.L Bobbert, K. Lietaert, J-H Dong, M.A. Leeflang, J. Zhou, A.A. Zadpoor. Corrosion fatigue behavior of additively manufactured biodegradable porous zinc. *Acta Biomaterialia* (in press)
2. F.S.L Bobbert, S. Janbaz, T. Manen, **Y. Li**, A.A. Zadpoor. Russian doll deployable meta-implants: fusion of kirigami, origami, and multi-stability. *Materials & Design* (under review)
3. **Y. Li**, P. Pavanram, J. Zhou, K. Lietaert, F.S.L Bobbert, Yusuke Kubo, M.A. Leeflang, H. Jahr, A.A. Zadpoor. Additively manufactured functionally graded biodegradable porous zinc. *Biomaterials Science* (in press)
4. **Y. Li**, P. Pavanram, J. Zhou, K. Lietaert, P. Taheri, W. Li, H. San, M.A. Leeflang, J.M.C. Mol, H. Jahr, A.A. Zadpoor. Additively manufactured biodegradable porous zinc. *Acta Biomaterialia* 101, 609-623 (2020)
5. **Y. Li**, H. Jahr, P. Pavanram, F.S.L Bobbert, U. Puggi, X-Y. Zhang, B. Pouran, M.A. Leeflang, H. Weinans, J. Zhou, A.A. Zadpoor. Additively manufactured functionally graded biodegradable porous iron. *Acta Biomaterialia* 96, 646-661 (2019)
6. **Y. Li**, K. Lietaert, W. Li, X-Y. Zhang, M.A. Leeflang, J. Zhou, A.A. Zadpoor. Corrosion fatigue behavior of additively manufactured porous iron. *Corrosion Science* 156, 106-116 (2019)
7. **Y. Li**, H. Jahr, X-Y. Zhang, M.A. Leeflang, W. Li, B. Pouran, F.D. Tichelaar, H. Weinans, J. Zhou, A.A. Zadpoor. Biodegradation affected fatigue behavior of additively manufactured porous magnesium. *Additive Manufacturing* 28, 299-311 (2019)
8. S.M. Ahmadi, R. Kumar, E.V. Borisov, R. Petrov, S. Leeflang, **Y. Li**, R. Huizenga, C. Ayas, A.A. Zadpoor, V.A. Popovich. From microstructural design to surface engineering: a tailored approach for improved fatigue life of additively manufactured porous titanium. *Acta Biomaterialia* 83, 153-166 (2019)
9. R. Hedayati, S.J. Salami, **Y. Li**, M. Sadighi, A.A. Zadpoor. Semi-analytical geometry-property relationships for some generalized classes of pentamode-like additively manufactured mechanical metamaterials. *Physical Review Applied* 11, 034057 (2019)
10. **Y. Li**, H. Jahr, K. Lietaert, P. Pavanram, A. Yilmaz, L.I. Fockaert, M.A. Leeflang, B. Pouran, Y. Gonzalez-Garcia, H. Weinans, J.M.C. Mol, J. Zhou, A.A. Zadpoor. Additively manufactured biodegradable porous iron. *Acta Biomaterialia* 77, 380-393 (2018)
11. **Y. Li**, J. Zhou, P. Pavanram, M.A. Leeflang, L.I. Fockaert, B. Pouran, N. Tümer, K.-U. Schröder, J.M.C. Mol, H. Weinans, H. Jahr, A.A. Zadpoor. Additively manufactured biodegradable porous magnesium. *Acta Biomaterialia*. 67, 378-392 (2018)
12. S.M. Ahmadi, R. Hedayati, **Y. Li**, K. Lietaert, N. Tümer, A. Fatemi, C.D. Rans, B. Pouran, H. Weinans, A.A. Zadpoor. Fatigue performance of additively manufactured meta-biomaterials: The effects of topology and material type. *Acta Biomaterialia*. 65, 292-304 (2018)
13. R. Hedayati, S.M. Ahmadi, K. Lietaert, **Y. Li**, S. Amin Yavari, A.A. Zadpoor.

Fatigue and quasi-static mechanical behavior of bio-degradable porous biomaterials based on magnesium alloys. *Journal of Biomedical Materials Research Part A* 106, 1798-1811 (2018)

14. R. Hedayati, S.M. Ahmadi, K. Lietaert, B. Pouran, **Y. Li**, H. Weinans, C.D. Rans, A.A. Zadpoor. Isolated and modulated effects of topology and material type on the mechanical properties of additively manufactured porous biomaterials. *Journal of the Mechanical Behavior of Biomedical Materials* 79, 254-263 (2018)

15. S.M. Ahmadi, R. Hedayati, R.K. Ashok Kumar Jain, **Y. Li**, S. Leeflang, A.A. Zadpoor. Effects of laser processing parameters on the mechanical properties, topology, and microstructure of additively manufactured porous metallic biomaterials: A vector-based approach. *Materials & Design* 134, 234-243 (2017)

16. **Y. Li,** W. Mao, W. Zhi, B. Yang, X. Song. Effect of stirring parameters on microstructure of semi-solid 7075 aluminum alloy slurry. *Special Casting & Nonferrous Alloys* 35, 717-719 (2015)

17. **Y. Li,** W. Mao, W. Zhi, B. Yang, Rheological behavior of semi-solid 7075 aluminum alloy at steady state, *China Foundry* 11, 79-84 (2014)

18. W. Mao, Z. Chen, H. Liu, **Y. Li.** Preparation and Rheo-Die casting of Semi-Solid A356 Aluminum Alloy Slurry through a Serpentine Pouring Channel, *Solid State Phenomena* 192, 404-409 (2013)

19. **Y. Li,** W. Mao, W. Zhi, B. Yang, D. Zhu. Microstructure and rheological behavior of semi-solid 7075 aluminum alloy in continuously cooling state, *The Chinese Journal of Nonferrous Metal* 23, 3289-3293 (2013)

ACKNOWLEDGEMENTS

I also want to thank all my colleagues at the Department of Biomechanical Engineering, past and present, **Behdad, Budi, Costanza, Eline, Eric, Helda, Hongshan, Ingmar, Jiahui, Juan, Julian, Khashayar, Kirsten, Lidy, Livia, Mahdiyeh, Mauricio, Marike, Mahya, Mohammad Fazel, Mohammad Mirzaali, Nazli, Niko, Pier, Reza, Sara, Saber, Seyed Mohammad, Sina, Sebastien, Shahram, Teunis, Vahid**. I would like to express my particular appreciation to **Françoise**, not only because of your selfless help during work, but also for your (and **Thomas**) enthusiasm and generosity during daily life that made me feel much better when I was homesick. I am also grateful to the help from my colleagues at the Department of Materials Science and Engineering, such as, **Wei** for the EBSD analysis, **Jun** and **Meng** for the TEM analysis, **Laura**, **Aytac**, and **Peyman** for the FTIR and electrochemical analysis, **Zhiyuan** for the chemicals, **Guoping** for the ceramics, **Yuliu**, **Zhaoying**, **Xiaohui**, **Ziyu**, **Jianing**, **Yang** and **Weichen** for the nice talks. Moreover, I am appreciated for the collaboration with **Prathyusha** from Aachen for the cell culture tests and **Karel** from Layerwise for printing the samples.

Life is not easy when living abroad. I would like to extend my gratitude to my friends who accompanied and supported me during the last three years. **Zhenji**, thanks for all the information before I came here. **Yueting**, thanks for all your help when I first came here. I always enjoy talking to you. Your experience and opinion about artificial intelligence inspired me a lot. **Yabin**, I really enjoyed the time when we both lived in Zusterlaan. We spent most of the spare time together for Chinese food, poker games, ping pong, movies, and volleyball. **Yong**, thanks for pulling me in many sports like badminton, football, and nintendo switch. The vitality you have always cheer me up. **Jian**, you are very considerate for others. I really appreciate the noodles and lamb chop you made on my birthday. All the dancers, **Jilong, Licheng, Zhipeng, Jieli, Lanwen, Hao, Eric, Jiulong, Bing,** I enjoyed all the performance, competition, and training with you together. Moreover, I appreciated all the moments with my friends: smart **Long**, rational **Kai**, organized **Qi**, and painter **Xiangyu**.

最后，我要感谢我的家人，感谢父母、妻子和女儿三年来支持我这个自私的决定，让我能够心无旁骛地、没心没肺地搞科研。父母年迈，我非但没能照顾父母，还要父母帮忙照顾女儿，而您们对我的要求只是好好工作、注意身体，这就是亲情吧。妻子在物欲横流的帝都 996，还要承担教育女儿的重任，压力之大可想而知。在 IT 高收入群体的包围下，你从来没有嫌弃我这个拿着房补的人，还总在我低落的时候让我不忘初心，这就是爱情吧。女儿尚小，爸爸没能陪伴你，你却用笑脸给了我前进的最大动力。谢谢你们的爱，我爱你们！